Strongly interacting phenomena in synthetic quantum systems: from nonlinear topological wave propagation to mobile quantum impurity physics

Nader Mostaan

München 2024

Strongly interacting phenomena in synthetic quantum systems: from nonlinear topological wave propagation to mobile quantum impurity physics

Nader Mostaan

Dissertation
der Fakultät für Physik
der Ludwig-Maximilians-Universität
München

vorgelegt von
Nader Mostaan
aus Esfahan

München, den 02.09.2024

Erstgutachter: Prof. Dr. Fabian Grusdt
Zweitgutachter: Prof. Dr. Nathan Goldman
Tag der Einreichung: 02.09.2024
Tag der mündlichen Prüfung: 16.10.2024

Contents

List of Tables

List of Figures

Zusammenfassung

Diese Dissertation behandelt zwei Hauptthemen von großem Interesse in der Forschung zur Physik synthetischer Quantensysteme: nichtlineare topologische Wellenfortpflanzungs phänomene und die Physik mobiler Quantenverunreinigungen in stark wechselwirkenden Vielteilchensystemen.

Das Thema des ersten Teils ist relevant für eine Vielzahl von schwach wechselwirkenden synthetischen Quantensystemen, wie z.B. photonische Systeme und ultrakalte bosonische Gase. In diesen Systemen ist das Zusammenspiel von Topologie und Nichtlinearitäten ein aktuelles Forschungsthema von großem Interesse. Im ersten Teil erklären wir das Phänomen des topologisch quantisierten Thouless-Pumpens von Solitonen in nichtlinearen eindimensionalen Gittern. Durch die Nutzung der speziellen topologischen Eigenschaften der Wannier-Funktionen der zugrunde liegenden Bandstruktur konstruieren wir ein effektives Modell, das es uns ermöglicht, den beobachteten experimentellen Effekt in experimentell relevanten Regimen mathematisch zu beweisen. Wir diskutieren ausführlich die Bedingungen, unter denen die Annahmen hinter unserem Beweis gültig sind. Wir nutzen dieses Rahmenwerk interdisziplinär und schlagen eine Art von interaktionsinduzierter topologischer Pumpung in eindimensionalen Bose-Bose-Mischungen vor, die nach den gleichen Prinzipien funktioniert.

Das zweite Thema von Interesse in dieser Dissertation sind die Quantenzustände einer mobilen Verunreinigung in stark wechselwirkenden Vielteilchensystemen. Wir betrachten diese Art von Quantenverunreinigungsproblemen in zwei verschiedenen Kontexten: einer mobilen Verunreinigung, die mit bosonischen Atomen in einem Bose-Einstein-Kondensat (BEC) wechselwirkt, und Interlayer-Exzitonen, die mit einem elektronischen fraktionalen Quanten-Hall-System in Van-der-Waals-Heterostrukturen interagieren.

Im Kontext kondensierter bosonischer Systeme führt die Einkleidung einer mobilen Verunreinigung durch Anregungen des BEC zur Bildung eines Quasiteilchens, das als Bose-Polaron bezeichnet wird. Im starken Kopplungsregime ist bekannt, dass Bose-Polaron-Modelle, die auf nicht wechselwirkenden Bosonen basieren, anomales Verhalten im Polaron-Spektrum vorhersagen. Wir beheben diese Anomalie, indem wir das Modell erweitern, um Wechselwirkungen zwischen den Bosonen einzubeziehen. Mit Hilfe eines in dieser Arbeit entwickelten Variationsansatzes zeigen wir, dass das stark wechselwirkende Problem einer mobilen Verunreinigung in einem BEC auf das Problem schwach wechselwirkender Phononen reduziert werden kann, die an *Vielkörper-Bindungszuständen* streuen. Wir zeigen, dass unser Variationsansatz im Gegensatz zu den bestehenden gaußschen Variation-

szuständen in der Lage ist, nicht gaußsche Korrelationen einzubeziehen, und es uns somit ermöglicht, Eigenschaften der Vielkörperresonanzen des Systems aufzudecken, die in der Literatur bisher nicht diskutiert wurden.

Im Kontext von Van-der-Waals-Heterostrukturen betrachten wir ein $MoSe_2$/WSe_2/graphene Gerät, bei dem Interlayer-Exzitonen im $MoSe_2$/WSe_2 Heterobilayer mit einem $\nu = 1/3$ elektronischen fraktionalen Quanten-Hall-Zustand in Graphen wechselwirken. Zunächst behandeln wir das Drei-Körper-Problem des Interlayer-Exziton-Karrierer-Streuens und charakterisieren die resultierenden Drei-Körper-Zustände. Wir zeigen, dass im Gegensatz zum Fall ohne Magnetfeld, bei dem keine gebundenen Zustände von Exzitonen und Karrierern entstehen können, im Magnetfeld das Exziton Karrierer binden kann. Anschließend betrachten wir das vollständige Vielkörperproblem und finden, dass ein Quasiloch an ein Interlayer-Exziton binden und anyonische Trionen bilden kann. Die Erzeugung und Beobachtung solcher anyonischer Trionen infolge der Quasiloch-Bindung an defekt lokalisierte Interlayer-Exzitonen kann zu einer räumlichen und bewegungstechnischen Kontrolle über Quasilöcher in Quantum Optical Twist and Scan Microscopes (QOTSM) führen, ein Weg, der letztlich den direkten Zugang zu den fraktionalen Statistiken der Quasilöcher ermöglichen kann.

Abstract

This thesis addresses two main topics of high interest in reserch on the physics of synthetic quantum systems: nonlinear topological wave propagation phenomena and the physics of mobile quantum impurities in strongly interacting many-body systems.

The topic of the first part is relevant for a wast variety of weakly interacting synthetic quantum systems, such as photonic systems and ultracold bosonic gases. In these systems, a recent topic of great interest concerns the interplay of topology and nonlinearities. In the first part, we explain the phenomenon of topologically quantized Thouless pumping of solitons in nonlinear one-dimensional lattices. Leveraging the special topological properties of the Wannier functions of the underlying band structure, we construct an effective model which enables us to mathematically prove the observed experimental effect in experimentally relevant regimes. We discuss in detail the conditions under which the assumptions behind our proof are valid. We exploit this framework interdisciplinarily and propose a type of interaction-induced topological pumping in one-dimensional Bose-Bose mixtures, which operators on the basis of the same principles.

The second topic of interest in this thesis is the quantum states of a mobile impurity in strongly interacting many-body systems. We consider this type of quantum impurity problems in two different settings: a mobile impurity interacting with bosonic atoms in a Bose-Einstein Condensate (BEC), and interlayer excitons interacting with an electronic fractional quantum Hall system in van der Waals heterostructures.

In the context of condensed bosonic systems, dressing of a mobile impurity by excitations of the BEC leads to the formation of a quasiparticle dubbed Bose polaron. In the strong coupling regime, it is known that Bose polaron models based on non-interacting bosons predict anomalous behavior of the polaron spectrum. We cure this anomaly by extending the model to incorporate inter-boson interactions. By means of a variational ansatz constructed in this work, we show that the strongly interacting problem of a mobile impurity in a BEC can be reduced to the problem of weakly interacting phonons scattering off *many-body bound states*. We show that, contrary to the existing Gaussian variational states, our variational ansatz is capable of including non-Gaussian correlations, and as such, enables us to reveal properties of the multi-body resonances of the system which were not previously discussed in the literature.

In the context of van der Waals heterostructures, we consider a $\mathrm{MoSe_2/WSe_2}$/graphene device, where interlayer excitons in the $\mathrm{MoSe_2/WSe_2}$ heterobilayer interact with $\nu = 1/3$ electronic fractional quantum Hall states in the graphene layer. First, we address the three-body problem of interlayer exciton-carrier scattering and characterize the resulting three-body states. We show that, contrary to the case with no magnetic field, where bound states of exciton and carriers can not form, in the presence of a magnetic field, the exciton can bind carriers. We then consider the full many-body problem, and find that a qausihole can bind to an interlayer exciton and form anyonic trions. Creation and observation of such anyonic trions as a result of quasihole binding to defect localized interlayer excitons can lead to spatial and motional control over quasiholes in Quantum Optical Twist and Scan Microscopes (QOTSM), a path that eventually can lead to direct access to the quasihole fractional statistics.

List of Publications

[1] **Mostaan, N.**, Grusdt, F., & Goldman, N. (2022). Quantized topological pumping of solitons in nonlinear photonics and ultracold atomic mixtures. nature communications, 13(1), 5997.

N.M. conceived the theoretical framework under the supervision of N.G., with inputs from F.G.. N.M. performed the analytic calculations and numerical simulations, with inputs from N.G.. All authors analyzed and discussed the results. N.M. and N.G. wrote the manuscript with inputs from F.G..

[2] **Mostaan, N.**, Goldman, N., Grusdt, F. (2023). A unified theory of strong coupling Bose polarons: From repulsive polarons to non-Gaussian many-body bound states, arXiv preprint arXiv:2305.00835

F. G. proposed the initial idea. N. M. extended the idea and performed all the analytical and numerical calculations. All authors contributed extensively to the analysis of the results. N. M. wrote the manuscript, with inputs from N. G. and F. G..

[3] Grusdt, F.,**Mostaan, N.**, Demler, E., Pena Ardila, L. (2024). Impurities and polarons in bosonic quantum gases: a review on recent progress, *to be submitted to Reports on Progress in Physics.*

N. M. wrote the chapters “Few-body effects and polaron physics" and “Finite temperature Bose polaron". F. G. wrote the chapters “From weak-coupling Fröhlich theory to strong-coupling Bose polarons", “Quantum dynamics and non-equilibrium polaron physics", “Bose polarons in low dimensions", “Bose polarons in other settings". F. G. and L. A. P. wrote the chapters “Introduction", “Overview of experiments". L. A. P. wrote the chapter “Interacting polarons and induced interactions" and “Strong coupling Bose polarons". All authors contributed to the content, discussions and the revision of the material.

In preperation:

[4] Grusdt, F., Goldman, N., İmamoğlu, A., **Mostaan, N.** [1] (2024) Realization of

---

[1] Names are organized in alphabetical order according to a Last Name-First Name basis.

anyon polarons in van der Waals heterostructres, *to be submitted to Physical Review X.*

Other publications:

[5] Englebert, N., Goldman, N., Erkintalo, M., **Mostaan, N.**, Gorza, S.P., Leo, F. and Fatome, J., 2023. Bloch oscillations of coherently driven dissipative solitons in a synthetic dimension. Nature Physics, 19(7), pp.1014-1021.

All authors contributed to the conception of the research and the analysis and interpretation of the results. N.E. performed the experiments and derived the reduced model with supervision from S.-P.G. and F.L. N.E., J.F. and M.E. performed simulations of the LLE and the reduced model. N.E., N.G., M.E. and J.F. prepared the manuscript, with input from all authors.

[6] Ravets, S., Pernet, N., **Mostaan, N.**, Goldman, N. and Bloch, J. Thouless pumping in a driven-dissipative Kerr resonator array, arXiv preprint arXiv:2407.02627

Chapter 1

Introduction

Information processing and communication technologies undeniably constitute a cornerstone of human civilization. From the ancient rudimentary tools of arithmetic like the abacus to today's cutting-edge computers, the capabilities of information systems has advanced at a breathtaking pace. These advancements are evident not only in the evolving conceptual design and architecture of these systems but also in the growing sophistication of the physical devices that handle information processing, storage, and communication tasks. Despite the vast variety of information systems and their diverse applications, every system includes a fundamental physical layer, which is essential for executing the basic tasks of information processing, storage and transmission. For instance, a basic central processing unit (CPU) implementing MIPS instruction set architecture (ISA) may comprise of hundreds of arithmetic logic units (ALU) and random access memories (RAM), which are built from circuit elements such as logic gates and memory cells. Both the logic gates and memory cells are made from transistors, which operate as current-controlled switches that store bits of information. While the higher level computation algorithms that the processor executes are independent of the physical realization of bits, numerous factors pertaining to the characteristics of the physical device significantly influence the performance of the entire system. A witness to this influence is the revolutionary impact on the information technologies brought about by the invention of transistors, which drastically transformed the capabilities of computers and communication systems previously based on vacuum tubes. This influence is particularly more evident today as the increase in complexity and scale of computational problems demands physical devices that surpass the current ones in speed, efficiency (both in energy consumption and performance), and reliability.

In addition to the classical information systems, the potential for realization of quantum information processing (QIP) and quantum communication systems has sparked a surge in research on various aspects of quantum information technology. In QIP, the connection between processing quantum information and physical effects such as increase in entropy is far more intricate – a minimal example being the Landauer's principle, also reflected in his famous quote "Information is physical". This deep connection between the abstract concepts of QIP and the physical quantum devices highlights the crucial importance of developing quantum devices that meet the stringent requirements demanded by the effective implementation of QIP tasks.

Beyond technological relevance, the progress in fundamental physics also drives the development of devices with unprecedented controllability and precision. Recent breakthroughs in fundamental physics such as the detection of gravitational waves through gravitational wave interferometry were made possible by the advancements in highly precise quantum sensors such as high-Q optomechanical resonators. Besides, progress in quantum metrology and precision measurement are expected to enable future experiments with groundbreaking impacts, aimed at testing general relativity, detection of dark matter, and scrutinizing the foundations of quantum mechanics. The influential consequences of device development extends beyond fundamental physics to the realm of condensed matter physics, where the exploration of strongly correlated many-body systems is now feasible both in semiconductor heterostructures and in ultracold atomic gases loaded in optical lattices. Notable recent experimental breakthroughs in this area includes the optical detection of kinetic magnetism and correlated electronic insulators such as Wigner crystals, detection of fractional Chern insulators, and realization of Harper-Hofstadter and Fermi-Hubbard models in ultracold atomic gases in Floquet-engineered optical lattices.

Despite their vastly different functionalities and purposes, all the devices mentioned above share a common characteristic: they are all *synthetic quantum systems* – quantum systems that do not occur naturally but are fabricated in laboratories under well-controlled experimental conditions using advanced fabrication processes. The remarkable technological growth in the sophisticated machinary used for constructing, operating and maintaining the synthetic quantum systems has enabled the realization of quantum phenomena so fragile and intricate that their observation using mainstream laboratory equipment seems inconceivable. Indeed, the scope of quantum phenomena and the synthetic platforms used to realize them is so extensive that listing even a fraction of them is impossible. However, some notable examples across markedly different platforms include the realization of metastable polaron quasiparticles in ultracold atomic mixtures and hybrid exciton-electron systems in semiconductor heterostructures , topologically ordered quantum spin liquids in Rydberg array tweezers, strongly correlated electronic states mentioned above, and creation and manipulation of unconventional states of light like topological frequency combs and solitons in diverse photonic structures (Although the later effects are not quantum mechanical strictly speaking, they are intimately connected with quantum mechanical wave phenomena). These examples highlight the breadth of physical effects and synthetic platforms involved.

In this thesis, we explore two fundamental domains of prime importance in the study of synthetic quantum systems: *mobile quantum impurity problems* and *wave propagation in nonlinear media*. In the following, we briefly discuss the scope and context of the research carried out in each of these fields, beginning with mobile quantum impurity problems and subsequently moving on to nonlinear wave propagation.

Quantum impurity problems represent a class of paradigmatic problems in the physics of synthetic quantum systems. In a broad sense, a quantum impurity problem is concerned with the physics of a quantum system with few degrees of freedom interacting with an extended quantum system described by a quantum field theory. From the early days of quantum mechanics, such problems have been at the center of theoretical and experimental research. An iconic example is the problem of a single atom interacting with electromagnetic radiation – a problem that underlies all of the developments in quantum optic and, in modern times, in the study of open quantum systems. Indeed, many relevant open quantum systems settings comprised of quantum devices - such as superconducting qubits and quantum dots - coupled to their environment fall within the category of quantum impurity problems.

While quantum impurity problems come in many shapes and forms and have incredibly diverse ramifications, the main focus in this thesis is on a subclass of them called *mobile quantum impurity problems*. Historically, these types of problems emerged in the study of electron mobility in polar semiconductors, leading to the formulation of the *polaron* concept by Landau and Pekar. In its original context, a polaron is a quasiparticle formed from an electron dressed by optical phonon excitations of a polar semiconductor, a concept that also became relevant in the study of electron-phonon interaction in superconductivity. Surprisingly, polaron physics gained relevance in areas completely separate from its original context. It turned out that the physics of ultracold atomic mixtures in the extreme population imbalance regime can be well described through polaron models, leading to significant attention in ultracold mixtures research. In parallel, polaron physics also appeared in the study of optical excitations in doped semiconductor heterostructures, where excitons can become dressed by particle-hole excitations of a two dimensional electron gas (2DEG), forming exciton Fermi polarons. In this thesis, we address two core problems pertaining to mobile impurities in both of these settings: in the former, we investigate the physics of many-body bound state formation in impurities strongly coupled to condensed bosonic ultracold gases. In the latter, we study how a topologically trivial impurity can inherit topological properties through interaction with a topologically ordered many-body system.

The problem of a mobile impurity in an ultracold bosonic gas in the condensed phase is gaining ever-increasing attention in the ultracold atom community. It is connected to many fundamental topics in condensed matter physics such as quasiparticle formation and interaction, orthogonality catasthrophe, quantum criticality, and the interplay of few- and many-body physics in ultracold gases. In this setting, the impurity is dressed by the excitations of the Bose-Einstein condensate (BEC) and forms a quasiparticle dubbed *the Bose polaron*. In the strong coupling regime, where the impurity-boson attractive interaction is strong enough that impurity-boson dimers can form, there is a consensus in the community that the many-body spectrum of the system becomes very rich due to the interplay of many length and energy scales and the presence of few-body correlations. However, except for certain limiting cases, little is known about the states of the impurity boson system. In the strong coupling regime, several theoretical works and numerical studies based on quantum Monte Carlo methods have predicted the emergence of multiple discrete resonances with negative energies, dubbed “many-body bound states”. Despite this, many aspects of these many-body resonances remain surrounded by uncertainty, and no in-depth study has adequately characterized them. This inadequacy is partly because the current theoretical models of strong coupling Bose polarons have significant shortcomings in modelling strong coupling phenomena.

The first original contribution of this thesis is to the understanding of strong coupling Bose polaron physics and the nature of the many-body bound states. Specifically, we have addressed a serious shortcoming of the existing models and extended them to include the inter-boson repulsive interaction, a crucial step in accurately modeling strong coupling Bose polaron physics. We then developed a theoretical scheme consisting of an effective model and a suitably tailored variational ansatz, focusing on the limit where the impurity-boson dimer energy far exceeds all other energy scales in the problem. Through this theoretical formalism, we were able to uncover striking characteristics of these many-body resonances. For instance, we revealed that the competition between the impurity-induced instability and the repulsive inter-boson interaction results in a finite number of resonances, as opposed to earlier works that predicted an infinite number of resonances. The number of these resonances, their energy spacing and their avoided crossings exhibit striking pattern that reflects the significance of the aforementioned competition. The inter-boson interactions further results in strong anti-bunching of bosons close to the impurity, leading to non-Gaussianity of their quantum state. Furthermore, we anticipate pronounced signatures of these resonances in future extensions of current experiments to include molecular spectroscopy protocols.

In addition to the above work on Bose polarons, the second original contribution of this thesis addresses another intriguing problem related to the physics of mobile impurities in topologically ordered many-body systems: *how does the impurity-medium interaction imprint signatures of topological order on the impurity?* This question is particularly relevant in light of the recent experiments on the optical manipulation of strongly correlated electronic systems in atomically thin semiconductor heterostructures composed of transition metal dichalcogenides (TMD). In these platforms, optical excitations induce tightly bound excitons which appear as neutral impurities scattering off the electrons doped into the system. When the electrons form a weakly interacting 2DEG, exciton Fermi polarons are formed. While exciton Fermi polaron formation is well understood, the exciton spectrum in the presence of strongly correlated incompressible electronic states such as fractional quantum Hall states remains unexplored. To address this question, we propose an experimental setup demonstrating that mobile interlayer excitons in a $MoSe_2/WSe_2$ heterobilayer can bind to quasihole excitations of a $\nu = 1/3$ fractional quantum Hall electronic state in a proximate monolayer graphene, forming *anyonic trions*. The anyonic trion formation is evidenced by a positive binding energy, on the order of the exciton Hartree shift, making it experimentally detectable via optical spectroscopy. Additionally, the exciton-electron spatial correlation function reveals the hallmark signature of a quasihole localized around the exciton. Given the fractional charge and statistics of the quasihole, the formation of exciton-quasihole bound states implies imprinting of gauge structures on a charge-neutral particle, an excellent example of how interaction with an exotic topologically-ordered many-body environment can induce non-trivial topological properties through imprinting a gauge structure on otherwise topologically trivial impurities. We also show that interlayer excitons localized in quantum defects at the tip of a Quantum Optical Twist and Scan

Microscope (QOTSM) can create quasiholes in the proximate graphene layer, allowing for spatial control over quasihole creation with nanometer precision. Furthermore, since defect potentials in TMD materials are generally stronger than those in graphene, the quantum defect can depin the quasihole, even enabling control over its motion. The ability to control the position and motion of quasiholes in QOTSMs, combined with the potential to create ground-state interlayer excitons with exceptionally long lifetimes, holds significant promise for performing anyon braiding and gaining direct access to their fractional statistics.

The second main topic of this thesis is the interplay of nonlinear physics and topology in wave propagation phenomena in one dimensional (1D) synthetic systems. Indeed, gaining control over wave properties, such as phase and amplitude profile, localization, decay, group velocity and scattering off defects is a topic of central importance in many areas such as atom optics, matter waves, and photonics, both in the classical and quantum regime. In photonics, the prospect of generating stable wave fronts with high tunability in their degree of localization, lifetime, propagation direction and robustness against disorder has a significant impact on the efficiency of many photonic processes of direct technological relevance, among them frequency conversion, non reciprocity and lasing. The advent of topological photonics has promised the engineering of electromagnetic modes that are robust against disorder and fabrication imperfections. The study of the implications of such topological robustness on established nonlinear effects and their potential improvement has recently emerged as an active research area in photonics, dubbed *nonlinear topological photonics*.

The third original contribution of this thesis is the explanation of the phenomenon of *quantized soliton transport in nonlinear topological lattices*. This phenomenon was first observed in photonic topological waveguide arrays under strong pump powers that drive the system into the nonlinear regime. Under quite general arguments, we demonstrate that this effect can occur in generic nonlinear topological 1D lattice systems when the nonlinearity remains below the bifurcation transition threshold. We further extended the paradigm to ultracold Bose-Bose mixtures, demonstrating that an interaction-induced topological pump can be activated for a topologically trivial species.

Outline of the thesis this thesis is organized as follows:

- In Chapter I, we explore the interplay of nonlinearity and topology in weakly interacting bosonic systems in the context of a recently observed nonlinear topological phenomenon: the topologically quantized transport of solitons in 1D topological lattices. By representing the actual model in terms of the maximally localized Wannier states of the underlying band structure, we construct an effective model which can explain the observed experimental effect. We investigate the applicability conditions and the validity of the assumptions in details, and provide conservative bounds for the parameters of the nonlinear system for which soliton transport is topologically robust. Exploiting the generality of the formalism developed in this chapter, we generalize it to the case of nonlinear matter waves in two-component Bose-Bose mixtures. We argue that an interaction induced topological pump is enabled for a topologically trivial minority atomic species as a result of its interaction with the majority species.

- In Chapters II we switch the context and investigate the problem of a mobile impurity in a Bose-Einstein Condensate (BEC), leading to the formation of a quasiparticle termed Bose polarons. In the strong coupling limit, the current Bose polaron models suffer from an anomaly which results in the prediction of binding indefinite number of particles to the impurity. We extend the model to include inter-boson interactions, which results in the stability of the system. In the limit of extremely strong interactions, we show that the construction of an effective model suggests a particular variational ansatz which is effective to describe the low energy spectrum of the system. We show that, contrary to the existing Gaussian variational states, our variational ansatz is capable of including non-Gaussian correlations, and as such, enables us to reveal properties of the multi-body resonances of the system which were not previously discussed in the literature.

- In Chapter III, we consider the setting of a mobile impurity in a fractional quantum Hall system, which is relevant in the context of current experiments on optical manipulation and control of electronic fractional quantum Hall states in van der Waals heterostructures. In this regard, we consider a $MoSe_2/WSe_2$/graphene van der Waals heterostructure, where interlayer excitons can form in the $MoSe_2/WSe_2$ heterobilayer, while a $\nu = 1/3$ fractional quantum Hall state of carriers in graphene can be prepared. First, we investigate the three-body problem of interlayer exciton-carrier scattering and characterize the resulting three-body states. We show that, contrary to the case with no magnetic field, where bound states of exciton and carriers can not form, in the presence of a magnetic field, the exciton can bind carriers. We then consider the many-body problem of an interlayer exciton interacting with a $\nu = 1/3$ fractional quantum Hall state at fillings corresponding to few quasiparticle/quasihole excitations in the system. We find that when a qausihole exists in the system, an interlayer exciton with repulsive interaction with charge carriers in graphene can bind quasiholes and form anyonic trions. Creation and observation of such anyonic trions as a result of quasihole binding to defect localized interlayer excitons can lead to spatial and motional control over quasiholes in Quantum Optical Twist and Scan Microscopes (QOTSM), a path that eventually can lead to direct access to the quasihole fractional statistics.

Chapter 2

Quantized transport of solitons in nonlinear Thouless pumps

This chapter is based on the following publication:

[1] **Mostaan, N.**, Grusdt, F., & Goldman, N. (2022). Quantized topological pumping of solitons in nonlinear photonics and ultracold atomic mixtures. nature communications, 13(1), 5997.

In this chapter, we investigate the interplay of nonlinearity and topology in the phenomena associated to wave propagation in a class of engineered quantum systems whose physics is described by bosonic fields. This class of quantum systems contain ultracold bosonic gases and photonic systems as two broad subclasses with great significance in both science and technology. These bosonic quantum systems also have a semiclassical mode of operation. In their semiclassical limit, the bosonic field which describe the system evolve predominantly in a coherent state. The dynamics of these systems in the semiclassical limit thus is described by semiclassical wave equations. Therefore, gaining control over wave dynamics in such systems is central to control their operation.

Controlling wave dynamics, whether in the form of matter waves in atomic media such as BECs, or electromagnetic fields, requires managing many properties of the waves such as the wave front, dispersion, phase and intensity profile, and decay channels, to name but a few. Due to its significance in applications in laser optics, photonics and telecommunication, this goal has driven the construction of many paradigmatic platforms, such as photonic crystals, waveguide arrays, and photonic metamaterials. In such platforms, it is possible to determine the operating frequencies and bandwidths of a device basically at will. The design principles and concepts for engineering the mode profile and frequency of the electromagnetic fields in such photonic systems are inspired by concepts originally developed in solid state physics to describe the motion of electronic waves in ionic crystals. These concepts include wave scattering by periodic structures, band structure and Bloch's theorem, the importance of symmetries, and many more. It didn't take long from the initial influences of such basic concepts on the design of photonic structures until solid state physics introduced another paradigm into the realm of photonics: topological protection. Indeed, triumphant developments in the discovery and explanation of topological phenomena such as the quantum Hall effect in two dimensional electron gases [96, 167] established the intimate connection between the band structure topology and the appearance of chiral edge and surface modes on the boundary of topological insulators which are robust to scattering. Finding photonic modes as solutions to the Maxwells equations in a photonic medium that are robust to fabrication imperfections (such as disorder or dielectric fluctuations) is of prime importance in making high efficiency devices. The topologically robust edge modes offer such an opportunity, and harnessing this topological protection is one of the major current research directions in photonics [156], as well as other synthetic systems [49].

The importance of topology is not restricted to the robustness of the edge mode, but also extends to the protection of certain responses. In particular, various forms of quantized responses have been identified associated to a variety of different band structures, for instance the quantized Faraday and Kerr rotations in three-dimensional topological insulators [215] and quantized circular dichroism [13] and topological Bloch oscillations [132, 97] in two-dimensional ultracold atomic gases.

From a completely different side, many fundamental physical processes that underlies the operation of photonic devices are based on notions of nonlinear optics [26]. Such processes include four wave mixing, second and higher harmonic generation, frequency conversion, non-reciprocity, and laser physics. For instance, the efficiently of some of these nonlinear processes, such as parametric amplification, depends on an effect called phase matching [26], which briefly refers to enhancement in the generated light intensity in the propagation direction as a result of the constructive interference of the nonlinearly generated signal. Thus, the potential to do nonlinear physics with topological robust modes means that the efficiency of these processes can be enhanced. This potential has attracted recently a lot of interest, giving rise to an emergent field called *nonlinear topological photonics*, which pursues exactly the above goal, namely, how one can improve the performance of photonic devices by properly controlling the underlying nonlinear processes by harnessing the favorable properties of topological modes [191]. This endeavor has motivated to drive the current known topological photonic systems into their nonlinear regime.

Typically, due to the weak interaction among photons, mediated by the matter interaction, nonlinear effects only get important at high light intensities. When the light intensity is increased in certain materials, the refractive index of the materials becomes intensity dependent. In certain cases, this intensity dependence increases the refractive index, whose increase beyond the certain threshold, leads to the trapping of light. In this situation, light intensity gets trapped by itself, a phenomenon called *self trapping*. The self-trapping effect is enabled by a competition between attractive nonlinearity and the inherent tendency of waves to disperse, and the complete cancellation of these two effects leads to the long lifetime of the self-trapped waveforms, leading to the creation of a *nonlinear stable state* of the system. Such nonlinear stable states can either be fixed in space, or propagate. In the latter case, they typically maintain their shape, thus leading to the emergence of waveforms which propagate in time and space, while their shape (intensity and phase profile) remain intact. Such a peculiar nonlinear wave is called *Soliton*, a term which also used to refer to their immobile counterparts. Studying different mechanisms behind soliton formation and propagation is one of the major areas in photonics, since solitons are valuable objects when it comes to applications. Indeed, many important waveforms in photonics, such as frequency combs [160] are solitons.

In this chapter, we focus on an interesting recently discovered phenomenon, the quantized pumping of solitons in nonlinear Thouless pumps [110]. The experiment reported the quantized propagation of a bright soliton created in a 1D nonlinear lattice, whose linear spectrum was designed to show *the Thouless pumping effect* [202, 219], a topological effect in periodically time dependent lattices. Thouless pumping is one of the minimal examples of quantized transport in 1D lattice systems. Its realization in synthetic lattice systems has attracted a lot of attention, both in photonics [121, 206, 230, 84, 36, 113] and ultracold atomic gases [135, 151]. The observation of nonlinear quantized Thouless pump is peculiar since topological protection is inherently a concept pertaining to linear systems, and there is no direct way to deduce its generalization to nonlinear systems. In this regard, studying the interplay between nonlinearities and the underlying topological structure of a model is a topic of central concern in the research on synthetic systems [131, 193, 196, 18, 104, 79, 148, 149, 218, 159, 146, 116, 146]. In relation to this problem, the first part of our work concerns the explanation of the quantization of soliton motion, and exploring its validity conditions. We introduce a theoretical framework which clarifies the connection between topological band indices and soliton transport in a broad class of 1D nonlinear topological lattice models described by the discrete nonlinear Schrödinger equation (DNLS) [199, 114]. The generality of our approach allows us to mathematically demonstrate the topological nature of nonlinear Thouless pumps, by relating the quantized motion of solitons to the Chern number of the underlying Bloch band. We then exploit the understanding gained in the first part to extend it to other settings relevant in synthetic quantum systems, where nonlinear wave physics occurs, a prime example of which is the dynamics of nonlinear matter waves in ultracold atomic media.

2.1 Topological pumping of solitons: a general theory

The theoretical description of soliton pumping relies on the topological character of Wannier functions, namely, the displacement of Wannier centers per pump cycle by the Chern number of the associated Bloch band, see Fig. 2.1(a). Intuitively, the reason behind soliton pumping is that solitons are formed around a single Wannier function and follow its motion throughout the pump sequence, resulting in their topologically quantized motion, see Fig. 2.1(b). Interestingly, nonlinearities can induce this drag effect in topologically trivial systems. To demonstrate this effect, we consider a 1D atomic Bose-Bose mixture in a species-selective optical lattice, where the majority (minority) atoms experience a topological (trivial) lattice. We show that a soliton of minority atoms undergoes quantized displacement by activating a Thouless pump sequence for the majority atoms; see

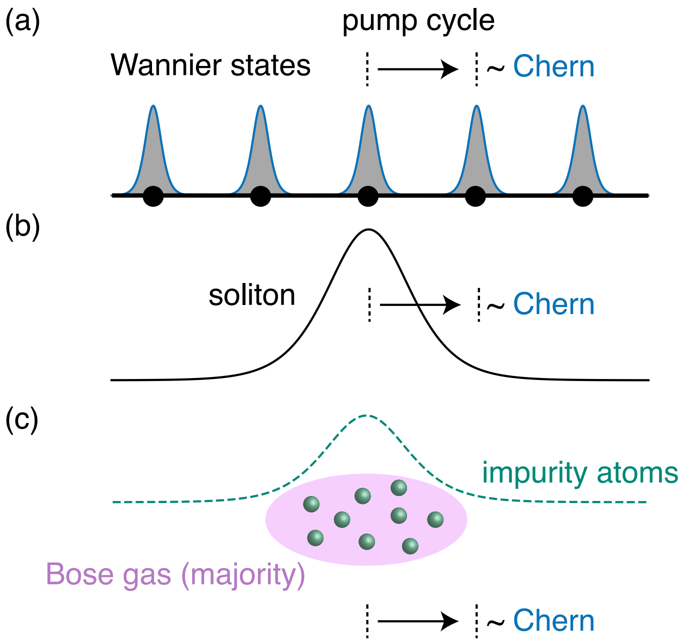

Figure 2.1: Schematics of the soliton pumping mechanism and the nonlinearity-induced pumping in ultracold mixtures. (a) In a Thouless pump, the Wannier functions undergo a quantized motion determined by the Chern number of the corresponding band. (b) When attractive nonlinearities are introduced, the motion of a soliton follows the quantized Wannier transport. (c) In a Bose-Bose atomic mixture, quantized pumping can be induced by interactions : a soliton of impurity atoms is dragged by the driven majority atoms, leading to interaction-induced topological transport.

Fig. 2.1(c). In the following, we elaborate on the theoretical description of soliton motion in nonlinear Thouless pumps and the interaction-induced topological pumps for atomic mixtures.

Our theoretical framework concerns a generic class of lattice models governed by the DNLS,

$$i\partial_t\phi_{i,\alpha} = \sum_{j,\beta} H_{ij}^{\alpha\beta}(t)\,\phi_{j,\beta} - g\,|\phi_{i,\alpha}|^2\phi_{i,\alpha}\,, \tag{2.1}$$

where the field $\phi_{i,\alpha}$ is defined at the lattice site α of the ith unit cell; $H(t)$ is a time-dependent Hamiltonian matrix, which includes a Thouless pump sequence [202, 12]; and $g>0$ is the (onsite) nonlinearity strength. Equation (2.1) preserves the norm of the field, which we set to $\sum_{\alpha,i}|\phi_{i,\alpha}|^2=1$, without loss of generality.

An illustrative model, used below to validate the general theory, is provided by the two-band Rice-Mele model [135]: a 1D chain with alternating couplings $J_{1,2}(t)$ and staggered potential $\pm\Delta(t)$. Considering the *nonlinear* Rice-Mele model, Eq. (2.1) takes the more explicit form

$$\begin{aligned} i\partial_t\phi_{i,1} &= J_1(t)\phi_{i,2} + J_2(t)\phi_{i-1,2} + \Delta(t)\phi_{i,1} - g\,|\phi_{i,1}|^2\phi_{i,1}, \\ i\partial_t\phi_{i,2} &= J_1(t)\phi_{i,1} + J_2(t)\phi_{i+1,1} - \Delta(t)\phi_{i,2} - g\,|\phi_{i,2}|^2\phi_{i,2}. \end{aligned} \tag{2.2}$$

Here, the Thouless pump cycle corresponds to a loop in the parameter space spanned by $(J_2 - J_1)$ and Δ, which encircles the origin $(J_1 = J_2, \Delta = 0)$. When $g = 0$, the Bloch bands defined in momentum-time space are associated with a Chern number $C = \pm 1$. This topological invariant is known to determine the quantized displacement for a filled band upon each cycle of the pump [12]. We come back to the Rice-Mele model in Sec. 2.2.

Our analysis starts by studying the adiabatic evolution associated to the general Eq. (2.1), which is characterized by the period of the pump T (exceeding all other time scales). To simplify notations, we use the multi-index $\mathbf{i} = (i, \alpha)$ and write $H_{\mathbf{ij}} \equiv H_{ij}^{\alpha\beta}(t)$. Introducing the *adiabatic time* $s = t/T$, Eq. (2.1) takes the form $i\varepsilon\partial_s\phi_{\mathbf{i}} = \sum_{\mathbf{j}} H_{\mathbf{ij}}(s)\,\phi_{\mathbf{j}} - g|\phi_{\mathbf{i}}|^2\phi_{\mathbf{i}}$, where $\varepsilon = 1/T$. The solutions to the adiabatic DNLS can be well approximated by stationary states of the form $\phi_{\mathbf{i}} \propto e^{-i\theta_s}\,\varphi_{\mathbf{i}}$, where θ_s is a time-dependent phase factor and $\varphi_{\mathbf{i}}$ is an instantaneous solution to the stationary nonlinear Schrödinger equation (see Refs. [73, 33])

$$\mu_s\,\varphi_{\mathbf{i}} = \sum_{\mathbf{j}} H_{\mathbf{ij}}(s)\,\varphi_{\mathbf{j}} - g\,|\varphi_{\mathbf{i}}|^2\varphi_{\mathbf{i}}\,, \tag{2.3}$$

where the instantaneous eigenvalue μ_s explicitly depends on the adiabatic time s. The adiabatic theorem for NLS (both continuous and discrete forms), follows closely the formulation of its linear counterpart [33, 73]. For a system with a time-dependent Hamiltonian $H(t)$, which varies on a time scale T much larger than all the time scales in the problem, the time-dependent NLS takes the following form

$$i\varepsilon\,\partial_s\phi = \; H(s)\,\phi - g|\phi|^2\phi, \tag{2.4}$$

The stationary state solutions of Eq. (2.4) are of the form

$$\phi_s = e^{-i\theta_s}\left(\varphi_s + \delta\,\varphi_s\right), \tag{2.5}$$

where φ_s is the instantaneous solution of the stationary NLS,

$$\mu_s\,\varphi_s = \; H(s)\,\varphi_s - g\,|\varphi_s|^2\varphi_s\,, \tag{2.6}$$

and $\theta_s = 1/\varepsilon\Big(\int_0^s ds'\,\mu_{s'} - \gamma_s\Big)$ is a global phase factor consisting of a dynamical contribution and a Berry phase, and it can be ignored. The correction term $\delta\,\varphi_s$ accounts for non-adiabatic variations, and for $\varepsilon \to 0$, it behaves as $||\delta\,\varphi|| \sim \varepsilon$, hence vanishes in the adiabatic limit $\varepsilon \to 0$. The relevant dynamical information is therefore encoded in the instantaneous solutions of Eq. (2.6).

Equation (2.3) admits (bright) solitons as stationary state solutions, which are stable localized structures in the bulk. For sufficiently weak nonlinearity, solitons predominantly occupy the band from which they bifurcate [201], while increasing nonlinearity leads to band mixing. In real space, solitons are immobile without external forcing, and are degenerate modulo a lattice translation set by the translational symmetry of the system. By adiabatically changing the Hamiltonian $H_{\mathbf{ij}}(s)$, a single soliton undergoes smooth deformation, and after one period, it is mapped to the manifold of initial solutions, implying translation by an integer multiple of the unit cell. The observations of Ref. [110] suggest that solitons bifurcating from a single Bloch band undergo a quantized displacement dictated by the Chern number of the band [202] over each pump cycle. Demonstrating this intriguing relation between the transport of nonlinear excitations and topological band indices is at the core of the present work.

To elucidate the topological nature of nonlinear pumps, we follow Ref. [7] and represent the solitons of Eq. (2.3) in the basis of maximally localized Wannier states,

$$\varphi_{\mathbf{i}} = \sum_n \varphi_{\mathbf{i}}^{(n)}, \qquad \varphi_{\mathbf{i}}^{(n)} = \sum_l a_l^{(n)}\, w_{\mathbf{i}}^{(n)}(l)\,, \tag{2.7}$$

where the superscript n denotes the occupied band; the index l labels the unit cell on which the Wannier state is localized; and all dependence on the adiabatic time s is henceforth implicit. The coefficients $a_l^{(n)}$ obey the analogue of Eq. (2.3) in the Wannier representation

$$\mu_s\, a_l^{(n)} = \sum_{l_1} \omega_{l-l_1}^{(n)}\, a_{l_1}^{(n)} - g \sum_{n_1,n_2,n_3} \sum_{l_1,l_2,l_3} W_{\underline{l}}^{(\underline{n})} a_{l_1}^{(n_1)*}\, a_{l_2}^{(n_2)}\, a_{l_3}^{(n_3)}\,, \tag{2.8}$$

where $\omega_l^{(n)} = 1/N \sum_{k=0}^{N-1} \exp(i\,(2\pi/N)\,k\,l)\,\epsilon_k^{(n)}$ is the Fourier transform of the nth Bloch band $\epsilon_k^{(n)}$ associated with $H_{\mathbf{ij}}(s)$; N is the number of unit cells; $\underline{n} = (n, n_1, n_2, n_3)$, $\underline{l} = (l, l_1, l_2, l_3)$; and $W_{(\underline{l})}^{(\underline{n})}$ are the following Wannier overlaps

$$W_{(\underline{l})}^{(\underline{n})} = \sum_{\mathbf{j}} w_{\mathbf{j}}^{(n)*}(l)\, w_{\mathbf{j}}^{(n_1)*}(l_1)\, w_{\mathbf{j}}^{(n_2)}(l_2)\, w_{\mathbf{j}}^{(n_3)}(l_3)\,. \tag{2.9}$$

To derive the simplified scalar DNLS from the original lattice DNLS, we consider a s independent version of Eq. 2.3

$$\mu\, \phi_{\mathbf{i}} = \sum_{\mathbf{j}} H_{\mathbf{ij}}\, \phi_{\mathbf{j}} - g\, |\phi_{\mathbf{i}}|^2\, \phi_{\mathbf{i}}\,. \tag{2.10}$$

The Wannier functions are related to the Bloch waves of the Hamiltonian by the following relations

$$w_{\mathbf{j}}^{(n)}(l) = \frac{1}{\sqrt{N}} \sum_{k=0}^{N-1} e^{i(2\pi/N)k(-l)}\, \psi_{\mathbf{j}}^{(n)}(k) = \frac{1}{\sqrt{N}} \sum_{k=0}^{N-1} e^{i(2\pi/N)k(j-l)}\, u_{\mathbf{j}}^{(n)}(k), \tag{2.11}$$

where $\psi_{\mathbf{j}}^{(n)}(k) = e^{i(2\pi/N)k(j)}\, u_{\mathbf{j}}^{(n)}(k)$ is the Bloch wave of band n with momentum k and $u_{\mathbf{j}}^{(n)}(k)$ is the corresponding Bloch function, which is periodic over the unit cells and does not depend on j. To represent the Hamiltonian part in Wannier basis, we evaluate the matrix elements of the Hamiltonian over the Wannier states

$$\begin{aligned}
&\langle w^{(n')}(l'), H\, w^{(n)}(l)\rangle \\
&= \frac{1}{N} \sum_{k,k'=0}^{N-1} e^{i(2\pi/N)(k'l'-kl)}\, \langle \psi^{(n')}(k'),\, H\, \psi^{(n)}(k)\rangle \\
&= \delta_{nn'} \cdot \frac{1}{N} \sum_{k=0}^{N-1} e^{i(2\pi/N)k(l'-l)}\, \epsilon_k^{(n)} \;=\delta_{nn'} \cdot \omega_{l'-l}^{(n)} \,,
\end{aligned} \tag{2.12}$$

where $\omega_l^{(n)} = 1/N \sum_{k=0}^{N-1} e^{i(2\pi/N)k(l)}\, \epsilon_k^{(n)}$ is the Fourier transform of the Bloch band $\epsilon_k^{(n)}$. Next, we express the nonlinearity in terms of Wannier functions,

$$\langle w^{(n)}(l),\, |\phi|^2\, \phi\rangle = \sum_{n_1,n_2,n_3} \sum_{l_1,l_2,l_3} \left(\sum_{\mathbf{i}} w_{\mathbf{i}}^{(n)*}(l) w_{\mathbf{i}}^{(n_1)*}(l_1) w_{\mathbf{i}}^{(n_2)}(l_2) w_{\mathbf{i}}^{(n_3)}(l_3) \right) a_{l_1}^{(n_1)*}\, a_{l_2}^{(n_2)}\, a_{l_3}^{(n_3)} \,. \tag{2.13}$$

Taking the inner product of Eq. (2.10) with $w_l^{(n)}$ and using Eqs. (2.12) and (2.13), we obtain the following DNLS

$$\mu_s\, a_l^{(n)} = \sum_{l_1} \omega_{l-l_1}^{(n)}\, a_{l_1}^{(n)} - g \sum_{n_1,n_2,n_3} \sum_{l_1,l_2,l_3} W_{\underline{l}}^{(\underline{n})} a_{l_1}^{(n_1)*}\, a_{l_2}^{(n_2)}\, a_{l_3}^{(n_3)} \,, \tag{2.14}$$

which is exactly in the form of Eq. 2.8.

The Wannier states of a Bloch band are not unique, as they depend on the gauge choice for the Bloch functions [225]. Nevertheless, a unique set of maximally localized Wannier functions is provided by the eigenstates of the position operator's projection onto the associated band. Since such Wannier functions are exponentially localized, the contribution to the Wannier overlaps in Eq. (2.14) from Wannier functions corresponding to different unit cells are negligible. The Wannier overlaps can thus be simplified as $W_{\underline{l}}^{(\underline{n})} = W^{(\underline{n})}\, \delta_{ll_1}\, \delta_{l_1 l_2}\, \delta_{l_2 l_3}$, where $W^{(\underline{n})} = \sum_{\mathbf{j}} w_{\mathbf{j}}^{(n)*}(l)\, w_{\mathbf{j}}^{(n_1)*}(l)\, w_{\mathbf{j}}^{(n_2)}(l)\, w_{\mathbf{j}}^{(n_3)}(l)$; we point out that $W^{(\underline{n})}$ does not depend on the index l, because of translational invariance.

Moreover, as we will discuss below, in the regime of weak nonlinearity, the initial state soliton occupies a single band [111, 110, 7], which allows us to neglect inter-band contributions to Eq. (2.8). We note that this simplification holds throughout the evolution of the pump, during which the soliton adiabatically follows the same band.

Under those realistic assumptions, the Wannier representation of the DNLS reduces to the form

$$\mu_s\, a_l^{(n)} = \sum_{l_1} \omega_{l-l_1}^{(n)}\, a_{l_1}^{(n)} \; - g W^{(n)} |a_l^{(n)}|^2 a_l^{(n)} \,, \tag{2.15}$$

where $W^{(n)} = \sum_{\mathbf{j}} |w_{\mathbf{j}}^{(n)}(l)|^4$. Equation (2.15) has the form of a scalar DNLS on a simple lattice with one degree of freedom per unit cell labeled by Wannier indices l, with hopping terms involving nearest and beyond-nearest neighbors. The properties of such scalar DNLS are well established [114, 117]: Equation (2.15) admits inter-site solitons, with maxima on two adjacent sites, and on-site solitons, with their maximum on a single site. The inter-site solitons are known to be unstable against small perturbations, we thus restrict ourselves to the stable on-site solitons. Crucially, on-site solitons are always peaked around a single site (l) throughout the pumping cycle, as there is a finite energy (Peierls-Naborro) barrier for delocalization [114, 117]. Interestingly, the Peierls-Naborro barrier plays a role analogous to the "gap condition" of conventional topological physics, by forbidding transitions to other stable states during the adiabatic time evolution. This observation suggests that solitons are dragged by Wannier states upon pumping, hence exhibiting a quantized displacement in real space established by the Chern number [12, 144, 135]; see Figs. 2.1(a)-(b).

To firmly prove the topological nature of the nonlinear Thouless pump, we evaluate the solitons center-of-mass displacement after one period $s=1$

$$\Delta\langle\varphi^{(n)}, X\varphi^{(n)}\rangle = \Delta\langle w^{(n)}(0), Xw^{(n)}(0)\rangle + \Delta\sum_{l\neq l'} a_{l'}^{(n)*}a_l^{(n)}\langle w^{(n)}(l'), Xw^{(n)}(l)\rangle\,, \tag{2.16}$$

where X is the position operator of the lattice; $\langle f, g\rangle \equiv \sum_{\mathbf{i}} f_{\mathbf{i}}^* g_{\mathbf{i}}$ is the inner product of fields on the lattice; and $\Delta(\cdot) \equiv (\cdot)_{s=1} - (\cdot)_{s=0}$. The first term in Eq. 2.16 reflects the displacement of Wannier functions upon one pump cycle, which is known to correspond to the Chern number of the band [12, 144, 135]; the additional terms displayed on the second line are possible corrections due to the finite overlap of different Wannier states. Importantly, we find that these small interference effects are periodic in time, such that these correction terms in Eq. 2.16 do not contribute to the solitons center-of-mass displacement over a pump cycle. In the following section we outline the proof of this statement. Altogether, proofing this statement completes the reasoning: the displacement of solitons is indeed quantized according to the Chern number of the band from which they emanate.

2.1.1 Derivation of the soliton center-of-mass displacement

Here, we prove that the quantized displacement of the solitons center-of-mass is determined by the Chern number of the related Bloch band. For later convenience, we derive the following identity for matrix elements of position operator over the Wannier functions,

$$\begin{aligned}\langle w^{(n)}(l'), Xw^{(n)}(l)\rangle &= \langle w^{(n)}(l'-l), (T_l^\dagger\, X\, T_l)\, w^{(n)}(0)\rangle \\ &= \langle w^{(n)}(l'-l), X\, w^{(n)}(0)\rangle + l\,\langle w^{(n)}(l'-l),\, w^{(n)}(0)\rangle \\ &= \langle w^{(n)}(l'-l), X\, w^{(n)}(0)\rangle + l\,\delta_{ll'}\end{aligned} \tag{2.17}$$

where T_l is the translation operator by l unit cells. In deriving Eq. (2.17) we used the relation $T_l^\dagger XT_l = X + l$ together with the orthogonality of Wannier functions. The soliton center-of-mass then reads

$$
\begin{aligned}
\langle \varphi^{(n)}, X\varphi^{(n)} \rangle_s &= \sum_{l,l'} a_{l'}^{(n)*}\, a_l^{(n)}\, \langle w^{(n)}(l'), X w^{(n)}(l) \rangle_s \\
&= \sum_{l} |a_l^{(n)}|^2\, \langle w^{(n)}(l), X w^{(n)}(l) \rangle_s + \sum_{l \neq l'} a_{l'}^{(n)*}\, a_l^{(n)}\, \langle w^{(n)}(l'), X w^{(n)}(l) \rangle_s \\
&= \Big(\sum_l |a_l^{(n)}|^2 \Big) \langle w^{(n)}(0), X w^{(n)}(0) \rangle_s + \Big(\sum_l |a_l^{(n)}|^2\, l \Big) \langle w^{(n)}(0), w^{(n)}(0) \rangle_s \\
&+ \sum_{\delta l \neq 0} \Big(\sum_l a_{l+\delta l}^{(n)*}\, a_l^{(n)} \Big) \langle w^{(n)}(\delta l), X w^{(n)}(0) \rangle_s \,,
\end{aligned}
\tag{2.18}
$$

where we used Eq. (2.17) in the last equality. The first term in the last equality of Eq. (2.18) reduces to $\langle w^{(n)}(0), X w^{(n)}(0) \rangle_s$ since we normalized the soliton intensity to unity, $N_\phi = \sum_l |a_l^{(n)}|^2 = 1$. The second term in the last expression is the mean value of the position of the Wannier functions indices, which is constant since the on-site solution is always peaked around a Wannier label and remains symmetric around it. Its contribution to the displacement over a pump cycle thus vanishes. The third term contains products of the form $\big(\sum_l a_{l+\delta l}^{(n)*}\, a_l^{(n)} \big) \langle w^{(n)}(\delta l), X w^{(n)}(0) \rangle_s$ and its treatment requires more care. The coefficient $\big(\sum_l a_{l+\delta l}^{(n)*}\, a_l^{(n)} \big)$ is time-periodic, since $a_l^{(n)}$ is, by assumption, the solution of the scalar DNLS in Eq. (2.15). To investigate the behavior of $\langle w^{(n)}(\delta l), X w^{(n)}(0) \rangle_s$, we note that after a pump cycle, the Wannier functions are displaced by the Chern number, $w^{(n)}(l)|_{s=1} = w^{(n)}(l + \mathcal{C}_n)|_{s=0}$, with $\mathcal{C}_n$ the Chern number of band n [12, 144, 135]. Thus, after a pump cycle, we have

$$
\langle w^{(n)}(\delta l), X w^{(n)}(0) \rangle|_{s=1} = \langle w^{(n)}(\delta l + \mathcal{C}_n), X w^{(n)}(\mathcal{C}_n) \rangle|_{s=0} = \langle w^{(n)}(\delta l), X w^{(n)}(0) \rangle|_{s=0} \,,
\tag{2.19}
$$

where we used Eq. (2.17) in the last step. This proves that the quantity $\langle w^{(n)}(\delta l), X w^{(n)}(0) \rangle|_s$, in the last equality of Eq. (2.18), is a time-periodic quantity.

Altogether, the third term in Eq. (2.18) is also time-periodic, and the soliton's center-of-mass displacement over a pump cycle is given by

$$
\Delta \langle \varphi^{(n)}, X\varphi^{(n)} \rangle = \Delta\, \langle w^{(n)}(0), X w^{(n)}(0) \rangle \,.
\tag{2.20}
$$

This result directly relates the soliton's displacement to the displacement of Wannier functions upon one pump cycle, as dictated by the Chern number of the band [12, 144, 135]. This proves the quantized pumping of the soliton according to the Chern number.

2.2 Numerical validation

We now demonstrate the validity of our assumptions numerically by solving the nonlinear Rice-Mele model (Eq. (2.2)). Throughout this work, we illustrate the general concepts and results using the Rice-Mele model, with periodic boundary conditions. This simple two-band model, which is reviewed in some detail below, is known to exhibit a topological (Thouless) pump sequence.

The Rice-Mele model is a 1D tight-binding model with alternating nearest-neighbor tunneling matrix elements (J_1, J_2, J_1, J_2, $\ldots$), and a staggered on-site potential. We denote the two sites within each unit cell by $\alpha = A, B$ and the unit cells by i, $0 \leq i \leq N-1$, where N is the number of unit cells. The hopping matrix element between sites A and B within each unit cell (resp. between adjacent unit cells) is written as $J_1 = -J(1+\delta)$ (resp. $J_2 = -J(1-\delta)$) and the magnitude of the staggered potential on site A (resp. B) equals Δ (resp. $-\Delta$). The Hamiltonian of the Rice-Mele model thus reads

$$\begin{aligned} H = &-\sum_{i=0}^{N-1}\Big[J(1+\delta)\,|i,A\rangle\langle i,B| + J(1-\delta)\,|i,A\rangle\langle i-1,B|\Big] \\ &+\frac{\Delta}{2}\sum_{i=0}^{N-1}\Big[\,|i,A\rangle\langle i,A| - |i,B\rangle\langle i,B|\Big] + \text{h.c.} \end{aligned} \tag{2.21}$$

The simulations shown here are performed on a lattice with $N = 100$ unit cells, and using the following pump sequence

$$\begin{cases} J(s) = J_0\Big(1 + 1/2\cos(2\pi s)\Big)\,, \\ \delta(s) = \delta_0 \cos(2\pi s)/(2+\cos(2\pi s))\,, \\ \Delta(s) = \ J_0 \sin(2\pi s), \end{cases} \tag{2.22}$$

with $J_0 = 0.5$ and $\delta_0 = 0.6$, corresponding to a topological pump with Chern number $C = -1$. The *nonlinear* Rice-Mele model, which is used in our simulations, is obtained by adding an on-site nonlinearity to this lattice model; see Eq. (2.2).

Later when we discuss the nonlinear pump in ultracold mixtures, Iin order to demonstrate the interaction-induced topological pumping, we assume that the two species experience the same Rice-Mele lattice described above, but with different pump sequences: the majority atoms experience the topological pumping sequence in Eq. (2.64), while the impurity atoms experience a trivial sequence with $J\delta = \Delta = 0$. The resulting center-of-mass displacement of both species are depicted in Fig. 2.11.

In Figs. 2.2(a)-(b), we compare the on-site soliton solution of the simplified Eq. (2.15), which emerges from the lowest band, with the Wannier representation of the exact soliton obtained by solving the full DNLS in Eq. (2.3). We then perform a similar comparison in real space, by convolving the soliton of Eq. (2.15) with the corresponding Wannier states, and by comparing this result to the exact soliton of the original nonlinear Rice-Mele model; see Figs. 2.2(c)-(d). The perfect agreement validates the description of the soliton in Wannier representation using the ordinary nonlinear Schrödinger equation (2.15).

We depict the motion of the exact soliton in Fig. 2.3, as obtained by solving Eq. (2.3) over two pump cycles $s \in [0, 2]$, and we compare this trajectory with the drift of its underlying Wannier function, i.e. the Wannier state that contributes the most to the expansion (2.7). In order to obtain a contiguous path for the Wannier center, we relabeled the

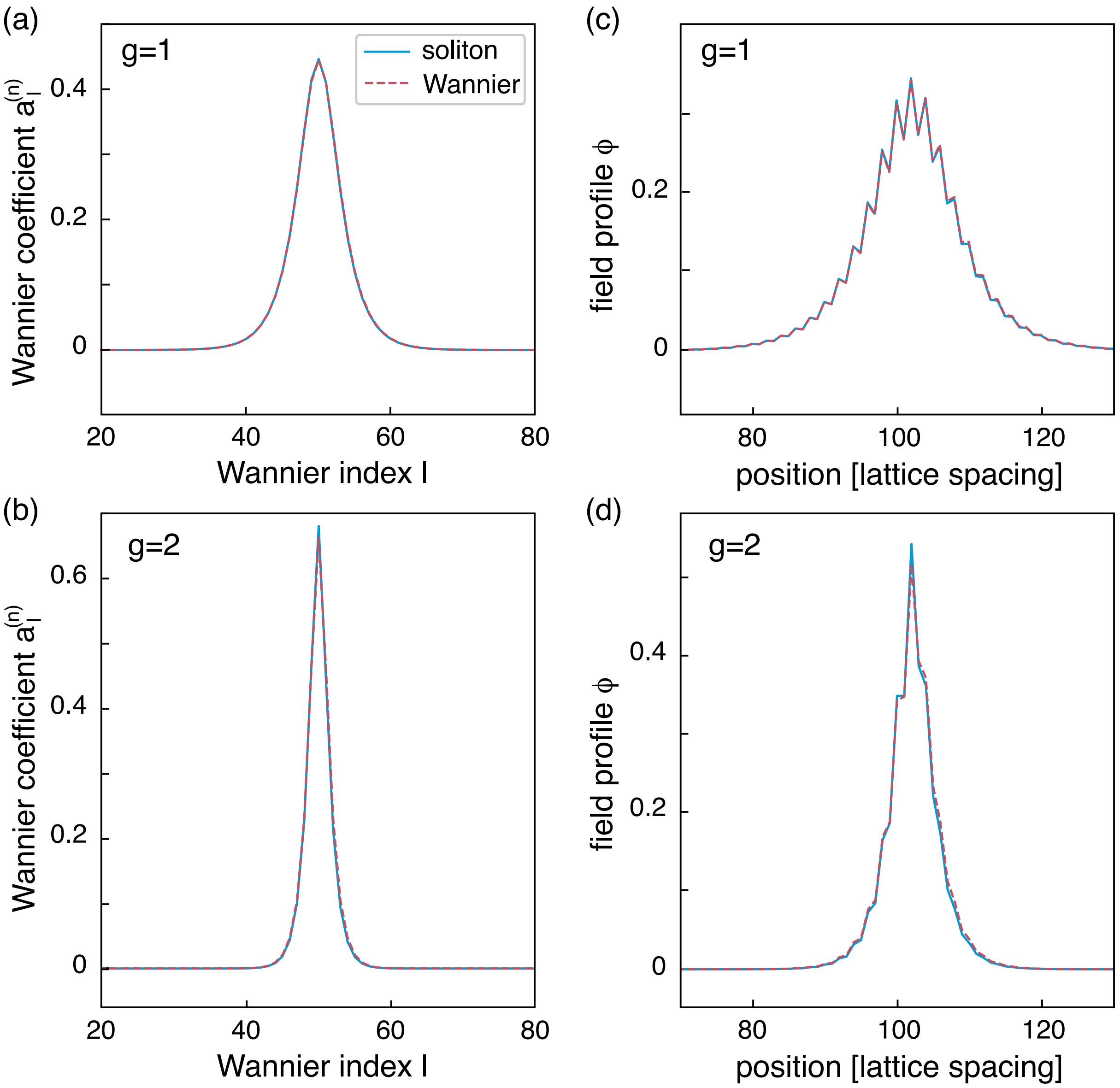

Figure 2.2: Numerical validation of the simplified theoretical scheme. (a)-(b): Wannier representation of a soliton in the lowest band (n=0) of the nonlinear Rice-Mele model (blue solid line), compared with the soliton obtained from the simplified DNLS Eq. (2.15) (dashed red line), for $g = J_0$ and $g = 2\,J_0$ and time $s = 0.12$. Here, J_0 is a characteristic hopping strength. Note how increasing the nonlinearity further localizes the soliton. (c)-(d) Same comparison in real space.

Wannier functions whenever the Wannier centers met discontinuities; this smoothing corresponds to a singular gauge transformation of the corresponding Bloch states, and has no physical implication. Figure 2.3 indicates that the trajectories of the soliton and Wannier center differ at intermediate times ($s \neq$ integer), which we attribute to the aforementioned interference effects involving different Wannier states; however, in agreement with our theoretical predictions, this deviation remains small and time-periodic over the whole pump cycle, and does not introduce any (integer) correction to the quantized center-of-mass displacement.

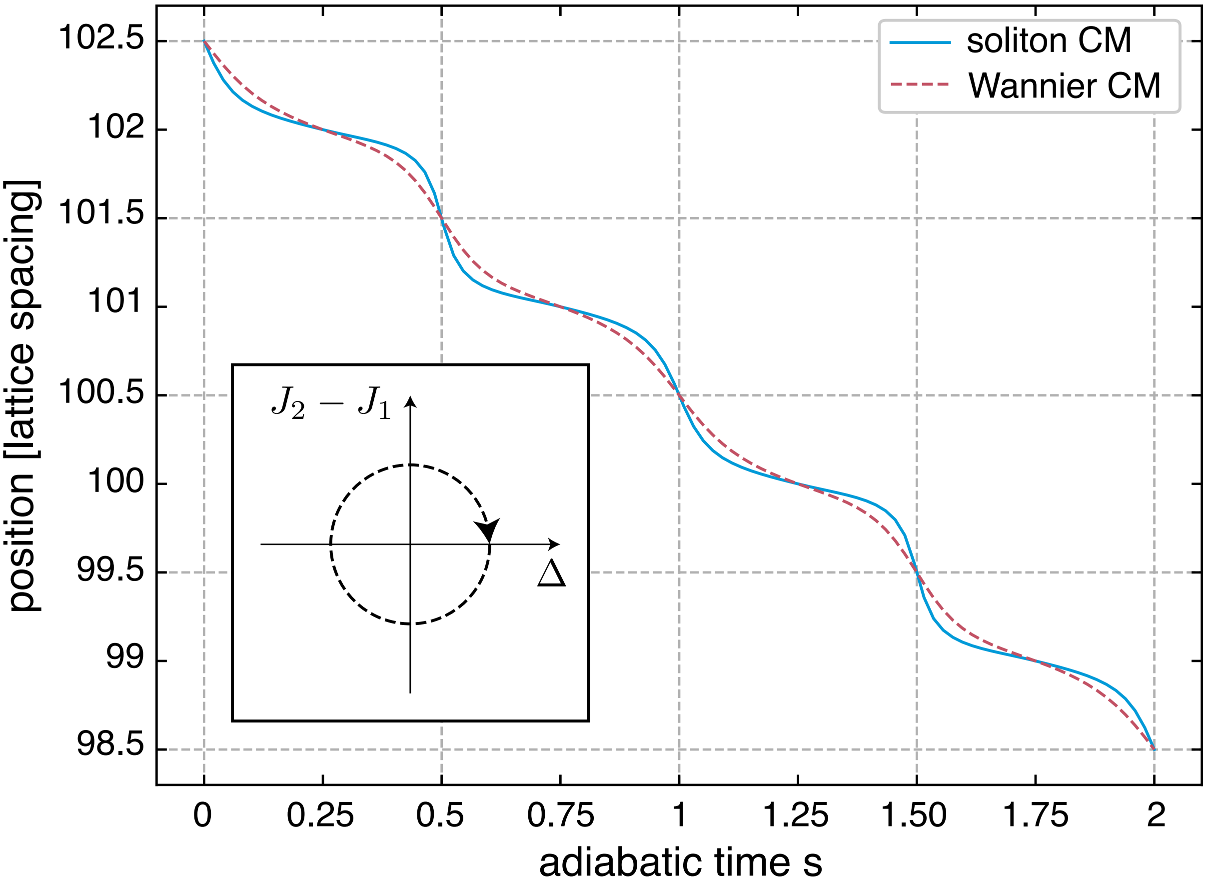

Figure 2.3: Comparison of soliton and Wannier function center-of-mass displacement. Adiabatic evolution of the soliton's center-of-mass (CM) during two full pump cycles (inset), as obtained by solving Eq. (2.3) on the Rice-Mele lattice with $g = J_0$, and selecting a soliton in the lowest band. This is compared to the evolution of the center-of-mass of the Wannier function with largest contribution to the soliton's expansion [Eq. (2.7)]. For clarity, the Wannier functions are relabeled during the pump cycle such that their center-of-mass follows a contiguous path instead of winding around a unit cell. The quantized displacement is set by the Chern number $C = -1$ of the occupied band.

2.3 Theoretical validity conditions

Here, we discuss the major phenomenological differences between the standard linear Thouless pump and the nonlinear (solitonic) Thouless pump discussed in this work. Especially, why a central difference with the linear case concerns the presence of the second term in the following equation,

$$\begin{aligned}\Delta\langle\varphi^{(n)},X\varphi^{(n)}\rangle &= \Delta\langle w^{(n)}(0),Xw^{(n)}(0)\rangle \\ &\quad+\Delta\sum_{l\neq l'} a_{l'}^{(n)*}a_l^{(n)}\langle w^{(n)}(l'),Xw^{(n)}(l)\rangle\,.\end{aligned} \tag{2.23}$$

There are several reasons why the phenomenology of the nonlinear system differs from the linear one:

- A necessary requirement for linear Thouless pumping is a uniform occupation of a topological Bloch band. However, a soliton's band occupation is non-uniform; thus, according to the linear theory, a band occupation corresponding to a soliton solution does not lead to quantized displacement. Nevertheless, the pumping of solitons is shown to be topologically quantized, which highlights the importance of nonlinearity in this solitonic-pump context.
- A localized wave packet (with either uniform or non-uniform band occupation) undergoes dispersion in the linear regime, whereas nonlinearity circumvents dispersion due to the formation of a soliton.

We provide further numerical evidence to support the above arguments. In Fig. 2.4(a) and (c), we demonstrate the time evolution of a localized wave packet in the linear and nonlinear regimes for identical initial states. The initial state corresponds to a stable state soliton of the nonlinear lattice at $t = 0$ and with nonlinearity strength $g = 1.8$. While in a nonlinear lattice (Fig. 2.4(a)), an initial stable state soliton propagates as a solitary wave, the same initial state undergoes diffraction in a linear lattice (Fig. 2.4(c)). Fig. 2.4(b) depicts the center-of-mass displacement of the soliton in Fig. 2.4(a), showing topological pumping according to the Chern number of the lowest Rice-Mele band $\mathcal{C} = -1$ (two lattice spacings per cycle). On the other hand, the center-of-mass displacement of the wave packet in the linear regime (Fig. 2.4(d)) shows no indication of quantized pumping due to non-uniform occupation of the lowest Rice-Mele band.

We also evaluate the power of the soliton projection on the higher ($n = 1$) Rice-Mele band, $P_1 = \sum_{\mathbf{j}} |\hat{\mathrm{P}}_{n=1}\varphi_{\mathbf{j}}|^2$, and compare it to the power of the soliton projection on the lower ($n = 0$) Rice-Mele band, $P_0 = \sum_{\mathbf{j}} |\hat{\mathrm{P}}_{n=0}\varphi_{\mathbf{j}}|^2$. The ratio P_1/P_0 is a degree of soliton band mixing. We plot in Fig. 2.5 the ratio P_1/P_0 over two pump cycles for values of nonlinearity strength g for which soliton pumps. This result indicates that a soliton can undergo topological pumping and at the same time have considerable occupation of other bands. This is in sharp contrast with the linear case, where quantized pumping is observed for completely filled bands.

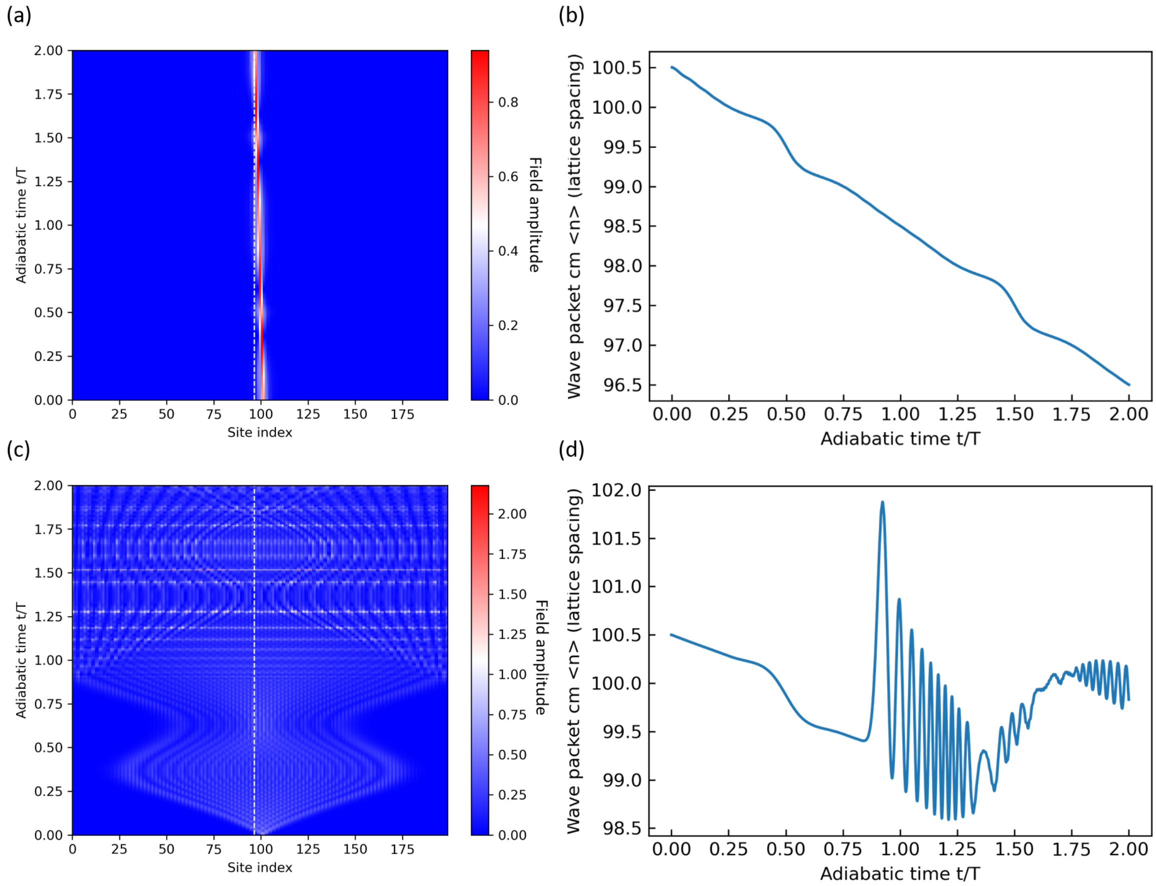

Figure 2.4: Wave packet evolution in the Thouless pump sequence as in Eq. 2.22 with $J_0 = 1$ and $\delta_0 = 2$ and the nonlinearity strength $g = 1.8$. in the linear and nonlinear regime for the same initial state. (a) Evolution of the initial state according to a stable state soliton of the stationary DNLS at $t = 0$ in the lowest Rice-Mele band. Although the initial wave packet has non-uniform band occupation, the wave packet pumps according to the Chern number of the lowest Rice-Mele band after one pump cycle. The dashed line represents the predicted topological displacement of the wave packet after two pump cycles. (b) Center-of-mass motion of the soliton in (a). The center-of-mass pumps according to the Chern number of the lowest Rice-Mele band $\mathcal{C} = -1$ (two lattice spacings per cycle). (c) Same as (a) but for a linear model ($g = 0$). The initial wave packet undergoes dispersion with a dramatic diffraction pattern. (d) Center-of-mass displacement of the wave packet in (c). Since the initial wave packet has non-uniform occupation of the bands, there is no indication of pumping in the center-of-mass displacement.

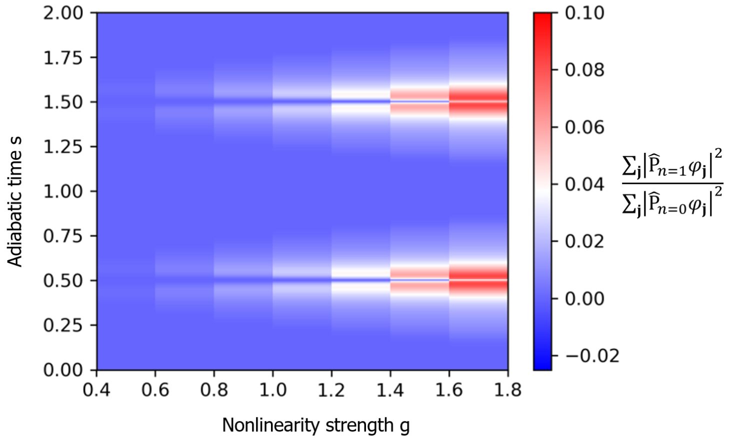

Figure 2.5: Ratio of the soliton power in the highest band to the lowest band of the Rice-Mele model (from which the soliton bifurcates). Over a pump cycle, the soliton center-of-mass follows a contiguous path with a topologically quantized displacement over a pump cycle, i.e. it pumps, for all the values of g denoted here. Even when the occupation of higher band is clearly non-negligible, the soliton undergoes topological pumping.

2.3.1 Existence of soliton solutions

We now discuss the requirements for the formation of a stable state soliton in the context of a stationary DNLS. Here we remark on the conditions for stable state soliton formation of the following equation

$$\mu_s\,\varphi_{\mathbf{i}} = \sum_{\mathbf{j}} H_{\mathbf{ij}}(s)\,\varphi_{\mathbf{j}} - g\,|\varphi_{\mathbf{i}}|^2\varphi_{\mathbf{i}}\,, \tag{2.24}$$

in terms of its Wannier representation

$$\mu_s\,a_l^{(n)} = \sum_{l_1} \omega_{l-l_1}^{(n)}\,a_{l_1}^{(n)} \;-gW^{(n)}|a_l^{(n)}|^2 a_l^{(n)}\,. \tag{2.25}$$

Both Eq. 2.24 and Eq. 2.25 have stable state solitons for arbitrary small values of $g > 0$. In the following, we present an argument for the existence of soliton solutions for every $g > 0$ based on continuous NLS and the properties of DNLS in the continuum limit.

To explore the conditions for soliton formation, we follow closely the treatment presented in Ref. [154] for the Nonlinear Schrödinger equation in continuum. The time dependent NLS

$$i\hbar\bar{\psi}_t(x,t) + \frac{\hbar^2}{2m}\bar{\psi}_{xx}(x,t) + g|\bar{\psi}(x,t)|^2\bar{\psi}(x,t) = 0\,, \tag{2.26}$$

with power $P = \int_{-\infty}^{\infty} dx\,|\bar{\psi}(x,t)|^2$, can be scaled by setting $\bar{\psi} = \lambda\psi$ and using dimensionless variables ($t \to Tt$, $x \to lx$) to take the universal form

$$i\psi_t(x,t) + \psi_{xx}(x,t) + 2|\psi(x,t)|^2\psi(x,t) = 0\,, \tag{2.27}$$

where $\hbar/T = \hbar^2/(2ml^2)$ and $\lambda^2 = \hbar^2/(2ml^2 g)$. Eq. 2.27 has solutions of the form

$$\psi(x,t) = 2i\eta\,\mathrm{sech}\Big(2\eta(x - x_0 + 4\xi t)\Big)\exp\Big(-2i\xi x - 4i(\xi^2 - \eta^2)t - i\phi_0\Big)\,. \tag{2.28}$$

The necessary condition for having a soliton solution is

$$\int_{-\infty}^{\infty} dx\,|\psi(x,0)| \geq \ln\Big(2+\sqrt{3}\Big) \simeq 1.32\,, \tag{2.29}$$

Using Eq. 2.28,

$$\int_{-\infty}^{\infty} dx\,2\eta\,\mathrm{sech}\Big(2\eta(x)\Big) = \pi \geq 1.32\,. \tag{2.30}$$

Thus, for an initial state according to $\psi(x,0) = 2\eta\mathrm{sech}(2\eta(x - x0))$, the NLS has soliton solutions for all $g > 0$. In the dimensionful units, the necessary condition reads

$$\int_{-\infty}^{\infty} dx\,|\bar{\psi}(x,0)| \geq \sqrt{\frac{\hbar^2}{mg}}\ln\Big(2+\sqrt{3}\Big)\,, \tag{2.31}$$

which means that, for arbitrary initial data, a necessary condition is that the integral $\int_{-\infty}^{\infty} dx\,|\bar{\psi}(x,0)|$ be larger than the quantity $\sqrt{(\hbar^2/m)/g}\,\ln\Big(2+\sqrt{3}\Big)$. In the case of DNLS, we can still use this argument since for small nonlinearities, the soliton mostly occupies the lowest band edge, where the dispersion relation is quadratic with an effective mass m_{eff} and we can substitute the discrete Hamiltonian with the continuous one, and the continuum limit works well. Thus, for a DNLS a necessary condition similar to Eq. 2.31 can be obtained by substituting m with the effective mass m_{eff}. In order to evaluate the integral on the left-hand side of Eq. 2.31, one has to make use of the continuous lattice model whose tight-binding limit results in the original DNLS of the problem under consideration. Thus, for every value of $g > 0$ we have a soliton solution of the DNLS provided that the initial data is suitably chosen to fulfill Eq. 2.31.

Although there exists stable state soliton solutions for arbitrary $g > 0$, formation of such stable states from an arbitrary initial data is a non-trivial question. One way for obtaining a stable state soliton from a suitable initial data is to first solve Eq. 2.24 numerically and obtain the stable state solutions, then use it as the initial waveform accordingly. This method is applicable in waveguide array experiments as the input profile of the excitation can be engineered. In the context of cold atoms in optical lattices, a detailed analysis of the creation of solitons in a realistic setting is presented in Ref. [1]

As mentioned above, a stable state soliton does not always emerge from an initially prepared localized state. Indeed, for weak powers (i.e. electric field power for light fields or particle number for matter waves), the initial wave packet disperses. We hereby present an alternative approach, following closely the discussion section 12.3 of Ref. [114] on threshold conditions for the non-integrable DNLS models, and obtain a sufficient condition for estimating the threshold power for solitary wave formation. To this end, we consider a setting where the initial excitation is a Wannier function with amplitude A (in Wannier representation, $a_l^{(n)}(s=0) = A\,\delta_{l,0}$). We find a threshold value A^* above which a soliton forms. The precise scenario for obtaining a stable state soliton from this on-site initial data is as follows:

- Consider an initial nonlinear lattice with given time-independent parameters (hoppings and on-site potentials).
- Choose the initial excitation to be localized on a single site in Wannier representation, i.e. $a_l^{(n)}(s=0) = A\delta_{l,0}$ (corresponding to a Wannier function of the lattice with amplitude A).
- A sufficient condition for soliton formation is that the initial excitation has negative energy with respect to the minimum of the excited band.
- The initial excitation undergoes time evolution and radiates some power to evolve into the localized stable state of the nonlinear lattice.

Considering this scenario, the initial energy of the system reads

$$H_0 = -\sum_{l\neq 0} \omega_l^{(n)} A^2 - \frac{g}{2} W^{(n)} A^4 \,. \tag{2.32}$$

Thus, the sufficient condition is $H_0 < 0$. We obtain the following threshold amplitude of the initial excitation above which soliton formation happens,

$$A^* = \sqrt{-\frac{2\sum_{l\neq 0}\omega_l^{(n)}}{gW^{(n)}}} \,. \tag{2.33}$$

Non-trivial questions that arise here are : how much power will radiate until a stable soliton forms, and what is the final stable state soliton? These questions, to the best of our knowledge, are still open [114][1]. All in all, since in this work we are not concerned with the precise dynamical mechanism of soliton emergence from an initially localized wave, we assume that a ratio $e < 1$ of the initial power dissipates. We assume e to be empirical and given, since in principle e depends on the details of the dynamical model of the dissipative processes in the nonlinear system and that does not concern us here. To connect to our work, we assume that after the dissipation, the soliton power equals unity, i.e. $P_{\text{soliton}} = (1-e)P_{\text{initial}} = 1$. The initial power P_{initial} relates to the amplitude of the on-site excitation A by $P_{\text{initial}} = A^2$. Thus, given the threshold condition $A > A^*$ and Eq. 2.33, the nonlinearity coefficient g of the problem should satisfy

$$g > g^* = -\frac{2(1-e)\sum_{l\neq 0}\omega_l^{(n)}}{W^{(n)}} \,. \tag{2.34}$$

In Fig. 2.6, we depict the values of g^* for $e = 0, 0.05, 0.1$, for lattice parameters corresponding to the pump sequence used in Eq. 2.22. It is clear that at $s = 0.5 + n$, $n \in \mathbb{Z}$,

---

[1] The statement of Ref. [114] in Chapter 12 page 244 in relation to the soliton formation process is "... Nevertheless, the precise mechanism of selection of the particular end state (i.e., of the particular "equilibrium") that a given initial state will result in remains a formidable outstanding question that would be especially interesting to address in the future. This is perhaps one of the fundamental remaining open questions in connection to the DNLS equation (see also the relevant discussion at the end of this special section)."

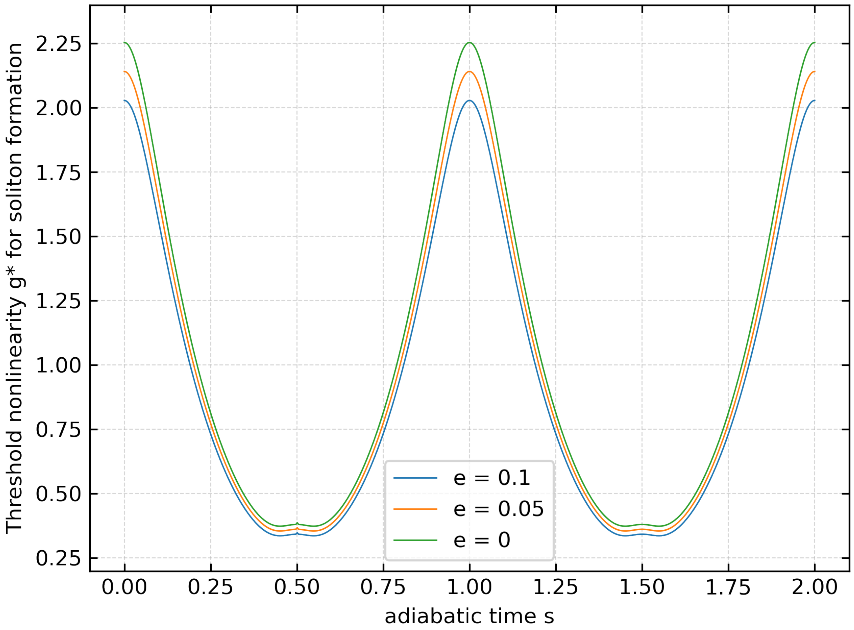

Figure 2.6: Nonlinearity threshold g^* in Eq. 2.34 evaluated over two cycles of the pump sequence. For $s = 0.5, 1.5, \cdots$, the threshold value is less than 0.5, thus an initial Wannier state of the lattice at $s = 0.5, 1.5, \cdots$ will evolve to a stable state soliton for nonlinearity strengths larger than 0.5.

the required nonlinearity strength is always less than 0.5, thus one can initialize the lattice with parameters corresponding to $s = 0.5 + n$, initialize the wave packet as a single Wannier function of the desired band (here taken to be the lowest band), wait until the soliton is formed, and then drive the pump cycle.

Another important difference of linear and nonlinear Thouless pumps is that the second term in Eq. 2.23 cannot be neglected based on the similarity of nonlinear Thouless pumping with the linear one. In general, because a soliton is a coherent structure, the second term in Eq. 2.23 is crucial to determine its displacement. Indeed, the non-trivial fact about soliton pumping is that one cannot ignore this term a priori. Still, using the theoretical framework developed in our work, one can prove that this term vanishes, provided the conditions mentioned above are satisfied.

To illustrate why the second term in Eq. 2.23 is crucial to determine the pumping of a coherent structure, we revisit the key meaning of Eq. 2.23 in more detail. Eq. 2.23 is about the displacement of the center-of-mass of a coherent structure in a single band n. Thus, such a coherent structure $\varphi_{\mathbf{j}}^{(n)}$ is a linear superposition of Wannier functions of that band, i.e. $\varphi_{\mathbf{j}}^{(n)} = \sum_l a_l^{(n)} w_{\mathbf{j}}^{(n)}(l)$. A priori, this coherent structure $\varphi_{\mathbf{j}}^{(n)}$ can be any coherent structure, such as a soliton, or the bound state of a pinning potential (with a negligible occupation of bands other than n). These two instances of a coherent structure, i.e. a soliton and a bound state, exhibit completely different pumping behavior: one (i.e. the soliton) undergoes topological pumping, while the other (i.e. the bound state) is always pinned to the potential location, and does not pump. The different behavior of these coherent structures is exactly reflected in the second term in Eq. 2.23.

In conclusion, it is not a priori possible to neglect the second term. Indeed, for the case of the pinning potential bound state, it cancels the first term in Eq. 2.23. However, within the current context of soliton pumping, it can be proved to be vanishing.

We now discuss the conditions for evaluating the degree of agreement between the actual soliton of the model and the real-space representation of the soliton obtained from the simplified DNLS in Eq. 2.25. In deriving this equation, we assumed that two approximations allow an accurate phenomenology of the physics: (1) the single band approximation, and (2) the Wannier locality approximation. These two approximations enabled us to neglect the nonlinear terms that mix different bands or different Wannier orbitals. The agreement between the actual soliton and its reconstruction via Eq. 2.25 depends on the accuracy of these approximations: the smaller the magnitude of the neglected terms compared to the remaining terms, the smaller the errors and the better the agreement. For an arbitrary nonlinear model, the validity conditions depend on the lattice properties such as the overlap of Wannier functions, band gap, band width, etc., but here we focus on the Rice-Mele model considered in this work. We derive a condition for the validity of band mixing approximation for unit power solitons, which reads as

$$4g^2/E_{\mathrm{G}}^2 \ll 1\,, \tag{2.35}$$

where E_{G} is the band gap. For solitons in the lowest Rice-Mele band (band index $n = 0$), the condition 2.35 can be relaxed to

$$4g^2/\left(E_{\mathrm{BW}}^{(0)} + E_{\mathrm{G}}\right)^2 \ll 1\,, \tag{2.36}$$

where $E_{\mathrm{BW}}^{(0)}$ is the lowest band width. For the Rice-Mele model, an explicit expression for Eqs. 2.35 and 2.36 reads as

$$\frac{4g^2}{E_{\mathrm{G}}^2} = \frac{g^2}{\left((2J\delta)^2 + \Delta^2\right)} \ll 1\,, \tag{2.37}$$

and

$$\frac{4g^2}{\left(\sqrt{(2J)^2 + \Delta^2} + \sqrt{(2J\delta)^2 + \Delta^2}\right)^2} \ll 1\,, \tag{2.38}$$

These conditions are derived from the requirement that the power in the undesired bands be much smaller than the target band. They are consistent with a first-order perturbation analysis of the occupation of the undesired band. Conditions 2.35 and 2.36 suggest that for small nonlinearities g, the single band approximation works well. We further discuss this condition in Sec. 2.3.2.

Note that these conditions are stringent sufficient conditions to guarantee small band mixing. We will show below that even when the left-hand side of Eqs. 2.35 and 2.36 exceed unity, the actual soliton of the model and the approximate soliton match to a good degree over the whole pumping sequence.

To investigate the validity of Wannier locality approximation, we note that generally for the Wannier overlaps

$$W^{(\underline{n})}_{(\underline{l})} = \sum_{\mathbf{j}} w^{(n)*}_{\mathbf{j}}(l)\, w^{(n_1)*}_{\mathbf{j}}(l_1)\, w^{(n_2)}_{\mathbf{j}}(l_2)\, w^{(n_3)}_{\mathbf{j}}(l_3)\,. \tag{2.39}$$

The following conditions hold,

$$\begin{aligned} |W^{(n)}_{0,0,0,0}| \gg |W^{(n)}_{0,0,0,1}| \gg |W^{(n)}_{0,0,0,2}| \gg \cdots\,, \\ |W^{(n)}_{0,0,1,1}| \gg |W^{(n)}_{0,0,1,2}| \gg |W^{(n)}_{0,0,2,2}| \gg \cdots\,. \end{aligned} \tag{2.40}$$

The reason is the exponential localization of Wannier functions. But for completeness, we obtain a sufficient condition for the degree of locality of Wannier states in terms of Rice-Mele model parameters. More formally, the Wannier locality approximation is valid when

$$\beta \equiv \frac{1-\delta^2}{1+\left(\frac{\Delta}{2J}\right)^2} \ll 1\,. \tag{2.41}$$

We derive the condition above in Sec. 2.3.3. Intuitively, this condition means that whenever $\delta \lesssim 1$, the Wannier states are localized over a single unit cell. Indeed, $\delta = 1$ correspond to a completely dimerized lattice, where Wannier functions are located entirely in a single unit cell.

We further provide a sufficient condition for testing the accuracy of these assumptions. This sufficient condition has to be checked a posteriori, i.e. one can solve Eq. 2.24, evaluate the terms in the Hamiltonian that are to be neglected and compare the magnitude of these terms to the remaining terms after making the approximations. The smaller the magnitude of the band mixing and non-local terms compared to the single-band and local terms, the more accurate the simplified model.

To make the above arguments quantitative, we define an a posteriori figure of merit for the accuracy of the approximate scheme. More specifically, suppose that $\varphi_{\mathbf{j}}$ is a solution of Eq. 2.24 bifurcating from band n, and $\{a^{(m)}_l\}$ are its Wannier coefficients, that is $\varphi_{\mathbf{j}} = \sum_m \sum_l a^{(m)}_l w^{(m)}_{\mathbf{j}}(l)$. The magnitude of the neglected terms in the Hamiltonian is

$$\Delta E_g = |E_g - \tilde{E}_g|\,, \tag{2.42}$$

where

$$E_g = \frac{g}{2}\sum_{\mathbf{j}} |\varphi_{\mathbf{j}}|^4\,, \quad \tilde{E}_g = \frac{g}{2} W^{(n)} \sum_l |a^{(n)}_l|^4\,. \tag{2.43}$$

A figure of merit for evaluating the validity of the approximations is

$$\alpha_g = \frac{\Delta E_g}{E_g}\,. \tag{2.44}$$

When $\alpha_g \ll 1$, one expects to find a good agreement between the actual soliton of the model and its reconstruction from the Wannier representation, while as α_g increases, the approximations get worse.

After making the above approximations, the soliton in Wannier representation is the solution $\hat{a}_l^{(n)}$ of Eq. 2.25. One can quantify the discrepancy between $\varphi_{\mathbf{j}}$ and its reconstruction via Eq. 2.25, that is $\hat{\varphi}_{\mathbf{j}} = \sum_l \hat{a}_l^{(n)} w_{\mathbf{j}}^{(n)}(l)$, by evaluating the norm-squared error between $\varphi_{\mathbf{j}}$ and $\hat{\varphi}_{\mathbf{j}}$,

$$\gamma = \frac{\sum_{\mathbf{j}} |\varphi_{\mathbf{j}} - \hat{\varphi}_{\mathbf{j}}|^2}{\sum_{\mathbf{j}} |\varphi_{\mathbf{j}}|^2} . \tag{2.45}$$

In Fig. 2.7 we depict the values for α_g and γ for values of g in the pumped soliton regime. Fig. 2.7(a) indicates that the energy of the neglected terms in α_g increases for stronger nonlinearities, and even for values of α_g as large as 0.4 one may still observe soliton pumping. In Fig 2.7 (b), we bring the error γ, which again shows that the main factor for increasing the error is strong nonlinearity. Furthermore, the variation pattern of α_g is in complete agreement with the error γ. Thus, examining the value of α_g is a good indicator for accuracy of the simplified model. Note that the condition is a sufficient condition, meaning that if α_g is small, say less than 0.05, then the approximations are better and the Wannier representation soliton is a good approximation for the real one. On the other hand, large values of α_g and γ does not indicate the pumping break down, they only indicate the reconstructed soliton deviates from the real one, although both undergo pumping.

In Fig. 2.8, we examine the conditions in Eqs. 2.37 and 2.41, for the validity of band-mixing and Wannier locality approximations, respectively. We observe that increase in the quantity $4g^2/E_{\mathrm{G}}^2$ increases the error γ in Fig. 2.7. The condition $4g^2/E_{\mathrm{G}}^2 \ll 1$ is a stringent sufficient condition for validity of band mixing approximation, and even for $4g^2/E_{\mathrm{G}}^2 \simeq 3$ we observe less than 10 percent error in soliton reconstruction. In Fig. 2.8(b), we check the sufficient validity condition for Wannier locality approximation. We observe that the pattern of increase in β as defined in Eq. 2.41 is in accordance with the increase in Wannier overlaps $W1 \equiv W^{(0)}_{0,0,0,1}$, $W2 \equiv W^{(0)}_{0,0,0,2}$, $W3 \equiv W^{(0)}_{0,0,0,3}, \cdots$ with respect to $W0 \equiv W^{(0)}_{0,0,0,0}$ for the lowest Rice-Mele band. Thus, it is a good indicator of the increase in non-local Wannier overlaps.

The nonlinear term in Eq. 2.24 (Eq. 2.25) leads to spontaneous breaking of lattice (Wannier lattice) translational symmetry . Thus, the minimum energy states, which are stable state solitons, are not translationally invariant, but are mapped to one another by a lattice translation. Continuous deformation of each stable state soliton to a neighboring one requires a finite amount of energy. This finite energy barrier between solitons localized on adjacent unit cells is reminiscent of the Peierls-Naborro barrier (PNB) known in the theory of dislocation dynamics in crystals. Under adiabatic evolution, a soliton in Wannier representation will always remain peaked on a single Wannier index, as the PNB prohibits the soliton to move and localize on any other Wannier index. This fact is crucial in proving the quantization of soliton displacement according to the Chern number.

We can estimate the strength of the Peierls-Naborro barrier by evaluating the difference between the variational energy over the ansätze $a_l^{(n)} = \eta\,\mathrm{sech}(\xi(\mathrm{l}-\mathrm{l}_0))$ for the on-site

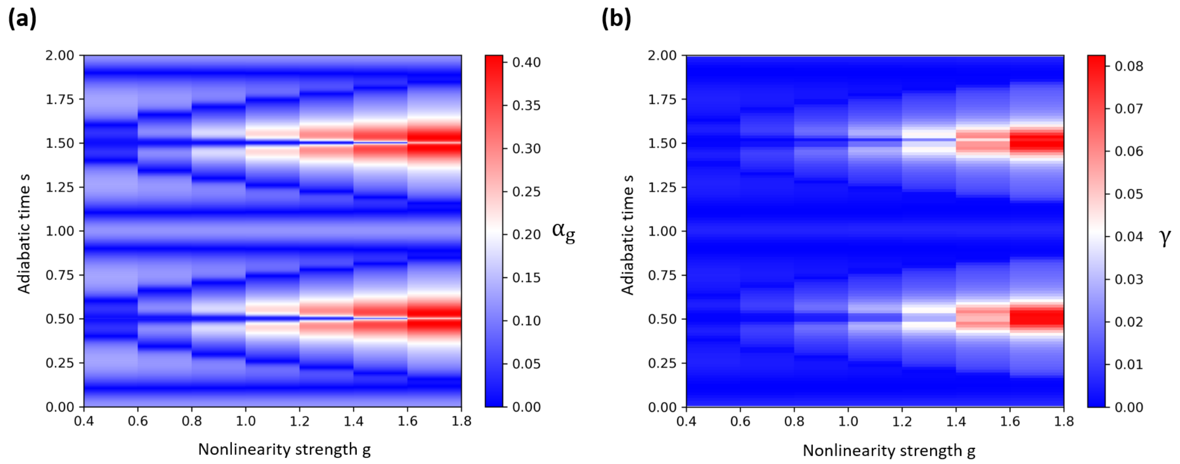

Figure 2.7: (a) Values of the figure of merit α_g for different values of g admitting soliton pumping, over two pump cycles. Even for energy difference of the order of 40 percent, the soliton still undergoes pumping. The accuracy of this scheme directly relates to the strength of the nonlinearity: as the nonlinearity strength increases, the deviation between the actual soliton and its effective counterpart starts to increase because of the increase in band mixing effects.

$(l_0 = 0)$ and inter-site$(l_0 = 1/2)$ solitons. More formally,

$$\Delta_{\mathrm{PN}} = H(\eta_{1/2}, \xi_{1/2}) - H(\eta_0, \xi_0) \tag{2.46}$$

where

$$H(\eta_{l_0}, \xi_{l_0}) = \min_{\eta,\xi} H(\eta, \xi, l_0), \qquad l_0 \in \{0, 1/2\}\,, \tag{2.47}$$

and the variational energy functional is

$$\begin{aligned} H(\eta, \xi, l_0) = \omega_0 \left[\frac{2}{\xi}\eta^2 + \sum_{m=1}^{\infty} \frac{4\pi^2\eta^2}{\xi^2} \frac{m\cos(2\pi m l_0)}{\sinh(\frac{\pi^2 m}{\xi})} \right] + \sum_{n=1}^{\infty} \frac{4n\,\eta^2}{\sinh(\xi n)}\omega_n \\ - \frac{2\,g}{3}\eta^4 \left[\frac{1}{\xi} + \sum_{m=1}^{\infty} \frac{2\pi^2}{\xi^2}\left(1 + \frac{\pi^2 m^2}{\xi^2}\right) \frac{m\cos(2\pi m l_0)}{\sinh(\frac{\pi^2 \mathrm{m}}{\xi})} \right]. \end{aligned} \tag{2.48}$$

A more descriptive form for Δ_{PN} in terms of system parameters can be obtained by noting that $\xi_{1/2} \simeq \xi_0$ and $\eta_{1/2} \simeq \eta_0$,

$$\Delta_{\mathrm{PN}} \simeq \sum_{m=1}^{\infty} \left[\frac{4\pi^2\omega_0\eta_0^2}{\xi_0^2} - \frac{4\pi^2\,g}{3\xi_0^2}\eta_0^4 \left(1 + \frac{\pi^2 m^2}{\xi_0^2}\right) \right] \frac{m\,(1 - (-1)^m)}{\sinh\left(\frac{\pi^2 m}{\xi_0}\right)}\,, \tag{2.49}$$

Which is in complete agreement with the expression of PNB in Ref. [114], chapter 2 section 2.1.1.2. Fig. 2.9 depicts the ratio of the variationally obtained Peierls-Naborro barrier to the soliton energy for different values of nonlinearity over two pump cycles. Fig. 2.9 suggests

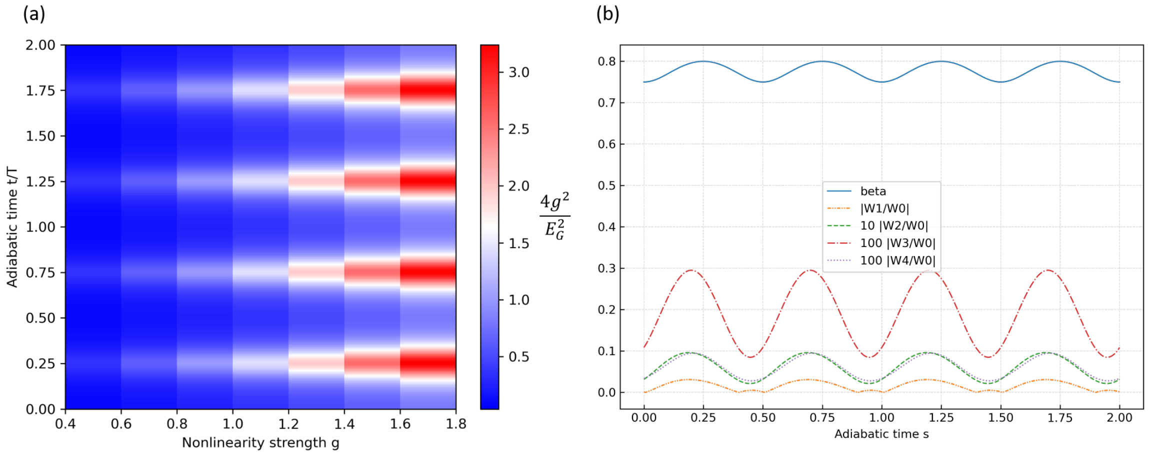

Figure 2.8: (a) Checking band mixing validity condition in Eq. 2.37. We observe that increase in the quantity $4g^2/E_\mathrm{G}^2$ increases the error γ in Fig. 2.7. The condition $4g^2/E_\mathrm{G}^2 \ll 1$ is a stringent sufficient condition for validity of band mixing approximation, and even for $4g^2/E_\mathrm{G}^2 \simeq 3$ we observe less than 10 percent error in soliton reconstruction. (b) Checking the sufficient validity condition for Wannier locality approximation. We observe that the pattern of increase in β as defined in Eq. 2.41 is in accordance with the increase in Wannier overlaps $W1 \equiv W^{(0)}_{0,0,0,1}$, $W2 \equiv W^{(0)}_{0,0,0,2}$, $W3 \equiv W^{(0)}_{0,0,0,3}, \cdots$ with respect to $W0 \equiv W^{(0)}_{0,0,0,0}$ for the lowest Rice-Mele band. Thus, it is a good indicator of the increase in non-local Wannier overlaps. The pump sequence considered here has the functional form $J(t) = 1$, $\delta(t) = 0.5\cos(2\pi t/T)$, $\Delta(t) = \sin(2\pi t/T)$.

that at certain time intervals during the pump cycle, the PNB is almost vanishing (note that it is always positive). However, the PNB calculated above is only an estimation of the true PNB through a variational ansatz, thus it only gives a lower bound of the actual energy barrier. Fig. 2.9 further suggests that the strength of PNB increases by increasing the nonlinearity.

2.3.2 Derivation of the band-mixing validity condition

Here we give a derivation of the sufficient condition for the validity of the band mixing approximation. We begin by the stationary DNLS of the lattice

$$\mu_s\,\varphi_\mathbf{i} = \sum_\mathbf{j} H_\mathbf{ij}(s)\,\varphi_\mathbf{j} - g\,|\varphi_\mathbf{i}|^2\varphi_\mathbf{i}\,, \tag{2.50}$$

and treat the band mixing terms perturbatively. In Eq. 2.50, the stable state soliton solution $\varphi_\mathbf{i}$ is a superposition of single-band components, $\varphi_\mathbf{i} = \sum_n \varphi_\mathbf{i}^{(n)}$. For simplicity, we assume that soliton occupies the lowest band ($n = 0$), and only consider its coupling to the immediate higher band ($n = 1$), since all the other bands are far off-detuned. Note that for the Rice-Mele model this two-band approximation is exact. Furthermore, generalization

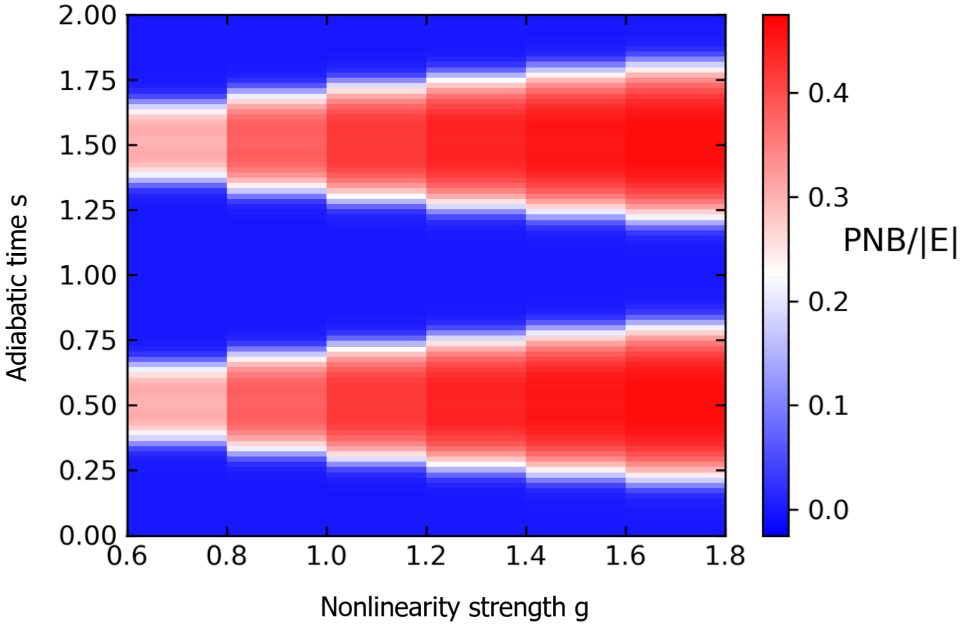

Figure 2.9: The Ratio of Peierls-Naborro barrier to the soliton energy for two pump cycles and different values of nonlinearity. Increase in the nonlinearity strength leads to stronger barrier between adjacent solitons in Wannier representation.

of our arguments for solitons bifurcating from higher bands is straightforward. Without loss of generality, we further assume that soliton is real-valued, $\varphi_{\mathbf{i}}^* = \varphi_{\mathbf{i}}$.

With the above assumptions, the soliton is expanded as $\varphi_{\mathbf{i}} = \varphi_{\mathbf{i}}^{(0)} + \varphi_{\mathbf{i}}^{(1)}$, where $\varphi_{\mathbf{i}}^{(0)}$ is the zeroth order approximation neglecting band mixing, and $\varphi_{\mathbf{i}}^{(1)}$ is the first order correction. The energy functional takes the form

$$\begin{aligned} H &= \sum_{\mathbf{i},\mathbf{j}} \varphi_{\mathbf{i}}^{(0)} H_{\mathbf{ij}}(s) \varphi_{\mathbf{j}}^{(0)} + \sum_{\mathbf{i},\mathbf{j}} \varphi_{\mathbf{i}}^{(1)} H_{\mathbf{ij}}(s) \varphi_{\mathbf{j}}^{(1)} - g \sum_{\mathbf{i}} \left(\varphi_{\mathbf{i}}^{(0)} + \varphi_{\mathbf{i}}^{(1)} \right)^4 \\ &= \left\{ \sum_{\mathbf{i},\mathbf{j}} \varphi_{\mathbf{i}}^{(0)} H_{\mathbf{ij}}(s) \varphi_{\mathbf{j}}^{(0)} - g \sum_{\mathbf{i}} \varphi_{\mathbf{i}}^4 \right\} + \left\{ \sum_{\mathbf{i},\mathbf{j}} \varphi_{\mathbf{i}}^{(1)} H_{\mathbf{ij}}(s) \varphi_{\mathbf{j}}^{(1)} - \sum_{\mathbf{i}} 6g\, \varphi_{\mathbf{i}}^{(0)2}\, \varphi_{\mathbf{i}}^{(1)2} \right. \qquad (2.51) \\ &\left. - \sum_{\mathbf{i}} 4g \varphi_{\mathbf{i}}^{(0)3} \varphi_{\mathbf{i}}^{(1)} \right\} + \mathcal{O}\left(\varphi^{(1)3}\right) = H^{(0)} + H^{(1)} + \mathcal{O}\left(\varphi^{(1)3}\right). \end{aligned}$$

In the last line of Eq. 2.51, we neglect the terms of the order of $\varphi_{\mathbf{i}}^{(3)}$ or higher since band mixing is a perturbative effect and soliton power in $n = 1$ band is sufficiently small. To study the effect of band mixing, we examine $H^{(1)}$ in Eq. 2.51 in detail,

$$H^{(1)} = \sum_{\mathbf{i},\mathbf{j}} \varphi_{\mathbf{i}}^{(1)} \left[H_{\mathbf{ij}}(s) - 6g\, \varphi_{\mathbf{i}}^{(0)2}\, \delta_{\mathbf{ij}} \right] \varphi_{\mathbf{j}}^{(1)} - \sum_{\mathbf{i}} 4g \varphi_{\mathbf{i}}^{(0)3} \varphi_{\mathbf{i}}^{(1)} . \qquad (2.52)$$

The first term in Eq. 2.52 is the hopping Hamiltonian of the lattice in an attractive potential well $-6g\varphi_{\mathbf{i}}^{(0)2}$, and the second term plays the role of a source term. Since $H^{(1)}$ is quadratice, we can obtain its minimum exactly. To this end, it is more convenient to rewrite Eq. 2.52 in vector notation by defining the vector $[\underline{\varphi}^{(1)}]_{\mathbf{i}} = \varphi_{\mathbf{i}}^{(1)}$, $[\underline{b}]_{\mathbf{i}} = 4g\varphi_{\mathbf{i}}^{(0)3}$ and the matrix $[\underline{\underline{\tilde{H}}}]_{\mathbf{ij}} = H_{\mathbf{ij}}(s) - 6g\,\varphi_{\mathbf{i}}^{(0)2}\,\delta_{\mathbf{ij}}$. Thus, Eq. 2.52 is written in a more compact form,

$$H^{(1)} = \underline{\varphi}^{(1)T}\underline{\underline{\tilde{H}}}\,\underline{\varphi}^{(1)} + \underline{b}^T\underline{\varphi}^{(1)} = \underline{\alpha}^{(1)T}\underline{\underline{\tilde{H}}}\,\underline{\alpha}^{(1)} + \underline{b}^T\underline{\alpha}^{(1)} + \underline{\Delta\varphi}^{(1)T}\underline{\underline{\tilde{H}}}\,\underline{\Delta\varphi}^{(1)} \tag{2.53}$$

where $\underline{\varphi}^{(1)} = \underline{\alpha}^{(1)} + \underline{\Delta\varphi}^{(1)}$ and

$$\underline{\alpha}^{(1)} = -\left(\underline{\underline{\tilde{H}}} + \underline{\underline{\tilde{H}}}^T\right)^{-1}\underline{b} = -\frac{1}{2}\,\underline{\underline{\tilde{H}}}^{-1}\,\underline{b}\,. \tag{2.54}$$

Inserting Eq. 2.54 in Eq. 2.53, we find

$$H^{(1)} = -\frac{1}{4}\underline{b}^T\,\underline{\underline{\tilde{H}}}^{-1}\,\underline{b} + \underline{\Delta\varphi}^{(1)T}\,\underline{\underline{H}}\,\underline{\Delta\varphi}^{(1)}\,. \tag{2.55}$$

The minimum of $H^{(1)}$ is achieved by setting

$$\underline{\varphi}^{(1)}_{\text{min}} = -\frac{1}{2}\underline{\underline{\tilde{H}}}^{-1}\underline{b} = -2g\,\underline{\underline{\tilde{H}}}^{-1}\,\underline{\varphi}^{(0)3}\,. \tag{2.56}$$

Thus, we obtain an estimate for soliton's power in band $n = 1$,

$$P^{(1)} = \sum_{\mathbf{i}}|\varphi_{\mathbf{i}}^{(1)}|^2 \simeq 4g^2\left(\underline{\varphi}^{(0)3}\right)^T\underline{\underline{\tilde{H}}}^{-2}\underline{\varphi}^{(0)3} < \frac{4g^2}{\left(\varepsilon^{(1)}_{\text{min}} - \varepsilon_{\text{B}}\right)^2}\,. \tag{2.57}$$

In Eq. 2.57, $\varepsilon^{(1)}_{\text{min}}$ is the minimum energy Bloch state of band $n=1$, ($n=1$ band edge) with respect to the minimum of band $n=0$ ($n=0$ band edge), and ε_{B} is the energy of the bound state of the Hamiltonian $H_{\mathbf{ij}}(s) - 6g\varphi_{\mathbf{i}}^{(0)2}\delta_{\mathbf{ij}}$ on band $n=1$, which is of the order $\sim g$ and can be neglected compared to $\varepsilon^{(1)}_{\text{min}}$ for small g. Since $\varepsilon^{(1)}_{\text{min}}$ is equal to the sum of bandwidth of $n=0$ band ($E^{(0)}_{\text{BW}}$) and the band gap E_{G}, we arrive at the sufficient condition

$$P^{(1)} \lesssim \frac{4g^2}{\left(E^{(0)}_{\text{BW}} + E_{\text{G}}\right)^2} \ll 1\,. \tag{2.58}$$

For the case where the target band is $n = 1$, the same analysis can be done, resulting in a stricter condition

$$P^{(0)} \lesssim \frac{4g^2}{E_{\text{G}}^2} \ll 1\,. \tag{2.59}$$

For the lowest Rice-Mele band with the Hamiltonian

$$\begin{aligned} H = &-\sum_{i=0}^{N-1}\Big[J(1+\delta)\,|i,A\rangle\langle i,B| + J(1-\delta)\,|i,A\rangle\langle i-1,B|\Big] \\ &+\frac{\Delta}{2}\sum_{i=0}^{N-1}\Big[\,|i,A\rangle\langle i,A| - |i,B\rangle\langle i,B|\,\Big] + \text{h.c.}\,, \end{aligned} \tag{2.60}$$

one has explicit expressions for $E_\mathrm{G} = 2\sqrt{(2J\delta)^2 + \Delta^2}$ and $E^{(0)}_\mathrm{BW} = \sqrt{(2J)^2 + \Delta^2} - \sqrt{(2J\delta)^2 + \Delta^2}$. Thus, the sufficient condition Eq. 2.58 reads as

$$\frac{4g^2}{\left(\sqrt{(2J)^2 + \Delta^2} + \sqrt{(2J\delta)^2 + \Delta^2}\right)^2} \ll 1\,. \tag{2.61}$$

For a pump sequence of the form

$$\begin{aligned} J(t) &= J_0\,, \\ \delta(t) &= \delta_0 \cos(2\pi t/T)\,, \\ \Delta(t) &= \ \Delta_0 \sin(2\pi t/T), \end{aligned} \tag{2.62}$$

with the condition $2J_0\delta_0 = \Delta_0$ (such that the band gap always remains constant, $E_\mathrm{G} = \Delta_0$), Eq. 2.63 takes the following form

$$\max_t \frac{4g^2}{\left(\sqrt{(2J(t))^2 + \Delta(t)^2} + \sqrt{(2J(t)\delta(t))^2 + \Delta(t)^2}\right)^2} = \left(\frac{2g}{1+\delta_0}\right)^2 \ll 1\,. \tag{2.63}$$

For the following pump sequence that we considered in this work,

$$\begin{aligned} J(t) &= J_0\Big(1 + 1/2\cos(2\pi t/T)\Big)\,, \\ \delta(t) &= \delta_0 \cos(2\pi t/T)/(2+\cos(2\pi t/T))\,, \\ \Delta(t) &= \ J_0 \sin(2\pi t/T), \end{aligned} \tag{2.64}$$

the condition in Eq. 2.63 reads as

$$\max_t \frac{4g^2}{\left(\sqrt{(2J(t))^2 + \Delta(t)^2} + \sqrt{(2J(t)\delta(t))^2 + \Delta(t)^2}\right)^2} = (g/J_0)^2 \ll 1\,. \tag{2.65}$$

Note that both conditions Eq. 2.63 and Eq. 2.65 point to the smallness of g.

2.3.3 Derivation of the Wannier locality validity condition

To derive the Wannier locality condition, we resort to the analytical expressions for the Wannier functions of the Rice-Mele model. The Bloch functions of the Rice-Mele model are

$$U(k) = \begin{pmatrix} u^{(1)}_\mathrm{A}(k) & u^{(0)}_\mathrm{A}(k) \\ u^{(1)}_\mathrm{B}(k) & u^{(0)}_\mathrm{B}(k) \end{pmatrix} = \frac{1}{\sqrt{2(1+\hat{d}_z)}} \begin{pmatrix} 1+\hat{d}_z & \hat{d}_x - i\hat{d}_y \\ \hat{d}_x + i\hat{d}_y & -(1+\hat{d}_z) \end{pmatrix} \tag{2.66}$$

where

$$\mathbf{d}(k) = \Big[J(1+\delta) + J(1-\delta)\cos(k)\Big]\,\hat{\mathbf{e}}_x + \Big[J(1-\delta)\sin(k)\Big]\,\hat{\mathbf{e}}_y + \Delta\,\hat{\mathbf{e}}_z\,, \tag{2.67}$$

and $\hat{d}(k) = \hat{d}_x\hat{\mathbf{e}}_x + \hat{d}_y\hat{\mathbf{e}}_y + \hat{d}_z\hat{\mathbf{e}}_z = \mathbf{d}(k)/|\mathbf{d}(k)|$. For the lowest Rice-Mele band ($n = 0$), the Wannier functions have the form

$$\begin{pmatrix} w^{(0)}_{j,A}(l) \\ w^{(0)}_{j,B}(l) \end{pmatrix} = \begin{pmatrix} w^{(0)}_{j-l,A}(0) \\ w^{(0)}_{j-l,B}(0) \end{pmatrix} , \tag{2.68}$$

with

$$\begin{aligned} w^{(0)}_{j-l,A}(0) &= \frac{1}{2\pi}\int_{-\pi}^{\pi} dk\, e^{ik(j-l)} u^{(0)}_{\mathrm{A}}(k) = \frac{1}{2\pi}\int_{-\pi}^{\pi} dk\, e^{ik(j-l)} \frac{\hat{d}_x}{\sqrt{2(1+\hat{d}_z)}} , \\ w^{(0)}_{j-l,B}(0) &= \frac{1}{2\pi}\int_{-\pi}^{\pi} dk\, e^{ik(j-l)}\, u^{(0)}_{\mathrm{B}}(k) = -\frac{1}{2\pi}\int_{-\pi}^{\pi} dk\, e^{ik(j-l)} \sqrt{\frac{1}{2}(1+\hat{d}_z)} \,. \end{aligned} \tag{2.69}$$

We can express $\hat{d}_x$ and $\hat{d}_z$ in terms of δ and $\Delta/2J$,

$$\hat{d}_x = \frac{1}{\sqrt{1+(\Delta/2J)^2}} + \mathcal{O}\Big(\frac{1-\delta}{1+(\Delta/2J)^2}\Big)(k) , \quad \hat{d}_z = \frac{(\Delta/2J)}{\sqrt{1+(\Delta/2J)^2}} + \mathcal{O}\Big(\frac{1-\delta^2}{1+(\Delta/2J)^2}\Big)(k) . \tag{2.70}$$

The band energies are the following,

$$\varepsilon^{(1)}(k) = |\mathbf{d}(k)| , \quad \varepsilon^{(0)} = -|\mathbf{d}(k)| , \quad |\mathbf{d}(k)| = \sqrt{2J^2(1+\delta^2) + \Delta^2 + 2J^2(1-\delta^2)\cos(k)} , \tag{2.71}$$

and the band width of both bands is

$$E^{(0)}_{\mathrm{BW}} = E^{(1)}_{\mathrm{BW}} = 2J\sqrt{1+\left(\frac{\Delta}{2J}\right)^2}\left[1 - \sqrt{1 - \frac{1-\delta^2}{1+\left(\frac{\Delta}{2J}\right)^2}}\right] \tag{2.72}$$

From Eqs. 2.69, 2.70 and 2.72 one can see that to the zeroth order in $(1-\delta)/(1+\eta^2)$ and $(1-\delta^2)/(1+\eta^2)$ ($\eta = \Delta/2J$), Wannier functions are completely localized on a single unit-cell and vanish outside. This fact is consistent with the $\delta = 1$ limit which corresponds to a completely dimerized lattice. By examining Eqs. 2.70 and 2.72 we choose $(1-\delta^2)/(1+\eta^2)$ as a suitable quantity to characterize the locality of the Wannier functions. The requirement for the locality of Wannier functions then reads as

$$\beta \equiv \frac{1-\delta^2}{1+\left(\frac{\Delta}{2J}\right)^2} \ll 1 . \tag{2.73}$$

2.4 An interaction-induced topological pump for ultracold atomic mixtures

The theoretical framework presented in this work is based on the general DNLS in Eq. (2.1), and hence, it applies to a broad range of nonlinear lattice systems. In particular, this equation corresponds to the Gross-Pitaevskii equation describing a weakly-interacting Bose gas evolving on a moving lattice potential. In this section, we propose to go beyond the paradigm of nonlinear pumps for single-component bosonic systems, by introducing a mapping to an imbalanced Bose-Bose atomic mixture, which encompasses the DNLS in Eq. (2.1) as its semiclassical limit (within the Thomas-Fermi approximation). As we explain below, this original approach reveals an interaction-induced topological pump, where solitons of impurity atoms undergo a quantized drift resulting from genuine interaction processes with their environment.

We start from a microscopic theory for an imbalanced Bose-Bose atomic mixture on a 1D lattice [194], as described by the second-quantized Hamiltonian

$$\begin{aligned}\hat{H} = &\sum_{\langle \mathbf{i},\mathbf{j}\rangle} \hat{\phi}^\dagger_{\mathbf{i}}\, H^{(\phi)}_{\mathbf{ij}}\, \hat{\phi}_{\mathbf{j}} + \sum_{\mathbf{i}} \frac{U_{\phi\phi}}{2}\, \hat{\phi}^\dagger_{\mathbf{i}}\hat{\phi}^\dagger_{\mathbf{i}}\hat{\phi}_{\mathbf{i}}\hat{\phi}_{\mathbf{i}} + \sum_{\langle \mathbf{i},\mathbf{j}\rangle} \hat{\sigma}^\dagger_{\mathbf{i}}\, H^{(\sigma)}_{\mathbf{ij}}\, \hat{\sigma}_{\mathbf{j}} + \sum_{\mathbf{i}} \frac{U_{\sigma\sigma}}{2}\, \hat{\sigma}^\dagger_{\mathbf{i}}\hat{\sigma}^\dagger_{\mathbf{i}}\hat{\sigma}_{\mathbf{i}}\,\hat{\sigma}_{\mathbf{i}} \\ &+ \sum_{\mathbf{i}} U_{\phi\sigma}\, \hat{\phi}^\dagger_{\mathbf{i}}\hat{\phi}_{\mathbf{i}}\, \hat{\sigma}^\dagger_{\mathbf{i}}\hat{\sigma}_{\mathbf{i}}\,, \end{aligned} \tag{2.74}$$

where $\hat{\phi}_{\mathbf{i}}$ and $\hat{\sigma}_{\mathbf{i}}$ are bosonic field operators on the lattice; note that we use the same conventions for indices $\mathbf{i} = (i, \alpha)$ as before. Specifically, the first line describes single-body processes (i.e. nearest-neighbor hopping and onsite potentials) and intra-species contact interaction processes for the majority atoms, which are described by the field operator $\hat{\phi}_{\mathbf{i}}$; the second line describes single-body processes and intra-species contact interactions for impurity atoms, represented by the field operator $\hat{\sigma}_{\mathbf{i}}$; and the third line describes inter-species interaction processes. We assume that the intra-species interaction strengths are both repulsive, ($U_{\sigma\sigma}, U_{\phi\phi} > 0$), whereas the inter-species interaction strength is attractive ($U_{\phi\sigma} < 0$).

In order to derive the equations governing the coherent state profiles of the two species in the mixture, we start from the microscopic Hamiltonian in Eq. (2.74). The coherent-state action of the system takes the following form ($\hbar = 1$),

$$S[\bar{\phi}, \phi; \bar{\sigma}, \sigma] = \int_{t_i}^{t_f} dt\, L[\bar{\phi}, \phi; \bar{\sigma}, \sigma]\,, \tag{2.75}$$

with the Lagrangian

$$\begin{aligned} L[\bar{\phi}, \phi; \bar{\sigma}, \sigma] = &\sum_{\mathbf{i}} \bar{\phi}_{\mathbf{i}} \Big[i\partial_t + \mu_\phi \Big] \phi_{\mathbf{i}} - \sum_{\langle \mathbf{i},\mathbf{j}\rangle} \bar{\phi}_{\mathbf{i}}\, t_\phi H^{(\phi)}_{\mathbf{ij}}\, \phi_{\mathbf{j}} - \sum_{\mathbf{i}} \frac{g_{\phi\phi}}{2} |\phi_{\mathbf{i}}|^4 \\ &+ \sum_{\mathbf{i}} \bar{\sigma}_{\mathbf{i}} \Big[i\partial_t + \mu_\sigma \Big] \sigma_{\mathbf{i}} - \sum_{\langle \mathbf{i},\mathbf{j}\rangle} \bar{\sigma}_{\mathbf{i}}\, H^{(\sigma)}_{\mathbf{ij}}\, \sigma_{\mathbf{j}} - \sum_{\mathbf{i}} \frac{g_{\sigma\sigma}}{2} |\sigma_{\mathbf{i}}|^4 - \sum_{\mathbf{i}} g_{\phi\sigma} |\sigma_{\mathbf{i}}|^2 |\phi_{\mathbf{i}}|^2 . \end{aligned} \tag{2.76}$$

where $\phi_{\mathbf{i}}$ and $\sigma_{\mathbf{i}}$ denote classical fields satisfying the constraints $\sum_{\mathbf{i}} |\phi_{\mathbf{i}}|^2 = N_\phi/(N_\phi + N_\sigma)$ and $\sum_{\mathbf{i}} |\sigma_{\mathbf{i}}|^2 = N_\sigma/(N_\phi + N_\sigma)$, with N_ϕ and N_σ the particle number of majority and impurity species, respectively; the interaction parameters are defined as $g_{\alpha\beta} = U_{\alpha\beta}(N_\phi + N_\sigma)$, with $\alpha, \beta = (\phi, \sigma)$; $\mu_{\phi,\sigma}$ denote the chemical potentials.

To proceed, we seek stationary state solutions for the coherent state fields of the form $\phi^{(\mathrm{ss})}_{\mathbf{i}}(t) = e^{-i\omega_0 t}\, \phi_{\mathbf{i}}$ and $\sigma^{(\mathrm{ss})}_{\mathbf{i}}(t) = e^{-i\omega_0 t}\, \sigma_{\mathbf{i}}$, which minimize $L[\bar{\phi}, \phi; \bar{\sigma}, \sigma]$. Such solutions are the saddle-point solutions of the quantum mechanical action, giving the mean-field stable states of the system. The Lagrangian then takes the time-independent form

$$\begin{aligned}L[\bar{\phi}, \phi; \bar{\sigma}, \sigma] = &\sum_{\mathbf{i}} \bar{\phi}_{\mathbf{i}} \Big[\omega_0 + \mu_\phi\Big]\phi_{\mathbf{i}} - \sum_{\langle \mathbf{i},\mathbf{j}\rangle} \bar{\phi}_{\mathbf{i}}\, H^{(\phi)}_{\mathbf{ij}}\, \phi_{\mathbf{j}} - \sum_{\mathbf{i}} \frac{g_{\phi\phi}}{2}\, |\phi_{\mathbf{i}}|^4 \\ &+ \sum_{\mathbf{i}} \bar{\sigma}_{\mathbf{i}} \Big[\omega_0 + \mu_\sigma\Big]\sigma_{\mathbf{i}} - \sum_{\langle \mathbf{i},\mathbf{j}\rangle} \bar{\sigma}_{\mathbf{i}}\, H^{(\sigma)}_{\mathbf{ij}}\, \sigma_{\mathbf{j}} - \sum_{\mathbf{i}} \frac{g_{\sigma\sigma}}{2}\, |\sigma_{\mathbf{i}}|^4 - \sum_{\mathbf{i}} g_{\phi\sigma}\, |\sigma_{\mathbf{i}}|^2\, |\phi_{\mathbf{i}}|^2 .\end{aligned} \tag{2.77}$$

To minimize the Lagrangian, the corresponding Euler-Lagrange equations are derived from $\delta L/\delta\,\bar{\phi}_{\mathbf{i}} = 0$ and $\delta L/\delta\,\bar{\sigma}_{\mathbf{i}} = 0$, which leads to the two coupled nonlinear Schrödinger equations (Ref. [194])

$$\begin{aligned}&(\omega_0 + \mu_\phi)\,\phi_{\mathbf{i}} - \sum_{\mathbf{j}} H^{(\phi)}_{\mathbf{ij}}\,\phi_{\mathbf{j}} - \Big(g_{\phi\phi}|\phi_{\mathbf{i}}|^2 + g_{\phi\sigma}|\sigma_{\mathbf{i}}|^2\Big)\phi_{\mathbf{i}} = 0\,, \\ &(\omega_0 + \mu_\sigma)\,\sigma_{\mathbf{i}} - \sum_{\mathbf{j}} H^{(\sigma)}_{\mathbf{ij}}\,\sigma_{\mathbf{j}} - \Big(g_{\phi\sigma}|\phi_{\mathbf{i}}|^2 + g_{\sigma\sigma}\,|\sigma_{\mathbf{i}}|^2\Big)\,\sigma_{\mathbf{i}} = 0\,.\end{aligned} \tag{2.78}$$

In the limiting case of heavy impurities, we neglect their kinetic-energy contributions ($H^{(\sigma)}_{\mathbf{ij}}$) to Eq. (2.78), the so-called Thomas-Fermi approximation. In this case, the second equation in Eq. (2.78) reduces to $(\omega_0 + \mu_\sigma) = g_{\phi\sigma}|\phi_{\mathbf{i}}|^2 + g_{\sigma\sigma}\,|\sigma_{\mathbf{i}}|^2$. For the bright soliton solutions of Eq. (2.78), $\phi_{\mathbf{i}}$ and $\sigma_{\mathbf{i}}$ decay exponentially away from the soliton center, thus, to zeroth order in the impurities hopping strength, $\omega_0 + \mu_\sigma = 0$. Eq. (2.78) then reduce to

$$(\omega_0 + \mu_\phi)\,\phi_{\mathbf{i}} = \sum_{\mathbf{j}} H^{(\phi)}_{\mathbf{ij}}\,\phi_{\mathbf{j}} + \Big(g_{\phi\phi}|\phi_{\mathbf{i}}|^2 + g_{\phi\sigma}|\sigma_{\mathbf{i}}|^2\Big)\phi_{\mathbf{i}}\,, \tag{2.79}$$

$$|\sigma_{\mathbf{i}}|^2 = -g_{\phi\sigma}/g_{\sigma\sigma}\,|\phi_{\mathbf{i}}|^2\,. \tag{2.80}$$

Inserting Eq. (2.80) into Eq. (2.79), we obtain an effective DNLS for $\phi_{\mathbf{i}}$,

$$(\omega_0 + \mu_\phi)\,\phi_{\mathbf{i}} = \sum_{\mathbf{j}} H^{(\phi)}_{\mathbf{ij}}\,\phi_{\mathbf{j}} + \Big(g_{\phi\phi} - g^2_{\phi\sigma}/g_{\sigma\sigma}\Big)|\phi_{\mathbf{i}}|^2\phi_{\mathbf{i}}\,, \tag{2.81}$$

with the effective nonlinearity strength $g = -g_{\phi\phi} + g^2_{\phi\sigma}/g_{\sigma\sigma}$, which for $g_{\phi\phi}g_{\sigma\sigma} < g^2_{\phi\sigma}$ corresponds to a defocusing nonlinearity.

Considering the case of heavy impurities, we neglect their kinetic-energy contributions ($H^{(\sigma)}_{\mathbf{ij}}$) to Eq. (2.78), the so-called Thomas-Fermi approximation. In this regime, one can relate the impurity mean-field profile to the majority profile as

$$|\sigma_{\mathbf{i}}|^2 = -(g_{\phi\sigma}/g_{\sigma\sigma})\,|\phi_{\mathbf{i}}|^2, \tag{2.82}$$

and Eq. (2.78) simplifies to the DNLS

$$(\omega_0 + \mu_\phi)\,\phi_{\mathbf{i}} = \left(\sum_{\mathbf{j}} H^{(\phi)}_{\mathbf{ij}} - u^{\mathrm{MF}}_{\mathbf{i}}\right)\phi_{\mathbf{i}}\,, \quad u^{\mathrm{MF}}_{\mathbf{i}} = g|\phi_{\mathbf{i}}|^2\,. \tag{2.83}$$

Interestingly, Eq. (2.83) is formally equivalent to the DNLS in Eq. (2.3): the majority atoms described by the field $\phi_{\mathbf{i}}$ can form a soliton and undergo a quantized motion upon driving a Thouless pump sequence in the corresponding lattice Hamiltonian, i.e. $H^{(\phi)}_{\mathbf{ij}}(s)$. Importantly, according to Eq. (2.82), the impurity atoms also form a soliton and undergo a quantized motion: the impurities exhibit topological pumping from genuine interaction processes with the majority atoms. In particular, this interaction-induced topological pumping occurs even when the lattice felt by the impurities $H^{(\sigma)}_{\mathbf{ij}}$ is associated with a trivial (non-topological) band structure. This intriguing phenomenon, which could be implemented in ultracold atomic mixtures in optical lattices [21, 40, 194], is reminiscent of topological polarons [89, 90, 30, 150, 161, 15], in the sense that impurities inherit the topological properties of their environment through genuine interaction processes.

We first analyze this interaction-induced topological effect by considering the Thomas-Fermi approximation. It appears from Eq. (2.83) that u^{MF} acts as an effective potential for the majority atoms; a soliton then emerges as the bound state of the impurity field. In the context of highly-imbalanced mixtures with strong impurity-majority coupling, i.e. in the strong-coupling Bose polaron regime, it is customary to assume a variational ansatz describing the profile of the impurity and majority fields [87]; the majority field is then found as the bound state of the impurity potential u^{MF} using the first relation in Eq. (2.83). Here, the variational problem for obtaining u^{MF} reduces to one for ϕ, because of the constraint $u^{\mathrm{MF}} = g|\phi|^2$. As before, we express ϕ in the Wannier basis, and the variational problem is then solved simultaneously for both u^{MF} and ϕ using the ansatz $a_l = \eta\,\mathrm{sech}(\xi\,(l-l_0))$ for the Wannier coefficients of ϕ. The bound state of the resulting impurity potential $u^{\mathrm{MF}} = g|\phi|^2$ then corresponds to the soliton.

Figures 2.10(a) and (b) show the adiabatic evolution of the amplitude η and width ξ of the variational solution $a_l = \eta\,\mathrm{sech}(\xi\,(l-l_0))$ used for the Wannier coefficients of ϕ. We compare these results with the amplitude and width extracted from the bound-state solution associated with the impurity potential $u_{\mathrm{MF}} = g|\phi|^2$, as well as to those extracted from the exact soliton of Eq. (2.3) expressed in Wannier representation. We also show the dependence of these parameters on the nonlinearity g in Fig. 2.10(c), for both the exact soliton and the variational solution. These results validate our variational approach, as well as the bound-state picture of our soliton.

The minimum-energy solutions obtained from the variational ansatz are realized for integer values of the Wannier index l_0, and thus correspond to stable on-site solitons. Moreover, this Wannier index l_0 remains constant over a pump cycle. Hence, this again suggests that the real-space motion of the soliton should follow the quantized Wannier drift, as established by the Chern number. This is verified in Fig. 2.10(d), where the center-of-mass displacement of the calculated bound state is shown to be quantized over a pump cycle (compare with Fig. 2.3).

In order to demonstrate the validity of our results, in particular, the robustness of the interaction-induced topological pump away from the Thomas-Fermi limit, we solve Eq. (2.78) numerically for a mass-balanced mixture, thus including the effects of the impurities' kinetic energy. We again use the Rice-Mele model, but consider two different pump sequences for the majority and impurity species: the majority feels the same (topological)

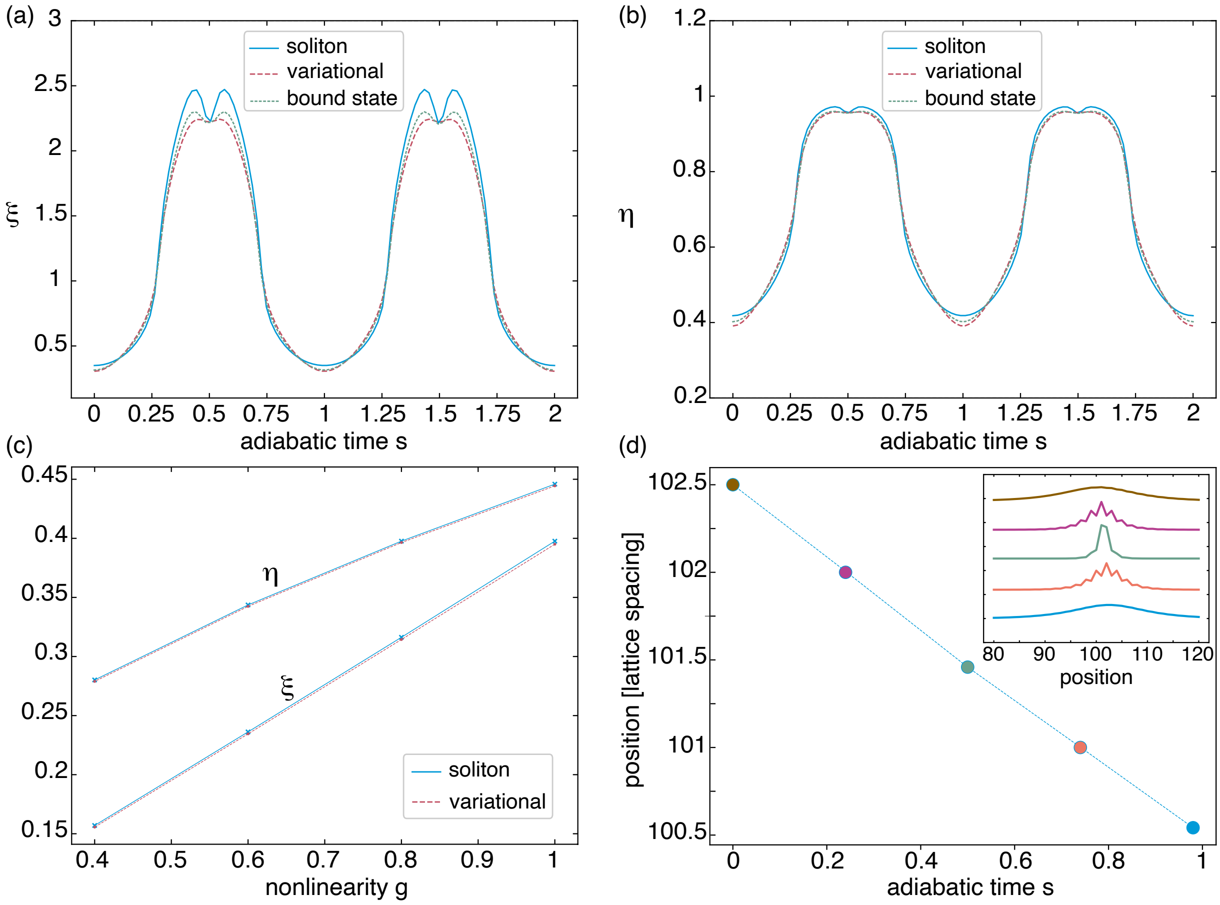

Figure 2.10: Characterizing soliton evolution during two pump cycles. (a) Evolution of the soliton's width ξ in Wannier space over two pump cycles, as obtained by fitting the numerical solution of Eq. (2.3) with a sech function (blue solid line). This is compared to the width of the variational-ansatz solution (dashed red line), and to that of the bound-state solution (green dotted line); here $g = J_0$. (b) Same for the amplitude of the soliton η. (c) Amplitude and width of the exact (solid blue line) and variational-ansatz (dashed red line) solutions as a function of g, at time $s = 0.12$. (d) Center-of-mass displacement of the calculated bound state over one pump cycle. The inset shows the corresponding bound state profiles. The quantized motion is dictated by the Chern number $C = -1$; compare with Fig. 2.3.

pump sequence as in Fig. 2.3, while we apply a trivial sequence for the impurity species. We obtain the steady state solution of Eq. (2.78) over two pump cycles, where the majority particles predominantly occupy the lowest Bloch band. The corresponding trajectories of the CM of both species are depicted in Fig. 2.11, where the impurity CM is shown to be dragged by the majority particles. While the exact form of the CM trajectories depend on the details of the model and pumping sequence, the CM displacement after one pump cycle is dictated by the Chern number of the topological band occupied by the majority

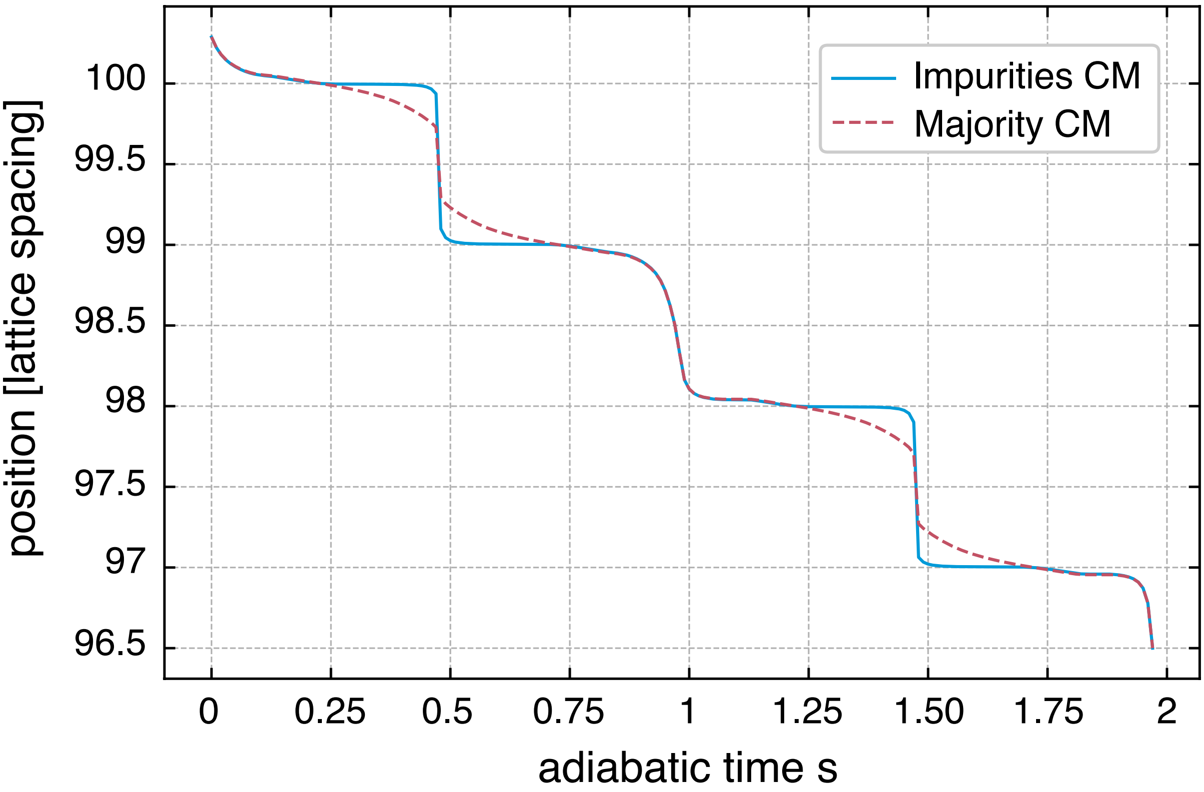

Figure 2.11: Nonlinearity-induced topological pumping in a Bose-Bose mixture. Center-of-mass (CM) trajectories of both species in a Bose-Bose mixture. Here, the interaction strengths are set as $g_{\phi\phi} \simeq 0.226\, J_0$, $g_{\phi\sigma} \simeq -11.32\, J_0$ and $g_{\sigma\sigma} \simeq 2.26\, J_0$. The majority atoms undergo the pumping sequence as in Fig. 2.3, while impurities feel a trivial sequence. Impurity atoms undergo quantized transport through interactions with their environment.

species ($C = -1$ in this case). Although the impurity atoms experience a topologically trivial lattice, they are shown to undergo topological pumping through genuine interaction effects with their environment.

2.4.1 Variational ansatz for the state of Bose-Bose mixture in the Thomas-Fermi limit

The variational treatment of Eqs. (2.82) and (2.83) accounts to minimizing the following energy functional for the field ϕ

$$H[\bar{\phi}, \phi] = \sum_{\mathbf{i},\mathbf{j}} \bar{\phi}_{\mathbf{i}}\, H^{(\phi)}_{\mathbf{ij}}\, \phi_{\mathbf{j}} - \frac{g}{2} \sum_{\mathbf{i}} |\phi_{\mathbf{i}}|^2 - \mu_\phi \left(\sum_{\mathbf{i}} |\phi_{\mathbf{i}}|^2 - N_\phi \right). \tag{2.84}$$

From the knowledge obtained from the soliton solutions of the DNLS, we assume that $\phi_{\mathbf{i}}$ belongs to a single band and expand it in terms of the Wannier functions of the corresponding band, $\phi_{\mathbf{i}} = \sum_l a_l^{(n)}\, w^{(n)}(l)$. We then use a sech variational ansatz for the coefficient amplitudes, $a_l^{(n)} = \eta/\operatorname{sech}\big(\xi(l-l_0)\big)$. The variational energy functional takes the following form

$$
\begin{aligned}
H/\eta^2 = \omega_0^{(n)}\, N_\phi/\eta^2 + \sum_{m=1}^{\infty} \frac{4m}{\sinh(\xi m)} \omega_m^{(n)} \\
- \frac{2\, g W^{(n)}}{3} \eta^2 \left[\frac{1}{\xi} + \sum_{m=1}^{\infty} \frac{2\pi^2}{\xi^2} \left(1 + \frac{\pi^2 m^2}{\xi^2}\right) \frac{m \cos(2\pi m l_0)}{\sinh(\frac{\pi^2 \mathrm{m}}{\xi})} \right],
\end{aligned}
\tag{2.85}
$$

subject to the constraint $N_\phi = \text{const.}$, where

$$
N_\phi/\eta^2 = \frac{2}{\xi} + \sum_{m=1}^{\infty} \frac{4\pi^2}{\xi^2} \frac{m \cos(2\pi m l_0)}{\sinh(\frac{\pi^2 m}{\xi})}\,. \tag{2.86}
$$

For the simulations presented (Fig. 2.10), we assume that $N_\phi = 1$; see Refs. [114, 115] for more details on variational ansätze for DNLS. From the solution of Eqs. (2.85) and (2.86) we then obtain the boson field, $\phi_{\mathbf{i}}$, which is then used to obtain the effective attractive potential $u_{\mathbf{i}}^{\mathrm{MF}} = g|\phi_{\mathbf{i}}|^2$; see Eq. (2.83).

2.4.2 Potential barrier preventing soliton delocalization

The nonlinear term in Eqs. (2.1) (resp. in Eq. (2.15)) leads to the formation of localized soliton solutions, which do not satisfy the lattice (resp. Wannier lattice) translational symmetry. While the stable-state solitons are not translationally invariant, they can be mapped to one another through lattice translations. It is known that an effective potential barrier exists for continuous deformations of each stable-state soliton to a neighboring one. This potential barrier is reminiscent of the Peierls-Naborro barrier (PNB) known in the theory of dislocation dynamics in crystals [8]. Under adiabatic evolution, a soliton in Wannier representation will always remain peaked on a single Wannier index since the potential barrier rules out the existence of solutions that interpolate continuously between two on-site solitons. The strength of this potential barrier can be estimated in terms of the model parameters using the variational ansatz $a_l^{(n)} = \eta/\operatorname{sech}\big(\xi(l-l_0)\big)$ for the Wannier soliton in band n, and the corresponding energy functional in Eq. (2.85),

$$
\begin{aligned}
\Delta_{\text{Barrier}} &\simeq H(\eta_0, \xi_0, l_0 = 1/2) - H(\eta_0, \xi_0, l_0 = 0) \\
&\simeq \sum_{m=1}^{\infty} \left[\frac{4\pi^2 \omega_0^{(n)} \eta_0^2}{\xi_0^2} - \frac{4\pi^2\, g}{3\xi_0^2} \eta_0^4 \left(1 + \frac{\pi^2 m^2}{\xi_0^2}\right) \right] \frac{m\,(1-(-1)^m)}{\sinh\!\left(\frac{\pi^2 m}{\xi_0}\right)}\,,
\end{aligned}
\tag{2.87}
$$

where

$$
H(\eta_0, \xi_0, l_0 = 0) = \min_{\eta,\xi} H(\eta, \xi, l_0 = 0). \tag{2.88}
$$

The estimated Δ_{Barrier} depends on the model parameters via the Fourier transform of the dispersion relation at $l = 0$, $\omega_0^{(n)} = 1/N \sum_{k=0}^{N-1} \epsilon_k^{(n)}$, and the interaction parameter g. We verified that the expression in Eq. (2.87) is in agreement with a result found in Ref. [114] for DNLS equations with nearest-neighbor hopping.

2.4.3 Implementation in ultracold atoms

The interaction-induced topological pump introduced above could be experimentally implemented in ultracold atomic gases involving two bosonic species [21, 40, 194]. In fact, the parameter values incorporated in our numerical simulations of Eq. (2.78), and displayed in Fig. 2.11, are compatible with an experimental realization based on bosonic $^7\text{Li} - ^7\text{Li}$ mixtures, with two different hyperfine states of ^7Li as "majority" and "impurity" atoms; we note that the formation of solitons in Lithium gases was previously investigated, both theoretically and experimentally [1, 198]. Following Ref. [101], the scattering lengths between atoms in state $(F=1, m_F=1)$ – "impurity" atoms – and $(F=1, m_F=0)$ – "majority" atoms – can be set to $a_{\phi\phi} \simeq 0.154\, a_0$, $a_{\phi\sigma} \simeq -7.57\, a_0$, $a_{\sigma\sigma} \simeq 1.514\, a_0$, at a magnetic field $B \simeq 575\, G$, where a_0 is the Bohr radius ($a_0 = 0.0529\,\text{nm}$); we note that these scattering lengths are highly tunable thanks to a broad Feshbach resonance. As further discussed below, this configuration is compatible with the interaction parameters $(g_{\phi\phi}, g_{\sigma\sigma}, g_{\phi\sigma})$ used in our numerics.

The lattice structure and pump sequence can be designed within a time-dependent optical lattice. For instance, following Ref. [151], the atoms can be loaded in a potential landscape comprised of two superimposed optical lattices, with a long-wavelength lattice ($\lambda_l = 1064\,\text{nm}$) and a shorter lattice ($\lambda_s = \lambda_l/2$), with different amplitudes ($V_l = 3.0\, E_R$ and $V_s = 1.0\, E_R$, with $E_R = h^2/(2m\, \lambda_l^2)$ the recoil energy of the long lattice). Such an optical lattice potential takes the form $V(x, \phi) = -V_l \cos^2(2\pi x/\lambda_l - \phi) - V_s \cos^2(2\pi x/\lambda_s)$, and it implements the Rice-Mele lattice considered in our numerics: the Thouless pump sequence is simply realized by sweeping the phase ϕ from 0 to 2π. The relevant parameters of the Rice-Mele model can be extracted from a tight-binding analysis of the optical lattice potential [151], and the resulting pump sequence is described by the following elliptic path in parameter space: $((J_1 - J_2)/a)^2 + (\Delta/b)^2 = 1$, with $a \simeq 0.19\, E_R$ and $b \simeq 0.475\, E_R$. In our numerics, we choose a closely related pumping sequence with $a = 0.15\, E_R$ and $b = 0.5\, E_R$; this choice does not affect our final conclusions, since topological pumping is robust against smooth deformations of the pumping sequence. Finally, to reveal the interaction-induced topological transport for impurities, we propose to implement a trivial pump sequence for that species only [see Fig. 2.11]; this could be realized by designing a state-dependent optical lattice [106], for instance, using the Floquet-engineering scheme of Ref. [109].

The particle numbers of the two species can be set to $N_\phi \simeq 1500$ [27] and $N_\sigma/N_\phi \simeq 1/30$. With this choice, we obtain the interaction parameters according to the relation $g_{\alpha\beta}/E_R = (N_\sigma + N_\phi)\, \sqrt{8/\pi}\, k_l\, a_{\alpha\beta} (V_s/E_R)^{3/4}$ [21], where $\alpha, \beta = (\phi, \sigma)$ and $k_l = 2\pi/\lambda_l$. Setting the pump parameter $J_0 = 0.5 E_R$, the numerical values for the interaction parameters are obtained as $g_{\phi\phi} \simeq 0.226\, J_0$, $g_{\phi\sigma} \simeq -11.32\, J_0$ and $g_{\sigma\sigma} \simeq 2.26\, J_0$, which are the values used in our numerical simulations [Fig. 2.11].

2.5 Conclusion and Outlook

In this work, we outlined a general theoretical framework that connects Bloch band's topology to nonlinear excitations, hence elucidating the topological transport of solitons in the context of nonlinear Thouless pumps. Solitons are stable states of nonlinear lattice systems described by the paradigmatic discrete nonlinear Schrödinger equation (DNLS), which is central in describing nonlinear phenomena in a wide range of physical settings, from nonlinear optics and photonics, to ultracold quantum matter, fluid dynamics and plasma physics. In this sense, characterizing the influence of Bloch band's topology on the behavior of the stable states of DNLS is of prime importance. This program is particularly challenging due to the lack of generic theoretical approaches connecting notions of topological physics to nonlinear systems and vice versa. Furthermore, introducing nonlinearities in more sophisticated topological systems, such as higher-dimensional settings, or lattices exhibiting higher-order topology and symmetry-protected features, could lead to exotic phenomena exhibited by the nonlinear modes of the system; see Ref. [57] and references therein. By providing a scheme that naturally connects topological indices of band structures to nonlinear excitations, our work opens the door to the exploration of novel nonlinear topological phenomena.

We also illustrated the universality of our approach, by introducing a topological pump for Bose-Bose atomic mixtures, where one species (impurity atoms) experience a quantized drift through genuine interaction processes with the other species (the surrounding majority atoms). Importantly, the impurity atoms inherit the topological properties of their environment through inter-species interactions. We note that such interaction-induced topology has been previously studied in the context of topological polarons, namely, in mixtures with strong population imbalance, where individual topological excitations can bind to mobile impurities [89, 90, 150, 15]. The present scheme extends those concepts to more complex majority-impurity states, such as coupled coherent states within a superfluid phase. We also point out that the proposed scheme can be implemented using available cold-atom technologies, and the quantized transport of impurities can be measured in-situ, using state-selective imaging techniques [20]. Besides, the Chern number characterizing the interaction-induced topological pump could also be directly extracted by interferometry [90].

This second part of our work explores an interesting interplay of nonlinearity and band topology, and it addresses the following question: can nonlinearities induce topological features within a multi-component system? This question is fascinating since different components can have different band structures with distinct topological features: as we demonstrate, a topologically trivial component can become non-trivial through genuine interaction processes. The interplay of interactions/nonlinearities and band topology in multi-component systems is yet a relatively unexplored territory with lots of open questions and potential for discovering new physics. For instance, the questions regarding the possible mechanisms for pumping break-down, in strongly interacting bosonic or fermionic systems or in the mean-field limit (where the interactions take the form of nonlinearities), are still active areas of recent experimental and theoretical research.

Moreover, aside from the scalar DNLS, which is ubiquitous in optics, photonics, atomic physics, and many other areas of physics, coupled scalar DNLS equations appearing in the form of vector DNLS equations also arise in many different contexts. For instance, various components of the vector DNLS can be different modes of an optical device coupled via nonlinearities. Furthermore, in the context of multi-component ultracold gases, each component can come from other species, or different coexisting phases of the gas, with interactions treated within the mean-field theory. Therefore, it is tempting to generalize the scheme developed here to address the interplay of band topology and nonlinearity in coupled nonlinear systems. We expect richer physics to arise in the multi-component DNLS case since different components can have different band structure topology.

Finally, we note that our proposal will motivate future studies of interaction-induced topological pumping beyond the mean-field regime. It will be interesting to see, then, how quantum fluctuations can modify the results.

Chapter 3

Quantum impurities strongly coupled to condensed bosonic systems

This chapter is based on the following publication:

[2] **Mostaan, N.**, Goldman, N., Grusdt, F. (2023). A unified theory of strong coupling Bose polarons: From repulsive polarons to non-Gaussian many-body bound states, arXiv preprint arXiv:2305.00835

3.1 Introduction

Explaining the behavior of quantum materials through the notion of quasiparticles is a central paradigm in condensed matter physics. While many phases of matter, such as conventional superconductors and Fermi liquids, possess quasiparticle-like excitations [16, 69, 162], in some strongly correlated phases, such as strange metals, the excitation spectra defy quasiparticle-based descriptions [122, 203, 204, 19, 54]. Thus, studying the detailed mechanisms of quasiparticle formation and breakdown is of prime interest. An emblematic scenario for quasiparticle formation is the dressing of electrons in solid-state systems by lattice vibrations, giving rise to a quasiparticle termed *polaron*. Since its first formulation by Landau and Pekar [124], the polaron concept has been central to describing electron mobility in organic semiconductors [5, 56, 48, 100, 210, 55], exciton transport in light-harvesting complexes [52, 67, 68], and phonon-based theories of high-temperature superconductivity [227, 23, 3, 2, 63, 4]. The problem of characterization and description of polarons naturally falls in the broader context of *mobile quantum impurity problems*, where a single mobile impurity interacts with the elementary excitations of a many-body medium and gives rise to a quasiparticle with renormalized properties.

Recent developments in the realization of synthetic quantum systems with increasing degrees of control and tunability resulted in an upsurge in research on mobile quantum impurity problems, both in fermionic [120, 176, 119, 189, 174, 143, 178, 164, 158, 166] and

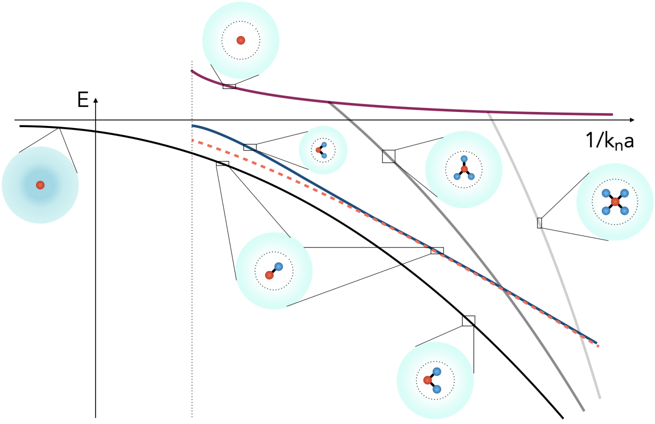

Figure 3.1: Schematic illustration of the Bose polaron spectrum across an impurity-boson Feshbach resonance for repulsively interacting bosons. In the presence of inter-boson interactions, the attractive polaron persists to the repulsive side as a well-defined resonance, while other metastable many-body bound states appear in addition to the repulsive polaron. These many-body bound states emerge due to the competition of multiple impurity-boson binding and inter-boson repulsion. The structure of the main component of each many-body bound state is shown schematically.

bosonic [108, 99, 220, 35, 72, 190, 195, 169, 133, 86, 145] systems. In the latter case, the quasiparticle formed from an impurity resonantly coupled to a bosonic medium in a Bose-Einstein Condensate (BEC) phase is called *Bose polaron*. Numerous theoretical works have studied different properties of Bose polarons, including spectral response and quasiparticle properties [108, 99, 169, 86, 184, 41, 129, 185], the implication of three-body correlations on the state of Bose polarons [222, 130, 42, 43, 200] and finite-temperature effects [91, 62, 70], to name a few. The powerful toolbox available in atomic gas settings has enabled the investigation of various aspects of Bose polaron physics, reaching impurity-medium interactions deep into the strong coupling regime. Contrary to its weak coupling counterpart, the strong coupling regime poses substantial challenges to both experiments and theory and comes with many aspects that, as we now review, are still poorly understood.

In particular, a unified theoretical framework is lacking that could describe the connection of repulsive and attractive polarons. The mainly employed theoretical methods so far either included an infinite number of weakly correlated excitations in the polaron cloud [185, 88, 60] or a highly restricted number of potentially strongly correlated excitations [169, 133, 108]. On the repulsive side of the Feshbach resonance the former approaches do not include an attractive polaron branch. In contrast, the latter approaches predict that the attractive polaron continuously evolves into the molecular dimer state, energetically well below the metastable repulsive polaron, as the Feshbach resonance is crossed. We will argue in this article that neither of these scenarios is completely correct.

The peculiar nature of the Bose polaron problem at strong couplings becomes clearer by considering a static impurity interacting with an ideal, i.e. non-interacting BEC via an attractive potential. The strong coupling regime occurs when the impurity-boson potential admits a bound state with energy $-E_{\mathrm{B}} < 0$. In this regime, beyond a certain scattering length, a long-lived metastable polaronic state with energy $E_{\mathrm{RP}} > 0$ emerges, known as repulsive polaron, that involves the depletion of bosons close to the impurity from the polaron cloud. The repulsive polaron is unstable against the decay of bosons to the bound state. However, the number of decaying particles is not restricted for bosons, unlike fermions where Pauli blocking inhibits multiple occupations of the bound state. Thus, successive decay of bosons is energetically favorable, with a gain in energy per particle equal to the impurity-boson binding energy. In this sense, the spectrum of the system consists of an incoherent continuum of excitations on top of the repulsive polaron, together with a discrete set of bound states with energies $E_n = E_{\mathrm{RP}} - n\,E_{\mathrm{B}}$ for $n = 1, 2, 3, \cdots$, involving n particles bound to the impurity.

This pathological behavior, first noted in Ref. [185] and discussed in further detail in [60], initiated active theoretical research to improve theoretical models that include the repulsive inter-boson interactions to counteract the impurity-induced instability of the ground state. To illustrate this effect, consider an even simpler model than the impurity-ideal gas model described above, where the bosons can only occupy a single state with vacuum energy E_{RP} and negative energy per particle $-E_{\mathrm{B}}$. In this single orbital model, including an effective inter-boson repulsion term $Un^2/2$ stabilizes the system. The ground state is then realized for $n^* = E_{\mathrm{B}}/U$ bosons, giving a finite ground state energy $E_{\mathrm{RP}} - E_{\mathrm{B}}^2/2U$ (see Fig. 3.1 for a schematic illustration). Thus, an effective repulsive interaction among bosons makes the model stable. While this simplified model offers a rough idea of how inter-boson repulsion can stabilize the system, the actual scenario involving a mobile impurity interacting with a Bose-Einstein condensate (BEC) is significantly more complex. This complexity arises due to the presence of a continuum of interacting bosonic modes, driven by two-body repulsion between bosons. In practice, this repulsion-induced stabilization is manifested via short-range repulsion of bosons close to the impurity, signifying the importance of short-range effects. Besides, an ideal theoretical description of strong coupling Bose polarons must involve an indefinite number of interacting bosons in the polaron cloud to properly capture the local correlations around the impurity while interpolating to long-length scales to account for the distortion of the condensate, rendering the problem theoretically challenging.

Recent theoretical works have analyzed the ground state energy by treating inter-boson interaction at the mean-field level [177, 221, 142, 92, 85, 98], showing that the ground state energy remains finite in the thermodynamic limit. Exact Monte Carlo results [38] demonstrated that the theoretically employed classical field treatment accurately describes the polaron cloud of a static impurity supporting a bound state, when the impurity-boson interaction range r_0 is much larger than the inter-boson scattering length a_{B}. Interestingly, in this framework, the polaron cloud contains infinitely many bosons with boson number N growing sub-dimensional with system's volume V (that is $N/V \to 0$ as $N, V \to \infty$). Nevertheless, the polaron ground state energy remains finite as the main contribution to the energy comes from the bosons localized around the impurity and not in the polaron tail.

In the opposite limit $r_0 \ll a_{\mathrm{B}}$, the standard one-parameter modeling of the low-energy scattering processes in three dimensions by the scattering length has to be amended by inclusion of short range details of the impurity-boson and boson-boson interaction potentials [92]. A non-local version of the Gross-Pitaevskii theory was proposed for the regime $r_0 \ll a_{\mathrm{B}}$ [59], including a method to account for finite range effects. Furthermore, truncated basis variational (TBV) methods exist that allow for the inclusion of impurity-boson correlations exactly up to a few particles [222, 129]. The TBV methods are especially suitable for cold atom realization of Bose polarons where the impurity-boson system is described by a two-channel model. In such models, another stabilization mechanism was identified [187, 223, 128] whereby the exchange of a closed-channel dimer effectively removes the impurity from the system and reduces the number of bound bosons to only a few, even in a non-interacting bosonic system. Although these TBV methods predict polaron energy accurately, their accuracy is limited by their few particle nature for observables such as quasiparticle residue that are sensitive to the particle number. On the other hand, inspecting the $(N+1)-$body problem for non-interacting bosons coupled to a static impurity via the two-channel model reveals that $(N+1)-$body bound states exist for positive scattering lengths close to two special scattering resonances, corresponding to $1/a \to 0^+$ and $a \to a^{*-}$, with a^* a critical value [223]. The binding energy of these $(N+1)-$body states increase monotonically with N close to the scattering resonances, while remaining lower-bounded [223]. For $0 < 1/a < 1/a^*$, it is conjectured in Ref. [223] that all $(N+1)-$body states exist, though a direct solution to this $(N+1)-$body scattering problem even with non-interacting bosons remains extremely challenging. The proper inclusion of an indefinite number of excitations while at the same time accounting for finite-range impurity-boson and boson-boson interactions remains a central challenge in the development of an all-coupling theory of Bose polarons in a BEC.

Thus far, theoretical works on strong coupling Bose polarons have mainly focused on the independent characterization of the repulsive and attractive Bose polaron branches. However, not much work has been carried out to characterize further many-body bound states on the repulsive side other than the attractive polaron. Such many-body bound states were studied before in the context of Rydberg [182] and ionic [14] impurities immersed in bosonic quantum gases, and for neutral impurities in two dimensions [10]. As mentioned, these bound states have also been explored for neutral static impurities interacting with an ideal Bose gas via a two-channel model, where they were shown to exist for all N as $1/a \to 0^+$ and $a \to a^{*-}$, and conjectured to exist for all $0 < 1/a < 1/a^*$. While the two-channel model introduces an effective inter-boson repulsion via impurity scattering to the closed channel, such a stabilization mechanism does not exist in single-channel models. Consequently, single-channel models remain unstable unless two-body inter-boson repulsion is explicitly included. Although metastable bound states have been predicted for Bose polarons in single-channel models [185], the crucial effects of inter-boson repulsion have not been included so far. On the repulsive side, the non-interacting single channel models of Refs. [185, 60] predict a series of many-body bound states and no attractive polaron, while Gross-Pitaevskii theories which include inter-boson interactions within the mean-field level [59, 142, 221, 92] predict only a single state with negative energy (i. e. the attractive polaron) and no further many-body bound states. The disagreement between different theoretical approaches for the Bose polaron on the repulsive side extends beyond the distinction between single- and two-channel models; even within the single-channel model, different variational methods yield qualitatively different predictions. These discrepancies further underscore that the nature and characteristics of many-body resonances remain unresolved, and a comprehensive understanding of the problem is still lacking.

In this chapter, we refine the understanding of strong coupling Bose polarons by addressing the physics of several metastable states that appear in this regime in the form of many-body bound states in addition to attractive and repulsive polarons. To characterize these metastable states, we develop a variational principle that is able to accommodate the effects outlined above in a numerically efficient manner, and is accurate as long as the bound state is well separated from the other states in the bosonic one-particle spectrum. This variational principle builds upon a solidly grounded phenomenological model we formulate that enables to capture the essential correlations relevant for strong coupling Bose polarons. Although this variational scheme is suitable for generic impurity-condensate systems in arbitrary dimensionality, as a concrete example we focus on cold atom systems and characterize the metastable bound states emerging on the repulsive side of an impurity-boson Feshbach resonance.

Our variational approach enables us to unveil interesting properties of these states. For instance, the variational energy of these metastable bound states lie in between the attractive and repulsive polaron branches, and behave non-monotonously with particle number, resulting in level-crossings among the states, in contrast to the wisdom gained from the previous studies on many-body resonances (see Fig. 3.1). Moreover, the statistics of bosons bound to the impurity in these states exhibit strong quantum mechanical features, including non-Gaussian quantum correlations and interaction-induced anti-bunching. Such non-Gaussian correlations directly affect the number of resonances as the impurity-boson interaction strength is tuned. In contrast to the non-interacting or mean-field models described above, we find that the number of resonances remain finite, is not fixed, and depends on the strength of the inter-boson interaction relative to the impurity-boson interaction. While the quantitative aspects of these effects depend on the particular setting considered, the underlying physical principles are general, and we expect such effects to occur in a broad class of impurity-BEC systems. Our results pave the way for investigating the implications of these metastable many-body bound states for Bose polaron physics at strong couplings.

Overall, our approach provides a unified theory of repulsive and attractive Bose polarons: we argue that the remnant of the attractive polaron branch on the repulsive side of the Feshbach resonance *coincides with* the lowest-lying multi-boson bound state around the metastable repulsive polaron. As the resonance is crossed the attractive polaron adiabatically evolves first into a molecular bound state with (approximately) one bound boson – as proposed in Ref. [108] – but then continues to adiabatically evolve into an (approximate) two-boson-plus-impurity bound state, and so on. Thereby, the stable attractive polaron on the repulsive side of the Feshbach resonance, along with additional metastable many-body bound states, is understood as a necessary and direct consequence of having a metastable repulsive-polaron saddle-point; i.e. the repulsive polaron cannot exist without its attractive counterpart. Put differently, for repulsive impurity-boson interactions, repulsive polaron is the stable ground state of repulsively interacting bosons, thus it exists without any attractive polaron or other lower energy resonances. However, for attractive impurity-boson interactions, whenever the repulsive polaron branch exists, other lower energy resonances such as the attractive polaron branch and/or, depending on the setting, further few- and many-body states such as clusters or many-body bound states necessarily have to exist. This is because the repulsive polaron is not anymore a stable lowest energy state. Thus, novel experimental schemes for detecting the low-lying states and characterizing their properties is worthy of more research efforts, although detection of these states is difficult with the conventional impurity spectroscopy techniques.

The rest of this chapter is organized as follows: in Sec. 3.2, we outline the theoretical formalism and introduce our variational principle. In Sec. 3.3, we apply our theoretical method to the special case of cold atomic Bose polarons, extract their energies and quantum correlated nature revealed by quantum statistics of bosons in the bound state, and discuss possible experimental detection of these states by molecular spectroscopy. In Sec. 3.4 we compare the variational scheme presented here to existing methods and discuss its merits and limitations. We conclude in Sec. 3.5 and draw several future directions.

3.2 Theoretical Formalism

3.2.1 Model

We consider a mobile impurity of mass M coupled to a bosonic medium, consisting of particles of mass m in a condensed phase with density n_0 in three dimensions. The boson-boson and impurity-boson interactions are modeled by single-channel central potentials $U_{\mathrm{BB}}(\mathbf{x})$ and $V_{\mathrm{IB}}(\mathbf{x})$, respectively. The impurity is described by its position and momentum operators $\hat{\mathbf{X}}$ and $\hat{\mathbf{P}} = -i\hbar\nabla_{\mathbf{X}}$, and the bosonic environment by the field operators $\hat{\phi}_{\mathbf{x}}$ and $\hat{\phi}^\dagger_{\mathbf{x}}$ satisfying bosonic commutation relations $[\hat{\phi}_{\mathbf{x}}, \hat{\phi}^\dagger_{\mathbf{x}'}] = \delta^{(3)}(\mathbf{x}-\mathbf{x}')$, $[\hat{\phi}_{\mathbf{x}}, \hat{\phi}_{\mathbf{x}'}] = [\hat{\phi}^\dagger_{\mathbf{x}}, \hat{\phi}^\dagger_{\mathbf{x}'}] = 0$. It is convenient to treat the condensed system in a grand-canonical ensemble by introducing a chemical potential μ fixing the condensate's mean particle number.

The total Hamiltonian $\hat{H}_{\mathrm{tot}}$ describing the system takes the form

$$\hat{H}_{\mathrm{tot}} = \hat{\mathbf{P}}^2/2M + \int_{\mathbf{x}} V_{\mathrm{IB}}(\mathbf{x}-\hat{\mathbf{X}})\,\hat{\phi}^\dagger_{\mathbf{x}}\hat{\phi}_{\mathbf{x}} + \hat{H}_{\mathrm{B}}\,, \tag{3.1}$$

with $\int_{\mathbf{x}} \equiv \int d^3x$. It consists of the impurity kinetic energy, impurity-boson interaction, and the bosonic Hamiltonian $\hat{H}_{\mathrm{B}}$, given by

$$\hat{H}_{\mathrm{B}} = \int_{\mathbf{x}} \hat{\phi}^\dagger_{\mathbf{x}}\Big(-\hbar^2\nabla^2/2m - \mu\Big)\hat{\phi}_{\mathbf{x}} + \frac{1}{2}\int_{\mathbf{x},\mathbf{x}'} U_{\mathrm{BB}}(\mathbf{x}-\mathbf{x}')\,\hat{\phi}^\dagger_{\mathbf{x}}\hat{\phi}^\dagger_{\mathbf{x}'}\hat{\phi}_{\mathbf{x}'}\hat{\phi}_{\mathbf{x}}\,. \tag{3.2}$$

The problem is further simplified by transforming to the frame co-moving with the impurity. This is achieved through the *Lee-Low-Pines* transformation [86] $\hat{U}_{\mathrm{LLP}} = \exp\Big(i/\hbar\,\hat{\mathbf{X}}\cdot$

$\hat{\mathbf{P}}_{\text{bath}}\Big)$, where $\hat{\mathbf{P}}_{\text{bath}} = \int_{\mathbf{x}} \hat{\phi}^\dagger_{\mathbf{x}}(-i\hbar\nabla_{\mathbf{x}})\hat{\phi}_{\mathbf{x}}$ is the total momentum operator of the bath. Under $\hat{U}_{\text{LLP}}$, a state $|\Psi(\mathbf{K}_0)\rangle$ with well-defined total momentum $\mathbf{K}_0$ transforms to

$$|\Psi(\mathbf{K}_0)\rangle_{\text{LLP}} = \hat{U}_{\text{LLP}}\,|\Psi(\mathbf{K}_0)\rangle = |\mathbf{K}_0\rangle_{\text{imp}} \otimes |\Psi_{\mathbf{K}_0}\rangle_{\text{bath}}\ , \tag{3.3}$$

which enables restricting the total Hilbert space to the sector with well-defined impurity momentum $\mathbf{K}_0$. The transformed total Hamiltonian under $\hat{U}_{\text{LLP}}$ reads

$$\begin{aligned}\hat{H}_{\text{LLP}} = \frac{\hbar^2}{2M}\mathbf{K}_0^2 - \frac{\hbar}{M}\mathbf{K}_0\cdot\hat{\mathbf{P}}_{\text{bath}} + \frac{:\hat{\mathbf{P}}^2_{\text{bath}}:}{2M} + \int_{\mathbf{x}} V_{\text{IB}}(\mathbf{x})\,\hat{\phi}^\dagger_{\mathbf{x}}\hat{\phi}_{\mathbf{x}} \\ + \int_{\mathbf{x}} \hat{\phi}^\dagger_{\mathbf{x}}\Big(-\hbar^2\nabla^2/2m_{\text{red}} - \mu\Big)\hat{\phi}_{\mathbf{x}} + \frac{1}{2}\int_{\mathbf{x},\mathbf{x}'} U_{\text{BB}}(\mathbf{x}-\mathbf{x}')\,\hat{\phi}^\dagger_{\mathbf{x}}\hat{\phi}^\dagger_{\mathbf{x}'}\hat{\phi}_{\mathbf{x}'}\hat{\phi}_{\mathbf{x}}\ ,\end{aligned} \tag{3.4}$$

where $\mathbf{K}_0$ is the total momentum of the system, $m_{\text{red}}^{-1} = m^{-1} + M^{-1}$ is the impurity-boson reduced mass, and $:\cdots:$ denotes normal ordering of field operators. Eq. 3.4 is obtained using $\hat{U}^\dagger_{\text{LLP}}\,\hat{\mathbf{P}}\,\hat{U}_{\text{LLP}} = \hat{\mathbf{P}} - \hat{\mathbf{P}}_{\text{bath}}$ and the replacement $\hat{\mathbf{P}} \to \mathbf{K}_0$ on the restricted Hilbert space. In the rest of the paper we focus on the case $\mathbf{K}_0 = 0$, which corresponds to the overall ground state.

After introducing the model Hamiltonian, it is instructive to adopt a path integral formalism to study strong coupling Bose polarons. Path integral formulation is able to represent Bose polaron models in dense and dilute media and capture crucial strong coupling effects such as impurity-induced instability and condensate deformation. The free energy F of the system in path integral representation takes the following form

$$e^{iF/\hbar} = \int \mathcal{D}[\varphi^*, \varphi]\, e^{i\mathcal{S}[\varphi^*,\varphi]/\hbar}\,, \tag{3.5}$$

where $\mathcal{S}[\varphi^*, \varphi]$ is the action in terms of the classical fields φ^* and φ, written as

$$\mathcal{S}[\varphi^*, \varphi] = \int d^{3+1}x\,\Big(\varphi^*\, i\hbar\partial_t\varphi - H_{\text{LLP}}[\varphi^*, \varphi]\Big)\,. \tag{3.6}$$

It is standard to treat F within a saddle point approximation, that involves finding the saddle points of $\mathcal{S}[\varphi^*, \varphi]$.

Crucially, the saddle point analysis of the action reveals the existence of repulsive and attractive polarons on the repulsive side of the Feshbach resonance as the unstable, respectively, stable saddle points of the action. It is a key messages of the work presented in this chapter to underline the necessity of going beyond the saddle point approximation to study the physics of metastable many-body bound states, as those states emerge due to the strong modification of the energy landscape around the repulsive polaron by inter-boson interactions. Nevertheless, as a starting point of the theoretical construction it is necessary to outline a detailed picture of the saddle point structure of the model. This is the topic of the next subsection.

3.2.2 Saddle point analysis

Mean-field decoupling of $\hat{H}_{\mathrm{LLP}}$

To obtain the saddle point solutions and analyze the associated energy landscape, it is instructive to perform a mean-field decoupling of the Hamiltonian. To this end, we separate $\hat{\phi}_{\mathbf{x}}$ into a classical component $\varphi_{\mathbf{x}}$ representing the condensate, and quantum fluctuations $\delta\hat{\phi}_{\mathbf{x}}$, i.e. $\hat{\phi}_{\mathbf{x}} = \varphi_{\mathbf{x}} + \delta\hat{\phi}_{\mathbf{x}}$. For notational convenience, we introduce the Nambu vector $\delta\hat{\Psi}$ with coordinate representation $\delta\hat{\Psi}_{\mathbf{x}} = (\delta\hat{\phi}_{\mathbf{x}}, \delta\hat{\phi}^{\dagger}_{\mathbf{x}})^T$.

Within the mean-field theory, the elementary excitations of the system are modeled by weakly interacting quasiparticles with Bogoliubov-type field operators $\hat{B}_{\mathbf{x}} = (\hat{\beta}_{\mathbf{x}}, \hat{\beta}^{\dagger}_{\mathbf{x}})^T$ related to $\delta\hat{\Psi}$ through the canonical transformation $\delta\hat{\Psi}_{\mathbf{x}} = \int_{\mathbf{y}} S_{\mathbf{xy}} \hat{B}_{\mathbf{y}}$, where $S_{\mathbf{xy}}$ are 2×2 matrices. Note that both the classical component $\varphi_{\mathbf{x}}$ as well as the Bogoliubov modes $\hat{B}_{\mathbf{x}}$ should be calculated in the presence of the impurity in the Lee-Low-Pines frame, as explained below.

Correspondingly, the vacuum state of elementary excitations $|\mathrm{GS}\rangle$, defined by $\hat{\beta}_{\mathbf{x}} |\mathrm{GS}\rangle = 0$, is connected to the bosonic vacuum $|\varnothing\rangle$ by $|\mathrm{GS}\rangle = \hat{\mathcal{S}} |\varnothing\rangle$ where

$$\hat{\mathcal{S}} = \exp\left(\frac{i}{2}\delta\hat{\Psi}^{\dagger}\, \Xi \, \delta\hat{\Psi}\right), \tag{3.7}$$

is a bosonic squeezing operator. In Eq. 3.7, Ξ is a Hermitian matrix related to S by $S = \exp\left(i\Sigma_z \Xi\right)$ with $\Sigma_z = \sigma_z\, \delta^{(3)}(\mathbf{x} - \mathbf{x}')$ and σ_z the Pauli-z operator. For shorthand notation, matrix multiplication implies integration over spatial coordinates and summation over Nambu components. To fulfill the bosonic commutation relations for $\hat{\beta}_{\mathbf{x}}$ and $\hat{\beta}^{\dagger}_{\mathbf{x}}$, S must be a symplectic matrix satisfying $S^{\dagger}\Sigma_z S = \Sigma_z$.

By means of Wick's theorem, $\hat{H}_{\mathrm{LLP}}$ takes the form (see Appendix 3.2.3)

$$\hat{H}_{\mathrm{LLP}} = E[\Phi,\Gamma] + \left(\delta\hat{\Psi}^{\dagger} \cdot \zeta[\Phi,\Gamma] + h.c.\right) + \frac{1}{2} : \delta\hat{\Psi}^{\dagger} \mathcal{H}_{\mathrm{MF}}[\Phi,\Gamma] \delta\hat{\Psi} \ : + \hat{H}_3 + \hat{H}_4 \,. \tag{3.8}$$

Here, $\Phi_{\mathbf{x}} = (\varphi_{\mathbf{x}}, \varphi^{*}_{\mathbf{x}})^T$, the covariance matrix Γ is defined by $2\Gamma = \langle \mathrm{GS}| \{\delta\hat{\Psi}, \delta\hat{\Psi}^{\dagger}\} |\mathrm{GS}\rangle - \mathbb{I}$ and can be expressed in terms of S by $2\Gamma + \mathbb{I} = SS^{\dagger}$, $\mathbb{I}$ is the identity matrix and $: \cdots :$ denotes normal ordering with respect to $\hat{\beta}_{\mathbf{x}}$ and $\hat{\beta}^{\dagger}_{\mathbf{x}}$. Furthermore, $\mathcal{H}_{\mathrm{MF}}[\Phi,\Gamma]$ is the mean-field Hamiltonian, $\hat{H}_3$ and $\hat{H}_4$ are the cubic and quartic Hamiltonians in the field operators, respectively, and $\zeta[\Phi,\Gamma]$ is defined in Appendix 3.2.3.

In standard mean-field theory, beyond quadratic terms are neglected, while Φ_0 and S_0 are found that correspond to the saddle point solution $\zeta[\Phi_0,\Gamma_0] = 0$ and diagonalize the mean-field Hamiltonian as $S_0^{\dagger}\mathcal{H}_{\mathrm{MF}}[\Phi_0,\Gamma_0]S_0 = \mathbb{I}_2 \otimes D$, with $\mathbb{I}_2$ the 2×2 identity matrix and D a diagonal matrix. The condition $2\Gamma_0 + \mathbb{I} = S_0 S_0^{\dagger}$ and the dependence of $\mathcal{H}_{\mathrm{MF}}$ on Γ_0 require that S_0 be obtained self-consistently. The resulting normal modes $\hat{B}_0 = S_0^{-1}\delta\hat{\Psi}$ are the well-known Bogoliubov modes.

In the following, we analyze the quadratic terms in $\hat{H}_{\mathrm{LLP}}$ from a mean-field viewpoint. However, as we elucidate later, it is crucial to retain the higher-order terms $\hat{H}_3$ and $\hat{H}_4$ to describe essential strong coupling effects such as the non-Gaussian correlations of Bose polaron many-body bound states at strong couplings.

Saddle point structure

Next, we analyze the saddle point and normal mode structure of the quadratic part of $\hat{H}_{\text{LLP}}$ across an impurity-boson scattering resonance. On the attractive side ($a < 0$, with a the impurity-boson scattering length), the saddle point condition is equivalent to the Gross-Pitaevskii equation and admits a single solution Φ_{att} that is the attractive polaron (dashed green line in Fig. 3.2). The static and dynamic properties of the attractive polaron obtained within Gross-Pitaevskii were investigated in [59, 142, 221, 92], and the predictions for cold atom settings are in excellent agreement with the experiments. Furthermore, the attractive polaron is a stable saddle point solution, meaning that all the corresponding fluctuation modes have positive energy, or equivalently, $\mathcal{H}_{\text{MF}}[\Phi_0, \Gamma_0]$ is positive-definite (see Fig. 3.2(b), panel (1)).

The attractive polaron solution extends to the repulsive side ($a > 0$) and remains a stable saddle point. Nevertheless, for the mean-field Hamiltonian $\mathcal{H}_{\text{MF}}[\Phi, \Gamma]$, there exists a dynamical instability window of impurity-boson interaction strength, where an unstable phase quadrature of a Bogoliubov mode emerges [88] (see Fig. 3.2(b), panel (2)).

Beyond the dynamical instability, another saddle point solution Φ_{rep} emerges that is the repulsive polaron. The repulsive polaron saddle point is unstable, as a single Bogoliubov mode with negative energy exists in the spectrum of $\mathcal{H}_{\text{MF}}[\Phi_{\text{rep}}, \Gamma_{\text{rep}}]$. The existence of this unstable mode is traced back to the bound state of the impurity-boson potential, therefore with a slight abuse of terminology, we call it “the bound state" or “dimer" as well (see Appendix A for further discussion on the bound Bogoliubov mode and its relation to the impurity-boson bound state). Analogously, we call the extended modes with positive energy “scattering Bogoliubov modes" or “scattering states". In fact, when V_{IB} admits ν bound states, there exists $2\nu + 1$ solution to the Gross-Pitaevskii equation; see Refs. [141, 221]. The third solution of the Gross-Pitaevskii equation is similar to the attractive polaron in amplitude, but has a negative sign. The absolute value of its energy is positive with the same magnitude as the attractive polaron. Thus, it is not physical, and we do not consider it in the following analysis.

In a mean-field treatment of the Bose polaron without including inter-boson interactions [88], the presence of the unstable mode implies that the system can decrease its energy by filling the bound state with bosons, resulting in the many-body ground state energy $E_{\text{GS}} = -\infty$. This pathological behavior signifies the need for a non-perturbative beyond mean-field treatment of the Bose polaron by the full Hamiltonian in Eq. 3.8, i.e. including the cubic and quartic terms.

While an exact non-perturbative solution for the spectrum of $\hat{H}_{\text{LLP}}$ is infeasible due to the strongly correlated nature of the problem, one can capture the essential correlations using a phenomenological model, while rendering a stable state analysis of the problem possible. The formulation of this phenomenological model is one of the main results in this chapter. In the following we introduce the effective model we devise for investigating Bose polarons at strong impurity-boson interactions.

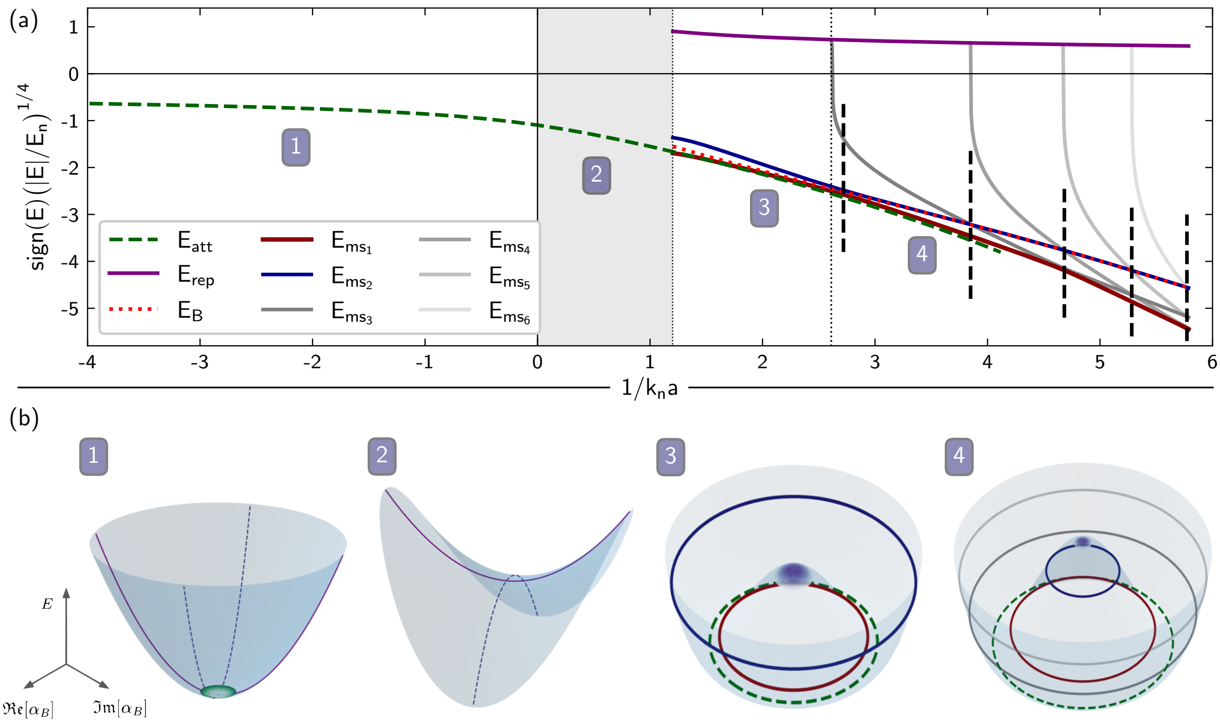

Figure 3.2: (a) Energy of polaron states, including attractive and repulsive polaron, and metastable states ms_1 to ms_6 (see text), across an impurity-boson Feshbach resonance. On the attractive side ($a < 0$), an impurity resonance exists corresponding to the attractive polaron branch (green dashed line), which extends to the repulsive side and remains the well-defined stable saddle point across the resonance. On the repulsive side, the repulsive polaron branch emerges as the unstable saddle point solution with a bound state, as well as two many-body bound states ms_1 and ms_2 (red and blue solid lines). The red dotted line indicates the bare dimer energy. Beyond a critical scattering length (denoted by a vertical black dotted line), further metastable many-body bound states ms_3 to ms_6 emerge in the spectrum (grey shaded solid lines). Note that the normalized energy is rescaled to show all bound states compactly. The grey-shaded region (2) on the repulsive side is bounded by $1/k_n a \simeq 1.2$ where $\mu/\varepsilon_{\mathrm{B}} \simeq 9 \times 10^{-3}$, providing a conservative bound for the validity of our theory. (b) The energy landscape over the phase space of the bound Bogoliubov mode, around the saddle points corresponding to different regions in (a). The real and imaginary parts of the coherent state variable α_{B} serve as coordinates for the phase space of the bound Bogoliubov mode. In (1), the attractive polaron (green shaded point) is a stable saddle point, with all the fluctuation modes having positive energy. Within region (2), a dynamical instability occurs as a precursor to the formation of the repulsive polaron, signified by a single unstable phase mode with a corresponding stable amplitude mode. In (3), the repulsive polaron (purple shaded dot) is a saddle point solution with a single unstable Bogoliubov mode. The energy and particle number of many-body bound states in (a) are depicted qualitatively on the energy surfaces. The radius of each circle denotes the mean bound state occupation number, while its position on the surface denotes the energy of the state. Repulsive inter-boson interaction increases the energy of the many-body bound state with a higher particle number. By increasing $1/k_n a$, further many-body bound-states enter the atom-dimer continuum (grey shaded solid lines). Increasing the binding energy increases the number of bound bosons in the lowest many-body bound state. The vertical black dashed lines mark the level crossings between many-body bound states.

3.2.3 Details of the mean-field decoupling of $\hat{H}_{\text{LLP}}$

Here we detail on the mean-field decoupling procedure. Using the Wick's theorem [212], for $\hat{H}_{\text{LLP}}$ in Eq. 3.4, the mean-field Hamiltonian takes the following form,

$$\hat{H}_{\text{LLP}} = E + \left(\delta\hat{\Psi}^{\dagger}\cdot\zeta + h.c.\right) + \frac{1}{2} : \delta\hat{\Psi}^{\dagger}\mathcal{H}_{\text{MF}}\delta\hat{\Psi} \ : + \hat{H}_3 + \hat{H}_4\,, \tag{3.9}$$

with explicit expressions for different terms as the following,

$$\begin{aligned} E =& \frac{\hbar^2\mathbf{K}_0^2}{2M} - \frac{\hbar\mathbf{K}_0}{M}\cdot\left(\int_{\mathbf{x}}\varphi_{\mathbf{x}}^*(-i\hbar\nabla_{\mathbf{x}})\varphi_{\mathbf{x}} + \int_{\mathbf{k}}\hbar\mathbf{k}\Gamma_{\mathbf{kk}}^{11}\right) \\ &+ \int\left(\frac{\hbar\mathbf{k}\cdot\hbar\mathbf{k}'}{2M}\right)\Big\{|\varphi_{\mathbf{k}}|^2|\varphi_{\mathbf{k}'}|^2 + \Big(\varphi_{\mathbf{k}}\varphi_{\mathbf{k}'}\Gamma_{\mathbf{k}'\mathbf{k}}^{21} + \varphi_{\mathbf{k}'}^*\varphi_{\mathbf{k}}\Gamma_{\mathbf{kk}'}^{11} + \varphi_{\mathbf{k}'}^*\varphi_{\mathbf{k}'}\Gamma_{\mathbf{kk}}^{11} + c.c.\Big) \\ &+ \Gamma_{\mathbf{kk}}^{11}\Gamma_{\mathbf{k}'\mathbf{k}'}^{11} + |\Gamma_{\mathbf{kk}'}^{11}|^2 + |\Gamma_{\mathbf{kk}'}^{12}|^2\Big\} \\ &+ \int_{\mathbf{x}}\varphi_{\mathbf{x}}^*\Big(-\frac{\hbar^2\nabla^2}{2m_{\text{red}}} + V_{\text{IB}}(\mathbf{x}) - \mu\Big)\varphi_{\mathbf{x}} + \int_{\mathbf{x}}\Big(-\frac{\hbar^2\nabla^2}{2m_{\text{red}}} + V_{\text{IB}}(\mathbf{x}) - \mu\Big)\Gamma_{\mathbf{xx}}^{11} \\ &+ \frac{1}{2}\int_{\mathbf{x},\mathbf{x}'}U_{\text{BB}}(\mathbf{x}-\mathbf{x}')\Big\{|\varphi_{\mathbf{x}}|^2|\varphi_{\mathbf{x}'}|^2 + \Big(\varphi_{\mathbf{x}}^*\varphi_{\mathbf{x}'}^*\Gamma_{\mathbf{xx}'}^{12} + |\varphi_{\mathbf{x}}|^2\Gamma_{\mathbf{x}'\mathbf{x}'}^{11} + \varphi_{\mathbf{x}'}^*\varphi_{\mathbf{x}}\Gamma_{\mathbf{xx}'}^{11} + c.c.\Big) \\ &+ |\Gamma_{\mathbf{xx}'}^{12}|^2 + |\Gamma_{\mathbf{xx}'}^{11}|^2 + \Gamma_{\mathbf{xx}}^{11}\Gamma_{\mathbf{x}'\mathbf{x}'}^{11}\Big\}\,. \end{aligned} \tag{3.10}$$

The linear Hamiltonian $\hat{H}_1$ has the following form,

$$\hat{H}_1 = \int_{\mathbf{x}}\hat{\phi}_{\mathbf{x}}^{\dagger}\zeta_{\mathbf{x}} + h.c.\,, \tag{3.11}$$

where we explicitly write the coordinate space integration instead of shorthand inner product. The vector $\zeta_{\mathbf{x}}$ then reads as

$$\begin{aligned} \zeta_{\mathbf{x}} =& h_0\varphi_{\mathbf{x}} + \left[\int_{\mathbf{x}'}U_{\text{BB}}(\mathbf{x}-\mathbf{x}')\Big(|\varphi_{\mathbf{x}'}|^2 + \Gamma_{\mathbf{x}'\mathbf{x}'}^{11}\Big)\right]\varphi_{\mathbf{x}} \\ &+ \int_{\mathbf{x}'}\left\{\left[U_{\text{BB}}(\mathbf{x}-\mathbf{x}') - \frac{1}{M}(-i\hbar\nabla_{\mathbf{x}})\cdot(-i\hbar\nabla_{\mathbf{x}'})\right]\Gamma_{\mathbf{x}'\mathbf{x}}^{11}\right\}\varphi_{\mathbf{x}'} \\ &+ \int_{\mathbf{x}'}\left\{\left[U_{\text{BB}}(\mathbf{x}-\mathbf{x}') + \frac{1}{M}(-i\hbar\nabla_{\mathbf{x}})\cdot(-i\hbar\nabla_{\mathbf{x}'})\right]\Gamma_{\mathbf{xx}'}^{12}\right\}\varphi_{\mathbf{x}'}^* \\ &+ \int_{\mathbf{x}'}\frac{1}{M}\Big[-i\hbar\nabla_{\mathbf{x}'}\Big(|\varphi_{\mathbf{x}'}|^2 + \Gamma_{\mathbf{x}'\mathbf{x}'}^{11}\Big)\Big]\cdot(-i\hbar\nabla_{\mathbf{x}}\varphi_{\mathbf{x}})\,, \end{aligned} \tag{3.12}$$

where $h_0 = -\hbar^2\nabla^2/2m_{\text{red}} + V_{\text{IB}}(\mathbf{x}) - \mu\,.$ With $\zeta_{\mathbf{x}}$ as in Eq. 3.12, the saddle point condition is $\zeta_{\mathbf{x}} = 0$. In the special case of $\Gamma_{\mathbf{xx}'}^{11} = \Gamma_{\mathbf{xx}'}^{12} = 0$ and $M \to \infty$, the saddle point condition reduces to the Gross-Pitaevskii equation for the condensate, including the distortion caused by the impurity (that is encoded in the impurity-boson potential in h_0). Given the saddle point condition $\zeta_{\mathbf{x}} = 0$, and the boundary condition on the condensate that $\lim_{|\mathbf{x}|\to\infty}\varphi_{\mathbf{x}} =$

$\sqrt{n_0}$, the chemical potential including the Lee-Huang-Yang and finite boson-boson range corrections reads as

$$\mu = (n_0 + \Gamma^{11}_{00}) \int_{\mathbf{x}} U_{\mathrm{BB}}(\mathbf{x}) + \int_{\mathbf{x}} U_{\mathrm{BB}}(\mathbf{x}) \mathrm{Re}(\Gamma^{12}_{\mathbf{x}0} + \Gamma^{11}_{\mathbf{x}0}) \,. \tag{3.13}$$

The quadratic Hamiltonian is of the following form

$$\hat{H}_2 = \frac{1}{2} : \int_{\mathbf{k},\mathbf{k}'} \begin{pmatrix} \delta\hat{\phi}^\dagger_{\mathbf{k}'} & \delta\hat{\phi}_{-\mathbf{k}'} \end{pmatrix} \mathcal{H}^{\mathrm{imp}}_{\mathbf{k}'\mathbf{k}} \begin{pmatrix} \delta\hat{\phi}_{\mathbf{k}} \\ \delta\hat{\phi}^\dagger_{-\mathbf{k}} \end{pmatrix} : + \frac{1}{2} : \int_{\mathbf{x},\mathbf{x}'} \begin{pmatrix} \delta\hat{\phi}^\dagger_{\mathbf{x}'} \delta\hat{\phi}_{\mathbf{x}'} \end{pmatrix} \mathcal{H}_{\mathbf{x}'\mathbf{x}} \begin{pmatrix} \delta\hat{\phi}_{\mathbf{x}} \\ \delta\hat{\phi}^\dagger_{\mathbf{x}} \end{pmatrix} : , \tag{3.14}$$

thus, $\mathcal{H}_{\mathrm{MF}}$ consists of two terms: $\mathcal{H}^{\mathrm{imp}}$ comes from the finite mass of the impurity, and $\mathcal{H}$ is the mean-field Hamiltonian in the limit $M \to \infty$. The explicit forms of $\mathcal{H}$ and $\mathcal{H}^{\mathrm{imp}}$ are of the following form,

$$\begin{cases} \mathcal{H}^{\mathrm{imp}}_{\mathbf{k}'\mathbf{k}} = \begin{pmatrix} \mathcal{E}^{\mathrm{imp}}_{\mathbf{k}'\mathbf{k}} & \Delta^{\mathrm{imp}}_{\mathbf{k}'\mathbf{k}} \\ \Delta^{\mathrm{imp}*}_{(-\mathbf{k}')(-\mathbf{k})} & \mathcal{E}^{\mathrm{imp}*}_{(-\mathbf{k}')(-\mathbf{k})} \end{pmatrix} , \\ \mathcal{H}_{\mathbf{x}'\mathbf{x}} = \begin{pmatrix} \mathcal{E}_{\mathbf{x}'\mathbf{x}} & \Delta_{\mathbf{x}'\mathbf{x}} \\ \Delta^*_{\mathbf{x}'\mathbf{x}} & \mathcal{E}^*_{\mathbf{x}'\mathbf{x}} , \end{pmatrix} , \end{cases} \tag{3.15}$$

where the diagonal and off-diagonal terms of $\mathcal{H}_{\mathrm{imp}}$ are as follows,

$$\begin{cases} \mathcal{E}^{\mathrm{imp}}_{\mathbf{k}'\mathbf{k}} = \frac{\hbar\mathbf{k}\cdot\hbar\mathbf{k}'}{M}\Big(\Gamma^{11}_{\mathbf{k}\mathbf{k}'} + \varphi^*_{\mathbf{k}}\varphi_{\mathbf{k}'}\Big) + \delta^{(d)}(\mathbf{k}-\mathbf{k}') \int_{\mathbf{k}''} \frac{\hbar\mathbf{k}'\cdot\hbar\mathbf{k}''}{M} \left(\Gamma^{11}_{\mathbf{k}''\mathbf{k}''} + \varphi^*_{\mathbf{k}''}\varphi_{\mathbf{k}''}\Big) , \right. \\ \Delta^{\mathrm{imp}}_{\mathbf{k}'\mathbf{k}} = -\frac{\hbar\mathbf{k}\cdot\hbar\mathbf{k}'}{M}\Big(\Gamma^{12}_{\mathbf{k}'(-\mathbf{k})} + \varphi_{\mathbf{k}'}\varphi_{-\mathbf{k}}\Big) \,. \end{cases} \tag{3.16}$$

The diagonal and off-diagonal terms in $\mathcal{H}$ read as

$$\begin{cases} \mathcal{E}_{\mathbf{x}'\mathbf{x}} = \delta^{(d)}(\mathbf{x}-\mathbf{x}')\Big[h_0 + \int_{\mathbf{x}''} U_{\mathrm{BB}}(\mathbf{x}'-\mathbf{x}'')\Big(\Gamma^{11}_{\mathbf{x}''\mathbf{x}''} + |\varphi_{\mathbf{x}''}|^2\Big)\Big] + U_{\mathrm{BB}}(\mathbf{x}-\mathbf{x}')\Big(\Gamma^{11}_{\mathbf{x}\mathbf{x}'} + \varphi^*_{\mathbf{x}}\varphi_{\mathbf{x}'}\Big) , \\ \Delta_{\mathbf{x}'\mathbf{x}} = U_{\mathrm{BB}}(\mathbf{x}-\mathbf{x}')\Big(\Gamma^{12}_{\mathbf{x}'\mathbf{x}} + \varphi_{\mathbf{x}'}\varphi_{\mathbf{x}}\Big) \,. \end{cases} \tag{3.17}$$

Finally, the cubic and quartic terms are of the following forms

$$\hat{H}_3 = \int_{\mathbf{k},\mathbf{k}'} \frac{\hbar\mathbf{k}\cdot\hbar\mathbf{k}'}{M}\Big(\varphi_{\mathbf{k}} : \delta\hat{\phi}^\dagger_{\mathbf{k}}\delta\hat{\phi}^\dagger_{\mathbf{k}'}\delta\hat{\phi}_{\mathbf{k}'} : + h.c.\Big) + \int_{\mathbf{x},\mathbf{x}'} U_{\mathrm{BB}}(\mathbf{x}-\mathbf{x}')\Big(\varphi_{\mathbf{x}} : \delta\hat{\phi}^\dagger_{\mathbf{x}}\delta\hat{\phi}^\dagger_{\mathbf{x}'}\delta\hat{\phi}_{\mathbf{x}'} : + h.c.\Big) \,. \tag{3.18}$$

The quartic term representing the interaction of fluctuation modes reads as

$$\hat{H}_4 = \int_{\mathbf{k},\mathbf{k}'} \frac{\hbar\mathbf{k}\cdot\hbar\mathbf{k}'}{2M} : \delta\hat{\phi}^\dagger_{\mathbf{k}}\delta\hat{\phi}^\dagger_{\mathbf{k}'}\delta\hat{\phi}_{\mathbf{k}'}\delta\hat{\phi}_{\mathbf{k}} : + \frac{1}{2}\int_{\mathbf{x},\mathbf{x}'} U_{\mathrm{BB}}(\mathbf{x}-\mathbf{x}') : \delta\hat{\phi}^\dagger_{\mathbf{x}}\delta\hat{\phi}^\dagger_{\mathbf{x}'}\delta\hat{\phi}_{\mathbf{x}'}\delta\hat{\phi}_{\mathbf{x}} : . \tag{3.19}$$

3.2.4 Effective Model and variational principle

The first step to obtain the effective model is to harness the large seperation of energy scales between the scattering states and the bound state of the mean-field Hamiltonian at strong couplings. This large separation of energy and length scales enables to treat the bound state separately from the rest of the modes. Formally, this separation is achieved by splitting the bosonic annihilation operator into two parts, $\hat{\phi}_{\mathbf{x}} = \hat{\phi}^{(\mathrm{B})}_{\mathbf{x}} + \hat{\phi}^{(\mathrm{sc})}_{\mathbf{x}}$. Here, $\hat{\phi}^{(\mathrm{B})}_{\mathbf{x}} = \left(u_{\mathrm{B},\mathbf{x}}\hat{b} + v_{\mathrm{B},\mathbf{x}}\hat{b}^{\dagger}\right)$, $u_{\mathrm{B},\mathbf{x}}$ and $v_{\mathrm{B},\mathbf{x}}$ are the real space form of Bogoliubov factors associated to the bound Bogoliubov mode, $\hat{b}$ is its annihilation operator, and $\hat{\phi}^{(\mathrm{sc})}_{\mathbf{x}} = \hat{\phi}_{\mathbf{x}} - \hat{\phi}^{(\mathrm{B})}_{\mathbf{x}}$ only consists of scattering Bogoliubov modes. We deploy this mode separation to recast the Hamiltonian $\hat{H}_{\mathrm{LLP}}$ to a form that is more appropriate for our variational treatment later on. With this mode separation, the Hamiltonian $\hat{H}_{\mathrm{LLP}}$ of Eq. 3.8 takes the following form,

$$\hat{H}_{\mathrm{LLP}} = \sum_{\substack{n,m \\ n+m\leq 4}} \hat{b}^{\dagger n}\hat{b}^{m}\, \hat{H}_{n,m}[\hat{\phi}^{(\mathrm{sc})\dagger}_{\mathbf{x}}, \hat{\phi}^{(\mathrm{sc})}_{\mathbf{x}}]\,, \tag{3.20}$$

where $\hat{H}_{n,m}[\hat{\phi}^{(\mathrm{sc})\dagger}_{\mathbf{x}}, \hat{\phi}^{(\mathrm{sc})}_{\mathbf{x}}]$ terms only act on the scattering Bogoliubov modes, and $n\,, m$ denote powers of the bound Bogoliubov mode operators. Note that to obtain the form in Eq. 3.20, the mean-field decoupling of $\hat{H}_{\mathrm{LLP}}$ has to be performed over the repulsive polaron saddle point, with the corresponding condensate field Φ_{rep} and covariance matrix Γ_{rep}. This is again because the bound Bogoliubov mode is a well-defined unstable mode of the repulsive polaron saddle point.

We now introduce the structure of variational states to model the metastable many-body bound states. First, we note that an arbitrary eigenstate of $\hat{H}_{\mathrm{LLP}}$ Eq. 3.20 with energy E can be decomposed into $|\psi_E\rangle = \sum_n a_{n,E}\, |n\rangle_{\mathrm{B}} \otimes |\psi_{n,E}\rangle_{\mathrm{sc}}$, where $a_{n,E}$ for $n = 0, 1, 2, \cdots$ are coefficients, $|n\rangle_{\mathrm{B}} = \hat{b}^{\dagger n}/\sqrt{n!}\ |\mathrm{GS}\rangle$ is the Fock state of the bound Bogoliubov mode, and $|\psi_{n,E}\rangle_{\mathrm{sc}}$ is a corresponding many-body state of the scattering Bogoliubov modes.

Using the separation of time scales over which the bound and scattering Bogoliubov modes evolve, we require the variational states $\left|\psi_{(\mathrm{var})}\right\rangle$ approximating $|\psi_E\rangle$ to be separable in the Hilbert space of the bound and scattering Bogoliubov modes as

$$\left|\psi_{(\mathrm{var})}\right\rangle = \left|\psi_{(\mathrm{B})}\right\rangle_{\mathrm{B}} \otimes \left|\psi_{(\mathrm{sc})}\right\rangle_{\mathrm{sc}}\,, \tag{3.21}$$

where the additional subscripts “B" and “sc" refer to the Hilbert spaces of the bound and scattering Bogoliubov modes, respectively, and we drop them hereafter. This approximation is in the spirit of the Born-Oppenheimer approximation [25] used frequently in quantum chemistry to determine the electronic structure of a molecule, by using the separation of energy scales between the fast and slow degrees of freedom. One then assumes that fast degrees of freedom adiabatically follow the dynamics of the slow degrees of freedom. In the present context, the bound and scattering Bogoliubov modes constitute the fast and slow degrees of freedom, respectively.

To make a more direct connection to the Born-Oppenheimer approximation in the context of quantum chemistry, we compare the impurity-boson system in the present setting to atoms and simple molecules. In such chemical systems, the energy scales for nuclear excitations are orders of magnitude higher than the electronic ones. Thus, one can assume a specific stable internal configuration of the nuclei and focus on the electronic degrees of freedom relevant to chemical reactions. Analogously, in the present context, when the energy scale of the impurity-boson dimer formation is far larger than the energy scale for dressing by long wavelength BEC excitations, one can treat the dynamics of the bound Bogoliubov modes separately from the scattering modes. In addition to this intuitive motivation, we further justify the separable structure of the variational ansatz of Eq. 3.21 by giving a rigorous derivation of it in Sec. 3.2.5 as the form of the exact eigenstates to leading order in a carefully defined perturbative description of the problem.

Following the same reasoning, we identify $\left|\psi_{(\mathrm{B})}\right\rangle$ as the eigenstate of the effective Hamiltonian

$$\hat{H}_{\mathrm{eff,B}} = \left\langle\psi_{(\mathrm{sc})}\right| \hat{H}_{\mathrm{LLP}} \left|\psi_{(\mathrm{sc})}\right\rangle = \sum_{\substack{n,m\\ n+m\leq 4}} \left\langle\psi_{(\mathrm{sc})}\right| \hat{H}_{n,m}[\hat{\phi}^{(\mathrm{sc})\dagger}_{\mathbf{x}}, \hat{\phi}^{(\mathrm{sc})}_{\mathbf{x}}] \left|\psi_{(\mathrm{sc})}\right\rangle \hat{b}^{\dagger n}\hat{b}^{m}\,, \tag{3.22}$$

while the effective Hamiltonian for scattering Bogoliubov modes reads

$$\hat{H}_{\mathrm{eff,sc}} = \left\langle\psi_{(\mathrm{B})}\right| \hat{H}_{\mathrm{LLP}} \left|\psi_{(\mathrm{B})}\right\rangle = \sum_{\substack{n,m\\ n+m\leq 4}} \left\langle\psi_{(\mathrm{B})}\right| \hat{b}^{\dagger n}\hat{b}^{m} \left|\psi_{(\mathrm{B})}\right\rangle \hat{H}_{n,m}[\hat{\phi}^{(\mathrm{sc})\dagger}_{\mathbf{x}}, \hat{\phi}^{(\mathrm{sc})}_{\mathbf{x}}]\,. \tag{3.23}$$

To determine the variational structure of $\left|\psi_{(\mathrm{B})}\right\rangle$ and $\left|\psi_{(\mathrm{sc})}\right\rangle$, we take $\left|\psi_{(\mathrm{B})}\right\rangle$ to be an unrestricted superposition of Fock states $|n\rangle_{\mathrm{B}}$ as $\left|\psi_{(\mathrm{B})}\right\rangle = \sum_n \psi_n |n\rangle_{\mathrm{B}}$, while we take $\left|\psi_{(\mathrm{sc})}\right\rangle$ to be a coherent state

$$|\alpha_{\mathbf{x}}\rangle = \exp\left(\int_{\mathbf{x}} \alpha_{\mathbf{x}}\, \delta\hat{\phi}^{\dagger}_{\mathbf{x}} - h.c.\right) |\Phi_{\mathrm{rep}}\rangle\ , \tag{3.24}$$

where $\alpha_{\mathbf{x}}$ is the real space profile of the coherent cloud of bosons occupying the scattering Bogoliubov modes. We then obtain the complete form of the variational state as

$$\left|\psi_{(\mathrm{var})}[\psi_n, \alpha_{\mathbf{x}}]\right\rangle = \left(\sum_n \psi_n |n\rangle_{\mathrm{B}}\right) \otimes |\alpha_{\mathbf{x}}\rangle\ . \tag{3.25}$$

The Hamiltonian $\hat{H}_{\mathrm{LLP}}$ displayed as in Eq. 3.20, together with the variational states presented in Eq. 3.25, constitute the basis of our variational principle. The variational parameters ψ_n, $\alpha_{\mathbf{x}}$ and $\alpha^*_{\mathbf{x}}$ are then determined by optimizing the energy functional

$$H[\psi^*_n, \psi_n, \alpha^*_{\mathbf{x}}, \alpha_{\mathbf{x}}] = \left\langle\psi_{(\mathrm{var})}[\psi_n, \alpha_{\mathbf{x}}]\right| \hat{H}_{\mathrm{LLP}} \left|\psi_{(\mathrm{var})}[\psi_n, \alpha_{\mathbf{x}}]\right\rangle\ , \tag{3.26}$$

with respect to ψ_n and $\alpha_{\mathbf{x}}$ subject to the conditions

$$\begin{cases} \left\langle\psi_{(\mathrm{var})}[\psi_n, \alpha_{\mathbf{x}}]\middle|\psi_{(\mathrm{var})}[\psi_n, \alpha_{\mathbf{x}}]\right\rangle = 1\,, \\ \int_{\mathbf{x}} \left(u^*_{\mathrm{B},\mathbf{x}}\alpha_{\mathbf{x}} - v_{\mathrm{B},\mathbf{x}}\alpha^*_{\mathbf{x}}\right) = 0\,. \end{cases} \tag{3.27}$$

The first condition in Eqs. 3.27 is the normalization of the variational wave function, while the second condition results from the requirement that $|\alpha_{\mathbf{x}}\rangle$ consists of the scattering Bogoliubov modes only, thus $\hat{b}\,|\alpha_{\mathbf{x}}\rangle = 0$. Note that the parameters $u_{\mathrm{B},\mathbf{x}}$, $v_{\mathrm{B},\mathbf{x}}$ are determined by the saddle-point solution of the repulsive polaron.

Some comments on the variational scheme presented above are in order. First, note that $\left|\psi_{(\mathrm{B})}\right\rangle$ is a many-body state composed of a superposition of Fock states of the bound Bogoliubov mode, hence the name “many-body bound state". The Hamiltonian $\hat{H}_{\mathrm{eff,B}}$ governing the dynamics of the bound Bogoliubov mode contains all the interaction terms including the interaction of the bound Bogoliubov mode with itself, as well as its interaction with the condensate. This Hamiltonian is easy to treat since it is the Hamiltonian of a single mode. Thus, one can use exact diagonalization to find its eigenstates and eigenenergies. In this sense, one can take into account the quantum correlations of the bound Bogoliubov excitations encoded in the obtained eigenstates *exactly*, without restricting the number of bound Bogoliubov excitations. Furthermore, the excitation number of scattering modes is also not restricted in the ansatz, since there is no restriction built into the ansatz to limit the coherent state amplitude of the scattering modes. Furethermore, in Sec. 3.2.5 we rigorously justify the assumption of the separability of the eigenstates between the bound and the scattering Bogoliubov modes.

To explain the intuitive meaning of this second condition, we again resort to the simple model presented in the introduction, and note that all states with n-times occupation of the bound state where $n^* \leq n < 2n^*$ have energy less than the repulsive polaron. If the energy difference of the $\lfloor 2n^* \rfloor$ state (with $\lfloor n \rfloor$ the integer part of n) to the repulsive polaron is comparable to the typical energy of phonon excitations (which is of the order of the BEC chemical potential μ), then a boson added to the bound state to construct the $\lfloor 2n^* \rfloor$ state from the $\lfloor 2n^* \rfloor - 1$ state would also have a comparable occupation of the scattering states. Requiring that $|E_{\lfloor 2n^* \rfloor}|$ be much larger than μ, leads to $\mu/|\varepsilon_{\mathrm{B}} - U/2| \ll 1$. Applying the same argument to the effective model introduced here leads to the condition

$$\mu \ll \left| H_{22} \lfloor 1 + \varepsilon_{\mathrm{B}}/H_{22} \rfloor \Big(\varepsilon_{\mathrm{B}}/H_{22} - \lfloor \varepsilon_{\mathrm{B}}/H_{22} \rfloor \Big) \right| , \tag{3.28}$$

with $H_{22} = 1/2 \int_{\mathbf{x},\mathbf{x}'} U_{\mathrm{BB}}(\mathbf{x} - \mathbf{x}') \, |u_{\mathrm{B},\mathbf{x}}|^2 |u_{\mathrm{B},\mathbf{x}'}|^2$.

Third, regarding the assumption of coherent state occupation of scattering Bogoliubov modes, note that the bosons occupying the bound state are localized around the impurity. Thus they screen the impurity potential for the rest of the condensed bosons. This screening results in a modification of the condensate field that leads to the excitation of scattering Bogoliubov modes of the unperturbed condensate. This condensate distortion effect is captured by the coherent field $\alpha_{\mathbf{x}}$. In principle, an exact many-body wavefunction for the Bose polaron includes higher-order correlations and entanglement among the excited scattering Bogoliubov modes that goes beyond the uncorrelated coherent state. Nevertheless, for heavy mobile impurities where the impurity mass is comparable but larger than the boson mass and the heteronuclear Efimov effect is highly suppressed, the scattering Bogoliubov modes are now weakly interacting and delocalized, so the entanglement among these modes caused by their interactions - either mediated by the impurity or from higher-order processes - plays a negligible role. Thus, modeling the excitation of scattering Bogoliubov modes by a coherent state $|\alpha_{\mathbf{x}}\rangle$ is justified.

A final remark concerns the influence of three-body correlations on the spectrum of the system. Our analysis ignores the more complicated three-body correlations underlying

Efimov states [130, 42, 43, 11]. This is fully justified for heavy impurities where the size of excited Efimov clusters is much larger than many-body bound states considered here. For lighter impurities, the few-body bound states we describe are expected to decay into deeply bound Efimov states but we leave a detailed analysis of their influence to future research.

In the following, we apply our theory to a relevant experimental cold atoms setting and discuss some of the main features of the resulting many-body bound states on the repulsive side of the Feshbach resonance. As a key result, we reveal non-Gaussian quantum mechanical correlations in the bound state occupation statistics of these states.

3.2.5 Justification of the effective model and the variational principle

Here, we give a rigorous justification of the variational principle described in Sec. 3.2.4. To this end, we present a formulation of the initial impurity-boson problem where many-body bound states emerge as an effective impurity with multiple internal states coupled to a bath of weakly interacting, renormalized phonons. The coupling causes transitions between different impurity internal states (i.e., many-body bound states) via phonon scattering. Due to the large separation of energy scales between the different impurity internal states compared to the strength of transitions, one can treat the impurity-bath coupling within perturbation theory. Crucially, the relevant eigenstates of the unperturbed Hamiltonian corresponding to different metastable branches have the same product state form of the variational state $\left|\psi_{(\mathrm{var})}\right\rangle$ in Eq. 3.21. Since the variational manifold includes the leading order term of the true eigenstates, optimizing the variational parameters enables an even better approximation of the eigenstates.

As stated in the main text, a suitable Gaussian transformation can eliminate the linear term in Eq. 3.9 by displacing the field operator to the repulsive polaron saddle point while at the same time diagonalizing $\mathcal{H}_{\mathrm{MF}}$ to give the fluctuation modes on top of the repulsive polaron. As in the main text, the fluctuation field operator can be written as

$$\delta\hat{\phi}_{\mathbf{x}} = \delta\hat{\phi}_{\mathbf{x}}^{(\mathrm{B})} + \delta\hat{\phi}_{\mathbf{x}}^{(\mathrm{sc})} \,, \tag{3.29}$$

where $\delta\hat{\phi}_{\mathbf{x}}^{(\mathrm{B})} = u_{\mathrm{B},\mathbf{x}}\,\delta\hat{b} + v_{\mathrm{B},\mathbf{x}}\,\delta\hat{b}^{\dagger}$ with $\delta\hat{b}$ the fluctuation operator of the unstable mode $\hat{b}$. Inserting the mode-separated form of the fluctuation operator Eq. 3.29 in Eq. 3.9 results in the following form of $\hat{H}_{\mathrm{LLP}}$,

$$\begin{aligned}\hat{H}_{\mathrm{LLP}} = E[\Phi_{\mathrm{rep}}, \Gamma_{\mathrm{rep}}] + \hat{H}_{\mathrm{B}}[\delta\hat{\phi}_{\mathbf{x}}^{(\mathrm{B})\dagger}, \delta\hat{\phi}_{\mathbf{x}}^{(\mathrm{B})}] + \hat{H}_{\mathrm{sc}}[\delta\hat{\phi}_{\mathbf{x}}^{(\mathrm{sc})\dagger}, \delta\hat{\phi}_{\mathbf{x}}^{(\mathrm{sc})}] \\ + \hat{H}_{\mathrm{int}}[\delta\hat{\phi}_{\mathbf{x}}^{(\mathrm{B})\dagger}, \delta\hat{\phi}_{\mathbf{x}}^{(\mathrm{B})}; \delta\hat{\phi}_{\mathbf{x}}^{(\mathrm{sc})\dagger}, \delta\hat{\phi}_{\mathbf{x}}^{(\mathrm{sc})}] \,.\end{aligned} \tag{3.30}$$

In Eq. 3.30,

$$\hat{H}_{\mathrm{B}}[\delta\hat{\phi}_{\mathbf{x}}^{(\mathrm{B})\dagger}, \delta\hat{\phi}_{\mathbf{x}}^{(\mathrm{B})}] = -\varepsilon_{\mathrm{B}}\,\delta\hat{b}^{\dagger}\delta\hat{b} + \hat{H}_{3}[\delta\hat{\phi}_{\mathbf{x}}^{(\mathrm{B})\dagger}, \delta\hat{\phi}_{\mathbf{x}}^{(\mathrm{B})}] + \hat{H}_{4}[\delta\hat{\phi}_{\mathbf{x}}^{(\mathrm{B})\dagger}, \delta\hat{\phi}_{\mathbf{x}}^{(\mathrm{B})}] \,, \tag{3.31}$$

where $\hat{H}_3[\delta\hat{\phi}^{(\mathrm{B})\dagger}_{\mathbf{x}}, \delta\hat{\phi}^{(\mathrm{B})}_{\mathbf{x}}]$ and $\hat{H}_4[\delta\hat{\phi}^{(\mathrm{B})\dagger}_{\mathbf{x}}, \delta\hat{\phi}^{(\mathrm{B})}_{\mathbf{x}}]$ are given in Eqs. 3.18 and 3.19 with $\delta\hat{\phi}^{(\dagger)}_{\mathbf{x}}$ substituted by $\delta\hat{\phi}^{(\mathrm{B})(\dagger)}_{\mathbf{x}}$. Similarly, the Hamiltonian $\hat{H}_{\mathrm{sc}}$ only involves $\delta\hat{\phi}^{(\mathrm{sc})(\dagger)}_{\mathbf{x}}$. Finally, $\hat{H}_{\mathrm{int}}$ describes the interaction between the bound and scattering modes. By means of direct manipulation, the interaction Hamiltonian can be absorbed into $\hat{H}_{\mathrm{sc}}$ to yield

$$
\begin{aligned}
\hat{H}'_{\mathrm{sc}} = \hat{H}_{\mathrm{sc}} + \hat{H}_{\mathrm{int}} = \left(\int_{\mathbf{x}} \delta\hat{\phi}^{(\mathrm{sc})\dagger}_{\mathbf{x}} \, \hat{\zeta}'_{\mathbf{x}} + h.c. \right) + \frac{1}{2} \int_{\mathbf{x},\mathbf{x}'} : \delta\hat{\Psi}^{(\mathrm{sc})\dagger}_{\mathbf{x}} \, \hat{\mathcal{H}}'_{2,\mathbf{x}\mathbf{x}'} \, \delta\hat{\Psi}^{(\mathrm{sc})}_{\mathbf{x}'} : \\
+ \left(\int_{\mathbf{x},\mathbf{x}'} : \delta\hat{\phi}^{(\mathrm{sc})\dagger}_{\mathbf{x}} \, \delta\hat{\phi}^{(\mathrm{sc})\dagger}_{\mathbf{x}'} \, \hat{\mathcal{H}}'_{3,\mathbf{x}\mathbf{x}'} \, \delta\hat{\phi}^{(\mathrm{sc})}_{\mathbf{x}'} : + h.c. \right) + \hat{H}_4[\delta\hat{\phi}^{(\mathrm{sc})\dagger}_{\mathbf{x}}, \delta\hat{\phi}^{(\mathrm{sc})}_{\mathbf{x}}] \, .
\end{aligned}
\tag{3.32}
$$

In Eq. 3.32, $\hat{\mathcal{H}}'_{2,\mathbf{x}\mathbf{x}'}$, $\hat{\mathcal{H}}'_{3,\mathbf{x}\mathbf{x}'}$ and $\hat{\zeta}'_{\mathbf{x}}$ are operators in terms of $\delta\hat{\phi}^{(\mathrm{B})(\dagger)}_{\mathbf{x}}$ as follows,

$$
\hat{\mathcal{H}}'_{2,\mathbf{x}\mathbf{x}'} = \begin{pmatrix} \hat{\mathcal{E}}'_{\mathbf{x}\mathbf{x}'} & \hat{\Delta}'_{\mathbf{x}\mathbf{x}'} \\ \hat{\Delta}'^{*}_{\mathbf{x}\mathbf{x}'} & \hat{\mathcal{E}}'^{*}_{\mathbf{x}\mathbf{x}'} \end{pmatrix} ,
\tag{3.33}
$$

$$
\begin{aligned}
\hat{\mathcal{E}}'_{\mathbf{x}\mathbf{x}'} = \mathcal{E}_{\mathbf{x}\mathbf{x}'} + \mathcal{E}^{\mathrm{imp}}_{\mathbf{x}\mathbf{x}'} + \bar{U}_{\mathrm{eff},\mathbf{x}\mathbf{x}'} \, \varphi_{\mathbf{x}} \, \delta\hat{\phi}^{(\mathrm{B})\dagger}_{\mathbf{x}'} + \bar{U}_{\mathrm{eff},\mathbf{x}\mathbf{x}'} \, \varphi^{*}_{\mathbf{x}'} \, \delta\hat{\phi}^{(\mathrm{B})}_{\mathbf{x}} + : \delta\hat{\phi}^{(\mathrm{B})\dagger}_{\mathbf{x}'} \, U_{\mathrm{eff},\mathbf{x}\mathbf{x}'} \, \delta\hat{\phi}^{(\mathrm{B})}_{\mathbf{x}} : \\
+ \delta^{(d)}(\mathbf{x} - \mathbf{x}') \left[\int_{\mathbf{x}''} \delta\hat{\phi}^{(\mathrm{B})\dagger}_{\mathbf{x}''} \, U_{\mathrm{eff},\mathbf{x}''\mathbf{x}'} \varphi_{\mathbf{x}''} + \int_{\mathbf{x}''} \varphi^{*}_{\mathbf{x}''} \, U_{\mathrm{eff},\mathbf{x}''\mathbf{x}'} \, \delta\hat{\phi}^{(\mathrm{B})}_{\mathbf{x}''} \right. \\
\left. + \int_{\mathbf{x}''} : \delta\hat{\phi}^{(\mathrm{B})\dagger}_{\mathbf{x}''} \, U_{\mathrm{eff},\mathbf{x}''\mathbf{x}'} \delta\hat{\phi}^{(\mathrm{B})}_{\mathbf{x}''} : \right] ,
\end{aligned}
\tag{3.34}
$$

$$
\hat{\Delta}'_{\mathbf{x}\mathbf{x}'} = \Delta_{\mathbf{x}\mathbf{x}'} + \Delta^{\mathrm{imp}}_{\mathbf{x}\mathbf{x}'} + 2 \, U_{\mathrm{eff},\mathbf{x}\mathbf{x}'} \, \varphi_{\mathbf{x}} \, \delta\hat{\phi}^{(\mathrm{B})}_{\mathbf{x}'} + U_{\mathrm{eff},\mathbf{x}\mathbf{x}'} \, : \delta\hat{\phi}^{(\mathrm{B})}_{\mathbf{x}'} \delta\hat{\phi}^{(\mathrm{B})}_{\mathbf{x}} : ,
\tag{3.35}
$$

$$
\hat{\mathcal{H}}'_{3,\mathbf{x}\mathbf{x}'} = U_{\mathrm{eff},\mathbf{x}\mathbf{x}'} \varphi_{\mathbf{x}} + U_{\mathrm{eff},\mathbf{x}\mathbf{x}'} \, \delta\hat{\phi}^{(\mathrm{B})}_{\mathbf{x}} ,
\tag{3.36}
$$

$$
\begin{aligned}
\hat{\zeta}'_{\mathbf{x}} = \int_{\mathbf{x}'} \left(\mathcal{E}_{\mathbf{x}\mathbf{x}'} + \mathcal{E}^{\mathrm{imp}}_{\mathbf{x}\mathbf{x}'} \right) \delta\hat{\phi}^{(\mathrm{B})}_{\mathbf{x}'} + \frac{1}{2} \int_{\mathbf{x}'} \left(\Delta_{\mathbf{x}\mathbf{x}'} + \Delta^{\mathrm{imp}}_{\mathbf{x}\mathbf{x}'} \right) \delta\hat{\phi}^{(\mathrm{B})\dagger}_{\mathbf{x}'} + \frac{1}{2} \int_{\mathbf{x}'} \left(\Delta_{\mathbf{x}'\mathbf{x}} + \Delta^{\mathrm{imp}}_{\mathbf{x}'\mathbf{x}} \right) \delta\hat{\phi}^{(\mathrm{B})\dagger}_{\mathbf{x}'} \\
+ \int_{\mathbf{x}'} : \delta\hat{\phi}^{(\mathrm{B})\dagger}_{\mathbf{x}'} \left(U_{\mathrm{eff},\mathbf{x}\mathbf{x}'} \varphi_{\mathbf{x}'} \right) \delta\hat{\phi}^{(\mathrm{B})}_{\mathbf{x}} : + \int_{\mathbf{x}'} : \delta\hat{\phi}^{(\mathrm{B})\dagger}_{\mathbf{x}'} \left(U_{\mathrm{eff},\mathbf{x}\mathbf{x}'} \varphi_{\mathbf{x}} \right) \delta\hat{\phi}^{(\mathrm{B})}_{\mathbf{x}'} : \\
+ \int_{\mathbf{x}'} \varphi^{*}_{\mathbf{x}'} \, U_{\mathrm{eff},\mathbf{x}\mathbf{x}'} \, : \delta\hat{\phi}^{(\mathrm{B})}_{\mathbf{x}} \delta\hat{\phi}^{(\mathrm{B})}_{\mathbf{x}'} : + \int_{\mathbf{x}'} : \delta\hat{\phi}^{(\mathrm{B})\dagger}_{\mathbf{x}'} \, U_{\mathrm{eff},\mathbf{x}\mathbf{x}'} \, \delta\hat{\phi}^{(\mathrm{B})}_{\mathbf{x}'} \delta\hat{\phi}^{(\mathrm{B})}_{\mathbf{x}} : \, .
\end{aligned}
\tag{3.37}
$$

In Eq. 3.34, $\bar{U}_{\mathrm{eff},\mathbf{x}\mathbf{x}'}$ is different from $U_{\mathrm{eff,B}}$ and is given by $\bar{U}_{\mathrm{eff},\mathbf{x}\mathbf{x}'} = U_{\mathrm{BB}}(\mathbf{x} - \mathbf{x}') - 1/M(-i\hbar\nabla_{\mathbf{x}}) \cdot (-i\hbar\nabla_{\mathbf{x}'})$, and in the third line integration by parts is carried out. The form of $\hat{H}'_{\mathrm{sc}}$ in Eq. 3.32 is the same as Eq. 3.9 up to a constant, suggesting that the Hamiltonian parameters of the scattering modes only get renormalized by the fluctuations of the unstable mode. The physical meaning of absorbing $\hat{H}_{\mathrm{int}}$ into $\hat{H}_{\mathrm{sc}}$ to obtain $\hat{H}'_{\mathrm{sc}}$ becomes more transparent if $\hat{H}'_{\mathrm{sc}}$ is partially expanded in terms of the eigenstate $|\psi_n\rangle_{\mathrm{B}}$ of $\hat{H}_{\mathrm{B}}$ with energy E_n ($\hat{H}_{\mathrm{B}} |\psi_n\rangle_{\mathrm{B}} = E_n |\psi_n\rangle_{\mathrm{B}}$) as $\hat{H}'_{\mathrm{sc}} = \sum_{n,m} |\psi_n\rangle\langle\psi_m|_{\mathrm{B}} \otimes \langle\psi_n| \, \hat{H}'_{\mathrm{sc}} \, |\psi_m\rangle_{\mathrm{B}}$. The operators $\langle\psi_n| \, \hat{H}'_{\mathrm{sc}} \, |\psi_m\rangle_{\mathrm{B}}$ are the same as in Eq. 3.32, but with $\hat{\zeta}'_{\mathbf{x}}$, $\hat{\mathcal{H}}'_{2,\mathbf{x}\mathbf{x}'}$ and $\hat{\mathcal{H}}'_{3,\mathbf{x}\mathbf{x}'}$ substituted by their matrix elements $\langle\hat{\zeta}'_{\mathbf{x}}\rangle_{nm}$, $\langle\hat{\mathcal{H}}'_{2,\mathbf{x}\mathbf{x}'}\rangle_{nm}$ and $\langle\hat{\mathcal{H}}'_{3,\mathbf{x}\mathbf{x}'}\rangle_{nm}$ ($\langle\cdot\rangle_{nm}$ denotes the matrix element $\langle\psi_n| \cdot |\psi_m\rangle_{\mathrm{B}}$). The diagonal part of $\hat{H}'_{\mathrm{sc}}$ consists of effective renormalized Hamiltonians $\langle\psi_n| \, \hat{H}'_{\mathrm{sc}} \, |\psi_n\rangle_{\mathrm{B}}$ for stable modes when the impurity forms a many-body bound state $|\psi_n\rangle$.

The off-diagonal part of $\hat{H}'_{\mathrm{sc}}$ describes interaction processes between the many-body bound states and phonons, where a phonon scatters off the many-body bound state $|\psi_m\rangle$ and triggers the transition from $|\psi_m\rangle$ to $|\psi_n\rangle$. In this sense, off-diagonal terms can be treated as a perturbation term

$$\hat{H}_{\mathrm{pert}} = \sum_{n\neq m} |\psi_n\rangle\langle\psi_m|_{\mathrm{B}} \otimes \langle\psi_n| \hat{H}'_{\mathrm{sc}} |\psi_m\rangle_{\mathrm{B}} \ , \tag{3.38}$$

added to the unperturbed Hamiltonian $\hat{H}_0$, defined by

$$\hat{H}_0 = \hat{H}_{\mathrm{B}} + \sum_{n} |\psi_n\rangle\langle\psi_n|_{\mathrm{B}} \otimes \langle\psi_n| \hat{H}'_{\mathrm{sc}} |\psi_n\rangle_{\mathrm{B}} \ . \tag{3.39}$$

Thus, the strong-coupling impurity-boson problem has reduced to finding the eigenstates of $\hat{H}_0$ and including $\hat{H}_{\mathrm{pert}}$ in perturbation theory. We still have to establish that $\hat{H}_{\mathrm{pert}}$ can indeed be treated perturbatively, but first, it is instructive to gain a better understanding of the low energy states of $\hat{H}_0$. The structure of $\langle\psi_n| \hat{H}'_{\mathrm{sc}} |\psi_n\rangle_{\mathrm{B}}$ is similar to Eq. 3.9, which is form invariant under Gaussian transformations. As a result, one can perform a Gaussian transformation $\hat{U}'_n = \hat{\mathcal{D}}[\alpha^{(\mathrm{sc})}_{n,\mathbf{x}}]\,\hat{\mathcal{S}}_n$, implementing n-dependent displacements $\alpha^{(\mathrm{sc})}_{n,\mathbf{x}}$ of $\delta\hat{\phi}^{(\mathrm{sc})}_{\mathbf{x}}$ to eliminate the linear term proportional to $\langle\hat{\zeta}'_{\mathbf{x}}\rangle_{nn}$ and diagonalize $\langle\hat{\mathcal{H}}'_{2,\mathbf{x}\mathbf{x}'}\rangle_{nn}$ by $\hat{\mathcal{S}}_n$. The resulting Bogoliubov modes with field operators denoted by $\hat{\beta}_{n,\mathbf{k}}$ have a vacuum state $|\mathrm{GS}_n\rangle = \hat{\mathcal{D}}[\alpha^{(\mathrm{sc})}_{n,\mathbf{x}}]\,\hat{\mathcal{S}}_n\,|\Phi_{\mathrm{rep}}\rangle$ and single-particle excitations $\hat{\beta}^{\dagger}_{n,\mathbf{k}}\,|\mathrm{GS}_n\rangle$. Thus, each many-body bound state has an eigenstate of $\hat{H}_0$ associated to it, of the form

$$\left|\Psi_{n,(0)}\right\rangle = |\psi_n\rangle \otimes \hat{\mathcal{D}}[\alpha^{(\mathrm{sc})}_{n,\mathbf{x}}]\,\hat{\mathcal{S}}_n\,|\Phi_{\mathrm{rep}}\rangle \ , \tag{3.40}$$

which is the lowest energy state associated with the many-body bound state $|\psi_n\rangle$. Accordingly, the single particle excitations on top of $\left|\Psi_{n,(0)}\right\rangle$ are of the form $\hat{\beta}^{\dagger}_{n,\mathbf{k}}\left|\Psi_{n,(0)}\right\rangle$. Intuitively, $\left|\Psi_{n,(0)}\right\rangle$ describes a “many-body bound state" polaron - the polaronic dressing of a many-body bound state instead of the bare impurity. As such, the many-body bound states emerge as internal states $|\psi_n\rangle$ of an effective impurity - the bare impurity with several bosons bound to it - whose dynamics and dressing by phonons is described by $\hat{H}_0$. In this regard, $\hat{H}_{\mathrm{pert}}$ describes transitions between internal states of this effective impurity via phonon scattering.

The notable character of the state $\left|\Psi_{n,(0)}\right\rangle$ is its product state form, which closely connects to the same form of the variational state $\left|\psi_{(\mathrm{var})}\right\rangle$ in Eq. 3.21. The difference of $\left|\Psi_{n,(0)}\right\rangle$ and $\left|\psi_{(\mathrm{var})}\right\rangle$ is in the additional Gaussian transformation $\hat{\mathcal{S}}_n$, which accounts for the renormalization of the phonons by many-body bound state formation. This renormalization occurs due to the underlying interactions among bosons bound to the impurity and bosons in the BEC. Thus, the effect of $\hat{\mathcal{S}}_n$ is to account for terms in $\langle\hat{\mathcal{H}}'_{2,\mathbf{x}\mathbf{x}'}\rangle_{nn}$ which contain expectation values over $|\psi_n\rangle$ of operators involving $\delta\hat{\phi}^{(\mathrm{B})(\dagger)}_{\mathbf{x}}$. Note that the $n-$independent part of the quadratic Hamiltonian is already diagonal by the initial Gaussian transformation and has no instability since all the involved scattering modes have positive energies. Furthermore, investigating the structure of $|\psi_n\rangle$ obtained from numerical diagonalization of $\hat{H}_\mathrm{B}$ reveals that the addition of n-dependent terms has a minute effect and, importantly, does not induce any instability. The absence of instability is confirmed by direct numerical evaluation which shows that expectation values of single field operators as well as $\langle :\, \delta\hat{\phi}^{(\mathrm{B})}_{\mathbf{x}} \delta\hat{\phi}^{(\mathrm{B})}_{\mathbf{x}'} :\rangle_{nn}$ over the relevant many-body bound states are vanishingly small. This demonstrates that the additional squeezing transformation $\mathcal{S}_n$ to redefine phonon modes in the presence of the many-body bound state $|\psi_n\rangle$ has a minimal effect; thus we can set $\hat{\mathcal{S}}_n \simeq \mathbb{I}$. In this way, we recover exactly the same form of $\left|\psi_{(\mathrm{var})}\right\rangle$ in Eq. 3.21.

In the following, we elaborate more on the perturbative treatment of $\hat{H}_\mathrm{pert}$ mentioned above. As discussed in the main text, Fock states are excellent approximations to the many-body bound states $|\psi_n\rangle$. Thus, combinations of $\delta\hat{\phi}^{(\mathrm{B})(\dagger)}_{\mathbf{x}}$ which change particle number have vanishingly small expectation values over $|\psi_n\rangle$, but the same is not true for transition matrix elements between two different many-body bound states. To estimate the effect of phonon-induced transitions, we consider the first-order perturbative correction to $\left|\Psi_{n,(0)}\right\rangle$. The first order correction to $\left|\Psi_{n,(0)}\right\rangle$ within perturbation theory reads

$$\begin{aligned}
\left|\Psi_{n,(1)}\right\rangle \propto & \left|\Psi_{n,(0)}\right\rangle \\
& + \sum_{m\neq n} \frac{\langle \mathrm{GS}_m | \, \langle \hat{H}'_\mathrm{sc}\rangle_{mn} \, |\mathrm{GS}_n\rangle}{E_{n,(0)} - E_{m,(0)}} \, |\mathrm{GS}_m\rangle \\
& + \sum_{m\neq n} \int_{\{\mathbf{k}_i\}_m} \frac{\langle \{\mathbf{k}_i\}_m | \, \langle \hat{H}'_\mathrm{sc}\rangle_{mn} \, |\mathrm{GS}_n\rangle}{E_{n,(0)} - E_{m,(0)} - \varepsilon_{\{\mathbf{k}_i\}_m}} \, |\{\mathbf{k}_i\}_m\rangle \ ,
\end{aligned} \tag{3.41}$$

where $E_{n,(0)}$ is the energy of $E_{n,(0)}$, and $|\{\mathbf{k}_i\}_m\rangle$ denotes the state containing elementary excitations of momenta $\mathbf{k}_1, \mathbf{k}_2, \cdots$ on top of $|\mathrm{GS}_m\rangle$. In the denominator of the third term in Eq. 3.41, $E_{n,(0)} - E_{m,(0)} \sim \varepsilon_\mathrm{B}$ is by far the largest energy scale. Thus the only relevant decay processes are those where $\left|\Psi_{n,(0)}\right\rangle$ decays to a lower energy state $\left|\Psi_{m,(0)}\right\rangle$ and emits high energy phonons with total energy $\varepsilon_{\{\mathbf{k}_i\}_m} \sim \varepsilon_\mathrm{B}$. Note that although $\langle \hat{H}'_\mathrm{sc}\rangle_{mn}$ contains three- and four-phonon terms, such phonon interaction terms are weak compared to phonon kinetic term which dominates. This can be seen from the structure of $\langle \hat{H}'_\mathrm{sc}\rangle_{nn}$ which resembles the Hamiltonian of a weakly interacting Bose gas with a linear coupling $\langle \hat{\zeta}'_{\mathbf{x}}\rangle_{nn}$ which leads to a coherent state of excitations $\alpha^{(\mathrm{sc})}_{n,\mathbf{x}}$ with total excitation number much less than unity (see the main text). Importantly, $\langle \hat{H}'_\mathrm{sc}\rangle_{nn}$ does not contain any instability to compete with the interaction terms. Thus, the true eigenstates of $\hat{H}'_\mathrm{sc}$ can be adiabatically connected to the non-interacting ones $|\{\mathbf{k}_i\}_m\rangle$, and especially for high energies, the interaction terms become irrelevant.

We now discuss the structure of the last term in Eq. 3.41. A full perturbative treatment of $\langle \hat{H}'_\mathrm{sc}\rangle_{mn}$, while systematically possible, is a formidable task and is excessively cumbersome even at the level of the first-order perturbative term in Eq. 3.41. Nevertheless, we estimate the magnitude of relevant terms in the expansion of $|\{\mathbf{k}_i\}_m\rangle$. Specifically, we focus on single-excitation states $|\mathbf{k}\rangle$. The relevant $|\mathbf{k}\rangle$ states have high energies $\varepsilon_\mathbf{k} \sim \varepsilon_\mathrm{B}$, thus the approximation $\hat{\mathcal{S}}_n \simeq \mathbb{I}$ is specifically more accurate here. After a rather lengthy algebra, it turns out that the dominant contribution of $|\mathbf{k}\rangle$ to $\left|\Psi_{n,(1)}\right\rangle$ is proportional to

$$\chi_{\mathbf{k}} = \int_{\mathbf{x},\mathbf{x}'} e^{i\mathbf{k}\cdot\mathbf{x}} \left(\langle \hat{\zeta}''_{\mathbf{x}} \rangle_{mn} + \langle \hat{\mathcal{E}}'_{\mathbf{x}\mathbf{x}'} \rangle_{mn} \, \alpha^{(\mathrm{sc})}_{n,\mathbf{x}'} + \alpha^{(\mathrm{sc})*}_{m,\mathbf{x}'} \, \mathrm{Re}\Big[\langle \hat{\Delta}'_{\mathbf{x}\mathbf{x}'} \rangle_{mn} \Big] \right) , \tag{3.42}$$

where $\hat{\zeta}''_{\mathbf{x}}$ equals $\hat{\zeta}'_{\mathbf{x}}$ without the first three terms in Eq. 3.37. The subleading contributions to $|\mathbf{k}\rangle$ contain higher powers of $\alpha^{(\mathrm{sc})}_{n,\mathbf{x}}$ and $\alpha^{(\mathrm{sc})*}_{m,\mathbf{x}}$, which are significantly smaller since $\int_{\mathbf{x}} |\alpha^{(\mathrm{sc})}_{(n,m),\mathbf{x}}|^2 \ll 1$ in accordance with the results presented in the main text. Note that the large value of $|\mathbf{k}| \sim \sqrt{2m_{\mathrm{red}}\varepsilon_{\mathrm{B}}/\hbar^2}$ also suppresses the magnitude of $\chi_{\mathbf{k}}$. Intuitively, the above formal arguments mean that the decay of a dressed many-body bound state $\left|\Psi_{n,(0)}\right\rangle$ by emitting a high-energy phonon is strongly suppressed. One can carry out the same type of argumentation for the second term in Eq. 3.41, where the leading term is found to be proportional to

$$\chi_m = \int_{\mathbf{x}} \frac{1}{\varepsilon_{\mathrm{B}}} \left(\alpha^{(\mathrm{sc})*}_{m,\mathbf{x}} \, \langle \hat{\zeta}''_{\mathbf{x}} \rangle_{mn} + \alpha^{(\mathrm{sc})}_{n,\mathbf{x}} \, \langle \hat{\zeta}''^{\dagger}_{\mathbf{x}} \rangle_{mn} \right) \left\langle \alpha^{(\mathrm{sc})}_{m,\mathbf{x}} \middle| \alpha^{(\mathrm{sc})}_{n,\mathbf{x}} \right\rangle . \tag{3.43}$$

Given that both estimates of the size of the first-order perturbative corrections quantified by the amplitudes χ_m and $\chi_{\mathbf{k}}$ are substantially smaller than unity, we conclude that the variational ansatz based on the product form of $\left|\Psi_{n,(0)}\right\rangle$ can provide qualitatively reliable information about general characteristics of the many-body bound states. Note that the structure of the variational ansatz in Eq. 3.21 provides more freedom to optimize the parameters and find better approximations to the true many-body bound states than the zeroth order state $\left|\Psi_{n,(0)}\right\rangle$, as the variational manifold includes $\left|\Psi_{n,(0)}\right\rangle$. As such, the optimization procedure partially accounts for higher-order perturbative corrections.
Ultimately, we emphasize that the proportionality constants mentioned above scale according to the occupation number of many-body bound states. As such, the above arguments are valid for cases where a few bosons are bound to the impurity, but in general, the validity of arguments has to be checked for each specific case under consideration. Problems that require caution include Rydberg and ionic impurities in a BEC, where hundreds of bosons are bound to the impurity. In such cases, the transition matrix elements of $\hat{H}_{\mathrm{pert}}$ can be large, which might require including perturbative corrections to high orders.

3.3 Results

Here we consider a Bose polaron setting comprised of impurity ^{40}K atoms immersed in a BEC of ^{87}Rb atoms with condensate density $n_0 = 1.8 \times 10^{14}\,\mathrm{cm}^{-3}$ and inter-boson scattering length $a_{\mathrm{B}} = 100\,a_0$ with $a_0 = 0.529\,\text{Å}$ the Bohr radius [99]. The natural length and energy units are then the inverse Fermi momentum $k_n = (6\pi^2 n_0)^{1/3}$ and energy $E_n = \hbar^2 k_n^2/2m_{\mathrm{B}}$, respectively. The impurity-boson potential is modeled by a squarewell of the form $V_{\mathrm{IB}}(\mathbf{r}) = V_0\,\Theta(r_0 - r)$ where $r = |\mathbf{r}|$ and r_0 is the potential range tuned properly to retrieve the impurity-boson effective range. The boson-boson scattering potential can be modeled by a zero-range contact interaction $U_{\mathrm{BB}}(\mathbf{x})=U_0\,\delta(\mathbf{x})$ compatible with the Born approximation. Note that the major effect of any finite boson-boson interaction range would appear in the interaction of bound Bogoliubov modes, while the bound-scattering and scattering-scattering mode interactions are still well modeled by contact boson-boson interactions. The latter is due to the fact that only low energy scattering Bogoliubov modes with momenta of the order of $1/\xi_{\mathrm{red}}$ are involved, with $\xi_{\mathrm{red}}^2 = \hbar^2/(2m_{\mathrm{red}}n_0U_0)$ the modified BEC healing length, which is much larger than the boson-boson interaction range. Thus, we expect the effect of non-zero boson-boson interaction to be quantitative and only result in marginal changes in the interaction strength of bound Bogoliubov modes.

Having described the system, we now use the variational principle explained before to obtain the relevant stable-state solutions across the impurity-boson scattering resonance. To this end, we apply the construction presented earlier step-by-step. Furthermore, at each step we carry out suitable approximations that are applicable to the problem considered here and illustrate the essential physics in a more transparent manner.

The first step is to find the repulsive polaron saddle-point solution by the procedure outlined in Sec. 3.2.2. To find Φ_{rep} and S_{rep}, we begin by an initial guess $S_{\mathrm{rep},0} = \mathbb{I}$, and solve $\zeta[\Phi_{\mathrm{rep},0},\mathbb{I}] = 0$. The resulting solution $\Phi_{\mathrm{rep},0}$ is the repulsive polaron without Bogoliubov approximation. Since for small positive impurity-boson scattering lengths a such that $a/\xi \ll 1$, the condensate distortion of the repulsive polaron relative to the unperturbed condensate is $\mathcal{O}(a/\xi)$ [142, 221], $\mathcal{H}_{\mathrm{MF}}[\Phi_{\mathrm{rep},0},\mathbb{I}]$ equals $\mathcal{H}_{\mathrm{MF}}[\sqrt{n_0},\mathbb{I}]$ up to perturbative terms coming from the condensate distortion. Thus, the Bogoliubov transformation $S_{\mathrm{rep},1}$ that diagonalizes $\mathcal{H}_{\mathrm{MF}}[\Phi_{\mathrm{rep},0},\mathbb{I}]$ is identical to the standard Bogoliubov transformation S_{Bog} of an unperturbed BEC, up to corrections of $\mathcal{O}\big((a/\xi)^2\big)$.

The next step correction to the repulsive polaron amounts to finding $\Phi_{\mathrm{rep},1}$ such that $\zeta[\Phi_{\mathrm{rep},1},\Gamma_{\mathrm{Bog}}] = 0$. The differential equation $\zeta[\Phi,\Gamma_{\mathrm{Bog}}] = 0$ differs from $\zeta[\Phi,\mathbb{I}] = 0$ only in the terms containing $\Gamma^{11}_{\mathrm{Bog}}$ and $\Gamma^{12}_{\mathrm{Bog}}$, both of the order $\mathcal{O}(\lambda^{3/2}) \sim 5\times 10^{-3}$, with $\lambda = n_0^{1/3}a_{\mathrm{B}}$ the BEC gas parameter [186, 163]. Due to the diluteness of cold atomic gases, $\lambda \ll 1$, and including bosonic correlations through Γ within Bogoliubov approximation and beyond does not affect the repulsive polaron solution and the quantum fluctuations atop. Thus, in connection to the special setting we consider here, hereafter we neglect corrections due to quantum fluctuations of the repulsive polaron and set $S_{\mathrm{rep}} = \mathbb{I}$.

Note that in general settings, especially pertaining to atomic BECs in lower dimensionality or exciton-polariton condensates in semiconductor heterostructures, it is essential to include the effects of quantum fluctuations through Γ, and our theory is capable to account for such effects in principle. In these lower dimensional settings, the role of quantum fluctuations is fundamentally different, and one must take great care in applying standard treatments of weakly interacting Bose gases in higher dimensions [197]. Even in three dimensions, the effect of quantum fluctuations is essential for long-range physics. However, for the setting we consider in this chapter, the excitations come either in the form of a bound Bogoliubov mode, which is highly localized around the impurity, and as such the effect of Bogoliubov transformation on it becomes insignificant (see Appendix A), or in the form of scattering modes which, as we show later, have a vanishingly small excitation number such that their state is almost a vacuum state. In both cases, Bogoliubov transformation does not add much information to the conclusions about the physics of the problem. However, Inclusion of quantum fluctuations through Γ terms is essential when considering light impurities and studying impurity-induced instabilities on attractive polaron, as studied for instance in Refs. [42, 43].

The next inputs to our variational theory are the bound state Bogoliubov factors $u_{\mathrm{B},\mathbf{x}}$ and $v_{\mathrm{B},\mathbf{x}}$, which form the bound state solution of $\mathcal{H}_{\mathrm{MF}}[\Phi,0]$. It can be shown that the contribution of the off-diagonal terms in $\mathcal{H}_{\mathrm{MF}}[\Phi,0]$ to the eigenstates and eigenenergies are of $\mathcal{O}\big(\mu/\varepsilon_{\mathrm{B}}\big) \sim 9 \times 10^{-3}$, and can be neglected to the leading order. This approximation amounts to setting $v_{\mathrm{B},\mathbf{x}} = 0$. Furthermore, the effective potential $U_0|\varphi_{\mathrm{rep},\mathbf{x}}|^2 - \mu$ caused by the repulsive polaron's condensate distortion around the impurity is much weaker than $V_{\mathrm{IB}}(\mathbf{x})$, thus $u_{\mathrm{B},\mathbf{x}}$ can be approximated by $\eta_{\mathbf{x}}$ that is the bound state solution of $-\hbar^2\nabla^2/2m_{\mathrm{red}} + V_{\mathrm{IB}}(\mathbf{x})$ - see Appendix A for a detailed derivation of these perturbative approximations. Note that the leading-order approximations made above can be extended to arbitrary higher orders in a systematic manner, and we expect that the quantitative changes will not alter any of the key physics of the many-body bound states.

By carrying out the previous steps, we are in a position to obtain the metastable states from finding the optimal solutions of Eqs. 3.26 and 3.27 by solving the variational equations (see Appendix B for the explicit form)

$$\begin{aligned} &\frac{\delta}{\delta\alpha^*_{\mathbf{x}}} H[\psi^*_n, \psi_n, \alpha^*_{\mathbf{x}}, \alpha_{\mathbf{x}}] - \lambda\eta_{\mathbf{x}} = 0\,, \\ &\frac{\delta}{\delta\psi^*_n} H[\psi^*_n, \psi_n, \alpha^*_{\mathbf{x}}, \alpha_{\mathbf{x}}] = E\,\psi_n\,. \end{aligned} \tag{3.44}$$

In Eq. 3.44, λ is a Lagrange multiplier determined to fulfill the second of Eqs. 3.27, and E is the energy of the metastable state that also acts as a Lagrange multiplier to fulfill the normalization condition Eq. 3.27. Solving Eqs. 3.44 gives access to the energies and variational states of the many-body bound states across the Feshbach resonance, which are discussed in the next sections.

3.3.1 Energy of the many-body bound states

In the regime $\mu/\varepsilon_{\mathrm{B}} \ll 1$, we already noted that the condensate distortion $\alpha_{\mathbf{x}}$ remains small in magnitude compared to the repulsive polaron field φ_{rep}, and as we will discuss at the end of this subsection, the energies and wave functions of the many-body bound states obtained by solving Eqs. 3.44 are well approximated by setting $\alpha_{\mathbf{x}}=0$, meaning a vacuum of scattering Bogoliubov modes on top of the repulsive polaron. Fig. 3.2(a) depicts the energies of the metastable states obtained by setting $\alpha_{\mathbf{x}}=0$. In the attractive side (region (1) in Fig. 3.2(a)), the only stable-state solution corresponds to the attractive polaron Φ_{att} (green dashed line), studied in Refs. [92, 142, 177]. All the fluctuation modes that are eigenstates of $\mathcal{H}_{\mathrm{MF}}[\Phi_{\mathrm{att}}, \mathbb{I}]$ have positive energy with a parabolic energy landscape as in panel (1) in Fig. 3.2(b).

On the repulsive side, there exists a range of scattering lengths where impurity-boson interactions lead to the instability of the phase quadrature of a Bogoliubov mode, leading to dynamical instability. The dynamical instability is a precursor to the formation of repulsive polaron, and occurs for a range of scattering lengths which lies inside the region (2) in Fig. 3.2(a). The energy landscape of the dynamically unstable mode is depicted in panel (2) of Fig. 3.2(b), where the negative- and positive-curvature directions correspond to the phase and amplitude quadratures, respectively.

In region (3) of Fig. 3.2(a), a well-defined unstable fluctuation mode emerges, that is the bound Bogoliubov mode. The possibility of multiple occupation of the bound Bogoliubov mode results in the emergence of the two metstable states ms_1 and ms_2, depicted by solid red and blue lines, respectively, in Fig. 3.2(a). The corresponding energy landscape in the form of a mexican hat, alongside the relative energies of various metastable states are depicted in panel (3) of Fig. 3.2(b). The origin of the energy landscape corresponds to the vaccum of the fluctuation mode, i.e. the repulsive polaron. The metastable states ms_1 and ms_2 are designated on the energy landscape schematically by circles whose radii and relative positions indicate the mean bound state occupation number and the relative energy of the states, respectively.

The energy landscape minimum corresponds roughly to the bound state component of the attractive polaron coherent state field, obtained by calculating the overlap $\alpha_{\text{att,B}} = \int_{\mathbf{x}} \eta^*_{\mathbf{x}} \varphi_{\text{att},\mathbf{x}}$. In fact, we interpret the lowest-lying many-body bound state as *nothing but* the remnant of the attractive polaron branch on the repulsive side of the Feshbach resonance. The two variational states we employ here, i.e. the attrative polaron and the ms_1 state have similar but not identical structures, which explains their slightly different variational energies. To further support our claim, in Fig. 3.3 we compare density-profile of bosons around the impurity for the different variational states. The qualitative similarity of the spatial structures of the lowest-lying many-body bound state and the attractive polaron further suggests that the two states describe the same ground state.

Beyond a certain critical scattering length, new stable solutions emerge from the repulsive polaron, denoted by ms_3 to ms_6 in Fig. 3.2. These states correspond to multiple occupation of the bound state. As the interaction strength rises, the bound state becomes more localized, resulting in an increase in the effective inter-boson repulsive interaction. At the same time, the system gains energy by binding more bosons. While both these effects compete, the increase in bound state energy dominates, lowering the energy of the states with higher bound state occupation. In terms of the saddle point structure, the increase in bound state energy means that the saddle point gets deeper, and the mean occupation number of the bound state increases, as depicted in panel (4) of Fig 3.2(b). Another implication of the competition between the increase in binding energy and the repulsive interaction is the emergence of level crossings among the metastable states in region (4) of Fig. 3.2(a). The presence of such level crossings can be explained again by the simple model laid out in the introduction. For a fixed bound state energy $\varepsilon_{\text{B},0}$, two metastable states with n_1 and n_2 occupation of the bound state with $n^*(\varepsilon_{\text{B},0}) < n_1 < n_2 < 2n^*(\varepsilon_{\text{B},0})$ have energies $E_{n_1} < E_{n_2}$. For larger $1/k_n a$, the increase in binding energy has the dominant effect on the energy of the many-body bound states, and the energy of the state

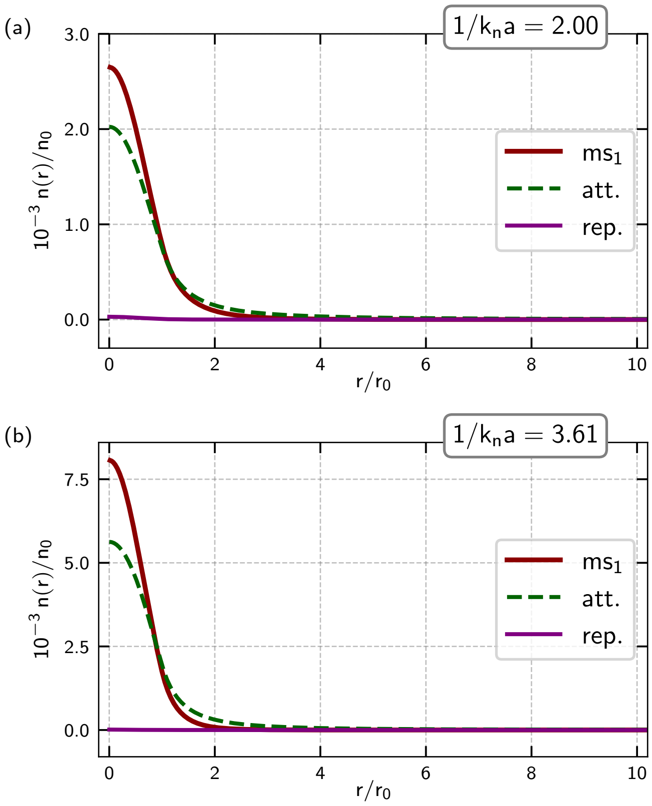

Figure 3.3: Density profile of the repulsive polaron (solid purple line), attractive polaron (green dashed line), and ms_1 state (solid red line), as a function of the radial distance from the impurity, for (a) $1/k_n a = 2.0$ and (b) $1/k_n a = 3.61$. The density profiles of the attractive polaron and the ms_1 state are qualitatively similar.

with higher bound state occupation decreases more rapidly, resulting in the level crossing pattern.

Fig. 3.4 depicts the behavior of energy and bound state occupation for the first few many-body bound states together with the attractive and repulsive polaron. The energy of the ms_1 state decreases monotonically, and its mean bound state occupation number saturates to double occupation for the range of scattering lengths considered. The ms_2 state approaches the bare dimer in energy and bound state occupation number. Across the level crossings of the two lowest-lying states, $\langle N_\mathrm{B} \rangle$ shows a non-monotonic behavior, and by increasing $1/k_n a$ saturates to single and double occupation for ms_2 and ms_1 states, respectively. The ms_3 state appears in the atom-dimer continuum at a critical scattering length (marked by the vertical dotted line in Fig. 3.4 (b)) and maintains a constant $\langle N_\mathrm{B} \rangle \simeq 3$. In contrast, the mean bound state occupation number of the attractive polaron increases monotonically with a value that remains larger than ms_1 and ms_2. At the level crossing of ms_1 and ms_3, the two states demonstrate strong mixing, resulting in spikes of $\langle N_\mathrm{B} \rangle$ for both states.

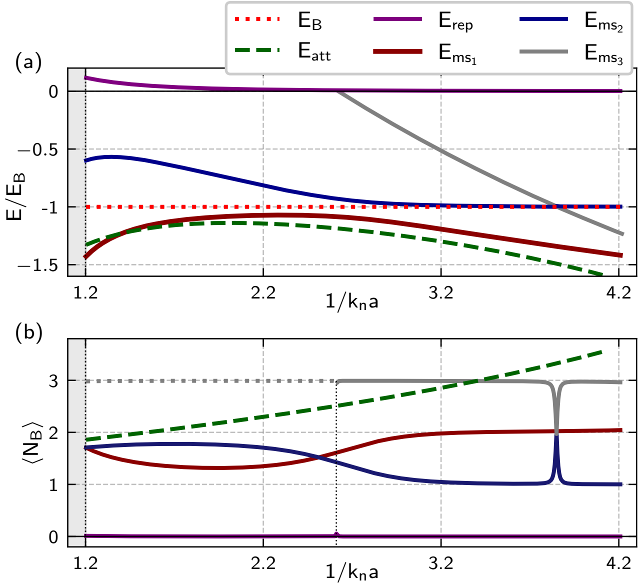

Figure 3.4: Energy in units of the dimer binding energy (a) and mean bound state occupation number (b) of the many-body bound states (red, blue and grey solid lines for ms_1, ms_2 and ms_3 respectively), attractive polaron (green dashed line), and repulsive polaron (purple solid line). Initially, the ms_2 state has higher mean bound state occupation number and energy than the ms_1 state, indicating the dominant effect of the inter-boson interaction on the energy of the states. Beyond the first level crossing, the mean occupation number of the ms_1 state increases above the ms_2 state due to the gain in energy from binding more bosons. The ms_3 state enters the dimer-boson continuum at the critical scattering length indicated by vertical dotted line in panel (b) and maintains an almost constant $N_{\mathrm{B}} \simeq 3$. For increasing $1/k_n a$, the mean bound state occupation number of ms_1 and ms_2 states approach integer values. At the level crossing between ms_1 and ms_3, the states strongly mix, resulting in sharp spikes in $\langle N_{\mathrm{B}} \rangle$ in panel (b).

Before moving on to the next section, we comment on the approximation $\alpha_{\mathbf{x}} = 0$ introduced earlier. In Fig. 3.5, we compare the energies of many-body bound states obtained from solving the full set of Eqs. 3.44, to the energies obtained under the assumption $\alpha_{\mathbf{x}} = 0$. We find that the effect of condensate distortion on the wave functions and energies of many-body bound states are only marginal, and setting $\alpha_{\mathbf{x}} = 0$ is a reasonable approximation.

The main reason behind the markedly different behavior of the many-body bound states compared to the attractive and repulsive polaron lies in the particular composition of each many-body state $\left|\psi_{(\mathrm{B})}\right\rangle$ out of dimer Fock states $\{|n\rangle_{\mathrm{B}}, \, n = 0, 1, 2, \cdots\}$. Indeed, inspection of $\langle N_{\mathrm{B}} \rangle$ in Fig. 3.4 suggests that $\left|\psi_{(\mathrm{B})}\right\rangle$ for each of the many-body bound states has to be close to a Fock state $|n\rangle_{\mathrm{B}}$ for some n. To gain further insight into the structure of the many-body bound states, in the next subsection, we investigate the dimer occupation statistics of the many-body bound states.

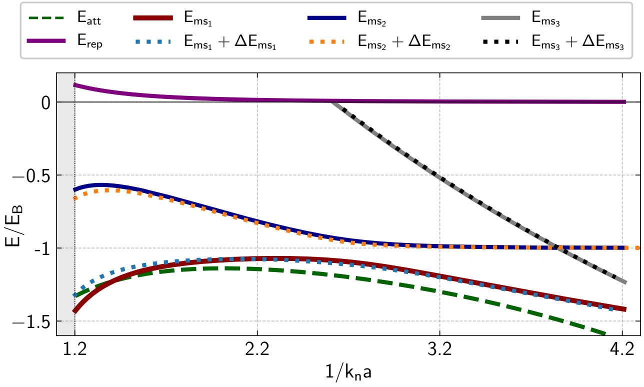

Figure 3.5: Energy of the many-body bound states including the effect of condensate distortion obtained by fully solving Eqs. 3.44 (dotted lines), compared to the energies obtained by setting $\alpha_{\mathbf{x}} = 0$. Including condensate distortion effects results in marginal changes in the energy (denoted by $\Delta E_{ms_i}, i = 1, 2, 3$), and wave function of many-body bound states.

3.3.2 Dimer occupation statistics of the many-body bound states

As mentioned at the end of Sec. 3.2.2, pure mean-field approaches to model the state of Bose polaron neglect the higher order terms $\hat{H}_3$ and $\hat{H}_4$, while the latter are crucial to capture the physics of many-body bound states. One consequence of including these higher order terms in the model is their non-perturbative effects reflected in the genuine quantum mechanical correlations of the wave function in the dimer Fock space, which is represented in our variational scheme by $\left|\psi_{(\mathrm{B})}\right\rangle$. To quantify the quantum mechanical correlations of $\left|\psi_{(\mathrm{B})}\right\rangle$, we note that it formally belongs to the Fock state of a single bosonic mode $\hat{b}$, thus its characteristics can be quantified via different quantum mechanical quasiprobability distributions used frequently in quantum optics to characterize the quantum states of light.

A quasiprobability distribution that is specially suitable for characterizing $\left|\psi_{(\mathrm{B})}\right\rangle$ is the Husimi Q representation, that in our context can be defined by [183]

$$Q(\alpha) = \frac{1}{\pi}\left\langle\alpha\middle|\psi_{(\mathrm{B})}\right\rangle\left\langle\psi_{(\mathrm{B})}\middle|\alpha\right\rangle . \tag{3.45}$$

In Eq. 3.45, $|\alpha\rangle$ is an arbitrary coherent state that is the eigenstate of $\hat{b}$, i.e. $\hat{b}\,|\alpha\rangle = \alpha\,|\alpha\rangle$.

In Fig. 3.6, we depict the Q representation of the states in Fig. 3.4 for $1/k_n a = 2.74$. The repulsive and attractive polaron, both include coherent state components of the bosonic mode $\hat{b}$ with a coherent state amplitude $\alpha^{(\mathrm{sp})} = \int_{\mathbf{x}} \eta^*_{\mathbf{x}}\, \varphi^{(\mathrm{sp})}_{\mathbf{x}}$ with the superscript “sp" indicating the respective saddle point. The Q representation of the saddle point state is thus $Q^{(\mathrm{sp})}(\alpha) = 1/\pi \exp\left(-|\alpha - \alpha^{(\mathrm{sp})}|^2\right)$, which is a Gaussian distribution localized on α^{sp}. In contrast, the many-body bound states have markedly different Q representations, reminiscent of Fock states. The Q representation already indicates that the state $\left|\psi_{(\mathrm{B})}\right\rangle$ contains quantum mechanical correlations with non-Gaussian characters, as opposed to coherent and

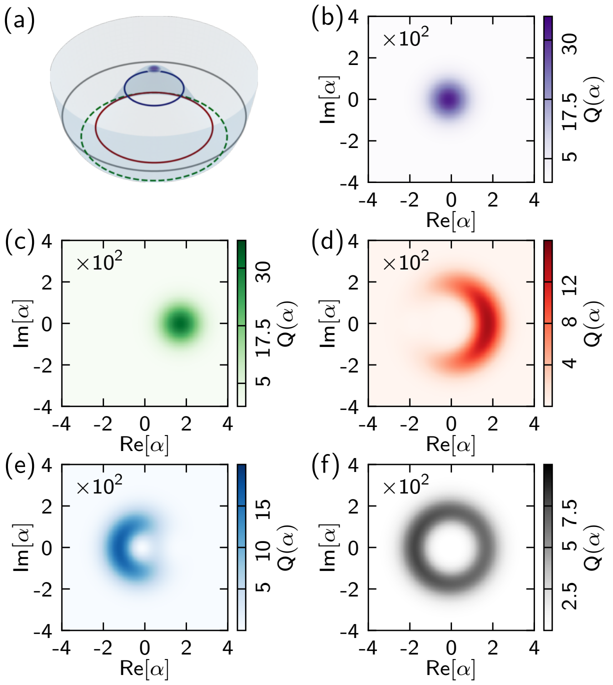

Figure 3.6: (a) Illustration of the energy landscape and the metastable states at $1/k_n a = 2.74$. As in Fig. 3.2 (b) panels (3) and (4), the radius, respectively, the vertical order of each circle on the energy surface reflect the mean bound state occupation number, respectively, the energy of the corresponding metastable state. Panels (b) and (c) show the quantitative calculations of the Q representation of the repulsive and attractive polaron, respectively. Panels (d) to (f) depict the Q representation of ms_1 to ms_3 states.

squeezed coherent states that are characterized by ellipsoidal Q distributions. We again highlight that the non-Gaussianity of the Q distribution is a result of including higher order terms $\hat{H}_3$ and $\hat{H}_4$ in the model, and treating the boson correlations in the dimer Fock state sector exactly. Note that with the strong boson-boson repulsions considered here, a truncated-basis variational ansatz can be accurate enough to predict essential features of the polaron, however, it is best suited for the limit of low densities. Our theory, on the other hand, has the capability to include a fluctuating number of particles in the polaron cloud even in dense bosonic media, as long as the binding energy is much larger than the BEC chemical potential.

Another useful quantity signifying the correlations of bosons occupying the bound state is $g_{\mathrm{B}}^{(2)}$ defined by

$$g_{\mathrm{B}}^{(2)} = \frac{\left\langle \psi_{(\mathrm{B})} \middle| \hat{b}^{\dagger 2} \hat{b}^{2} \middle| \psi_{(\mathrm{B})} \right\rangle}{\left\langle \psi_{(\mathrm{B})} \middle| \hat{b}^{\dagger} \hat{b} \middle| \psi_{(\mathrm{B})} \right\rangle^{2}} . \tag{3.46}$$

Fig. 3.7 depicts $g_{\mathrm{B}}^{(2)}$ for different many-body bound states. We again observe that due

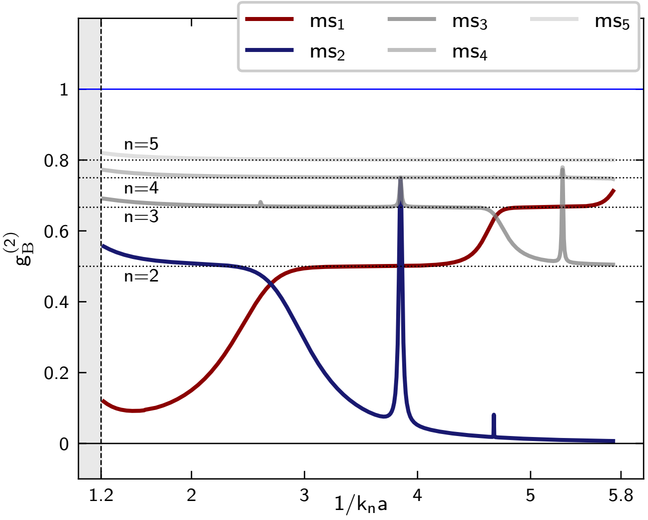

Figure 3.7: $g_{\mathrm{B}}^{(2)}$ of the many-body bound states. Clear deviations from the results of a Gaussian state indicates the non-Gaussian nature of bosons spatial correlations occupying the bound state.

to the effect of boson-boson repulsion, $g_{\mathrm{B}}^{(2)}$ shows strong boson anti-bunching for all the many-body bound states. Especially, the states beyond ms_2 have $g_{\mathrm{B}}^{(2)} \simeq 1-1/n$ with $n \geq 3$, a hallmark signature of Fock states in contrast to coherent states that have $g^{(2)}(0) = 1$.

3.3.3 Spectral signatures of the many-body bound states

Here we consider the experimental observability of the many-body bound states we predicted above. An experimentally relevant quantity in polaron spectroscopy is the quasiparticle residue, defined as

$$Z(E) = \sum_i | \langle \mathrm{GS}_0 | i \rangle |^2 \, \delta(E - E_i) \, , \tag{3.47}$$

where $|i\rangle$ is an eigenstate of the interacting system with energy E_i, and $|\mathrm{GS}_0\rangle$ is the non-interacting ground state. In the case of Bose polarons, the non-interacting ground state consists of an impurity and an unperturbed condensate with no mutual interactions. In contrast, the interacting state is of the form $\hat{\mathcal{O}}_i \, |\mathrm{GS}\rangle$, where $\hat{O}_i$ creates the appropriate excitations of the eigenstate i on top of the interacting ground state.

In Fig. 3.8 (a), the variation of Z across the Feshbach resonance is depicted for each stable states, as well as the Z factor for attractive and repulsive polaron. We observe that although the quasiparticle weights of ms_1 and ms_2 states are higher than the attractive polaron, all the other many-body states have essentially vanishing quasiparticle residue. This observation is compatible with the conclusion that beyond ms_2, the many-body states are well characterized by Fock states $|n\rangle_{\mathrm{B}}$ for $n \geq 3$ with vanishing quasiparticle residue. Furthermore, as the repulsive inter-boson interaction is decreased, the Z factor of attractive

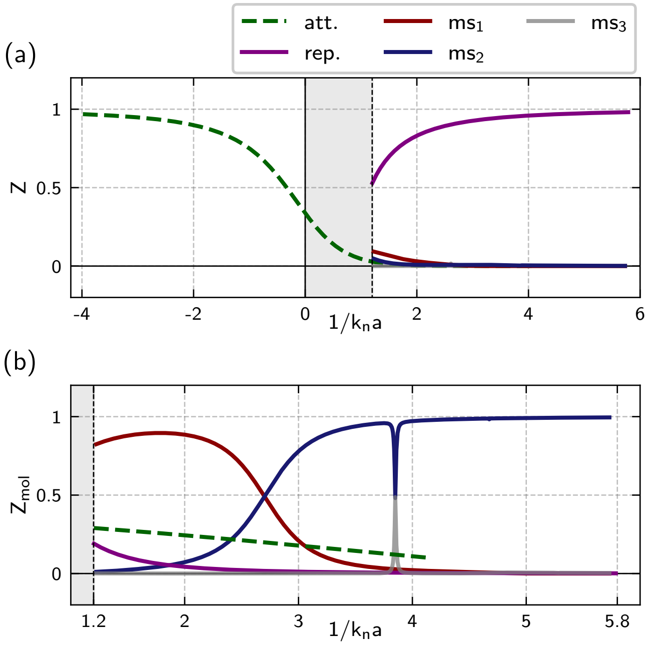

Figure 3.8: (a) Quasiparticle residue of different many-body bound states, compared to the attractive and repulsive polaron. At strong couplings, the quasiparticle residue of attractive polaron and all the many-body bound states are substantially smaller than the repulsive polaron for strong couplings. (b) Molecular quasiparticle residue of the states in (a). The states ms_1 and ms_2 have substantial molecular weight with non-monotonic behavior as a function of $1/k_n a$, in contrast to the prediction for the attractive polaron. The sharp spikes in Z_{mol} of ms_1 and ms_3 occurs at the corresponding level crossing.

polaron and all the many-body bound state excitations decrease due to an increasing number of bound state excitations.

Furthermore, in connection with detecting molecular spectra in ultracold mixtures, a molecular quasiparticle residue can be defined as

$$Z_{\text{mol}}(E) = \sum_n |\langle \text{GS}_{\text{mol}}|n\rangle|^2 \, \delta(E - E_n)\,, \tag{3.48}$$

where $|\text{GS}_{\text{mol}}\rangle$ is a state comprised of an unperturbed condensate and a single impurity-boson dimer. This quasiparticle residue is suggested in [168, 58] to detect molarons and observe polaron-molecule transition in impurity-Fermi systems. Fig. 3.8(b) shows Z_{mol} of the many-body bound states. Interestingly, ms_1 and ms_2 states have substantial Z_{mol}, with the non-monotonous variation with $1/k_n a$ compatible with their bound state occupation number. For the attractive polaron, the magnitude of Z_{mol} is of the same order of magnitude as ms_1, although quantitative differences point to the remaining differences of these variational states. Thus, Z_{mol} can be a sensitive probe for detection of many-body bound states and to elucidate the exact nature of the overall ground state.

The ms_3 state exhibits a vanishing Z_{mol} except for values of $1/k_n a$ close to the level crossing with ms_1 state, where Z_{mol} of both states vary rapidly and coincide at $Z_{\text{mol}} = 0.5$.

3.4 Comparison to the existing methods

As mentioned earlier, the crucial assumption of the variational formalism developed in this chapter is the large separation of energy scales between the dimer binding energy ε_{B} and the typical energy of the Bogoliubov excitations (of the order of μ). This condition is violated close to the unitarity on the repulsive side. The other important assumption concerns the existence of a well-defined unstable Bogoliubov mode on top of the repulsive polaron saddle point, which breaks down in the presence of a dynamical instability.

Variational schemes such as truncated basis methods or Gaussian state theories including boson-boson inteactions are in principle able to surpass these limitations. Truncated basis methods are able to give access to the full excitation spectrum and include multi-body correlations exactly, however, they are limited in the number of particles included in the variational state. In comparison, our approach includes exact correlations only among excitations bound to the impurity and neglects some correlations of excited scattering states, that is suitable for heavy mobile impurities. Nevertheless, it does not restrict the number of excitations included in the ansatz. Gaussian state theories are able to access the exact stable saddle point of the system by optimizing Φ and Γ. However, the states with non-Gaussian correlations are not included in the variational manifold.

An improvement to our ansatz is to include Bogoliubov transformation as a variational parameter, and obtain the modifications of the Bogoliubov spectrum due to the presence of the impurity. This approach has already been incorporated to study the modification of local boson correlations in the vicinity of the impurity [42, 43], and predicted many-body shifts of Efimov states. Including these correlations in our ansatz partially accounts for three-body correlations on a many-body level. However, it is a numerically challenging task to obtain metastable variational solutions and we leave this problem for future research.

3.5 Conclusion and outlook

In this chapter, we addressed the problem of Bose polaron at strong couplings. We introduced a variational scheme that is suitable for the regime when the impurity-boson binding energy is much larger than the BEC chemical potential. We presented a comprehensive theoretical formalism that is sufficiently general to be applicable to dilute and dense bosonic media in any dimensions, ranging from ultracold atomic mixtures to excitonic condensates in semiconductor heterostructures, and include effects that are crucial to describe Bose polarons at strong couplings. We demonstrated that the interplay of impurity-induced instability and repulsive inter-boson interactions leads to the existence of multiple metastable states in the form of many-body bound states with intermediate energies lying between the attractive and repulsive polaron.

Crucially, the existence and properties of the many-body bound states we predict are closely linked to the non-perturbative nature of the problem captured by the higher order interaction processes $\hat{H}_3$ and $\hat{H}_4$, involving three- and four-boson terms, respectively. Within our variational approach, we showed that including the resulting correlations among the bound bosons exactly leads to the emergence of genuine quantum mechanical characteristics of the wave function, especially non-Gaussian correlations and interaction-induced anti-bunching. Furthermore, these many-body bound states can have observable signatures in molecular spectroscopy techniques with quasiparticle weights considerably different from the coherent state theory prediction for the attractive and repulsive polarons.

The improvement to the standard Bose polaron models presented here - by including $\hat{H}_3$ and $\hat{H}_4$ terms, alongside the variational ansatz derived in detail in Appendix 3.2.5 - reveals characteristics of the many-body bound states beyond the predictive scope of the current Bose polaron models. Unlike non-interacting single-channel models, we predict that the number of many-body resonances is finite and varies depending on the impurity-boson and inter-boson interaction strength. Additionally, their binding energies exhibit non-monotonic behavior as a function of particle number, leading to level crossings between the many-body bound states. Near these level crossings, the many-body bound states do not possess a well-defined particle number due to the low-energy particle exchange processes with the condensate.

Furthermore, through the rigorous theoretical analysis detailed in Appendix 3.2.5, we show that the strong-coupling Bose polaron problem can be mapped to the problem of many-body bound states weakly coupled to the renormalized phonon modes. This emergent weak-coupling theory is amenable to perturbative treatments, allowing for further characterization of the many-body resonances, including the determination of lifetimes and decay rates.

The theoretical developments in this chapter present one natural scheme to separate the modes of the strong coupling impurity-boson system into a few strongly interacting modes requiring non-perturbative treatment, and a continuum of weakly interacting modes. With this theory we are able to explore a broad range of parameters and map out the phase diagram of the strong coupling Bose polaron. In particular, we clarified how the attractive polaron continuously evolves into a multi-body bound state as one crosses the Feshbach resonance into the repulsive side. Thereby we arrive at a unified theory of repulsive and attractive Bose polarons.

We emphasize that the theoretical analysis in this chapter applies to a wide range of experimentally relevant Bose polaron settings where mobile impurities have masses comparable or even smaller than the boson masses, as long as the impurity mass is not too light such that three-body correlations lead to dramatic qualitative changes in the polaron spectra such as polaronic instability [42, 43]. Indeed, most of the experimentally relevant mixtures, such as ^{40}K-^{87}Rb (JILA [99]), ^{39}K-^{39}K (Aarhus [108], Cambridge [64]), and ^{40}K-^{23}Na (MIT [220], Munich [61]), exhibit a smooth variation in the attractive polaron energy across the Feshbach resonance. Additionally, the attractive polaron energy, for which the influence of short-range correlations is the strongest, shows excellent agreement with the predictions of the Gross-Pitaevskii theory [92] for the ^{40}K-^{87}Rb and ^{39}K-^{39}K mixtures, where the impurity-boson mass ratio is the smallest. Therefore, the theoretical framework developed here applies to the above settings without the need for extension of the variational ansatz to include three-body correlations by treating the covariance matrix Γ as a variational parameters, as done in Refs. [42, 43]. Nevertheless, the present variational ansatz is capable of incorporating three-body correlations by including Γ as a variational parameter, and promoting the coherent state part of the ansatz in Eq. 3.25 to a Gaussian state or a truncated basis variational state.

Another interesting future direction is to apply the present framework to study strong coupling polarons in one and two dimensions. The intricate physics of polarons in low dimensions, together with the availability of multiple theoretical approaches for benchmarking such as DMRG and exact diagonalization in one dimension and Quantum Monte Carlo in one and two dimensions makes this direction particularly promising.

In the present context, we pointed out the crucial role of phonon nonlinearities on the physics of strong coupling Bose polarons. It would be interesting to expand the scope of the work presented in this chapter by considering other models where phonon nonlinearities play a crucial role, for instance, to study impurity motion in nonlinear bosonic models with non-perturbative solitonic excitations (e.g. in the Ferenkel-Kontorova model [28], or models described by the nonlinear Schrodinger equation [114]). As another avenue, one could apply this framework to study the motion of single holes in quantum antiferromagnets [112, 214, 22] or the formation of magnon-impurity bound states [51].

In conclusion, the developments presented in this chapter highlight the intriguingly rich physics of many-body resonances in strong-coupling Bose polarons and point toward the need for further theoretical research to clarify the remaining unknown aspects of these resonances. On the experimental side, the distinct behavior of the molecular quasiparticle residue encourages the exploration of bold signatures of these states by going beyond the conventional spectroscopic techniques.

Chapter 4

Realization of anyonic trions in van der Waals heterostructures

In the previous chapter, we were mostly concerned with the physics of a heavy impurity interacting with bosonic particles in a BEC. The many-body system in this case, although ubiquitous and of prime interest in numerous synthetic quantum systems platforms, is a well understood system, in the sense that there is a vast body of theoretical works that investigate the physics of weakly interacting Bose gases. Moreover, the experimental advancement in preparation and manipulation of such ultracold gases is phenomenal by now, and posses an extremely advanced and powerful toolbox.

At the same time, current research efforts across multiple fields, from quantum science and technology to condensed matter physics, focus on the realization of strongly correlated phases of matter that demonstrate exotic characteristics such as long-range entanglement and topological order. This is largely due to the presence of anyonic excitations of these states, which hold promise in realizing topological quantum computation, a form of quantum computation that is robust to noise [153], and by themselves feature exotic physical properties. Nevertheless, there are incredible challenges in experimental realization of such phases, since they have a very subtle structure of quantum mechanical superpositions between an exponential number of many-body configurations, giving them their genuine quantum mechanical nature and their intricate characteristics.

In 1982, Tsui, Stormer and Gossard [205] discovered a new phase of matter, the FQH liquid, that defies classification according to Landau's paradigm, as it does not break any symmetry when compared to normal Fermi liquids, but it exhibits a markedly different transport response: the fractional quantum Hall effect (FQH). In 1990, the concept of topological order was introduced by Wen [211] as a new type of order characterizing FQH liquids. Since then, classification of phases of matter according to topological order has been largely recognized as a distinct paradigm alongside Landau's symmetry breaking framework. In Landau's classification of phases according to symmetry breaking, phases realized with different symmetries in a system for different parameter sets can not be transformed to one another by continuous change of parameters without encountering a singularity in the free energy - a phase transition. In contrast, topological order is defined for systems with gapped ground states and is characterized by certain topological invariants (in the case of FQH states, this topological invariant is the ground state degeneracy on a torus). Two topologically ordered states belong to the same universality class if they can be transformed to one another by smooth deformation of the Hamiltonian without closing the gap.

Aside from strange properties of their ground states, topologically ordered states posses anyonic excitations as their low energy excitations. Such anyonic excitations are fundamental ingredients needed to construct topological qubits [153]. This requirement has initiated intense research efforts to realize and control anyons in various synthetic quantum settings such as solid-state platforms and digital quantum processors. On digital quantum processors, braiding of both abelian and non-abelian anyons have been realized [173, 103]. In solid-state experiments, signatures of anyons and their fractional charge and statistics have been observed by means of various anyon interferometry techniques [17, 152, 77, 172, 107, 126, 171]. In other synthetic platforms, efforts have been made to realize analogues of fractional quantum Hall states for atoms [127], and photons [44]. When anyons are potentially realized in such analogue quantum simulation platforms, it is possible to gain spatial control over their position via the well-developed tools in ultracold atom experiments, to directly create anyons and perform direct braiding in its most basic form. Nevertheless, such systems suffer from severe finite size effects, thus the generalization of the concepts and results available for continuum FQH systems in thermodynamic limit to such finite sized systems is not straightforward. This problem is especially tricky since topological properties are well defined in the thermodynamic limit. On the other hand, in solid-state platforms, FQH states in the thermodynamic limit are far more straightforward to realize. However, direct control over position and motion of anyons remains an arduous task.

Impurity binding as a means of detection and control of fractional excitations of a strongly correlated synthetic topological system has been studied in previous theoretical works [229, 150, 137, 83, 89], mostly targeting cold atomic systems, where there is a potential to realize mesoscopic scale fractional quantum Hall fluids. Since in cold atoms, the synthetic magnetic field is realized by rotating the atoms using laser light, the impurity is naturally experiencing the same artifical gauge field as the majority atoms, and thus, its motion is quantized in Landau levels. Besides, many of these proposals are addressing the impurity-quantum Hall systems in idealized settings where the gap to the excited states is assumed to remain open even in the interacting system, an assumption which is suitable for heavy impurities and theoretically accurate when Born-Oppenheimer approximation is valid. On the other hand, fractional quantum Hall states of electrons are ubiquitious in van der Waals semiconductor heterostructures, where these states can also be addressed optically.

In this chapter, we study a solid-state setup in the form of an atomically thin graphene-transition metal dichalcogenides (TMD) heterostructure, to optically investigate fractional quantum Hall states and to explore the creation of anyons in an optically controlled manner. The heterostructure consists of an hBN-encapsulated graphene monolayer in the proximity of a $MoSe_2/WSe_2$ heterobilayer in a strong perpendicular magnetic field. The carrier density in graphene is gate-tunable, where $\nu = 1/3$ FQH states of electrons and holes can be realized [24]. In addition, interlayer excitons (IX) can be created in the TMD heterobilayer, where the type-II band alignment makes the electron (hole) reside in the $MoSe_2$ (WSe_2) layer [170], see Fig. 4.6 (a). Depending on the IX configuration and the carrier charges, the IX-carrier interaction can be either attractive or repulsive (Fig. 4.6 (a)).

Inspired by the developments in Ref. [86], we make use of a unitary transformation, called the Lee-Low-Pines (LLP) transformation to address the problem of a mobile exciton interacting with a many-body system comprised of electrons forming a $\nu = 1/3$ fractional quantum Hall state. The reduction in the complexity of the problem, enabled by the LLP transformation leads us to the observation of two bound states between an exciton and excitations of the quantum Hall system, at fillings corresponding to a single quasihole on top of the Laughlin state. We identify the lower energy bound state as an anyonic trion, a bound state of an exciton and the quasihole.

We first focus on the attractive IX-hole interaction in the few-body limit, where only a single hole is present in the graphene valence band. By solving the three-body problem of an electron and two holes residing in the $MoSe_2$, WSe_2 and graphene, respectively, we find that the three-body spectrum contains a bound IX-hole state, that is an *interlayer magnetic trion*. The existence of this state is interesting since in the absence of a magnetic field, IX can not bind massless graphene quasiparticles. Thus, the formation of interlayer magnetic trions is a direct consequence of the effect of a magnetic field on the few-body spectrum of the system. Inspecting the trion state shows that the contribution of excited IX Rydberg states are negligible, due to the large $1s$ IX binding energy. Furthermore, we find that the admixture of higher hole Landau levels is negligible, justifying a lowest Landau level approximation for the many-body problem.

4.1 Strongly correlated electronic states in van der Waals heterostructures

Semiconductor materials form the foundational platform for electronics from the beginning of its history [6]. In semiconductor electronic devices, through variation of chemical composition with position, it is possible to adjust the local electrostatic potential felt by the electrons, and thus control their transport. Such semiconductor structures are called *heterostructures*, a celebrated example of which is the $p-n$ junction, used in various forms of diodes (e. g. LEDs, varactors, photodiodes), transistors and many other electronic devices. Heterostructures allow the investigation of electronic transport in low dimensional mesoscopic semiconductor heterostructures, a well-established field encompassing numerous research areas. Confinement of electron motion in low-dimensional geometries such as quantum dots (0D), quantum wires (1D) and quantum wells and inversion layers (2D) leads to the quantization of electronic states, which are electrically and optically accssible.

By 2004, various heterostructure geometries such as III-V semiconductor quantum wells

[1] were extensively studied. In 2005, mechanical exfoliation of graphite led to the experimental realization of graphene [155]. Later, the mechanical exfoliation techniques were extended to create atomically thin monolayers of other types of crystals, where stacks of monolayers are held together via the weak van der Waals interlayer interaction. The van der Waals interaction further allows to stack different types of monolayers and form multilayer structures, leading to the construction of van der Waals (vdW) heterostructures. The extreme confinement of electrons in these heterostructures and the high carrier mobility, together with the possibility of engineering band structures for these materials made the research on vdW materials into a vibrant and flourishing field [74, 9].

The particular appeal of the research on vdW heterostructures is the possibility of realizing strongly correlated electronic states - such as unconventional superconductivity [32], quantum spin Hall effect [217] and correlated insulator states [31], among a multitude of others.

In this chapter, the emphasis is on optical spectroscopy of fractional quantum Hall states of a graphene monolayer using interlayer excitons in a proximate heterobilayer of transition-metal dichalcogenides (TMD). Below we outline physics of these materials relevant for our purposes.

4.1.1 Graphene

Graphene is a monolayer 2D material exfoliated from bulk graphite, and is composed of carbon atoms arranged in a hexagonal lattice. The Fermi level of undoped graphene is located at the Dirac points in the K and K' points of the hexagonal Brillouin zone (see Fig. 4.2). Thus, the low energy quasiparticle excitations of the graphene are massless Dirac fermions, giving graphene its unique transport properties [34, 53].

The band structure of electrons close to the Fermi surface can be understood by considering the chemical composition of graphene [78]. A carbon atom C has 6 electrons, arranged in an electronic configuration $[\mathrm{He}]\,2s^2\,2p^2$. The $2p$ manifold is ~ 4 eV higher in energy that the $2s$ manifold (note that each electronic state contains 2 electrons with both spin-down and spin-up configurations). To form covalent bonds with other atoms, it may be more energetically favorable to excite an electron in the $2s^2$ orbital to the $2p_z$ orbital. The remaining three electrons in the $2s$, $2p_x$ and $2p_y$ orbitals form sp^2 hybridized orbitals, which are located $2\pi/3$ with respect to one another. Two carbon atoms can form a molecule by a $\sigma-$bond (a covalent bonding which is rotationally symmetric with respect to the inter-nuclear axis). This $\sigma-$bonding results in the hexagonal lattice structure of the monolayer graphene. The remaining electrons per carbon atom in $2p_z$ orbitals are fully delocalized in the $\pi-$bonds across the crystal. In addition, each graphene unit cell contains two carbon atoms, whose $2p_z$ orbitals can form bonding ($\pi-$bond) or antibonding (π^*-bond) configurations. In the presence of only the nearest neighbor hopping, resulting energy bands are particle-hole symmetric, with dispersion $\epsilon_\lambda(\mathbf{k}) = \lambda\epsilon(\mathbf{k})$, where $\lambda = +$ for

---

[1] The III-V quantum wells are formed out of layers composed of group III and group V elements of the periodic table. The most typical group III elements used in heterostructures include Gallium(Ga), Aluminium (Al) and Indium (In), and group V include Arsenic (As) and Phosphorus (P) [175].

(a)

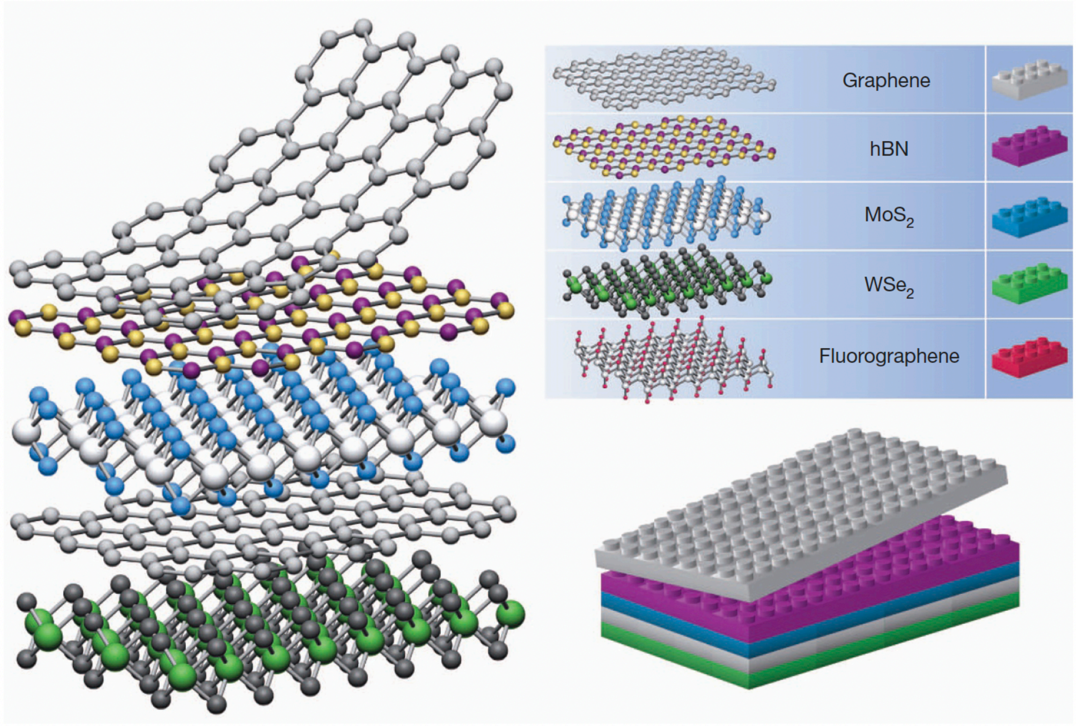

(b)

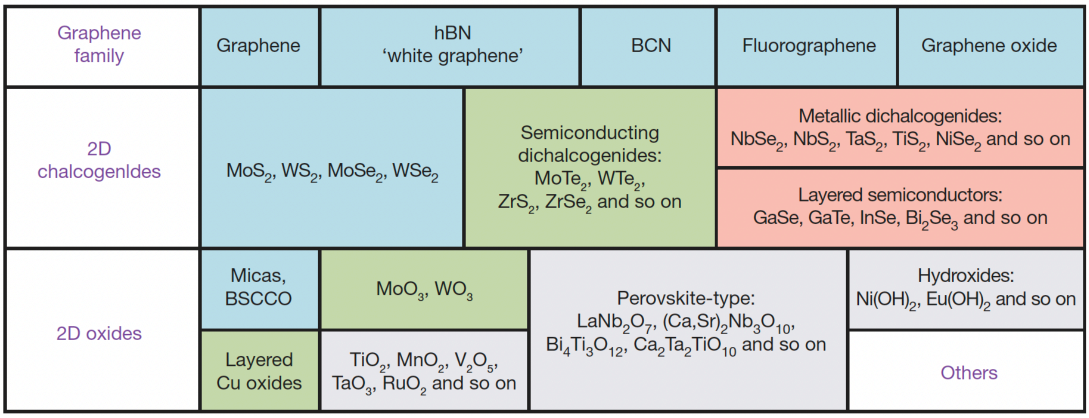

Graphene family	Graphene	hBN 'white graphene'	BCN	Fluorographene	Graphene oxide
2D chalcogenldes	MoS_2, WS_2, $MoSe_2$, WSe_2		Semiconducting dichalcogenides: $MoTe_2$, WTe_2, ZrS_2, $ZrSe_2$ and so on	Metallic dichalcogenides: $NbSe_2$, NbS_2, TaS_2, TiS_2, $NiSe_2$ and so on Layered semiconductors: GaSe, GaTe, InSe, Bi_2Se_3 and so on	
2D oxides	Micas, BSCCO Layered Cu oxides	MoO_3, WO_3 TiO_2, MnO_2, V_2O_5, TaO_3, RuO_2 and so on	Perovskite-type: $LaNb_2O_7$, $(Ca,Sr)_2Nb_3O_{10}$, $Bi_4Ti_3O_{12}$, $Ca_2Ta_2TiO_{10}$ and so on	Hydroxides: $Ni(OH)_2$, $Eu(OH)_2$ and so on Others	

Figure 4.1: (a) By stacking different monolayers exfoliated from different types of crystals, van der Waals multilayer structures can be made. The multilayer structure is put together due to the weak van der Waals force between the layers. (b) Example crystals from different families of material heterostructures. Different color codes indicate the stability of the monolayers in various circumstances: stable under ambient conditions (blue), probably stable in air (green), unstable in air but potentially stable in the absence of reactive gases (pink). Monolayers have been sucessfully exfoliated from the materials shaded with grey. Figure is reprinted from Ref. [74].

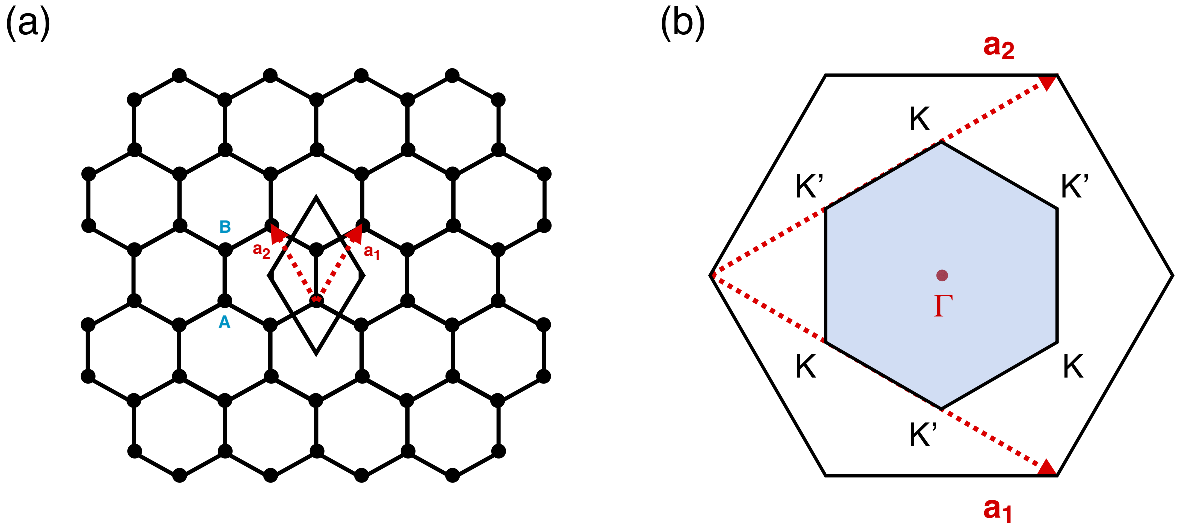

Figure 4.2: (a) Hexagonal lattice structure of graphene. The unit cell (denoted by the rhombus) consists of two inequivalent lattice sites A and B. The lattice vectors are denoted by $\mathbf{a}_1$ and $\mathbf{a}_2$. (b) The Brillouin zone of the hexagonal lattice with the K and K' points.

the π^* band and $\lambda = -$ for the π band [78]. Since there are only two electrons per unit cell, the $\lambda = -$ $(\lambda = +)$ band is completely full (empty). The two bands touch at the K and K' points where they form Dirac cones, at momenta $\mathbf{K}$ and $-\mathbf{K}$ at the corners of the Brillouin zone, respectively. The low energy excitations close to the K (K') valley have momenta $\mathbf{k} = \pm\mathbf{K} + \mathbf{q}$, where $+$ $(-)$ is used for the K (K') valley. If we denote the valley pseudo spin by the Pauli matrices $\hat{\tau}_\mu = (\hat{\mathbb{I}}, \hat{\tau}_x, \hat{\tau}_y, \hat{\tau}_z)$, then the effective Hamiltonian close to the Dirac points reads

$$\hat{H}(\mathbf{q}) = \hbar v_{\mathrm{F}}\, \hat{\boldsymbol{\tau}} \otimes \mathbf{q} \cdot \hat{\boldsymbol{\sigma}}\,. \tag{4.1}$$

Hereafter, since we work with strong magnetic fields, we assume spin polarized electrons. Since valley physics is also not important for us, we further assume full valley polarization in the K valley. Thus, the Hamiltonian reduces to

$$\hat{H}_K(\mathbf{q}) = \hbar v_{\mathrm{F}}\, \mathbf{q} \cdot \hat{\boldsymbol{\sigma}}\,. \tag{4.2}$$

In a magnetic field, according to Peierls substitution, the momentum $\hat{\mathbf{q}}$ (which now is promoted to an operator) is substituted by the gauge invariant kinetic momentum $\hat{\boldsymbol{\Pi}}$ (see Appendix C for the definition of the kinetic and magnetic momenta). Thus, the kinetic Hamiltonian in the magnetic field takes the form

$$\hat{H}_K(\hat{\boldsymbol{\Pi}}) = \hbar v_{\mathrm{F}}\, \hat{\boldsymbol{\Pi}} \cdot \hat{\boldsymbol{\sigma}}\,. \tag{4.3}$$

Expressing $\hat{\mathbf{\Pi}}$ in terms of the associated creation and annihilation operators, the eigenstates of $\hat{H}_K(\hat{\mathbf{\Pi}})$ are given by

$$|\psi_{n,m}\rangle = \frac{1}{\sqrt{2}} \begin{pmatrix} |n-1, m\rangle \\ |n, m\rangle \end{pmatrix} , \tag{4.4}$$

where as usual, n is the Landau level index and m is the magnetic momentum quantum number. The positive energy states have energies $\varepsilon_{n,m} = \sqrt{2n}\,\hbar v_{\mathrm{F}}/l_{\mathrm{B}}$. These results will be essential in finding the few-body states of the IX scattering off a carrier in the strong magnetic field.

Having reviewed few aspects of the electronic states in graphene which are relevant to the present work, we move to give an introduction about transition metal dichalcogenide vdW heterostructures, which have enabled to do quantum optics with strongly correlated electronic systems in a highly controllable fashion.

4.1.2 Transition metal dichalcogenides: quantum optics meets strongly correlated electronic systems

As brought in Fig. 4.1, transition metal dichalcogeneides form another important group of vdW materials [209]. Their chemical composition consists of a transition metal atom (typically Mo, W) bound to two chalcogen atoms (typically S, Se, Te), arranged in a hexagonal crystal with D_{3h} symmetry (see Fig. 4.3). In the monolayer limit, these materials are direct band gap, and as such are optically active. Furthermore, the strong spin-orbit splitting of the valence band leads to optical selection rules, stating that the transitions in the K (K') valley can be excited only by σ^+ (σ^-) circularly polarized light.

The optical excitations in semiconductors are in the form of tightly bound excitons. Excitons are electron-hole pairs, which are bound together as a result of the Coulomb interaction. They form the elementary optical excitations in the TMD materials. The reason for large binding energy of excitons in these materials is the tight 2D confinement of the charge carriers, together with the reduced dielectric screening of the environment (the electric field generated by an electron-hole pair penetrates the surrounding space, which leads to a more efficient binding). The reduced dielectric screening, together with large carrier effective masses ($m_e^* \simeq 0.8\, m_0$ in MoSe$_2$) leads to sharp excitonic resonances in these materials with a large binding energy ($\simeq 512$ meV in MoSe$_2$). In the presence of electrons, either in the same layer as the exciton, or in the proximate layers, the electric field of the environment affects the exciton binding, and leads to the modification of its binding energy, polarization, and other characteristics. Since this resonance is very sharp and strong (as compared to excitonic resonances in more standard GaAs based quantum wells, where the exciton binding energy ~ 10 meV), its sensitivity to the electronic environment can be used as a probe for many-body physics in the proximate electronic system. In the following, we touch upon the exciton spectra in doped systems, which can be explained by means of Fermi polaron physics.

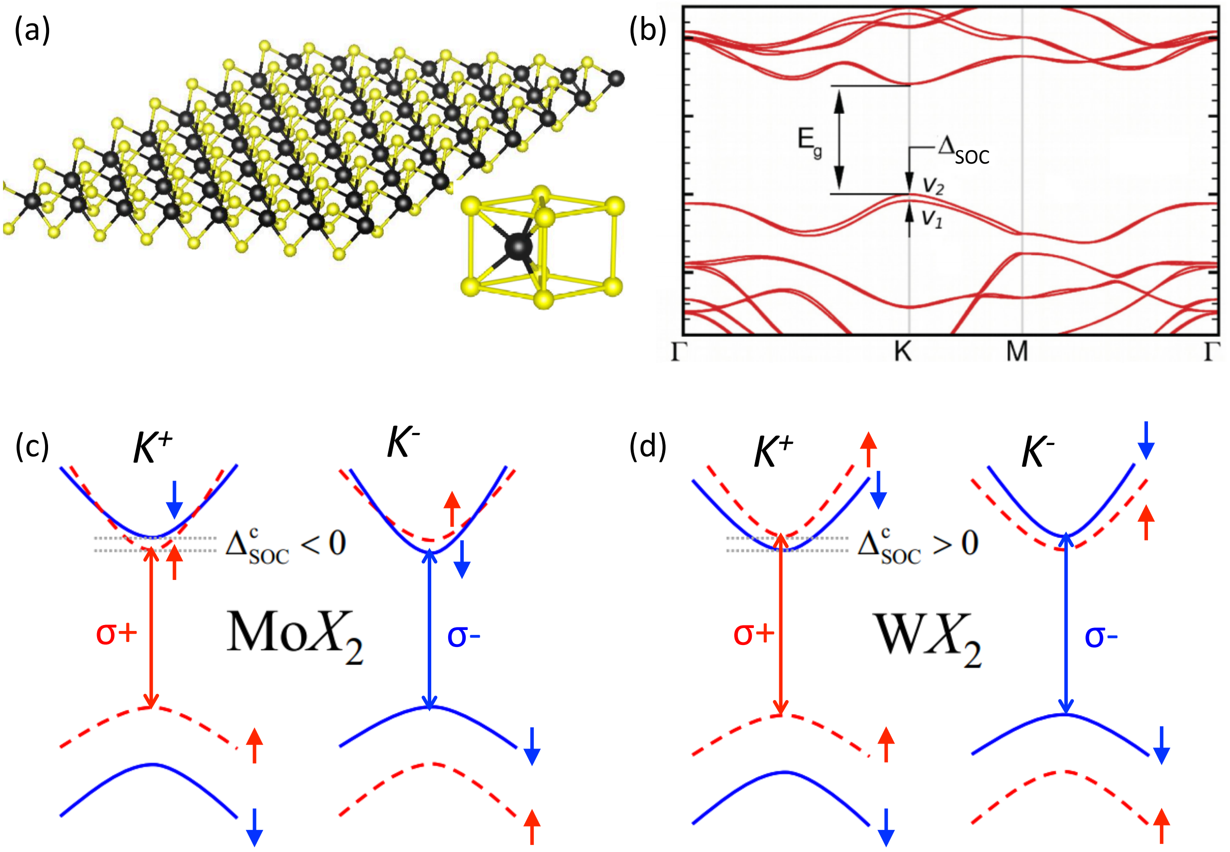

Figure 4.3: (a) Crystal structure of TMD materials in the monolayer form. The unit cell contains a transition metal atom (black) and two chalcogen atoms (yellow). (b) In monolayer, TMDs admit a direct band gap in the K (shown in the figure) and K' points. The spin-orbit splitting Δ_{soc} is strongest in the valence band, while in the conduction band it is much smaller. (c) and (d) Qualitative band structure near K and K' points in $\mathrm{MoX_2}$ (c) and $\mathrm{WX_2}$ (d) monolayers. Figure reprinted from Ref. [209].

4.2 Exciton Fermi polarons dominate the optical spectra of doped TMDs

The idea of probing correlations of the electronic states of vdW heterostructures using TMD excitons gained significant interest after the observation of attractive and repulsive exciton-Fermi polaron resonances in electron and hole-doped TMDs [188]. The experimental setup in this experiment is a classic example for experiments set up to observe exciton-Fermi polaron effect. The device consists of an hBN-encapsulated $\mathrm{MoSe_2}$ monolayer, gated by the gold contacts and doped via the graphene layer on top. The whole heterostructure is placed between two Distributed Bragg Reflector (DBR) mirrors, which constitute a high finesse cavity. The monolayer TMD is placed on the antinode of the cavity mode, to efficiently hybridize the excitons with the cavity mode, see Fig. 4.4, left side, panel (a). In the low doping limit, it is known that a single electron on the Fermi surface can polarize the exciton, such the exciton-electron interaction becomes attractive. Since the system is tightly confined in 2D, the attractive two-body potential always leads to the formation of a bound state. The exciton electron bound state is typically called *a charged exciton* or a *trion*. Thus, at low dopings excitons can bind electrons and form trions. But at higher dopings, when the inter electron distance (characterized by the electron density $1/\sqrt{n_e}$ is comparable to the trion Bohr radius, the excitons gain energy by forming a coherent superposition of trions with the electrons on the Fermi surface, leading to dressing by coherent electron-hole excitations of the Fermi sea [102], and formation of *an attractive exciton-Fermi polaron*. The formation of attractive exciton-Fermi polarons comes hand in hand with another quasiparticle excitation, *the repulsive exciton-Fermi polaron*, which can be understood as a blue-shifted exciton resonance, dressed by a repulsive cloud of electron-hole excitations (see Fig. 4.4, left side, panel (c)).

In the experiment of Ref. [188], the hybridization of the exciton with the cavity mode leads to the formation of exciton-polariton Fermi polaron. However, the signatures of the Fermi polaron formation is also evident in reflectance spectroscopy experiments, such as the one on the right hand side of Fig. 4.4. In these experiments, the measured signal is *the reflectance contrast* ΔR, defined as the ratio of the difference in the reflectance signal with respect to the background reflectance,

$$\Delta R(E) = \frac{R(E) - R_0(E)}{R_0(E)}\,, \tag{4.5}$$

where E is the photon energy. The reflectance contrast is a direct measure of the absorption in the material, since the fraction of the intensity that is not reflected is absorbed. The reflectance contrast in a vdW device similar to the one in Ref. [188] is shown in the right hand side of Fig. 4.4. This device is used in the experiment of Ref. [192] to measure the interaction-induced Shubnikov de Hass oscillations in the optical response of monolayer $MoSe_2$. In the absence of the magnetic field, the reflectance spectrum shows hallmarks of the exciton-polaron formation in the doped regime. As is plotted in panel (b) of Fig. 4.4, in the charge neutral regime, a sharp exciton resonance appears. When the device is electron or hole doped, two spectral features are notable: a sharp resonance appears abruptly on the red side of the bare exciton resonance, which blueshifts with electron doping. The resonance gains oscillator strength as the doping is increased, and is associated to the attractive exciton polaron. the blueshift of the attractive exciton polaron is due to the increase in the Fermi energy, which increases both the resonance position of the exciton and the electron energy on the Fermi surface. The other resonance is continuously connected to the bare exciton. It also blueshifts with doping and loses oscillator strength. This resonance corresponds to the repulsive exciton polaron.

The above spectral features in the optical conductivity of doped monolayer TMDs can be adequately explained by the theory of Fermi polaron formation in two dimensions. Exctions by nature are delocalized excitations that have a dipole and carry momenta. Although excitons are themselved composite objects, due to the large exciton binding energy which is by far the largest energy scale in the system, they can be treated as pointlike particles with creation operator $\hat{x}^\dagger_{\mathbf{k}}$. Furthermore, due to the spin-valley locking in TMDs, excitons in a valley interact attractively (repulsively) with electrons in the opposite (same) valley. To understand this, assume an exciton in the K valley of MoSe$_2$, which is composed of a spin-$\uparrow$ electron and a spin-$\downarrow$ hole. An electron in the opposite valley can gain energy from the Coulomb exchange interaction (it can recombine with the hole of the exciton), which leads to an attractive interaction [45]. The attractive exciton electron interaction leads to the formation of a bound state in two dimensions, which is the trion. In a classical picture, trions can gain binding energy by polarizing excitons, attracting the exciton's hole and repelling the exciton's electron. Polarizing the exciton means that the exciton-electron interaction excites the exciton to excited intermediate Rydberg states, where the electron hole separation is larger, and as a result, the exciton dipole is stronger. However, these processes are relevant only in second order perturbative corrections to the trion binding energy in terms of E_T/E_X, the ratio of the trion binding energy to the exciton binding energy. Thus, the exciton electron interaction can be modelled by a two-body potential. The Hamiltonian to describe this system reads

$$\hat{H} = \sum_{\mathbf{k}} \varepsilon_{X,\mathbf{k}}\, \hat{x}^\dagger_{\mathbf{k}} \hat{x}_{\mathbf{k}} + \sum_{\mathbf{k}} \varepsilon_{c,\mathbf{k}}\, \hat{e}^\dagger_{\mathbf{k}} \hat{e}_{\mathbf{k}} + \sum_{\mathbf{k},\mathbf{q},\mathbf{p}} g_{\mathbf{q}}\, \hat{x}^\dagger_{\mathbf{k}} \hat{x}^\dagger_{\mathbf{k}+\mathbf{q}}\, \hat{e}^\dagger_{\mathbf{p}} \hat{e}_{\mathbf{p}-\mathbf{q}} \,, \tag{4.6}$$

where $\varepsilon_{X,\mathbf{k}}$ and $\varepsilon_{c,\mathbf{k}}$ are the exciton and conduction band electron dispersions, respectively, and $g_{\mathbf{q}}$ is the electron-exciton interaction strength. It turns out that the spectrum of this system can be very well described by assuming a variational ansatz for the eigenstates of $\hat{H}$, the so called *Chevy ansatz* [39, 50, 143, 179]

$$|\phi_{\mathbf{k}}\rangle = \left(\varphi_{\mathbf{k}} \hat{x}^\dagger_{\mathbf{k}} + \sum_{\mathbf{p},\mathbf{q}} \varphi_{\mathbf{kpq}}\, \hat{x}^\dagger_{\mathbf{k}-\mathbf{p}-\mathbf{q}} \hat{e}^\dagger_{\mathbf{p}} \hat{h}^\dagger_{\mathbf{q}} \right) |\emptyset\rangle \;, \tag{4.7}$$

where $|\phi_{\mathbf{k}}\rangle$ is approximating an eigenstate of $\hat{H}$ with momentum $\mathbf{k}$. the Chevy ansatz was first introduced to study the normal state of highly imbalanced Fermi gases. Despite its simplicity, provides excellent predictions for many properties of the two dimensional Fermi polarons in the context of exciton-electron systems. Its success comes back to a nearly perfect cancellation of the contribution of states with more than one particle-hole pair as a result of destructive interference [207, 165, 46]. Intuitively, the Chevy ansatz describes a polaron state as a coherent superposition of a bare exciton with particle-hole fluctuations of the Fermi sea. It was also discovered that application of the Chevy ansatz is equivalent to a non self consistent diagrammatic approach [47].

All in all, the Chevy ansatz, though increadibly successful in predicting the results for a single exciton interacting with non-intercting electrons in a Fermi sea, and can describe polaron response to weak external field. For instance, it can explain the changes in polaronic features due to the effects of a weak magnetic field on the Fermi surface, which leads for instance to the Shubnikov de Haas oscillations of the optical conductivity [192]. However, it can not be applied a priori to settings such as polaron formation in strongly interacting settings, such as FQH systems, or electronic states in flat bands, due to the relevance of inter-electron interactions in these systems, and the absence of a kinetic energy scale, such as the Fermi energy, for electrons. In this thesis, where we are interested in polaron formation in a FQH setting, which is by nature a strongly correlated system. Thus, it is essential to go beyond the Chevy ansatz to describe the physics of a mobile impurity interacting with the excitations of a FQH system. Before delving into the physics of polaron formation in FQH systems, it is necessary to review the basics of the FQH effect. We cover this topic in the next section.

4.3 The Hall Effect: quantum, integer, and fractional

Hall effect was discovered by the Americal physicist Edwin Hall in 1879 [95]. It occurs when a two dimensional current is subject to a perpendicular magnetic field. In this situation, a voltage V_{H} transverse to the current I appears between the two edges of the current-carrying slab, that is proportional to the current. The proportionality constant is called *the Hall resistance* R_{H}, defined by

$$R_{\mathrm{H}} = \frac{V_{\mathrm{H}}}{I} \,. \tag{4.8}$$

The Hall effect has a simple explanation based on the balance of the electric and magnetic components of the Lorentz force. For a two dimensional gas of non-interacting classical charge carriers with charge q with density n, *the Hall resistivity* ρ_{H} (which is equal to the Hall resistance assuming a uniform current density) is the ratio between the transverse electric field $E_{\perp}$ and the current density $J_{\parallel}$,

$$\rho_{\mathrm{H}} = \frac{E_{\perp}}{J_{\parallel}} = \left(\frac{1}{qnc}\right) B \,. \tag{4.9}$$

Thus, ρ_{H} is linear as a function of B with a proportionality constant $1/qnc$, which depends on the density and sign of carriers. It took almost a century until von Klitzing, Dorda and Pepper discovered *the integer quantum Hall (IQH) effect* [118]. It was discovered that R_{H} is quantized in plateaus according to

$$R_{\mathrm{H}} = \frac{h}{ne^2} \,. \tag{4.10}$$

Its origin goes back to the quantization of two dimensional electronic states into Landau levels in strong magnetic fields is low disorder samples (see Appendix C for a comprehensive review on the quantum theory of charged particles in a magnetic field). However, a finite but small amount of disorder is needed for the stability of the plateau. The further details on the physics of the IQH effect can be found in many textbook on the subject [29, 224, 105, 37, 65]. Briefly, the electronic kinetic energy becomes quantized in macroscopically degenerate Landau levels, which are manifolds spaced in energy by $\hbar\omega_{\mathrm{B}}$, where ω_{B} is the cyclotron frequency. The edges act as potentials to lift the Landau levels to the Fermi surface. When the Fermi level resides between Landau levels n and the $n + 1$, there are n

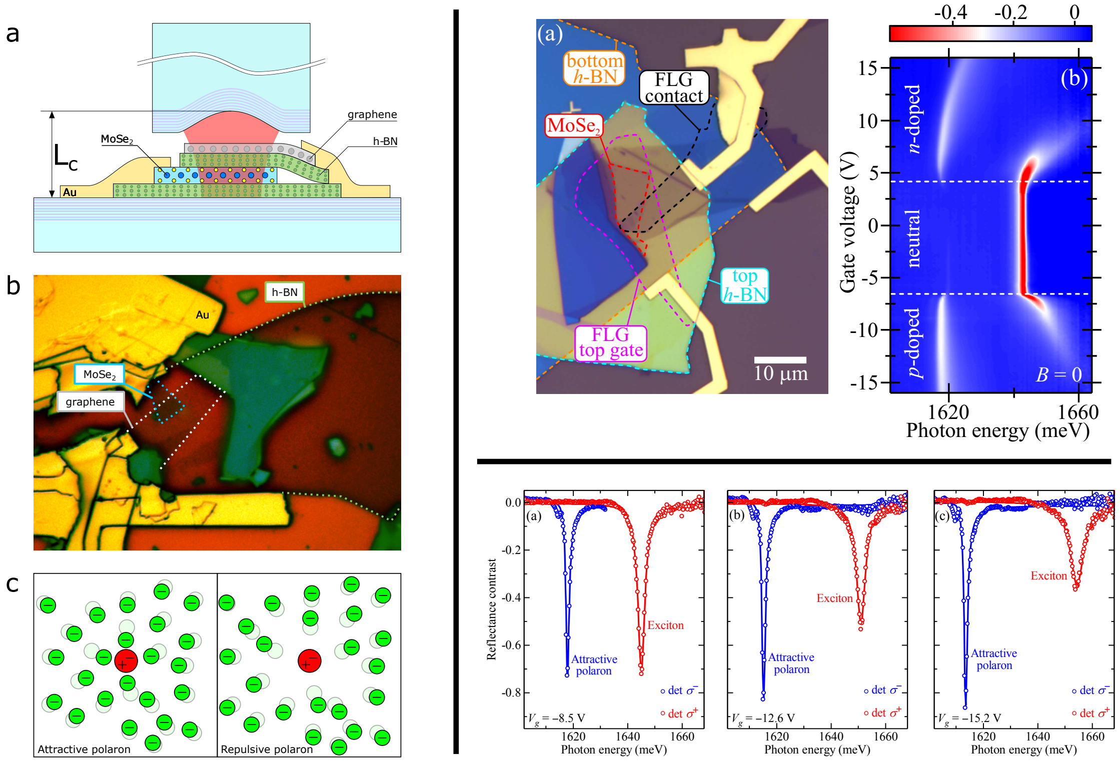

Figure 4.4: Left side: (a) Schematic of the device used for optical spectroscopy of an hBN-encapsulated MoSe$_2$ monolayer. The gold contacts control the electric potential of the layers. The graphene layer is used to dope the heterostructure. The MoSe$_2$ monolayer is at the antinode of a Distributed Bragg Reflector (DBR) cavity, whose frequency is tunable by changing the cavity length L_c via a piezoelectric device. (b) Optical microscope of the device. (c) Cartoon depicting the electron density around the exciton in an attractive and repulsive polaron state. Figures on the left side are reprinted from Ref. [188]. Top right: (a) a similar device structure, used to observe Shubnikov de Haas oscillations in the exciton-polaron spectra in Ref. [192]. (b) Gate tunability of the exciton spectrum, appearing in the reflectance contrast. In the charge neutral regime, a sharp excitonic resonance exists, that does not change by the gate voltage. In the electron or hole doped regime, excitons get dressed by electron-hole excitations of the Fermi sea and form Fermi polarons. The attractive polaron branch (red shifted in energy) appears alongside the repulsive polaron branch, which is connected to the bare exciton resonance. The sharp blueshift of the repulsive polaron resonance can be used as a probe of the electron density. Bottom right: The reflectance contrast as a function of the gate voltage. in the hole doped side, the attractive polaron resonance is less sensitive to the changes in the hole density rather than the electron density, due to the heavy mass of the hole, while the repulsive polaron resonance (indicated also as exciton) blueshifts and loses oscillator strength by increasing the hole doping. Figures on the right side are reprinted from Ref. [192]

edge channels through which current can be conducted. These conducting edge states are responsible to give R_{H} its quantized values h/ne^2.

A few years later , Tsui, Störmer and Gossard discovered the FQH effect in samples with even lower disorder and in stronger magnetic fields. It was ovserved that the transverse resistivity acquires plateau only in certain odd-denominator fractional filling of the lowest Landau level, while the longitudinal resistivity drops to zero, an effect similar to the IQH effect, but with a marked difference that the only energy scale in the problem is the Coulomb interaction energy between the charge carriers, as the kinetic energy is fully quenched due to the strong magnetic field. The theoretical explanation of the FQH is far richer than the IQH which only relies on a non-interacting model for electrons, and has led to many groundbreaking developments in condensed matter physics. Excellent pedagogical presentations of the topic can be found in textbooks [29, 224, 105, 37, 65, 71, 213]. In the rest of this chapter, we only briefly touch upon the known results in the literature, and do not intend to give a pedagogical exposition to the fundamentals. Nevertheless, to enable the readers to convenienty reproduce the results of this thesis from scratch, we give a thorough exposition to the analytical background necessary for the calculations involved in the theory of FQH effect in Appendix C. In the following, we touch upon the basics of the FQH physics.

4.3.1 Basics of the FQH effect

As mentioned above, the FQH effect occurs when the electron system partially occupies the lowest Landau level manifold. The Hamiltonian of N spin-polarized particles with charge q and mass m in a perpendicular magnetic field, interacting via a two-particle potential $V(\mathbf{x})$ is given in first quantization by

$$\hat{H} = \sum_{i=1}^{N} \frac{\hat{\mathbf{\Pi}}_i^2}{2m} + \sum_{i<j}^{N} V(\hat{\mathbf{x}}_i - \hat{\mathbf{x}}_j)\,, \tag{4.11}$$

where $\hat{\mathbf{\Pi}}_i = \hat{\mathbf{p}}_i - (q/c)\mathbf{A}(\hat{\mathbf{x}}_i)$ is the kinetic momentum (Appendix C), and $\mathbf{A}(\mathbf{x})$ is the magnetic vector potential. When all the particles are in the lowest Landau level, The kinetic energy term plays no role, and the physics is entirely governed by the interaction term, projected on the lowest Landau level,

$$\hat{H}_{\mathrm{FQH}} = \hat{\mathcal{P}}_{\mathrm{LLL}} \left(\sum_{i<j}^{N} V(\hat{\mathbf{x}}_i - \hat{\mathbf{x}}_j) \right) \hat{\mathcal{P}}_{\mathrm{LLL}} \tag{4.12}$$

where $\hat{\mathcal{P}}_{\mathrm{LLL}}$ is the lowest Landau level projection operator. The whole problem is now to obtain the low energy states of the Hamiltonian $\hat{H}_{\mathrm{FQH}}$ and characterize their properties. The difficulty here is that the whole effect is non-perturbative, and the problem has to be solved exactly for a thermodynamically large number of particles. Thus, the explanation of FQH effect seemed exceptionally challenging at the beginning of its discovery.

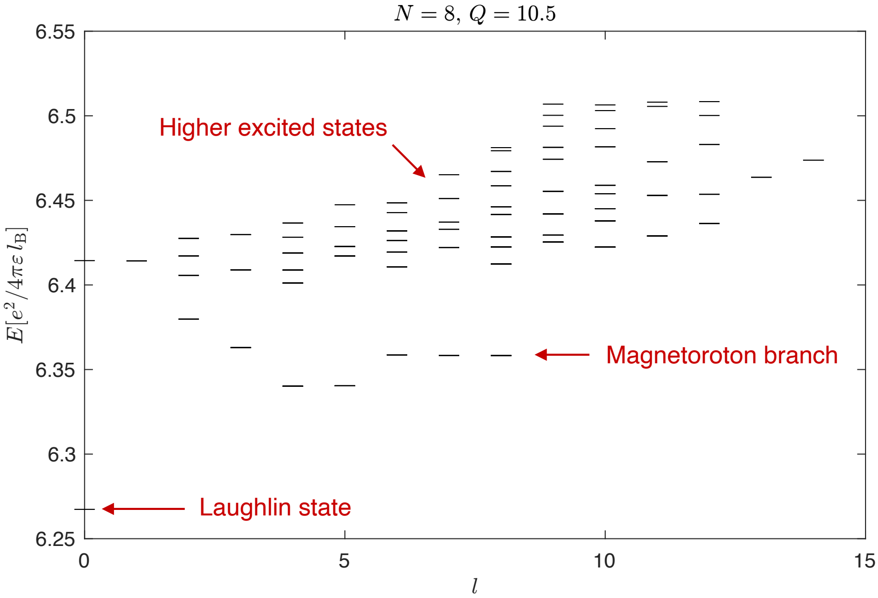

Figure 4.5: Spectrum of a $\nu = 1/3$ FQH system on a sphere for $N = 8$ and $Q = 3/2(N - 1) = 11$ as a function of the total angular momentum of the state. At this monopole strength, the spectrum contains the Laughlin state as the fully isotropic state at $L = 0$. The magnetoroton branch is visible, as well as the higher excited states. The interparticle potential here is taken as the Coulomb interaction with the dielectric constant $\varepsilon = 3.5$ corresponding to the dielectric constant of hBN.

To explain the FQH effect, a theoretical breakthrough came by the work of Laughlin, who constructed a Jastrow-type variational ansatz based on very general considerations to describe the observed plateau in electronic FQH states at the filling $\nu = 1/3$. These general considerations are: 1) the electrons all reside in the lowest Landau level, 2) the wave function of every two electron must be anti-symmetric with respect to the exchange of two electrons, 3) the electronic state must have the correct filling factor $\nu = 1/3$ of the lowest Landau level, and 4) it must describe an incompressible liquid state, that is a liquid state with excitations which remain gapped in the thermodynamic limit. The arguments behind these requirements are thoroughly discussed in textbooks on FQH [29, 224, 105, 37, 65]. Giving these requirements, Laughlin propsed the following wave function for N electrons in the symmetric gauge (Appendix C), known as *the Laughlin state* for the $\nu = 1/3$ FQH effect

$$\Psi_{\mathrm{LN}}(z) = \mathcal{N}_{\mathrm{LN}} \cdot \prod_{i<j}^{N} (z_i - z_j)^3 \cdot \exp\left(-\frac{1}{2} \sum_{i=1}^{N} |z_i|^2 \right) , \tag{4.13}$$

where $\mathcal{N}_{\mathrm{LN}}$ is a normalization constant and $z = (z_1, \cdots, z_N)$, where z_i is the complex coordinate of the i'th electron. Since all many-body states of N electrons contain the exponential factor, and all quantum states can be properly normalized, hereafter we drop the normalization constant and the exponential factor, unless explicitly needed in the discussion.

The Laughlin state was proved to be an excellent variational ansatz with no variational parameters which has a large overlap with exact eigenstates of the quantum Hall Hamiltonian for small systems [94, 66]. The Laughlin state suggest two types of *charged* excitations,

- a *quasihole* excitation with a variational state

$$\Psi_{\mathrm{qh}}(\xi; z) = \prod_{i=1}^{N} (z_i - \xi) \cdot \Psi_{\mathrm{LN}}(z) , \tag{4.14}$$

- a *quasiparticle* excitation, whose variational state can be

$$\Psi_{\mathrm{qp}}(\xi; z) = \prod_{i=1}^{N} (\partial_{z_i} - \xi) \cdot \Psi_{\mathrm{LN}}(z) . \tag{4.15}$$

Besides, FQH liquids can host neutral excitations, known as *magnetorotons*, which resemble the roton excitations of a superfluid. A single-mode approximation theory of magnetorotons was developed by Girvin, McDonald and Plazman [75, 76]. While quasiparticles and quasiholes are immobile excitations (they remain at the same place they are created, delocalized in an area the size of the magnetic length), magnetoroton modes can have definite momentum $\mathbf{k}$ and a well-defined dispersion. The structure of a magnetoroton further can be understood as a bound state of a quasiparticle and a quasihole, which unbinds for large momenta [228].

In this chapter, we are mostly interested in quasihole excitations of a Laughlin liquid at $\nu = 1/3$. The reason is multifold: 1) quasiholes have fractional charge $e^* = \nu e$ and statistics $\alpha = 2\pi\nu$, which means that the wave function of two quasiholes acquired a phase $e^{i\alpha}$ upon exchange of two quasiholes. 2) they are exact eigenstates of a delta-function repulsive potential, and an approximate ground state of many local attractive potentials, thus they can be created by localized repulsive potentials, thus there is a potential that they can be realized in experiments [157, 139]. Indeed, we will show later that the IX potential can localize a quasihole, both for a mobile and a localized exciton.

Having discussed the FQH, its ground state and excitations, we now introduce a single mobile impurity in the system and study the impurity-FQH system. Introducing a mobile impurity significantly increases the complexity of the problem, since now the Hilbert space of the impurity-FQH system is the tensor product of the many-body Hilbert space of the

FQH system and that of the mobile impurity, which has a continuous family of momentum eigenstates. Computations in this huge Hilbert space is thus intractable as one needs to include an indefinite number of impurity modes to correctly describe the strong coupling phenomena, such as impurity-quasihole binding. As will be shown, it is possible to reduce the complexity of the prolem substantially by moving the system into the impurity frame, by the so called *Lee-Low-Pines* (LLP) transformation. We make crucial use of the Lee-Low-Pines transformation for obtaining the IX-quasihole bound states and higher excited states in the subsequent sections, which were not possible without using the LLP transformation. In the following, we first lay out the general theory of application of the LLP transformation to the problem of a mobile impurity.

4.4 A mobile impurity in a FQH system

In this section, we consider a neutral mobile impurity of mass M interacting with a FQH system in 2D. We introduce *the magnetic Lee-Low-Pines transformation* (magnetic LLP), to bring the FQH system to the impurity frame. We show that application of the magnetic LLP transformation to the problem of a mobile impurity in a FQH environment leads to the imprinting of a gauge potential on the impurity, through the appearance of the FQH system's total magnetic momentum in the impurity's kinetic term. Since the magnetic LLP transformation translates the entire FQH system to the impurity frame, a gauge potential proportional to the vector potential of the magnetic field is also imprinted on the impurity. This gauge potential scales with the particle number in the FQH system, an effect which is expected since all the particles in the FQH are translated, leading to an Aharonov-Bohm phase in the impurity-FQH wave function which scales with the particle number. We show that there exists a non-unitary transformation which translates wave functions that are similar to quasiholes, only depend on a single complex coordinate, without translating the entire system. Fortunately, it is possible to apply the typical LLP transformation on the sphere and as we will discuss, it has been crucial in enabling us to find all the numerical results in the many-body part.

4.4.1 A neutral mobile impurity in FQH system

To keep the formalism general in the beginning, we consider a two-species population-imbalanced system in a two-dimensional plane span$(\hat{\mathbf{e}}_1, \hat{\mathbf{e}}_2)$, confined in a 2-D volume with area $\mathcal{A}$, which in the extreme population imbalance reduces to a single mobile impurity in a FQH system. The majority particles are fermionic with field operator $\hat{\psi}(\mathbf{x})$ and experience a uniform magnetic field $\mathbf{B} = B\,\hat{\mathbf{e}}_3$ perpendicular to the confinement plane. The minority (impurity) particles field operator are not affected by the magnetic field. The total Hamiltonian of the system is

$$\hat{H} = \hat{H}_{\text{imp}} + \hat{H}_{\text{majority}} + \hat{H}_{\text{int}}\,. \tag{4.16}$$

In the second quantized form, the Hamiltonians of the impurity ($\hat{H}_{\text{imp}}$), the majority particles ($\hat{H}_{\text{majority}}$) and the interaction term ($\hat{H}_{\text{int}}$) read

$$\hat{H}_{\text{imp}} = \int d^2x\, \hat{\phi}^\dagger(\mathbf{x}) \Big(-\frac{\hbar^2}{2M}\nabla^2 \Big) \hat{\phi}(\mathbf{x}) \,, \tag{4.17}$$

$$\hat{H}_{\text{majority}} = \int d^2x\, \hat{\psi}^\dagger(\mathbf{x}) \left[-\frac{\hbar^2}{2m}\Big(\nabla - i\frac{2\pi}{\Phi_0}\mathbf{A}(\mathbf{x}) \Big)^2 + \frac{1}{2}\int d^2x'\, V(\mathbf{x}-\mathbf{x}')\hat{\psi}^\dagger(\mathbf{x}')\hat{\psi}(\mathbf{x}') \right] \hat{\psi}(\mathbf{x}) \,, \tag{4.18}$$

$$\hat{H}_{\text{int}} = \int d^2x\, d^2x'\, \hat{\phi}^\dagger(\mathbf{x})\hat{\phi}(\mathbf{x})\, U(\mathbf{x}-\mathbf{x}')\, \hat{\psi}^\dagger(\mathbf{x}')\hat{\psi}(\mathbf{x}') \,, \tag{4.19}$$

with $\hat{\psi}(\mathbf{x})$, $\hat{\phi}(\mathbf{x})$ and m, M the field operators and masses of the majority and impurity particles, respectively. The interaction between the majority particles are described by $V(\mathbf{x})$, whereas the inter-species potential $U(\mathbf{x})$ characterises the interaction between the impurity and the majority particles. Here we express the relevant quantities of the problem in dimensionless form (see Table. C.1),

$$\hat{H}_{\text{imp}} = \int d^2x\, \hat{\phi}^\dagger(\mathbf{x}) \Big(-\frac{\beta}{2}\nabla^2 \Big) \hat{\phi}(\mathbf{x}) \,, \tag{4.20}$$

$$\hat{H}_{\text{majority}} = \int d^2x\, \hat{\psi}^\dagger(\mathbf{x}) \left[-\frac{1}{2}\Big(\nabla - i\mathbf{A}(\mathbf{x}) \Big)^2 + \frac{1}{2}\int d^2x'\, V(\mathbf{x}-\mathbf{x}')\hat{\psi}^\dagger(\mathbf{x}')\hat{\psi}(\mathbf{x}') \right] \hat{\psi}(\mathbf{x}) \,, \tag{4.21}$$

$$\hat{H}_{\text{int}} = \int d^2x\, d^2x'\, \hat{\phi}^\dagger(\mathbf{x})\hat{\phi}(\mathbf{x})\, U(\mathbf{x}-\mathbf{x}')\, \hat{\psi}^\dagger(\mathbf{x}')\hat{\psi}(\mathbf{x}') \,, \tag{4.22}$$

where $\beta = m/M$ is the impurity-majority mass ratio.

4.4.2 The magnetic Lee-Low-Pines transformation

Let us make a short recap of group theory in quantum mechanics. Consider a system with a Hilbert space $\mathcal{H}$ and a set of complete orthonormal (distinguishable) states $\{|m\rangle\}$ with $m \in \mathcal{M}$ a set of labels, together with an action of a group G on $\mathcal{M}$, i.e. $\mu \,:\, G\times\mathcal{M} \longrightarrow \mathcal{M}\,.$ For a unitary representation of G, we have

$$\hat{U}(g)^\dagger\,|m\rangle = |\mu(g,m)\rangle \quad \forall g \in G \,,$$

which induces a transformation rule for creation operators $\hat{a}^\dagger_m$ as

$$\hat{a}^\dagger_{\mu(g,m)}\,|\emptyset\rangle = \hat{U}^\dagger(g)\,\hat{a}^\dagger_m\hat{U}(g)\,\hat{U}^\dagger(g)\,|\emptyset\rangle \;. \tag{4.23}$$

For a system with a *unique vaccum state* and a symmetry operation $g \in G$, $\hat{U}^\dagger(g)\,|\emptyset\rangle = |\emptyset\rangle\,,$ so the creation operators transform according to

$$\hat{U}^\dagger(g)\,\hat{a}^\dagger_m\hat{U}(g) = \hat{a}^\dagger_{\mu(g,m)} \,. \tag{4.24}$$

Note that for a FQH system on a torus where the ground state is degenerate, $\hat{U}(g)$ acts non-trivially on the ground state manifold. Nevertheless, in the following we focus on the case where $\hat{U}(g)\,|\emptyset\rangle = |\emptyset\rangle$. We define *the magnetic Lee-Low-Pines transformation* as

$$\hat{U}_{\mathrm{LLP}} \equiv \exp\Big(- i\, \hat{\mathbf{x}}_{\mathrm{imp}} \cdot \hat{\mathbf{\Gamma}}_{\mathrm{cm}} \Big)\,, \tag{4.25}$$

where

$$\hat{\mathbf{x}}_{\mathrm{imp}} = \int d^2x\, \mathbf{x}\, \hat{\phi}^\dagger(\mathbf{x})\hat{\phi}(\mathbf{x})\,, \tag{4.26}$$

$$\hat{\mathbf{X}}_{\mathrm{cm}} = \int d^2X\, \mathbf{X}\, \hat{\psi}^\dagger(\mathbf{X})\hat{\psi}(\mathbf{X})\,, \tag{4.27}$$

$$\hat{\mathbf{P}}_{\mathrm{cm}} = \int d^2X\, \hat{\psi}^\dagger(\mathbf{X})\,\Big(- i\nabla_{\mathbf{X}} \Big)\, \hat{\psi}(\mathbf{X})\,, \tag{4.28}$$

$$\hat{\mathbf{\Gamma}}_{\mathrm{cm}} = \hat{\mathbf{P}}_{\mathrm{cm}} - \mathbf{A}(\hat{\mathbf{X}}_{\mathrm{cm}}) + \hat{\mathbf{B}} \times \hat{\mathbf{X}}_{\mathrm{cm}}\,. \tag{4.29}$$

Using Eqs. 4.26, 4.27, 4.28, 4.29, we obtain the transformation rules for the impurity and majority field operators,

$$\begin{aligned}\hat{U}^\dagger_{\mathrm{LLP}}\, \hat{\phi}^\dagger(\mathbf{x})\, \hat{U}_{\mathrm{LLP}} &= \exp\Big(- i\mathbf{x} \cdot \bar{\mathbf{A}}\Big(\hat{\mathbf{X}}_{\mathrm{cm}} + N\,\mathbf{x}/2\Big)\Big) \exp\Big(i\mathbf{x}\cdot \hat{\mathbf{P}}_{\mathrm{cm}}\Big)\, \hat{\phi}^\dagger(\mathbf{x}) \\ &= \exp\Big(i\mathbf{x}\cdot \hat{\mathbf{\Gamma}}_{\mathrm{cm}}\Big)\, \hat{\phi}^\dagger(\mathbf{x}),\end{aligned} \tag{4.30}$$

$$\hat{U}^\dagger_{\mathrm{LLP}}\, \hat{\psi}^\dagger(\mathbf{X})\, \hat{U}_{\mathrm{LLP}} = \exp\Big(- i\hat{\mathbf{x}}_{\mathrm{imp}} \cdot \bar{\mathbf{A}}\Big(\mathbf{X} - N\,\hat{\mathbf{x}}_{\mathrm{imp}}/2\Big)\Big)\, \hat{\psi}^\dagger(\,\mathbf{X} - \hat{\mathbf{x}}_{\mathrm{imp}}\,)\,, \tag{4.31}$$

where we have defined $\bar{\mathbf{A}}(\mathbf{x}) = \mathbf{A}(\mathbf{x}) - \mathbf{B} \times \mathbf{x}$. Eqs. 4.30 and 4.31 imply the following transformations for density operators,

$$\hat{U}^\dagger_{\mathrm{LLP}}\hat{\phi}^\dagger(\mathbf{x})\hat{\phi}(\mathbf{x})\hat{U}_{\mathrm{LLP}} = \hat{\phi}^\dagger(\mathbf{x})\hat{\phi}(\mathbf{x})\,, \tag{4.32}$$

$$\hat{U}^\dagger_{\mathrm{LLP}}\hat{\psi}^\dagger(\mathbf{X})\hat{\psi}(\mathbf{X})\hat{U}_{\mathrm{LLP}} = \hat{\psi}^\dagger(\mathbf{X} - \hat{\mathbf{x}}_{\mathrm{imp}})\hat{\psi}(\mathbf{X} - \hat{\mathbf{x}}_{\mathrm{imp}})\,, \tag{4.33}$$

where we used the fact that the majority and impurity operators commute so that one acts as a c-numbers on the other's Hilbert space. This results in the invariance of the interaction terms in the Hamiltonians 4.21 and 4.20. To obtain the transformation of the kinetic term of the majority Hamiltonian, we note that the magnetic and kinetic translations commute (Eq. C.5), so the kinetic term of the majority Hamiltonian also remains invariant under U_{LLP} . The transformation of the impurity can be obtained as follows,

$$\hat{U}^\dagger_{\mathrm{LLP}}\, \hat{H}_{\mathrm{imp}}\, \hat{U}_{\mathrm{LLP}} \;=\; \int d^2x\, \hat{\phi}^\dagger(\mathbf{x}) \exp\Big(i\mathbf{x}\cdot \hat{\mathbf{\Gamma}}_{\mathrm{cm}}\Big) \Big(- \frac{\beta}{2}\nabla^2 \Big) \exp\Big(- i\mathbf{x}\cdot \hat{\mathbf{\Gamma}}_{\mathrm{cm}}\Big)\, \hat{\phi}(\mathbf{x})\,. \tag{4.34}$$

To calculate the RHS of Eq. 4.34, we make use of the following expression,

$$\nabla_{\mathbf{x}} \exp\Big(-i\mathbf{x}\cdot\hat{\mathbf{\Gamma}}_{\mathrm{cm}}\Big) = \exp\Big(-i\mathbf{x}\cdot\hat{\mathbf{\Gamma}}_{\mathrm{cm}}\Big) \left[\nabla_{\mathbf{x}} - i\left(\hat{\mathbf{P}}_{\mathrm{cm}} - \bar{\mathbf{A}}(\,\hat{\mathbf{X}}_{\mathrm{cm}}\,)\right) + N\left\{i\bar{\mathbf{A}}(\mathbf{x}) - i\nabla_{\mathbf{x}}\left(\frac{1}{2}\mathbf{x}\cdot\bar{\mathbf{A}}(\mathbf{x})\right)\right\}\right]. \tag{4.35}$$

We can further simplify the last two terms in the RHS of Eq. 4.35 as

$$\left[i\bar{\mathbf{A}}(\mathbf{x}) - i\nabla_{\mathbf{x}} \left(\frac{1}{2}\mathbf{x} \cdot \bar{\mathbf{A}}(\mathbf{x}) \right) \right]_k = i\bar{A}_{kl}x_l - \frac{i}{2}\Big(\bar{A}_{kl}x_l + \bar{A}_{lk}x_l \Big) = \frac{i}{2}\Big(\bar{A}_{kl} - \bar{A}_{lk} \Big) x_l \,. \tag{4.36}$$

The last expression in Eq. 4.36 is the antisymmetric part of the matrix $\bar{A}$ acting on x. One can show [2] that the antisymmetric part of any gauge potential $\mathbf{A}(\mathbf{x})$ which is linear in $\mathbf{x}$ is exactly the symmetric gauge $A_{\mathrm{sym},k} = \frac{1}{2}\epsilon_{kl}\, x_l$ and the symmetric part $A_{S,kl} = 1/2\,(A_{kl} + A_{lk})$ is a pure gauge contribution. Thus,

$$\frac{1}{2}\left(\bar{A}_{kl} - \bar{A}_{lk} \right) = -\frac{1}{2}\,\epsilon_{kl}\,, \tag{4.37}$$

and using Eq. 4.36,

$$i\bar{\mathbf{A}}(\mathbf{x}) - i\nabla_{\mathbf{x}} \left(\frac{1}{2}\mathbf{x} \cdot \bar{\mathbf{A}}(\mathbf{x}) \right) = -i\mathbf{A}_{\mathrm{sym}}(\mathbf{x})\,. \tag{4.38}$$

Substituting Eq. 4.38 in Eq. 4.34 yields

$$U^{\dagger}_{\mathrm{LLP}}\, \hat{H}_{\mathrm{imp}}\, U_{\mathrm{LLP}} \;=\; \int d^2x\, \hat{\phi}^{\dagger}(\mathbf{x}) \left[-\frac{\beta}{2} \left(\nabla_{\mathbf{x}} - iN\,\mathbf{A}_{\mathrm{sym}}(\mathbf{x}) - i\hat{\mathbf{\Gamma}}_{\mathrm{cm}} \right)^2 \right] \hat{\phi}(\mathbf{x})\,. \tag{4.39}$$

Interestingly, we see that the symmetric gauge *always* arises in the expression for the LLP-transformed impurity Hamiltonian, independent of the gauge potential. At the first sight, this seems worrysome because it seems to violate gauge freedom. However, it should be noted that the gauge freedom is intact since there is a freedom in choosing the path over which the system is translated to the position of the impurity. Indeed, one can show (left as an exercise for the reader) that the straight path from the impurity position to the origin corresponds to the symmetric gauge, and the paths along the x and y directions corresponds to the choice of two different Landau gauges, depending on the order taken.

Finally, the full impurity-majority Hamiltonian in the LLP frame takes the following form,

$$\begin{aligned} \hat{U}^{\dagger}_{\mathrm{LLP}}\, \hat{H}_{\mathrm{tot}}\, \hat{U}_{\mathrm{LLP}} = & \int d^2x\, \hat{\phi}^{\dagger}(\mathbf{x}) \left[-\frac{\beta}{2} \left(\nabla_{\mathbf{x}} - iN\,\mathbf{A}_{\mathrm{sym}}(\mathbf{x}) - i\hat{\mathbf{\Gamma}}_{\mathrm{cm}} \right)^2 \right] \hat{\phi}(\mathbf{x}) \\ & + \int d^2x\, \hat{\psi}^{\dagger}(\mathbf{x}) \left[-\frac{1}{2}\Big(\nabla - i\mathbf{A}(\mathbf{x}) \Big)^2 + \frac{1}{2} \int d^2x'\, V(\mathbf{x} - \mathbf{x}')\hat{\psi}^{\dagger}(\mathbf{x}')\hat{\psi}(\mathbf{x}') \right] \hat{\psi}(\mathbf{x}) \\ & + \int d^2x \hat{\phi}^{\dagger}(\mathbf{x})\hat{\phi}(\mathbf{x}) \int d^2x'\, U(\mathbf{x}')\, \hat{\psi}^{\dagger}(\mathbf{x}')\hat{\psi}(\mathbf{x}')\,. \end{aligned} \tag{4.40}$$

If we take a (N + 1) - particle system with a single impurity and N particles in the majority, we have

$$\int d^2x\, \hat{\phi}^{\dagger}(\mathbf{x})\hat{\phi}(\mathbf{x}) = 1\,, \quad \int d^2x\, \hat{\psi}^{\dagger}(\mathbf{x})\hat{\psi}(\mathbf{x}) = \mathrm{N}\,. \tag{4.41}$$

---

[2] We show in the appendix that this is indeed the case.

in this case we can treat the impurity in first quantization, in which case Eq. 4.40 reads

$$\begin{aligned}\hat{U}^{\dagger}_{\mathrm{LLP}}\,\hat{H}_{\mathrm{tot}}\,\hat{U}_{\mathrm{LLP}} = &\frac{\beta}{2}\Big(\hat{\mathbf{p}}_{\mathrm{imp}} - N\,\mathbf{A}_{\mathrm{sym}}(\hat{\mathbf{x}}_{\mathrm{imp}}) - \hat{\mathbf{\Gamma}}_{\mathrm{cm}}\Big)^2 \\ &+ \int d^2x'\,U(\mathbf{x}')\,\hat{\psi}^{\dagger}(\mathbf{x}')\hat{\psi}(\mathbf{x}') \\ &+ \int d^2x\,\hat{\psi}^{\dagger}(\mathbf{x})\left[-\frac{1}{2}\Big(\nabla - i\mathbf{A}(\mathbf{x})\Big)^2 + \frac{1}{2}\int d^2x'\,V(\mathbf{x}-\mathbf{x}')\hat{\psi}^{\dagger}(\mathbf{x}')\hat{\psi}(\mathbf{x}')\right]\hat{\psi}(\mathbf{x})\,.\end{aligned} \tag{4.42}$$

To proceed further, first let us focus on the kinetic term in Eq. 4.42. It is clear that the gauge field emerged in the impurity's kinetic term has two components: $N\mathbf{A}_{\mathrm{sym}}(\hat{\mathbf{x}}_{\mathrm{imp}})$ and $\hat{\mathbf{\Gamma}}_{\mathrm{cm}}$. The latter is the total magnetic momentum of the system, and the former is the gauge field that the center-of-mass of the whole FQH system experiences. This term is anomalous, since it scales by the full particle numbers in the system. Indeed, this term emerged due to the translation of the FQH center-of-mass, which acts as a particle with mass Nm and charge Nq. However, this is not a physical effect, since translation to the impurity frame is only meaningfull for the excitations of the FQH system, without translating the entire system.

To understand the above points, consider translation of a single charge q in a magnetic field. The kinetic Hamiltonian of the charge is translation invariant, while the vector potential is not. However, one can show that translation of the vector potential amount only to a gauge transformation (see Chapter 2 of Ref. [105]). This is apparent when considering translation of an arbitrary lowest Landau level state $f(z)e^{-|z|^2/2}$ in the symmetric gauge [3]. The translated state to a position z_0 has the form

$$\begin{aligned}f(z-z_0)\,e^{-|z-z_0|^2/2} &= e^{-|z|^2/2}e^{-|z_0|^2/2}e^{(\bar{z}_0 z + z_0\bar{z})/2}\,f(z-z_0) \\ &= e^{-(\bar{z}_0 z - z_0\bar{z})/2}\;\cdot\;e^{-|z_0|^2/2}e^{\bar{z}_0 z}\;\cdot\;\Big(f(z-z_0)\,e^{-|z|^2/2}\Big)\,.\end{aligned} \tag{4.43}$$

The first term in the second line of Eq. 4.43 is a pure gauge term of the form $-i/\hbar(q/c)\mathbf{A}(\mathbf{x}_0)\cdot\mathbf{x}$, where z and z_0 are the complex coordinates associated to $\mathbf{x}$ and $\mathbf{x}_0$, respectively. The last term is the translation of the polynomial part of the wavefunction, without changing the Gaussian term. This is exactly the form of the wave function we are after. To understand this, let us consider the form of the quasihole wave function in Eq. 4.15. The polynomial factor alone is a translation of the quasihole wave function centered at 0 to the position ξ, while the exponential factor remains unchanged. It turns out that putting the whole FQH system on a sphere does not suffer from these problems, and one can apply the normal LLP to reduce the complexity of the problem substantially. The reason for application of the normal LLP transformation is that on the sphere, the system is rotationally symmetric. Since the generators of rotation on the sphere, which are angular momenta, are also

---

[3] Here, with a slight abuse of notation, we consider z to be the complex coordinate of a single particle, as opposed to $z = (z_1, \cdots, z_N)$ for N particles. We also drop the charge carrier sign ς.

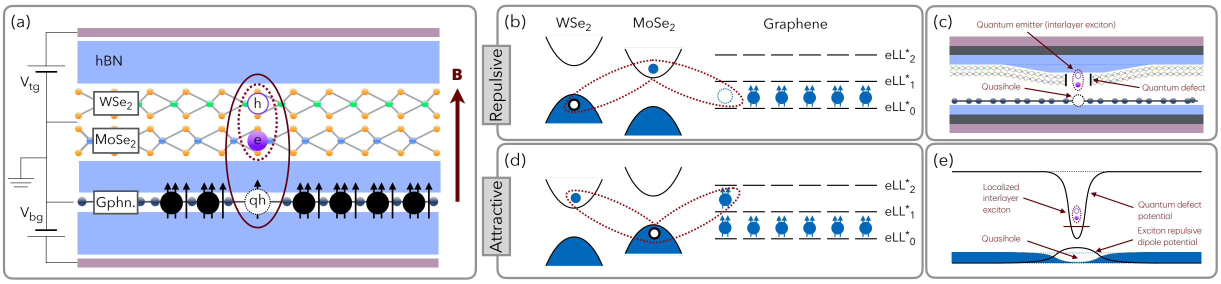

Figure 4.6: (a) Schematic of the device configuration considered in this work to study IX-FQH physics. A MoSe$_2$/MoSe$_2$ heterobilayer constitutes the optically active layer. At strong magnetic fields, the 2DES in the proximate graphene monolayer can form quantum Hall states. A representative $\nu = 1/3$ quantum Hall state in the composite fermion picture is illustrated as a $\nu^* = 1$ state of ^{2}CF composite fermions. For type-II band alignment of the MoSe$_2$/MoSe$_2$ heterobilayer [170], the electron (hole) resides in the conduction band (valence band) of the MoSe$_2$ (WSe$_2$). (b)-(d) In the type-II (type-I) band alignment, the interlayer exciton interction with graphene charge carriers is repulsive (attractive), resulting in exciton binding to single quasihole (quasiparticle) excitations of the $\nu = 1/3$ FQH state and formation of *anyonic trions*. (c) A localized exciton in an optically active quantum defect can bind a quasihole, in a Quantum Optical Twist and Scan Microscope (QOTSM). The movable upper part of the device allows spatial control over the quasihole position. (e) schematic of the spatial profile of the electric potential corresponding to (c). The repulsive exciton-carrier interaction creates a local repulsive potential, and effectively binds a quasihole.

generators of translations, one can use normal translation instead of magnetic translation to move to the impurity frame.

We close the discussion on the magnetic LLP transformation by noting that, the idea behind the magnetic LLP is to reduce the complexity of the problem as much as possible by transforming to the impurity frame, while performing a suitable gauge transformation on the background. In the following sections on the few-body physics of excitons scattering off charge carriers in graphene, we will incorporate a generalization of this idea, and show that application of a suitable gauge transformation leads to a striking property of the trion states, akin to that of point like charge particles in a magnetic field. This property is the conservation of the trion magnetic momentum quantum number. For investigations of the many-body IX-FQH system, we apply the normal LLP transformation on the sphere, and we demonstrate its effectiveness is giving consistent results for the low energy states of the many-body system. Below, we outline the experimental setup and parameters used for the modeling.

4.5 From few- to many-body body physics in exciton-quantum Hall systems: exciton quantum Hall polarons and anyonic trions

After a rather abstract discussion on the theory of mobile impurities interacting with a quantum Hall system, we are now at a position to descibe the concrete experimental setup we propose to observe the physics of mobile-impurities interacting with a quantum Hall system. The considered gate-controlled device is shown in Fig. 4.6 (a), consisting of an hBN-encapsulated $MoSe_2/WSe_2$ heterobilayer with layer distance $d = 0.6\,nm$, in the proximity of a graphene monolayer in a distance $l = 1.2\,nm$ from the $MoSe_2$ layer, containing the quantum Hall system. In this thesis we are mostly interested in the physics of IX interacting with a FQH state near filling $\nu = 1/3$, since it is the most stable FQH experimentally observed. In the composite fermion picture of the FQH effect ([105]), a $\nu = 1/3$ FQH state can be viewed as an IQH state of composite fermions, which are the electrons carrying two flux quanta (see Fig. 4.6). A quasihole excitation of the $\nu = 1/3$ FQH liquid can be viewed as a charge defect carrying a single flux quantum. In this picture, three flux quanta at the same position thus represent a single vacant electron, giving an intuitive explanation for the fractional charge of a $\nu = 1/3$ FQH liquid equal to $e^* = e/3$.

We first study the few-body states of an exciton interacting attractively with a single hole in the graphene layer. Studying this setting is particularly necessary for modeling the many-body case, since excitons are not structureless particles, and treating them as a single point like particle in the present context has to be justified. Moreover, the lowest Landau level approximation which underlies a significant number of results on FQH systems needs to be checked, as the exciton-carrier interaction might lead to Landau level mixing. We will see that both the assumption of a point like exiton and confinement of carriers to the lowest Landau level approximations are excellent approximations.

In the many-body limit, we investigate two separate cases, where the exciton is entirely delocalized, and the case where it is strongly localized in an optically active quantum defect in the TMD heterobilayer. For mobile excitons, we consider both attractive and repulsive exciton electron interactions. The sign of the exciton-carrier interaction can be tuned, either electrically by changing the default type-II band alignment of the TMD system ([170]), or by changing the particle doping of the graphene layer from electrons to holes. For the purpose of our numerical investigations, we consider electrons in graphene, while changing the IX configuration. Regarding the FQH system, we investigate the low energy spectrum of the IX-FQH system at filling factors corresponding to the Laughlin $\nu = 1/3$ state, a single $\nu = 1/3$ quasihole, two $\nu = 1/3$ quasiholes and a single $\nu = 1/3$ quasiparticle, for both attractive and repulsive interactions.

For repulsive exciton-electron interactions, in the setting where the FQH contains one quasihole as an excess flux quantum on top of the Laughlin state, we observe clear signatures of two bound states in the low energy spectrum of the system. We identify the lowest energy state as an *anyonic trion*, since the exciton-electron spatial correlation function, called $g^{(2)}$, has an excellent agreement with that of a single quasihole of the FQH system. This result is particularly striking since this signature appears to be independent of the total angular momentum of the system, which in the present context of FQH on the system, constitutes another well-defined quantum number alongside the energy. The $g^{(2)}$ of the other bound state is also very similar to that of the quasihole, however it does not vanish at the position of the exciton, giving it a higher energy than the first bound state. By analysing the spectrum of the system in the limit of a lozalized exciton, we interpret the formation of the second bound state as the result of a coherent superposition of delocalized quasiholes and higher excited states, in such a way that they destructively interfere at the exciton position, thus reducing the energy cost of the repulsive interaction with the exciton. We further analyze the observed energy gaps for these two bound states, and find that they show a saturation behaviour, suggesting that they acquire a definite value in the thermodynamic limit.

For attractive exciton-electron interactions, we do not find meaningful signatures of exciton-quasiparticle binding, such as a well-defined gap, and agreement of the exciton-electron $g^{(2)}$ function with that of a bare quasiparticle. Instead, we find that the $g^{(2)}$ function resembles the one for an excited state of the FQH system, which is more peaked at the exciton position than the quasiparticle. Again, this result is expected since a superposition of the excitations which constructively interfere at the exciton position can lead to a higher gain in binding energy.

In the following, we first investigate the few-body problem and gain insight to analyze the many-body setting.

4.6 Few-body physics in the lowest Landau level

In the previous sections, we focused on the rather abstract problem of a point like neutral mobile impurity moving in the background of massive charged particles in a magnetic field. However, our main focus is the interaction of excitons with a FQH system in graphene, and we have to take the particularities of this system into account. Especially, excitons are composite objects made of electrons and holes, and it is a priori unknown if the charge carriers in the FQH system have any effect on the internal structure of the excitons. This problem is particularly relevant, as it is known that in systems such as GaAs quantum wells, the electron and hole motion of the exciton is quantized in Landau levels. Thus, one has to model a magnetoexciton interacting with the FQH system, and the assumption of pointlike excitons will drastically fail [82] (see also [136] for a discussion on abrupt changes in the exciton structure in high magnetic fields). Besides, the whole FQH effect occurs in the lowest Landau level, whereas it is not clear whether the scattering of the exciton excites the carriers into higher landau levels. Thus, it is necessary to quantify the admixture of the interlayer exciton $1s$ state with the excited excitonic Rydberg series, the Landau level mixing of the charge carrier as a result of scattering off the interlayer exciton, and the binding energy of the existing interlayer trion states.

In the following, we address the above questions, we investigate the few-body physics of the IX and a single graphene charge carrier by considering the problem of an electron and a hole in the $MoSe_2$ and WSe_2 layers, and a single positive charge in the graphene (see Fig. 4.6 (a) for the schematics of the device). The reason for considering a hole carrier in graphene is that we consider the $MoSe_2$ monolayer to be closer to the graphene layer, thus the net potential of the IX is attractive for a hole excitation in graphene. We solve the problem by means of exact diagonalization of the three-body Hamiltonian, and find the exact eigenstates. We will show that both the admixture of the $1s$ exciton with excited Rydberg states, as well as the contribution of higher Landau levels to the trion state is negligible. These results firmly establish that treating the exciton as a point like particle in the $1s$ state, as well as the lowest Landau level approximation for the charge carriers are excellent approximations.

Before moving on to the full three-body problem, we first consider the problem of an exciton in a magnetic field, and find the energy levels.

	r_*	m_e	m_h	a_0^*	Ry^*
unit	nm	m_0	m_0	nm	meV
$MoSe_2$	3.9	0.84	0.6	0.6804	235.2
WSe_2	4.5	0.34	0.53	1.1497	139.2

Table 4.1: Material parameters for $MoSe_2$ and WSe_2. Values are taken from [80, 123, 134, 216, 125].Note that theoretical values of effective masses are very different, and where ever they do not agree with the experimental value, the experimental value is taken.

4.6.1 Exciton Hamiltonian

To find the energy levels of an exciton in a magnetic field, we follow Gor'kov and Dzyaloshinskii [81]. The total magnetic momentum $\hat{\mathbf{\Gamma}}_\mathrm{X} = \hat{\mathbf{\Gamma}}_e + \hat{\mathbf{\Gamma}}_h$ of the exciton is a conserved quantity. In terms of the exciton's relative (center-of-mass) position and momentum $\hat{\mathbf{r}}_{eh}$, $\hat{\mathbf{p}}_{eh}$ ($\hat{\mathbf{R}}_\mathrm{X}$, $\hat{\mathbf{P}}_\mathrm{X}$), the total exciton magnetic momentum operator reads

$$\begin{aligned}\hat{\mathbf{\Gamma}}_\mathrm{X} &= \left(\hat{\mathbf{p}}_e + \hat{\mathbf{p}}_h\right) + \frac{e}{c}\mathbf{A}(\hat{\mathbf{r}}_e - \hat{\mathbf{r}}_h) - \frac{e}{c}\mathbf{B} \times (\hat{\mathbf{r}}_e - \hat{\mathbf{r}}_h) \\ &= \hat{\mathbf{P}}_\mathrm{X} + \frac{e}{c}\mathbf{A}(\hat{\mathbf{r}}_{eh}) - \frac{e}{c}\mathbf{B} \times \hat{\mathbf{r}}_{eh} \,.\end{aligned} \tag{4.44}$$

From Eq. 4.44, $[\hat{\Gamma}_{\mathrm{X},1}, \hat{\Gamma}_{\mathrm{X},2}] = 0$, therefore both components of $\hat{\mathbf{\Gamma}}_\mathrm{X}$ are good quantum numbers. On an eigenstate $\psi_\mathbf{K}(\mathbf{R}_\mathrm{X}, \mathbf{r}_{eh})$ of $\hat{\mathbf{\Gamma}}_\mathrm{X}$ with $\hat{\mathbf{\Gamma}}_\mathrm{X}\, \psi_\mathbf{K}(\mathbf{R}_\mathrm{X}, \mathbf{r}_{eh}) = \mathbf{K}\, \psi_\mathbf{K}(\mathbf{R}_\mathrm{X}, \mathbf{r}_{eh})$, the action of $\hat{\mathbf{P}}_\mathrm{X}$ follows from Eq. 4.44 to be

$$\hat{\mathbf{P}}_\mathrm{X}\, \psi_\mathbf{K}(\mathbf{R}_\mathrm{X}, \mathbf{r}_{eh}) = \left(\mathbf{K} - \frac{e}{c}\mathbf{A}(\mathbf{r}_{eh}) + \frac{e}{c}\mathbf{B} \times \mathbf{r}_{eh}\right) \psi_\mathbf{K}(\mathbf{R}_\mathrm{X}, \mathbf{r}_{eh}) \,, \tag{4.45}$$

Thus, $\psi_{\mathbf{K}}(\mathbf{R}_\mathrm{X}, \mathbf{r}_{eh})$ is of the following form

$$\psi_{\mathbf{K}}(\mathbf{R}_\mathrm{X}, \mathbf{r}_{eh}) = \exp\left(\frac{i}{\hbar}\left(\mathbf{K} - \frac{e}{c}\mathbf{A}(\mathbf{r}_{eh}) + \frac{e}{c}\mathbf{B}\times\mathbf{r}_{eh}\right)\cdot\mathbf{R}_\mathrm{X}\right)\psi_{\mathbf{K}}(\mathbf{r}_{eh})\,. \tag{4.46}$$

In Eq. 4.46, $\psi_{\mathbf{K}}(\mathbf{r}_{eh})$ is only a function of $\mathbf{r}_{eh}$, and is an eigenstate of the Hamiltonian $\hat{H}'_X = \hat{U}^\dagger_G\,\hat{H}_\mathrm{X}\,\hat{U}_G$ with $\hat{U}_G = \exp\Big(\frac{i}{\hbar}\Big(\mathbf{K} - \frac{e}{c}\mathbf{A}(\mathbf{r}_{eh}) + \frac{e}{c}\mathbf{B}\times\mathbf{r}_{eh}\Big)\cdot\mathbf{R}_\mathrm{X}\Big)$. Explicitly, $\hat{H}'_\mathrm{X}$ is given by

$$\hat{H}'_\mathrm{X} = \frac{\mathbf{K}^2}{2M_\mathrm{X}} + \frac{e}{M_\mathrm{X}c}\mathbf{K}\cdot\Big(\mathbf{B}\times\mathbf{r}_{eh}\Big) + \hat{H}'_\mathrm{X,internal} \tag{4.47}$$

where the Hamiltonian of the internal exciton degrees of freedom reads

$$\begin{aligned}\hat{H}'_\mathrm{X,internal} = &\frac{1}{2m_e}\left(\hat{\mathbf{p}}_{eh} + \frac{e}{c}\eta\mathbf{A}(\hat{\mathbf{r}}_{eh}) + \frac{e}{c}\frac{m_e}{M_\mathrm{X}}\mathbf{B}\times\hat{\mathbf{r}}_{eh}\right)^2 \\ &+ \frac{1}{2m_h}\left(\hat{\mathbf{p}}_{eh} + \frac{e}{c}\eta\mathbf{A}(\hat{\mathbf{r}}_{eh}) - \frac{e}{c}\frac{m_h}{M_\mathrm{X}}\mathbf{B}\times\hat{\mathbf{r}}_{eh}\right)^2 \\ &+ V_{eh}(\hat{\mathbf{r}}_{eh})\,,\end{aligned} \tag{4.48}$$

where $\eta = (m_h - m_e)/M_\mathrm{X}$. In the symmetric gauge $\mathbf{A}(\mathbf{r}_{eh}) = 1/2\,\mathbf{B}\times\mathbf{r}_{eh}$, $\hat{H}'_\mathrm{X,internal}$ reduces to

$$\begin{aligned}\hat{H}'_\mathrm{X,internal} &= \frac{1}{2m_e}\left(\hat{\mathbf{p}}_{eh} + \frac{e}{2c}\mathbf{B}\times\hat{\mathbf{r}}_{eh}\right)^2 + \frac{1}{2m_h}\left(\hat{\mathbf{p}}_{eh} - \frac{e}{2c}\mathbf{B}\times\hat{\mathbf{r}}_{eh}\right)^2 + V_{eh}(\hat{\mathbf{r}}_{eh}) \\ &= \left[\frac{1}{2\mu_\mathrm{X}}\hat{\mathbf{p}}^2_{eh} + V_{eh}(\hat{\mathbf{r}}_{eh})\right] + \frac{e^2}{8\mu_\mathrm{X}c^2}(\mathbf{B}\times\hat{\mathbf{r}}_{eh})^2 + \frac{e}{2\mu_\mathrm{X}c}\eta\,\mathbf{B}\cdot\hat{\mathbf{L}}_{eh}\,.\end{aligned} \tag{4.49}$$

In the last line of Eq. 4.49, the first term in braces is the internal exciton Hamiltonian, the rest are the diamagnetic and an effective paramagnetic term, respectively.

From Eqs. 4.49 and 4.47, the exciton states are of the form $|\mathbf{K}, n_\mathrm{X}, l_\mathrm{X}\rangle_\mathrm{X}$, where n_X and l_X are the exciton principle quantum number and angular momentum, respectively. A suitable orthonormal basis for the internal excitonic state, thus, are $|n_\mathrm{X}, l_\mathrm{X}\rangle_\mathrm{X} \equiv |\mathbf{K} = 0, n_\mathrm{X}, l_\mathrm{X}\rangle_\mathrm{X}$.

To perform the numerical diagonalization and find the excitonic states, we first need to find the electrostatic potential between the charges. The standard procedure is to solve the Poisson equations for point charges in each layer [208]. We obtain the electrostatic potentials for a device with $d = 0.6\,nm$ distance between the TMD layers and $l = 1.2\,nm$ distance between the MoSe$_2$ and the graphene layers. The material parameters needed to find the interparticle potentials are listed in Table. 4.6. Of special importance is the screening length r_*, which is related to the 2D polarizability of the layered materials by $r_* = \chi_\mathrm{2D}/2$. In Fig. 4.7, the energy levels of the interlayer exciton are reported in terms of exciton Rydberg energy $Ry^*_X = \hbar^2/2\mu_X a^{*2}_{0,X}$, where μ_X is the reduced mass of the exciton, and $a^*_{0,X} = 4\pi\varepsilon_\mathrm{hBN}\hbar^2/\mu_X e^2$ is the exciton Bohr radius, and $\varepsilon_\mathrm{hBN} = 4.5\varepsilon_0$. The obtained ground state exciton energy is $E_\mathrm{BX} = 0.4242\,Ry^*_\mathrm{X}$.

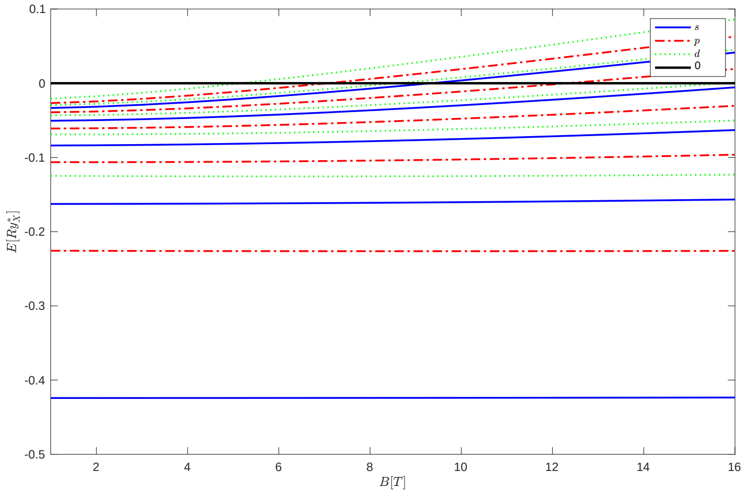

Figure 4.7: Energy levels of the s, p, d interlayer exciton for magnetic fields from $B = 1\,T$ up to $B = 16\,T$. The $1s$ exciton is the least susceptible of all the states to the magnetic field, due to the smallness of the exciton Bohr radius compared to the magnetic length. Higher excited Rydberg states ns with $n > 1$ as well as higher angular momentum states are more susceptible to the magnetic field due to the diamagnetic effect and the $\mathbf{L} \cdot \mathbf{B}$ coupling. At large magnetic fields, higher excited states become unbound.

4.6.2 Three-body problem of the interlayer exciton-graphene hole scattering

To describe trion formation, the Hamiltonian is very similar to Eqs. 4.47 to 4.49. However, we can transform the Hamiltonian in a suitable form by means of a unitary transformation akin to a magnetic LLP transformation.

The proper coordinate system for trion, are the trion COM and the relative coordinates with respect to the hole. Denoting the electron, hole and the carrier positions by $\mathbf{r}_e$, $\mathbf{r}_h$ and $\mathbf{r}_q$, respectively, the relative coordinates are $\mathbf{r}_{eh} = \mathbf{r}_e - \mathbf{r}_h$ and $\mathbf{r}_{qh} = \mathbf{r}_q - \mathbf{r}_h$. The total magnetic momentum of the trion in the symmetric gauge reads

$$\hat{\mathbf{\Gamma}}_{\text{tot}} = \hat{\mathbf{P}}_{\text{T}} + \frac{q}{c}\mathbf{A}(\hat{\mathbf{R}}_{\text{T}}) - \frac{e}{c}\left(1 + \frac{q}{e}\frac{m_e}{M_{\text{X}}}\right)\mathbf{A}(\hat{\mathbf{r}}_{eh}) + \frac{q}{c}\mathbf{A}(\hat{\mathbf{r}}_{qh})\,. \tag{4.50}$$

Similar to the gauge transformation we perfomed on the exciton Hamiltonian in Eq. 4.47, Equation 4.50 suggests to perform a gauge transformation of the following form on the trion Hamiltonian

$$\hat{U}_{\text{G}} = \exp\left[-\frac{i}{\hbar}\left(\hat{\mathbf{\Gamma}}_{\text{tot}} - \hat{\mathbf{P}}_{\text{T}} - \frac{q}{c}\mathbf{A}(\hat{\mathbf{R}}_{\text{T}})\right) \cdot \hat{\mathbf{R}}_{\text{T}}\right]. \tag{4.51}$$

After performing the above gauge transformation, one obtains the following trion Hamil-

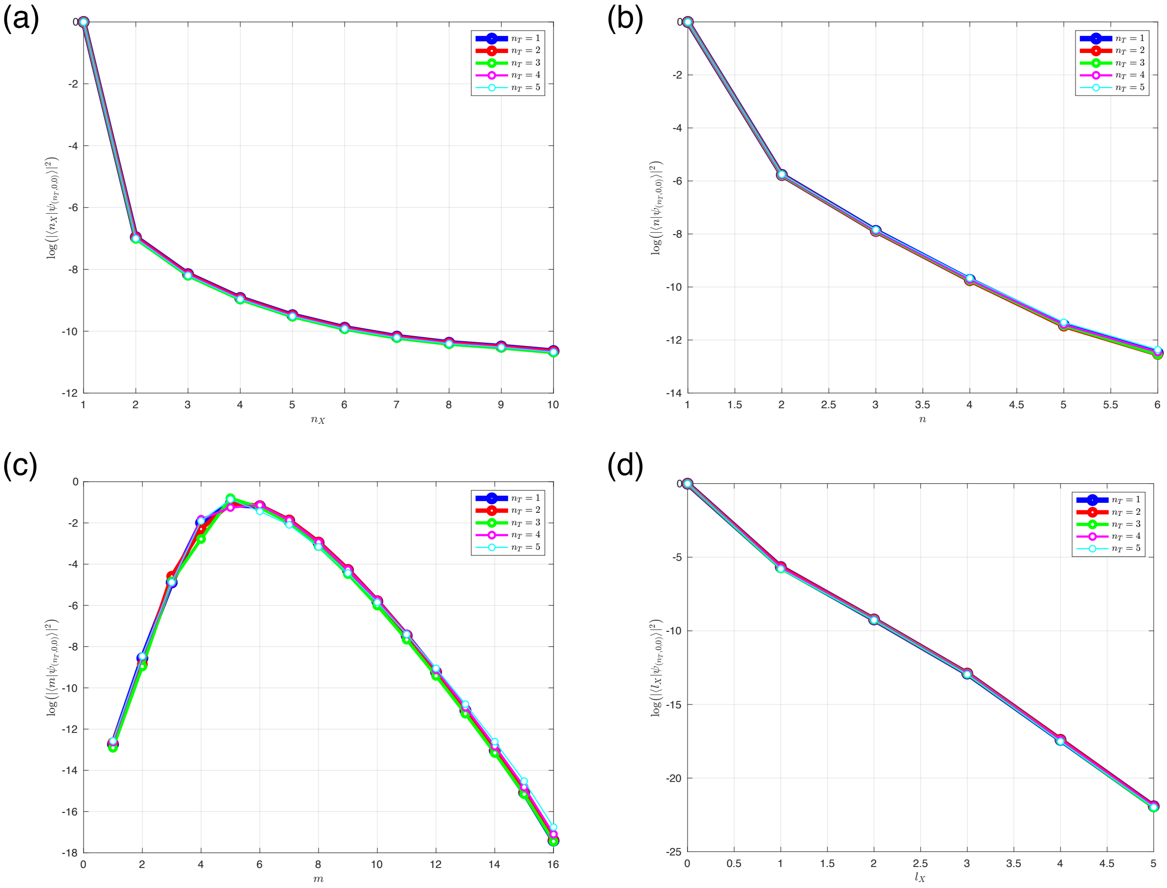

Figure 4.8: Characterization of the five lowest trion states, obtained by exact diagonalization of the trion Hamiltonian in Eq. 4.52. The trion states ψ_{n_T,M_T,L_T} are indexed by three quantum numbers: n_T is the principle quantum number, labeling the trion states in ascending order in energy; M_T is the magnetic degeneracy quantum number which is conserved akin to the Landau level states of point like charges in a uniform magnetic field, and as such, the trion energy levels are independent of M_T; L_T is the trion total orbital angular momentum. Here we drop the spin as we assume spin polarized graphene carriers. Furthurmore, particles belonging to different layers are assumed distinguishable, thus we neglect the particles spins. Shown in different panels are weight corresponding to different exciton Rydberg states (n_X) (a), hole Landau levels (n) (b), angular momentum eigenstates of the hole in the lowest Landau level (m), and exciton states with different angular momenta (l_X) (d), contributing to the trion states $\psi_{(n_T,0,0)}$, with $n_T = 1, \cdots, 5$ on a logarithmic scale. The main contribution to the trion state comes from the exciton $1s$ state and the hole lowest Landau level manifold.

tonian,

$$\begin{aligned}\hat{H}_{\mathrm{T}} = &\frac{\hat{\boldsymbol{\Pi}}_{\mathrm{T}}^2}{2M_{\mathrm{T}}} + \frac{\hat{\boldsymbol{\Pi}}_{\mathrm{T}}}{M_{\mathrm{T}}} \cdot \Big[-\hat{\mathbf{p}}_{qh} + \Big(\gamma_{eq} + \gamma_{hq}\Big)\mathbf{A}(\hat{\mathbf{r}}_{qh}) + \Big(\gamma_{eh} + \beta_e\Big)\mathbf{A}(\hat{\mathbf{r}}_{eh})\Big] \\ &+ \frac{1}{2m_e}\Big[\hat{\mathbf{p}}_{eh} + \beta_e\mathbf{A}(\hat{\mathbf{r}}_{eh}) + \gamma_{eq}\mathbf{A}(\hat{\mathbf{r}}_{qh})\Big]^2 + \frac{1}{2m_h}\Big[\hat{\mathbf{p}}_{eh} - \gamma_{eh}\mathbf{A}(\hat{\mathbf{r}}_{eh}) + \hat{\mathbf{p}}_{qh} - \gamma_{hq}\mathbf{A}(\hat{\mathbf{r}}_{qh})\Big]^2 \\ &+ v_{\mathrm{F}}\Big[\hat{\mathbf{p}}_{qh} + \beta_q\mathbf{A}(\hat{\mathbf{r}}_{qh}) + \gamma_{qe}\mathbf{A}(\hat{\mathbf{r}}_{eh})\Big] \cdot \hat{\boldsymbol{\sigma}}\,.\end{aligned} \tag{4.52}$$

In Eq. 4.52, the parameters β_e, β_q, γ_{eh}, γ_{eq} and γ_{hq} are defines as

$$\begin{cases}\beta_e = \Big(1 + \Big(m_e/M_{\mathrm{X}}\Big)^2 q/e\Big)\, e/c\,,\\ \beta_q = -q/c\,,\\ \gamma_{eh} = \Big(1 + \Big(m_e m_h/M_{\mathrm{X}}^2\Big)\, q/e\Big)\, e/c\,,\\ \gamma_{eq} = \Big(m_e/M_{\mathrm{X}}\Big)\, q/c\,,\\ \gamma_{hq} = -\Big(m_h/M_{\mathrm{X}}\Big)\, q/c\,.\end{cases} \tag{4.53}$$

The first term in the RHS of Eq. 4.52 gives the trion Landau level structure with trion cyclotron frequency $\omega_{\mathrm{T}} = |q|B/M_T c$, the second term is coupling of trion COM motion to the internal degrees of freedom, and the rest is the internal trion Hamiltonian. However, different trion Landau levels are mixed as a result of the interaction with the internal states, described by the second term in $\hat{H}_{\mathrm{T}}$. Using this result, the quantum numbers that characterize the trion states, are as the following

- Total angular momentum $L_{\mathrm{T}} = \mathrm{sign}(q)(m-n)+l_{\mathrm{X}}+\mathrm{sign}(q)(M_{\mathrm{T}}-N_{\mathrm{T}})$, where M_{T} and N_{T} are the magnetic and Landau level quantum numbers of the trion center-of-mass.
- Total spin S: Here we assumed spin-polarized particles, but it is possible to include the spin configurations of the particles if Zeeman splitting is negligible.
- Principle quantum number n_{T} : Indexes different bound states of H_{T}.
- Magnetic degeneracy number M_{T}: The total trion magnetic momentum $\boldsymbol{\Gamma}_{\mathrm{T}}$ leads to the degeneracy number M_T, similar to an electron in a magnetic field.

A typical trion state, thus is indexed by quantum numbers $(n_{\mathrm{T}}, M_{\mathrm{T}}, L_{\mathrm{T}}, S_{\mathrm{T}})$. However, since we assume the particles in different layers to be distinguishable, and the hole is assumed to be spin polarized, we neglect S_{T} hereafter.

To diagonalize the Hamiltonian $\hat{H}_{\mathrm{T}}$, we calculate the matrix elements of $\hat{H}_{\mathrm{T}}$ over the product states $|n_X, l_X\rangle \otimes |n, m\rangle$, where n_X and l_X are the exciton principle quantum number and orbital angular momentum quantum numbers, respectively, and n, m are the usual Landau level indices of the hole. Particularly, in the context of the disk geometry used here,

m is related to the angular momentum of the hole by $\mathrm{sign}(q)(n-m)$. The interlayer trion binding energy that we calculate for $B = 1\,T$ is $E_T = 0.0037\,Ry^*_X \simeq 0.8056\,\mathrm{meV}$, which is $0.87\,\%$ of the interlayer exciton binding energy, a quantity that is directly experimentally observable.

4.7 From few- to many-body body physics in exciton-quantum Hall systems: exciton quantum Hall polarons and anyonic trions

Having characterized in detail the three-body scattering problem of an IX and a graphene hole, we are now at the position to apply the obtained insights to model the physics of IX and charge carriers in the quantum Hall regime. We are particularly interested to see if an exciton can bind a quasihole.

To this end, we first introduce the LLP transformation on a sphere, and then use it to simplify the system Hamiltonian. In particular, LLP implies a particular structure for the eigenstates of the system in the impurity frame, which make the angular momentum conservation manifest, and also can guide the intuition into the formation of anyonic trions and the other bound state discussed above.

4.7.1 Lee-Low-Pines transformation on the sphere

Here we elaborate on the application of the Lee-Low-Pines transformation to the impurity-quantum Hall system which was crucial to obtain the results in this work. To this end, we again consider the problem of a neutral mobile impurity X interacting with a quantum Hall system of N particles with mass m and charge q with fractionally filled lowest Landau level. Both systems are put on a sphere with radius R enclosing a magnetic monopole with strength Q. The full Hamiltonian reads

$$\hat{H} = \frac{\hat{\mathbf{L}}_{\mathrm{X}}^2}{2M_{\mathrm{X}}R^2} + \sum_{i=1}^{N} V_{XC}(\hat{\mathbf{r}}_i - \hat{\mathbf{r}}_{\mathrm{X}}) + \hat{H}_{\mathrm{FQH}}\,. \tag{4.54}$$

In Eq. 4.54, M_{X}, $\hat{\mathbf{r}}_{\mathrm{X}}$ and $\hat{\mathbf{L}}_{\mathrm{X}}$ are, respectively, the impurity's mass, position and angular momentum, V_{XC} is the impurity-carrier interaction potential, $\hat{\mathbf{r}}_i$ is the position of the i'th carrier, and $\hat{H}_{\mathrm{FQH}}$ is given in Eq. 4.12. The full rotational symmetry of the impurity-quantum Hall system implies that the spectrum is invariant under the rotation which bring the impurity at a position $\mathbf{r}_{\mathrm{X}}$ to $\mathbf{r}_0 = R\,\mathbf{e}_z$, where $\mathbf{e}_z$ is the unit vector along the z axis. This rotation is performed by the following unitary

$$\hat{U}_{\mathrm{LLP}} = e^{-i\hat{\varphi}\otimes\hat{L}_z}\, e^{-i\hat{\theta}\otimes\hat{L}_y}\, e^{-i\hat{\gamma}\otimes\hat{L}_z}\,. \tag{4.55}$$

In Eq. 4.55, $\hat{U}_{\mathrm{LLP}}$ acts on the whole quantum Hall system with total angular momentum $\hat{\mathbf{L}} = \sum_{i=1}^{N}\hat{\mathbf{L}}_i$ to rotate it by a rotation which brings a rigid body in the state $|\varphi,\theta,\gamma\rangle$

characterized with Euler angles $(\varphi, \theta, \gamma)$ to $|\varphi = 0, \theta = 0, \gamma = 0\rangle$. This transformation is very similar to the angulon transformation used in the study of quantum rotors like dimers in BECs and formation of angulon quasiparticles [181, 180]. Note, however, that the physics of angulons and the thermodynamic limit of its setting is completely different from the setting considered here, and the only formal similarity between the two settings is the rotational symmetry of the problem. Note also that, although for a point-like impurity the Euler angle γ is not defined, it should be kept throughout the calculations to maintain the entire group structure of the rotations of the quantum Hall system.

To make use of the LLP transformation, it is necessary to understand its effect on the full Hamiltonian $\hat{H}$ as well as an arbitary state $|J, M, n; \alpha\rangle_{\mathrm{X,QH}}$ of the whole system with angular momentum quantum numbers J, M and n (we discuss the meaning of the quantum number n later). First, we inspect different terms in the Hamiltonian. The quantum Hall Hamiltonian $\hat{H}_{\mathrm{FQH}}$ is obviously rotationally invariant. Application of $\hat{U}_{\mathrm{LLP}}$ on $V_{XC}(\hat{\mathbf{r}}_i - \hat{\mathbf{r}}_{\mathrm{X}})$ yields

$$\hat{U}^{\dagger}_{\mathrm{LLP}}\, V_{XC}(\hat{\mathbf{r}}_i - \hat{\mathbf{r}}_{\mathrm{X}})\, \hat{U}_{\mathrm{LLP}} = V_{XC}(\hat{\mathbf{r}}'_i - \mathbf{r}_0)\,, \tag{4.56}$$

where $\mathbf{r}'_i = \mathcal{R}(\varphi, \theta, \gamma)[\mathbf{r}_i]$ is the rotated position of the i'th particle. In Eq. 4.56, it is noticable that the action of $\hat{U}_{\mathrm{LLP}}$ has removed the impurity degree of freedom, thus instead of interacting with a mobile impurity, all the particles in the quantum Hall system interact with a static potential localized around $\mathbf{r}_0$.

The action of $\hat{U}_{\mathrm{LLP}}$ on the impurity kinetic energy is more involved. To proceed with the analytics, it is more convenient to work with the spherical tensor components of the angular momentum operators. For any vector operator $\hat{\mathbf{O}} = \hat{O}_x \mathbf{e}_x + \hat{O}_y \mathbf{e}_y + \hat{O}_z \mathbf{e}_z$, the spherical tensor components are defined by and $\hat{O}_\mu = (-\mu)/\sqrt{2}\,(\hat{O}_x + i\mu\hat{O}_y)$, $\mu = \pm 1$.

$$\begin{cases} \hat{O}_0 = \hat{O}_z\,, & \mu = 0\,, \\ \hat{O}_\mu = -\frac{\mu}{\sqrt{2}}\left(\hat{O}_x + i\mu\hat{O}_y\right), & \mu = \pm 1\,. \end{cases} \tag{4.57}$$

Accordingly, the spherical tensor components of the impurity angular momentum operator in coordinate space read

$$\begin{cases} \hat{L}_{X,0}(\varphi, \theta, \gamma) = -i\partial_\varphi\,, \\ \hat{L}_{X,\pm 1}(\varphi, \theta, \gamma) = \frac{i}{\sqrt{2}}\, e^{\pm i\varphi}\left[\pm \cot(\theta)\partial_\gamma + i\partial_\theta \mp \frac{1}{\sin(\theta)}\partial_\varphi \right]. \end{cases} \tag{4.58}$$

Applying $\hat{U}_{\mathrm{LLP}}$ to $\hat{L}_{X,\mu}$ directly gives

$$\hat{U}^{\dagger}_{\mathrm{LLP}}\, \hat{L}_{X,\mu}\, \hat{U}_{\mathrm{LLP}} = \hat{L}_{X,\mu} - \sum_{\nu} D^{(1)*}_{\mu\nu}(\hat{\varphi}, \hat{\theta}, \hat{\gamma})\, \hat{L}_\nu\,, \tag{4.59}$$

where $D^{(1)*}_{\mu\nu}(\varphi, \theta, \gamma)$ is the complex conjugate of the Wigner D-matrix $D^{(1)}$, and L_ν is the ν-component of the total angular momentum of the quantum Hall system. From Eq. 4.59, it is evident that $\hat{U}_{\mathrm{LLP}}$ imprints the effect of the many-body medium on the impurity through the total angular momentum components $\hat{L}_\nu$. The LLP transformation of $\hat{\mathbf{L}}^2$ is then achieved by using Eq. 4.59 as the following,

$$\hat{U}^\dagger_{\mathrm{LLP}}\,\hat{\mathbf{L}}^2_{\mathrm{X}}\,\hat{U}_{\mathrm{LLP}} = \hat{\mathbf{L}}'^2_{\mathrm{X}} - \sum_\mu (-1)^\mu \hat{L}'^{(-\mu)}_{\mathrm{X}}\,\hat{L}_\mu + \hat{\mathbf{L}}^2 = \left(\hat{\mathbf{L}}'^{(c)}_{\mathrm{X}} - \hat{\mathbf{L}}\right)^2 , \tag{4.60}$$

In Eq. 4.60, $\hat{\mathbf{L}}'^{(c)}_{\mathrm{X}} = \sum_\mu \hat{L}'^\mu_{\mathrm{X}}\,\mathbf{e}_\mu$ is *the contravariant angular momentum* of the impurity, with $\hat{L}'^\mu_{\mathrm{X}} = (-1)^\mu \hat{L}'_{\mathrm{X},-\mu}$, and $\hat{L}'_{\mathrm{X},\mu}$ is the impurity angular momentum in *the body-fixed frame*, that is the frame rotated with respect to *the space-fixed frame by* the Euler angles φ, θ, γ. Explicitly, these components are related to one another by

$$\begin{cases} \hat{L}'^\mu_{\mathrm{X}} = \sum_\nu D^{(1)}_{\nu\mu}(\varphi,\theta,\gamma)\,\hat{L}_{\mathrm{X},\nu}\,, \\ \hat{L}_{\nu,\mathrm{X}} = \sum_\mu D^{(1)*}_{\nu\mu}(\varphi,\theta,\gamma)\,\hat{L}'^\mu_{\mathrm{X}}\,. \end{cases} \tag{4.61}$$

From the definition of $\hat{\mathbf{L}}'^{(c)}_{\mathrm{X}}$, it is straightforward to show that

$$\hat{L}'^\mu_{\mathrm{X}} = -\hat{\mathcal{I}}^\dagger\,\hat{L}^\mu_{\mathrm{X}}\,\hat{\mathcal{I}}\,, \tag{4.62}$$

where $\hat{\mathcal{I}}\,|j,m\rangle = |j,-m\rangle$. Equation. 4.62 leads to the result that the eigenvalues of the spherical LLP term is the same as the total angular momentum $\hat{\mathbf{L}}_{\mathrm{tot}} = \hat{\mathbf{L}}_{\mathrm{X}} + \hat{\mathbf{L}}$. In order to come from Eq. 4.59 to Eq. 4.60, the following identities that are the defining differential equations for $D^{(j)}_{\mu\lambda}(\hat{\varphi},\hat{\theta},\hat{\gamma})$ must be used,

$$\begin{cases} [\hat{L}_\nu, D^{(j)}_{\mu\lambda}(\hat{\varphi},\hat{\theta},\hat{\gamma})] = (-1)^{1+\nu}\sqrt{j(j+1)}\,C^{j,\mu-\nu}_{j,\mu;1,-\nu}\,D^{(j)}_{(\mu-\nu)\lambda}(\hat{\varphi},\hat{\theta},\hat{\gamma})\,, \\ [\hat{L}'^\nu, D^{(j)}_{\mu\lambda}(\hat{\varphi},\hat{\theta},\hat{\gamma})] = -\sqrt{j(j+1)}\,C^{j,\lambda+\nu}_{j,\lambda;1,\nu}\,D^{(j)}_{\mu(\lambda+\nu)}(\hat{\varphi},\hat{\theta},\hat{\gamma})\,, \end{cases} \tag{4.63}$$

where $C^{j,\mu}_{j_1,\mu_1;j_2,\mu_2} = \langle j_1,\mu_1;j_2,\mu_2|j,\mu\rangle$ are Clebsch-Gordan coefficients. After performing all the steps above, the total system Hamiltonian in the LLP frame takes the following form

$$\hat{H}_{\mathrm{LLP}} = \frac{1}{2M_X R^2}\left(\hat{\mathbf{L}}'^{(c)}_{\mathrm{X}} - \hat{\mathbf{L}}\right)^2 + \sum_{i=1}^{N} V_{XC}(\hat{\mathbf{r}}'_i - \mathbf{r}_0) + \hat{H}_{\mathrm{FQH}}\,, \tag{4.64}$$

The next step is to find the form an arbitrary state $|J,M,n;\alpha\rangle_{\mathrm{X,QH}}$ of the full system with angular momentum quantum numbers J, M and n, and the rest of the quantum numbers summarized in α. To this end, we note that $|J,M,n;\alpha\rangle_{\mathrm{X,QH}}$ takes the most general form

$$|J,M,n;\alpha\rangle_{\mathrm{X,QH}} = \sum_{j,L,\beta} c_{j,L;\alpha,\beta} \sum_{m,N} C^{J,M}_{j,m;L,N}\,|j,m,n\rangle_{\mathrm{X}} \otimes |L,N;\beta\rangle_{\mathrm{QH}} = \sum_{j,L,\beta} c_{j,L;\alpha,\beta}\,|j,L;\beta\rangle_{\mathrm{X,QH}}\,. \tag{4.65}$$

In Eq. 4.65, $|j,m,n\rangle_{\mathrm{X}}$ is an angular-momentum-j eigenstate of $\hat{\mathbf{L}}^2_{\mathrm{X}}$, and the quantum numbers m and n denote the angular momentum projections along the z axis in the space-fixed and body-fixed frames, respectively. More explicitely,

$$\begin{cases} \hat{\mathbf{L}}^2_{\mathrm{X}}\,|j,m,n\rangle_{\mathrm{X}} = \hbar\,j(j+1)\,|j,m,n\rangle_{\mathrm{X}}\,, \\ \hat{L}_{\mathrm{X},z}\,|j,m,n\rangle_{\mathrm{X}} = \hbar\,m\,|j,m,n\rangle_{\mathrm{X}}\,, \\ \hat{L}'_{\mathrm{X},z}\,|j,m,n\rangle_{\mathrm{X}} = \hbar\,n\,|j,m,n\rangle_{\mathrm{X}}\,. \end{cases} \tag{4.66}$$

The state $|L, N; \beta\rangle_{\mathrm{QH}}$ is an eigenstate of $\hat{H}_{\mathrm{FQH}}$ with angular momentum quantum numbers L and N, and labeled by β. It is clear from the form of $|J, M, n; \alpha\rangle_{\mathrm{X,QH}}$ in Eq. 4.65 that it suffices to evaluate $\hat{U}^{\dagger}_{\mathrm{LLP}}$ on $|j, m, n\rangle_{\mathrm{X}} \otimes |L, N; \beta\rangle_{\mathrm{QH}}$,

$$\begin{aligned}\hat{U}^{\dagger}_{\mathrm{LLP}}\, |j, m, n\rangle_{\mathrm{X}} \otimes |L, N; \beta\rangle_{\mathrm{QH}} = \int_0^{2\pi} d\gamma \int_0^{\pi} d\theta \sin(\theta) \int_0^{2\pi} d\varphi \sqrt{\frac{2j+1}{8\pi^2}}\, D^{(j)*}_{mn}(\varphi, \theta, \gamma)\, |\varphi, \theta, \gamma\rangle_{\mathrm{X}} \\ \otimes\, \hat{U}^{\dagger}(\varphi, \theta, \gamma)\, |L, N; \beta\rangle_{\mathrm{QH}} \; .\end{aligned} \tag{4.67}$$

To proceed, we use the transformation of angular momentum representations under arbitrary rotations

$$\hat{U}^{\dagger}(\varphi, \theta, \gamma)\, |L, N; \beta\rangle_{\mathrm{QH}} = \sum_{N'} D^{(L)*}_{NN'}(\varphi, \theta, \phi)\, |L, N'; \beta\rangle_{\mathrm{QH}} \; , \tag{4.68}$$

together with several identities involving angular momentum summations and symmetry properties of the Wigner D matrices and Clebsch-Gordan coefficients to finally arrive at

$$\hat{U}^{\dagger}_{\mathrm{LLP}}\, |j, L; \beta\rangle_{\mathrm{X,QH}} = \sum_{N'} (-1)^{L+N'}\, C^{j,(-n)*}_{J,-(n+N');L,N'}\, |J, M, n+N'\rangle_{\mathrm{X}} \otimes |L, N'; \beta\rangle_{\mathrm{QH}} \; . \tag{4.69}$$

Inserting Eq. 4.69 into Eq. 4.65,

$$\hat{U}^{\dagger}_{\mathrm{LLP}}\, |J, M, n; \alpha\rangle_{\mathrm{X,QH}} = \sum_{L,N',\beta} f_{L,N',n;\alpha,\beta}\, |J, M, n+N'\rangle_{\mathrm{X}} \otimes |L, N'; \beta\rangle_{\mathrm{QH}} \; , \tag{4.70}$$

where $f_{L,N',n;\alpha,\beta} = \sum_j (-1)^{L+N'} C^{j,(-n)*}_{J,-(n+N');L,N'}\, c_{j,L;\alpha,\beta}$. For a point-like impurity, one can set $n = 0$, and n drops out of the equations. The final form of the state in the LLP frame is thus

$$\hat{U}^{\dagger}_{\mathrm{LLP}}\, |J, M; \alpha\rangle = \sum_{L,N,\beta} f_{L,N;\alpha,\beta}\, |J, M, N\rangle_{\mathrm{X}} \otimes |L, N; \beta\rangle_{\mathrm{QH}} \; , \tag{4.71}$$

with $f_{L,N;\alpha,\beta} = \sum_j (-1)^{L+N'} C^{j,0\,*}_{J,-N;L,N}\, c_{j,L;\alpha,\beta}$. Application of the special form of the states in the LLP frame as in Eq. 4.71 for exact diagonalization of $\hat{H}_{\mathrm{LLP}}$ forms the foundations of the results obtained in this work.

We apply the spherical LLP transformation above to the IX-FQH system by numerically diagonalizing the Hamiltonian $\hat{H}_{\mathrm{LLP}}$ in Eq. 4.64 over the states $|J, M, N\rangle_{\mathrm{X}} \otimes |L, N; \beta\rangle_{\mathrm{QH}}$. In the following section, we discuss the results.

4.7.2 Results

To understand the results in the section, we first lay out some basic facts about the numerical diagonalization of $\hat{H}_{\mathrm{FQH}}$ in spherical geometry. The details about the Landau level structure of charged particles on a sphere are outlined in Appendix C. Direct construction of Laughlin states on the sphere [93, 105] shows that for N particles, the incompressible

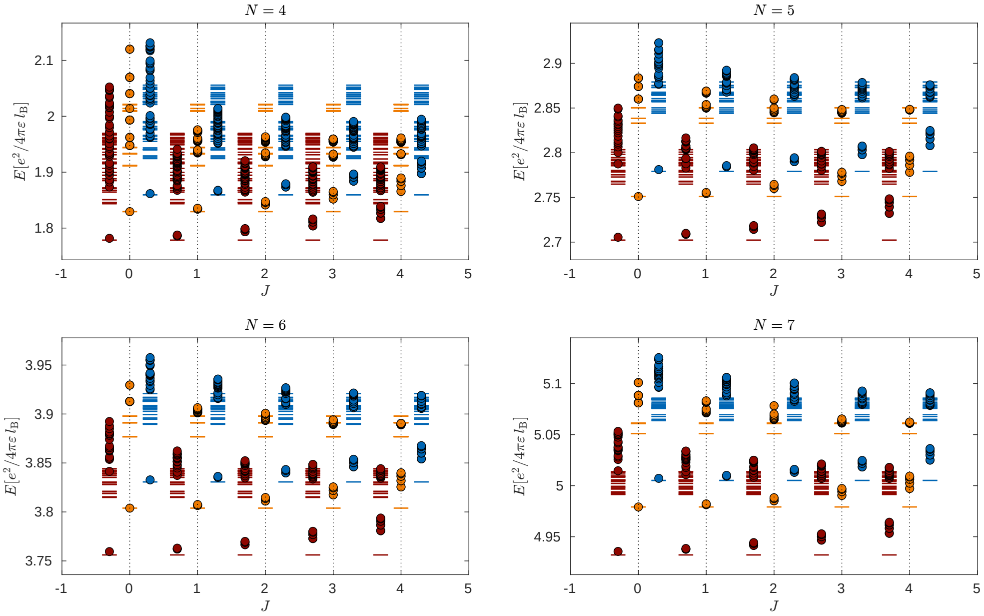

Figure 4.9: Many-body energies of the exciton interacting with a $\nu=1/3$ system of $N=4-7$ electrons (panels (a)-(e)), at fillings characterized by monopole strengths in the range $Q_{\mathrm{LN}}=3/2(N-1)$, associated to the presence of the Laughlin state. The red and blue dots corresponds to the attractive and repulsive exciton-electron interactions, respectively, while the orange dots correspond to zero exciton-electron interaction. For comparison, the lowest energy states of the infinitely heavy impurity is also shown (dashed), with the same color code denoting the exciton-electron interactions. The spectrum for all particle numbers is characterized by a dispersive low energy branch of quasiparticles on top of the Laughlin state, for both attractive and repulsive interactions. This branch correspond to the dressing of the exciton with magnetorotons. States with definite total angular momenta $J=0-4$ are considered. For FQH systems with even particle number, the ground state is realized in the $J=N/2$ sector. For the purpose of visibility, the energies in the repulsive and attractive cases are shifted to the right and left, respectively.

Laughlin state at filling $\nu=1/m$ occurs for magnetic monopoles $Q_{\mathrm{LN}}=m/2(N-1)$, which in the thermodynamic limit gives the correct filling factor. Indeed, the spectrum of a FQH liquid at Q_{LN} has a gapped ground state at total angular momentum $L=0$ (the fully isotropic liquid), a magnetoroton branch, and further higher excitations. Fig. 4.5 shows the lowest part of the energy spectrum for $N=8$ electrons. The Laughlin gap converges to a constant ($\sim 0.1\,E_C$ where E_C is the characteristic Coulomb energy scale at the magnetic length, $E_C=e^2/4\pi\varepsilon l_{\mathrm{B}}$) in the thermodynamic limit and the magnetoroton remains a well-defined excitation branch, while higher excited states are non-universal and their values depend on the specific system under consideration.

To create a quasihole, one single unit of flux has to be introduced in the system. This can be accomplished by: 1) removing particles from the system, 2) increasing the magnetic flux at fixed area and particle number, and 3) by increasing the area at fixed magnetic flux

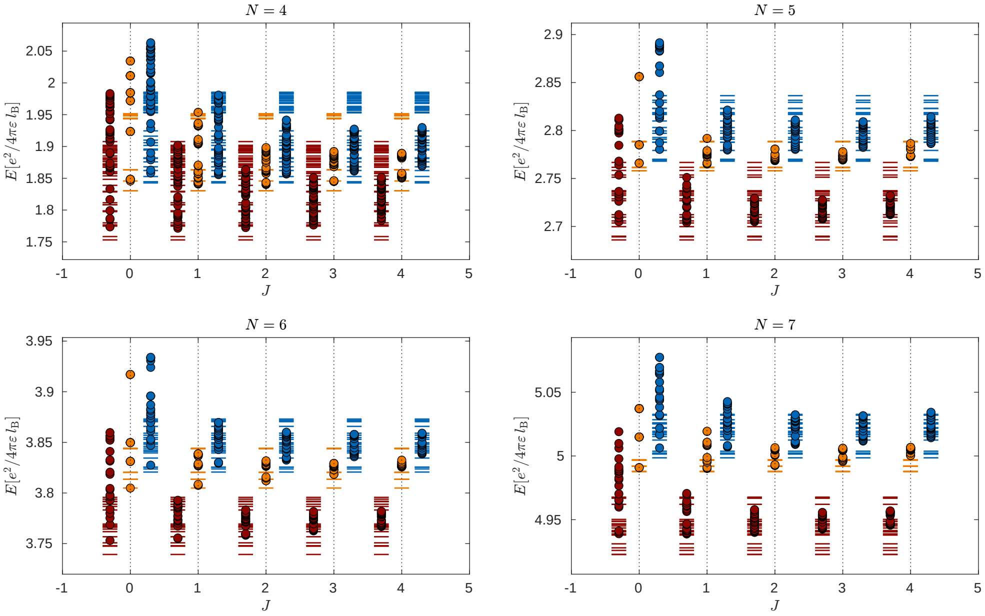

Figure 4.10: Same as Fig. 4.9, but for a magnetic monopole $Q = Q_{\rm LN} + 1$, corresponding to two quasiholes on top of the Laughlin state. The strong mixing of the exciton kinetic energy states, the higher density of two-quasihole states and the smaller gap of those states to the excited states results in a featureless pattern of excitations, for both attractive and repulsive interactions.

density and particle number [140, 147]. However, to compare the energetics of the system in different cases (presence/absence of the exciton), it is more convenient to increase the magnetic flux at fixed particle number and area, especially since the FQH system is not charge neutral. To increase the flux by one quantum means to increase Q by a half integer, thus the monopole strength at which a single flux defect is introduced to the system is $Q_{\rm qh} = Q_{\rm LN} + 1/2$. Counting the degeneracy of the ground state manifold reveals that the total angular momentum of the ground state is $L = N/2$ [93]. Similarly, removing a flux quantum from the system creates a quasiparticle defect. In this case, the system again has a total angular momentum $L = N/2$ (see [94] for more details).

We diagonalize the system described by $\hat{H}_{\rm LLP}$ in Eq. 4.64 over the states $|J, M, N\rangle_{\rm X} \otimes |L, N; \beta\rangle_{\rm QH}$ for $B = 16\,T$, and obtain the few lowest eigenstate (~ 20), for different values of J depending on the particle number and different monopole strengths corresponding to one and two quasiholes, one quasiparticle and the Laughlin filling, for repulsively interacting, non-interacting, and attractively interacting exciton-FQH systems. Note that, since the quasihole and quasiparticle occur at total angular momentum $N/2$ of the FQH alone, the value of the total angular momentum of exciton-FQH system has to be a half-integer when N is odd. Aside from energy eigenvalues, another interesting quantity that gives useful information into the structure of the eigenstates is the exciton-electron $g^{(2)}(\mathbf{r})$ function, defined as ([105])

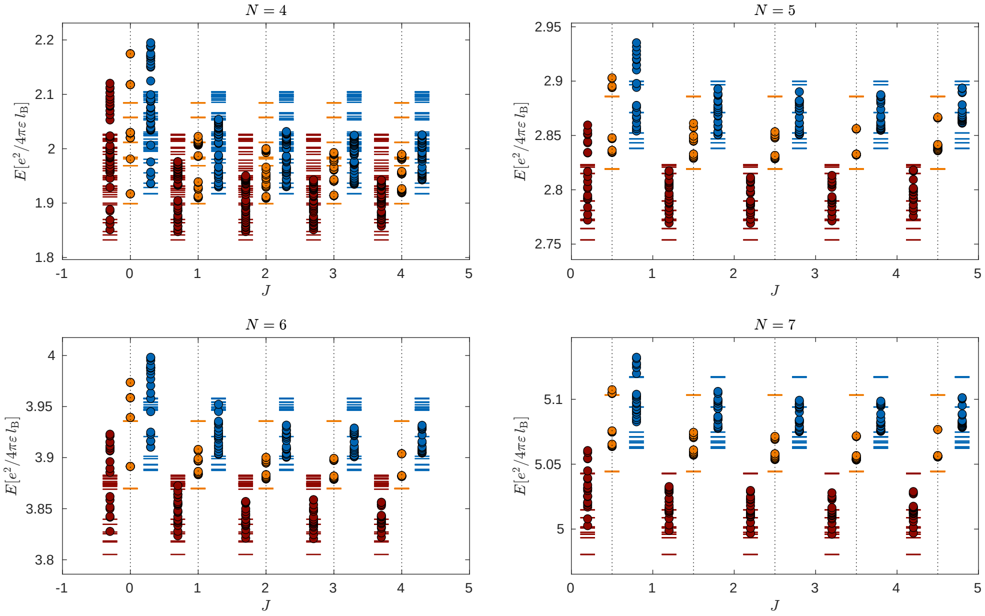

Figure 4.11: Same as Fig. 4.9, but for a magnetic monopole $Q = Q_{\mathrm{LN}} - 1/2$, corresponding to a single quasiparticle on top of the Laughlin state. Contrary to the single quasihole case, no well defined dispersive quasiparticle branch is visible.

$$g^{(2)}(\mathbf{r}) = \frac{1}{\rho N} \sum_{i=1}^{N} \langle \delta^{(2)}(\mathbf{r}_i - \mathbf{r}_X - \mathbf{r}) \rangle \,. \tag{4.72}$$

Intuitively, $g^{(2)}(\mathbf{r})$ means that for an exciton at position $\mathbf{r}_X$, what is the probability to find an electron at a distance $\mathbf{r}$ away. It turns out that in the LLP frame, $g^{(2)}$ takes a rather simple form as below

$$g^{(2)}(\mathbf{\Omega}) = \frac{\langle \hat{\tilde{\rho}}(\mathbf{\Omega}) \rangle}{\frac{1}{4\pi} \int d\Omega \, \langle \hat{\tilde{\rho}}(\mathbf{\Omega}) \rangle} \,, \tag{4.73}$$

since in the LLP frame, the impurity is exactly localized at the north pole of the sphere. It is more convenient to work with $g^{(2)}(\theta)$ which is the angular average of $g^{(2)}(\mathbf{\Omega})$ in the azimuthal direction, $g^{(2)}(\theta) = 1/2\pi \int d\varphi \, g^{(2)}(\mathbf{\Omega})$.

First we discuss the cases for the Laughlin, one quasiparticle, and two quasihole fillings (see Fig. 4.9). When $Q = Q_{\mathrm{LN}}$, the spectrum for all particle numbers is characterized by a dispersive low energy branch of quasiparticles on top of the Laughlin state, for both attractive and repulsive interactions. This branch correspond to the dressing of the exciton with magnetorotons, and is also obtained in the context of magnetoexcitons in GaAs [82]. For increasing J, the lower branch splits into closely spaced eigenstates, suggesting that this branch acquires a finite lifetime with increasing total momentum in the thermodynamic limit. For the J values considered here, the gap to the higher excited states remains open, while its magnitude decreases. For the purpose of visibility, the energies in the repulsive and attractive cases are shifted to the right and left, respectively.

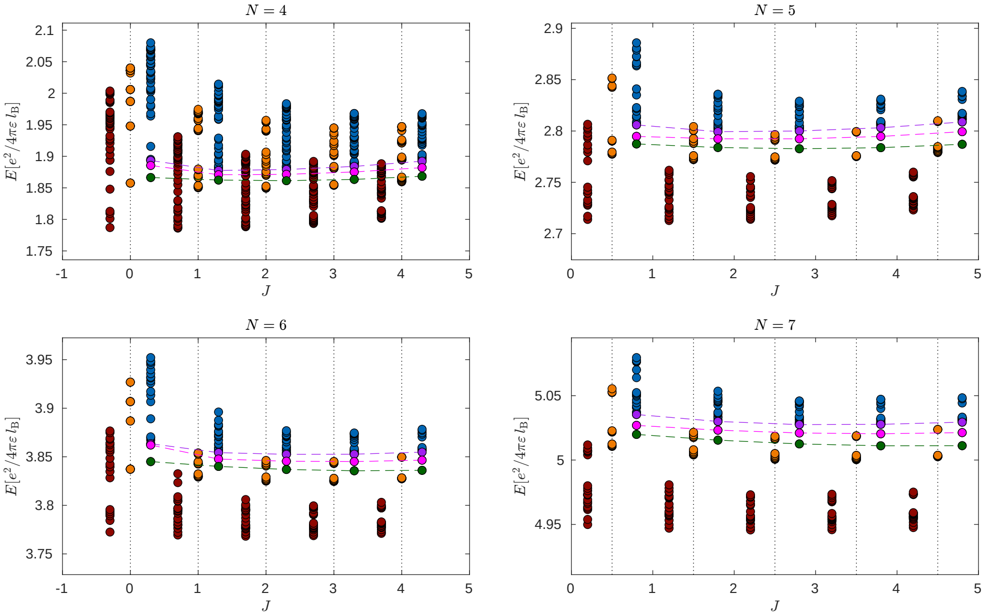

Figure 4.12: Same as Fig. 4.9, but for a magnetic monopole $Q = Q_{\mathrm{LN}} + 1/2$, corresponding to a single quasiholes on top of the Laughlin state. For attractive interactions, clear signatures of bound state formation does not appear, while for repulsive interactions, for all particle numbers, two gapped non-degenerate states appear as the lowest energy states for all the angular momenta $J = 0 - 4$ for even particle numbers and $J = 0.5 - 4.5$ for odd particle numbers. The ground state particle is marked by dark green, the first gapped excited state by pink, and the second excited state which occurs at the onset of the continuum in purple. The ground state of the system occurs at $J = N/2$ for all the particle numbers (the difference is not visible in the case of $N = 7$), corresponding to the total angular momentum sector at which the quasihole occurs.

The next filling factor corresponds to the two quasihole case, where the FQH system contains two additional flux quanta. The spectrum in this case is depicted in Fig. 4.10. In the absence of the exciton, the lowest energy eigenstates of the two quasihole system occur at total angular momenta $L = N, N-2, N-4, \cdots$ [94]. This is because the two quasiholes are indistinguishable particles that can be both bosons or fermions (note that all loops on a sphere are contractible). The gap of two quasihole states with definite relative and total angular momenta to their excited states is much smaller, and the number of states in the low energy manifold comprised by these states are larger. This leads to a stronger mixing of these states when the mobile exciton is added to the system, resulting in a featureless pattern of excitations, for both attractive and repulsive interactions.

The case corresponding to the single quasiparticle also shows no well-defined gap in the low energy spectrum, as depicted in Fig. 4.11. In this case, instead of binding to a quasiparticle, we find that the density distribution around the exciton more resembles the one for a excited state of the FQH higher than the quasipartile, that has higher density at the position of the exciton, see Fig. 4.13.

More interesting than the above cases is the exciton-FQH spectrum at a single quasihole, depicted in Fig. 4.12. In this case, we consistently find the signatures of two non-degenerate bound states below the continuum for repulsive interactions, for electron numbers $N=4$ to $N=7$. The first bound state (shown in dark green in Fig. 4.12) acquires its minimum energy at $J=N/2$, corresponding to the angular momentum at which the quasihole forms the gapped ground state manifold of the system. The second bound state (shown in pink in Fig. 4.12) also shows a similar behavior as a function of the total angular momentum of the system. The second excited state (shown in purple in Fig. 4.12), marks the onset of the continuous spectrum. The energy gaps of these states are also depicted in Fig. 4.14 as a function of $1/N$, for various values of the angular momenta. We observe that both gaps show a saturation behavior with respect to $1/N$, suggesting that they go to a finite value in the thermodynamic limit. Furthermore, both of the gaps have a value $\sim 0.009\,E_C$. For $E_C \simeq 49.9$ meV at $B=16\,T$, this gap is around 0.45 meV, which can be observed in the experiments.

Having found the peculiar emergence of these states, we try to gain more insight into their structure. To this end, we evaluate the $g^{(2)}(\theta)$ function associated to these states and few higher excitations, depicted in Figs. 4.15, 4.16 and 4.17. The excellent agreement of the $g^{(2)}(\theta)$ function of the ground state to the single quasihole state strongly suggests that this state is the exciton-quasihole bound state we were after, that is *the anyonic trion*. The structure of the $g^{(2)}$ function also does not depend on J, suggesting that this state is robust even when the kinetic energy of the exciton is increased.

The $g^{(2)}$ function of the first excited state (the second bound state) shows very similar signatures as the ground state one. However, it is notable in Fig. 4.16 that the electron density does not vanish entirely at the origin. The non vanishing electron density at the origin further increases with J, which is a feature different than the ground state.

The $g^{(2)}$ function of the second excited state again shows a marked difference compared to the above to situations. Importantly, as strong density fluctuation is observed with a strong density increase at the exciton density, consistent with the higher energy of this state compared to the two bound states.

One might ask the question: why there are only two bound states arising in the spectrum, and not more? While we do not have a full answer to this questions, we can obtain some insight on the composition of different states constituting the two bound states. To this end, we compared the excitation spectrum of the system without any exciton, to the one containing a single immobile exciton, a situation which is experimentally relevant for the setting of a Quantum Optical Twist and Scan Microscope (QOTSM). Fig. 4.18 depicts this comparison. In panel (a), the spectrum of the FQH system for $N=7$ electrons containing one quasihole in the form of an additional flux quantum is depicted in black lines, together with the spectrum with a single exciton localized around $\mathbf{r}_0 = R\,\mathbf{e}_z$ in red circles. The three visible gaps in the FQH spectrum are also highlighted. It is evident that the presence of the localized exciton potential singles out the quasihole localized around the exciton, and the rest of the states in the degenerate quasihole manifold are raised in energy, forming a band akin to a magnetoroton branch. All these states still remain in the quasihole gap, with a non-vanishing gap to the higher excited states. This behavior also

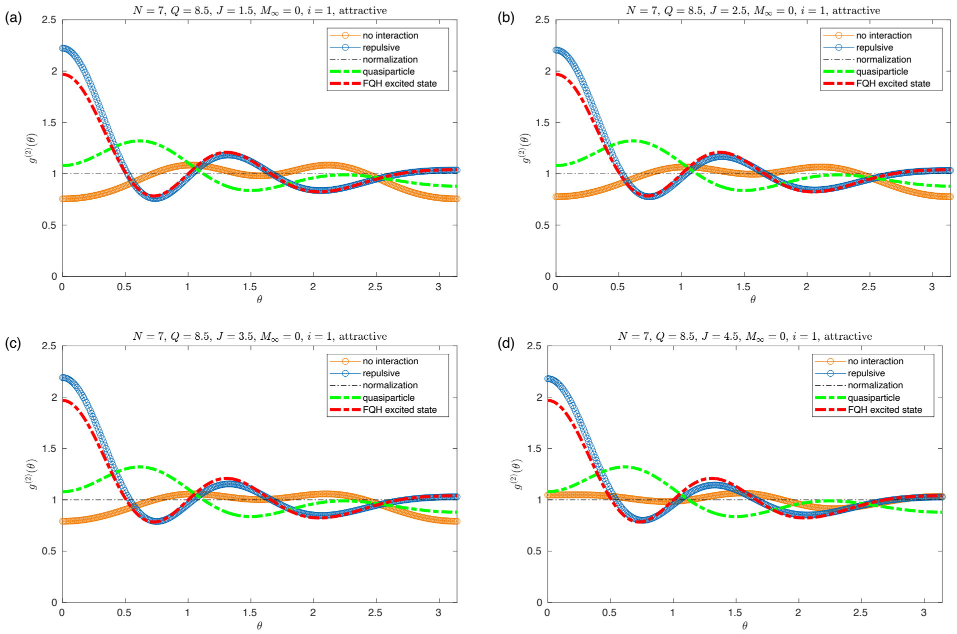

Figure 4.13: The exciton-electron $g^{(2)}(\theta)$ function, marked by the blue line, for the case of a mobile exciton, calculated using Eq. 4.73, for $N = 7$ electrons at a single quasiparticle filling. The exciton-electron interaction is attractive, $i = 1$ indicates that the $g^{(2)}$ belongs to the ground state, and $M_\infty = 0$ indicates that the exciton is mobile. (a)-(c) are the $g^{(2)}$ values for $J = 1.5{-}4.5$, respectively. For comparison, The $g^{(2)}$ function for the quasiparticle localized around $\mathbf{r}_0$ in a FQH with no impurity is also depicted by green dashed-dotted line. However, the $g^{(2)}$ function of the interacting system more resembles the one of an excited state of the FQH system, which has higher magnitude around the impurity. The $g^{(2)}$ function of the non-interacting state (mobile exciton with no interaction with the FQH system) is also depicted.

persists for $N = 8$ particles, depicted in panel (b) of Fig. 4.18. This fact suggests that, if the exciton kinetic term, present in $\hat{H}_{\text{LLP}}$ in Equation. 4.64, is turned on, the only relevant states that mix and contribute to the structure of the low energy parts of the spectrum, are first, the quasihole state localized on the north pole, and second, the magnetoroton branch. In Fig. 4.19, we compare the lowest part of the full interacting system (with the same color code as the one in Fig. 4.12) to the energies depicted in Fig. 4.18. As it is observed, the energies of the two bound states lie very close to the bottom of the magnetoroton branch for all values of $J = 1.5 - 4.5$, with the ground state lying slightly lower in energy. This observation suggests that these two states are composed of a coherent superposition of the two aforementioned classes of low energy states corresponding to the immobile exciton, and this superposition is formed in a way that the states destructively interfere to reduce their repulsive energy at the exciton position, leading to the emergence of the two bound states.

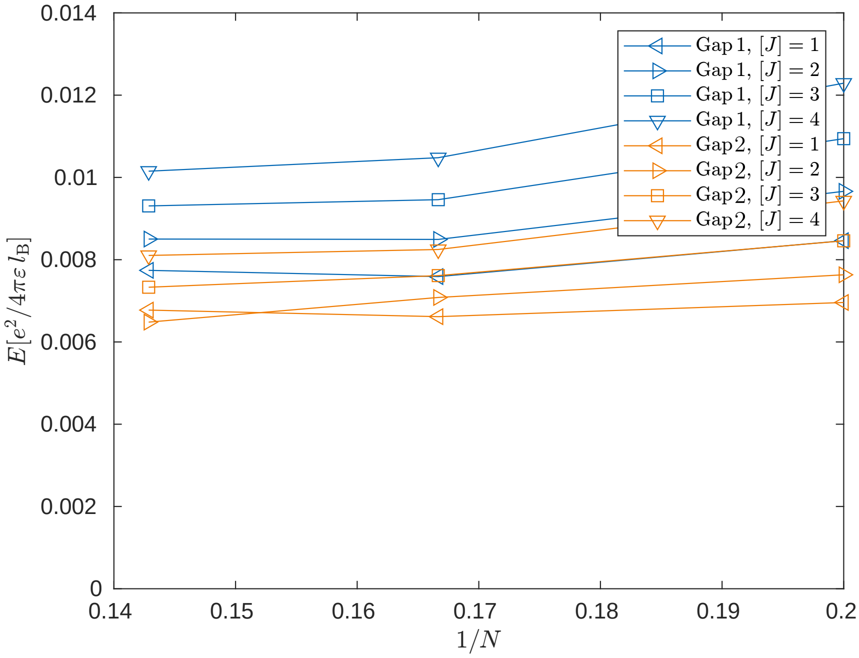

Figure 4.14: Scaling of the first gap (energy difference between the green and pink states in Fig. 4.12) and the second gap (energy difference between the pink and the purple states in Fig. 4.12) as a function of $1/N$ for $N = 5, 6, 7$. The scaling suggests that the first gap saturates to an energy $\sim 0.009\, E_C$, which at $B = 16\, T$ is ~ 0.45 meV.

4.8 Conclusion and Outlook

In this chapter, we considered the problem of exciton-electron interaction in the quantum Hall regime in a vdW heterostructure consisting of a TMD heterobilayer in the proximity of a monolayer graphene. We discussed the few- and many-body aspects of the problem, and argued that in the quantum Hall regime, the physics is even richer than the setting in the absence of the magnetic field. In the few-body limit of an interlayer exciton interacting attractively with a single charge carrier in graphene, we found the emergence of a magnetic trion even at magnetic fields $B \simeq 1\, T$, forming from $1s$ excitons scattering off the carrier in the lowest Landau level. In the many-body limit, when a single quasiparticle is present in a fractional quantum Hall system at $\nu = 1/3$, we demonstrated the emergence of two bound states, where the lower energy bound state can be identified as an anyonic trion which inherits the fractional charge and statistics of the bound quasihole. In the limit of a localized impurity, we found that the exciton potential also can bind the quasihole, leading to a sizable gap to the magnetoroton excitations $\sim 0.054\, E_C$.

The results in this section indicate that having spatial control over the position of a quasihole excitation by optical means is now within experimental reach. Furthermore, realization of ground state excitons, as for instance observed in excitonic insulators in the experiments of Ref. [138], in the setup described in the chapter, can enable the realization of long lifetime excitons. Binding quasiholes to such long lifetime excitons can enable

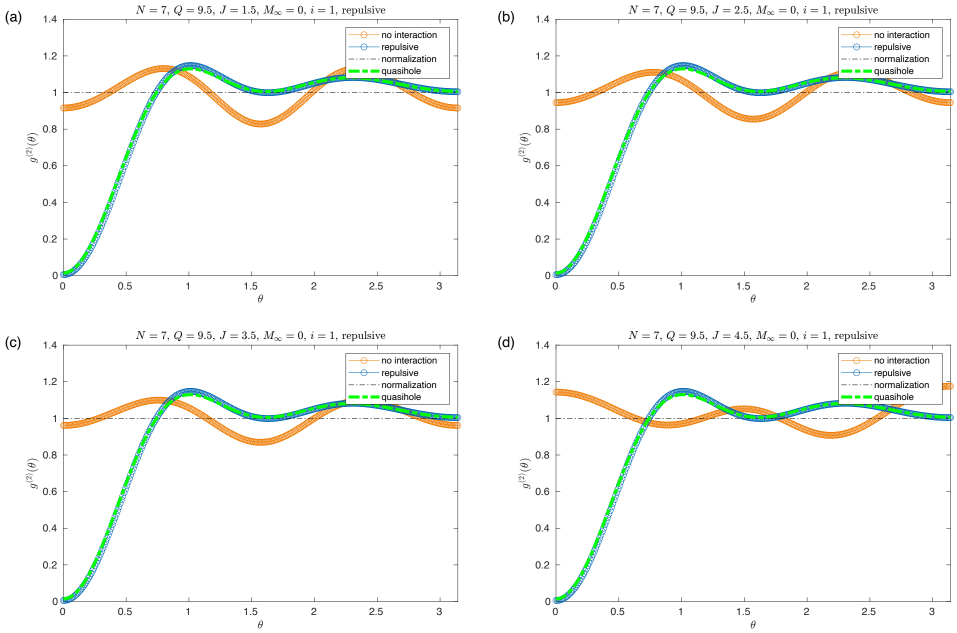

Figure 4.15: The exciton-electron $g^{(2)}(\theta)$ function, marked by the blue line, for the case of a mobile exciton, calculated using Eq. 4.73, for $N=7$ electrons at a single quasihole filling. The exciton-electron interaction is repulsive, $i = 1$ indicates that the $g^{(2)}$ belongs to the ground state (dark green state in Fig. 4.12), and $M_\infty = 0$ indicates that the exciton is mobile. (a)-(c) are the $g^{(2)}$ values for $J = 1.5 - 4.5$, respectively. For comparison, The $g^{(2)}$ function for the quasihole localized around $\mathbf{r}_0$ in a FQH with no impurity is also depicted by green dashed-dotted line. The $g^{(2)}$ function of the non-interacting state (mobile exciton with no interaction with the FQH system) is also depicted.

moving the quasiholes across the sample and even perform braiding.

Another exciting direction that our work suggests is to investigate exciton polaron formation in other quantum Hall systems such as twisted MoTe$_2$ moire structures, where formation of fractional Chern insulators have been experimentally observed [226].

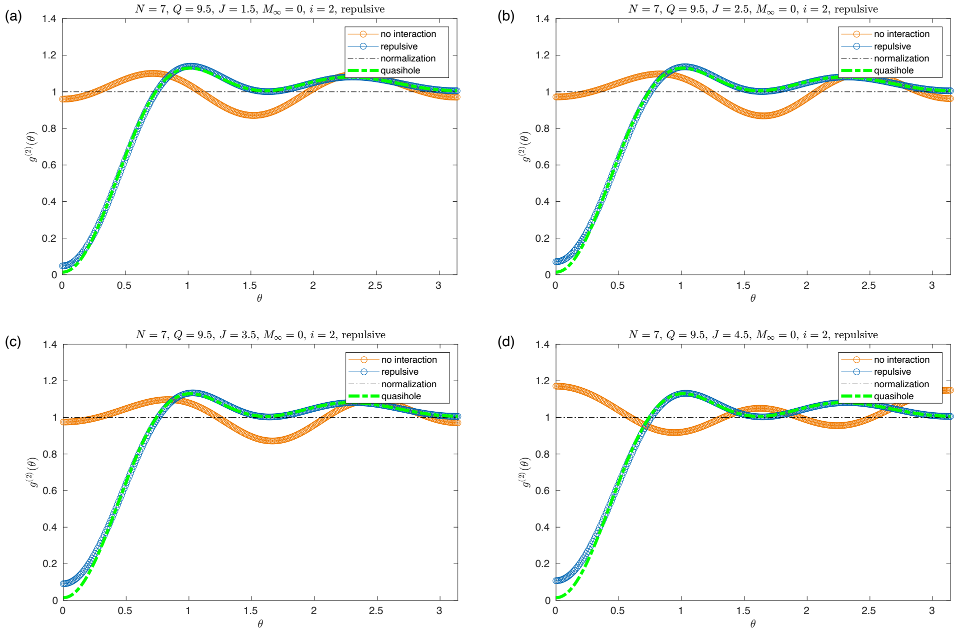

Figure 4.16: Same as Fig. 4.15, but for the first excited state (the state denoted by pink in Fig. 4.12).

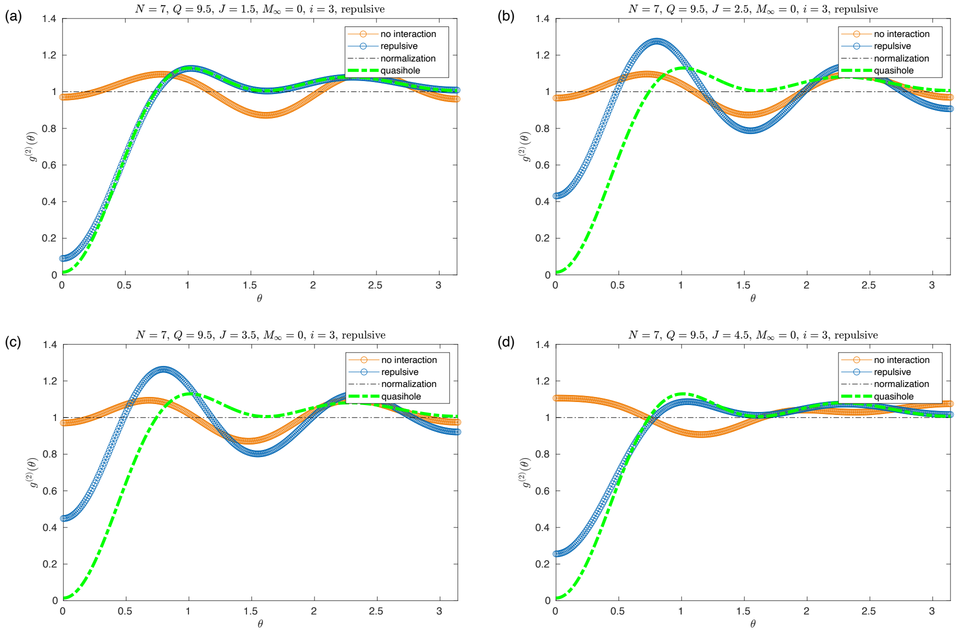

Figure 4.17: Same as Fig. 4.15, but for the second excited state (the onset of the continuum, the state denoted by purple in Fig. 4.12).

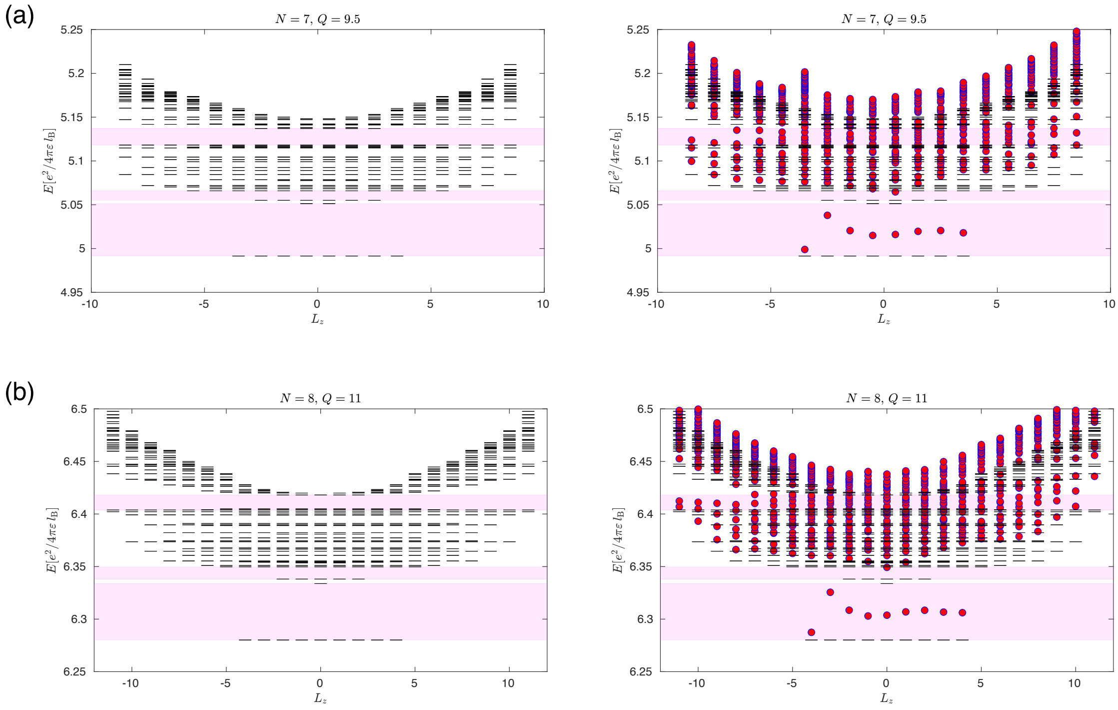

Figure 4.18: Comparison of the energy of levels of the FQH system as a function of the total L_z at the magnetic monopole corresponding to a single quasihole in the presence and absence of a localized exciton at $\mathbf{r}_0 = R\,\mathbf{e}_z$, for $N\!=\!7$ (a) and $N\!=\!8$ particles. The energy levels in the absence of the exciton are depicted by horizontal lines, whereas the energies in the presence of the localized exciton are marked with red circles. Three visible gaps in the FQH spectrum are highlighted. For both cases, the presence of the exciton gaps out the quasihole state at $L_z = -N/2$ localized around $\mathbf{r}_0$. The degeneracy of the other quasihole states are lifted, and a spectrum akin to magnetorotons appear, with a well-defined gap to the higher excited states. The magnetoroton branch still lies in the original quasihole gap.

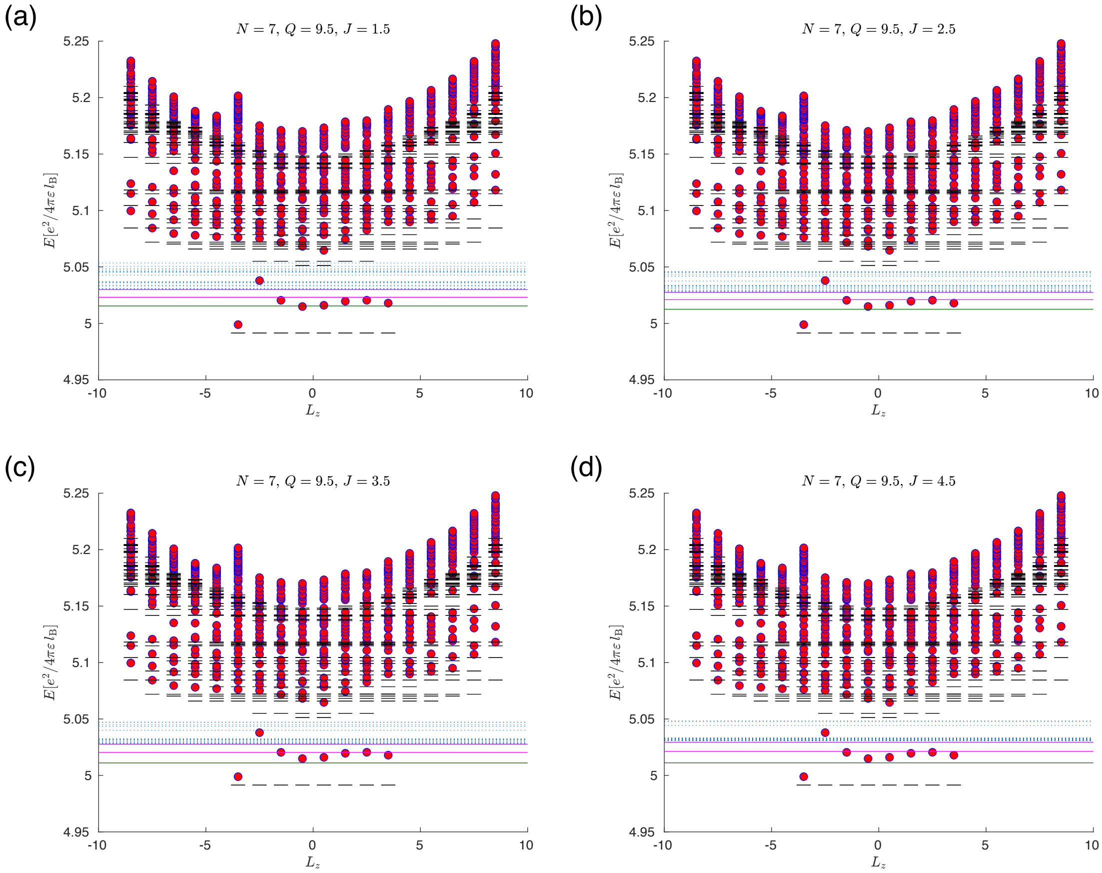

Figure 4.19: Same as Fig. 4.18, but for $N = 7$. The lowest energy states of the full interacting Hamiltonian for a mobile exciton is also shown. The green, pink and purple lines show the energies of the states with the same color code as in Fig. 4.12, while the higher excited states are shown in blue dotted lines.

Chapter 5

Conclusion and outlook

Without repeating the summary of the work done in this thesis - which has already been stated many times in different parts of this thesis - we outline several possible extensions of the works.

An interesting avenue to pursue in the study of topological nonlinear phenomena is the study of multi-component solitons. In the context of the multi-component solitons, different components can experience bands with different Chern numbers. The implication of the band structure topology and pseudo spin degrees of freedom can lead to non-trivial pseudo spin structures of the solitons. It would be interesting to classify various types of solitons that potentially can arise in systems governed by multi-component (D)NLS equations. Another research area is to find genuine topological indices which can characterize solitons of nonlinear models. In this direction, a direct generalization of the application of Wannier functions used in this work is to construct nonlinear models which are topologically trivial in terms of basis functions which do not possess all the properties of Wannier functions, but nevertheless undergo spectral flow by changing a system parameter periodically, for instance Landau levels in two dimensions. Thus, this construction can enable the generalization of the above framework to topological models in dimensions higher than one.

In the direction of strong coupling Bose polarons, development of novel spectroscopy technics that can resolve the many-body bound states would be of great interest. This many-body bound states have been predicted in various non-interating models, however, their interplay with higher few-body states such as cluster or Efimov type states are not known. It would also be interesting to apply the current framework to calculate other quasiparticle properties of these states, such as lifetime and decay rate, or dressing by phonons. Including few-body physics into the proposed variational ansatz is also possible if the coherent state ansatz is promoted to Gaussian states or truncated basis states.

Regarding the exciton-fractional quantum Hall systems, an interesting extension is to go beyond the single exciton regime and explore situations where excitonic many-body states play a role. This setting is particularly interesting in the context of proximity induced effects, where, for instance, an excitonic insulator in the proximity of a fractional quantum Hall can induce anyonic condensation or further exotic states. All in all, driving the current hybrid exciton-electron systems in semiconductor structures deep into the quantum Hall regime and investigate the physics of *quantum Hall Bose-Fermi mixtures* can attract attention both in the community of solid state physics and cold atomic gases.

Appendix A

Connection of the bound Bogoliubov mode to the bare impurity-boson bound state

Here we try to find the bound state of the quadratic Hamiltonian Eq. 3.14. As mentioned in the text, the exact excitation spectrum of the system is determined by finding $\varphi_{0,\mathbf{x}}$ and $S_{0,\mathbf{xy}}$ such that $\zeta[\Phi_0, \Gamma_0] = 0$ and $S_0^\dagger \mathcal{H}_{\mathrm{MF}}[\Phi_0, \Gamma_0] S_0 = \mathbb{I}_2 \otimes D$, while fulfilling $2\Gamma_0 + \mathbb{I} = S_0 S_0^\dagger$. The self-consistent solution can be obtained iteratively, starting from an unperturbed weakly-interacting Bose gas $\varphi_{\mathbf{x}}^{i=0} = \sqrt{n_0}$ and $S^{i=0} = \mathbb{I}$ as initial guess. At each step, the updated condensate field $\Phi_{\mathbf{x}}^{i+1} = (\varphi_{\mathbf{x}}^{i+1}, \varphi_{\mathbf{x}}^{i+1*})^{\mathrm{T}}$ satisfies $\zeta[\Phi^{i+1}, \Gamma^i] = 0$, and S^{i+1} diagonalizes $\mathcal{H}_{\mathrm{MF}}[\Phi^i, \Gamma^i]$, giving the updated covariance matrix Γ^{i+1}. Iterations are then carried out until convergence.

In the first iteration, the quadratic Hamiltonian is

$$\begin{aligned} \hat{H}_2^{i=0} = & \frac{1}{2} : \int_{\mathbf{k}} \begin{pmatrix} \delta\hat{\phi}_{\mathbf{k}}^\dagger & \delta\hat{\phi}_{-\mathbf{k}} \end{pmatrix} \mathcal{H}_{\mathrm{Bog}}(\mathbf{k}) \begin{pmatrix} \delta\hat{\phi}_{\mathbf{k}} \\ \delta\hat{\phi}_{-\mathbf{k}}^\dagger \end{pmatrix} : \\ & + \frac{1}{2} : \int_{\mathbf{k},\mathbf{k}'} \begin{pmatrix} \delta\hat{\phi}_{\mathbf{k}'}^\dagger & \delta\hat{\phi}_{-\mathbf{k}'} \end{pmatrix} \tilde{V}_{\mathrm{IB}}(\mathbf{k}' - \mathbf{k}) \, \mathbb{I}_{2\times 2} \begin{pmatrix} \delta\hat{\phi}_{\mathbf{k}} \\ \delta\hat{\phi}_{-\mathbf{k}}^\dagger \end{pmatrix} : , \end{aligned} \tag{A.1}$$

where $\mathcal{H}_{\mathrm{Bog}}(\mathbf{k})$ is the standard Bogoliubov Hamiltonian

$$\mathcal{H}_{\mathrm{Bog}}(\mathbf{k}) = \begin{pmatrix} \epsilon_{\mathbf{k}} + n_0 U_{\mathrm{BB}}(\mathbf{k}) & n_0 U_{\mathrm{BB}}(\mathbf{k}) \\ n_0 U_{\mathrm{BB}}(\mathbf{k}) & \epsilon_{\mathbf{k}} + n_0 U_{\mathrm{BB}}(\mathbf{k}) \end{pmatrix} , \tag{A.2}$$

with $\epsilon_{\mathbf{k}} = \hbar^2 \mathbf{k}^2 / 2m_{\mathrm{red}}$, and $\tilde{V}_{\mathrm{IB}}(\mathbf{k})$ is the Fourier transform of $V_{\mathrm{IB}}(\mathbf{x})$. $\mathcal{H}_{\mathrm{Bog}}(\mathbf{k})$ is diagonalized by the matrix $S_{\mathbf{k}}$ given by

$$S_{\mathbf{k}} = \begin{pmatrix} u_{\mathbf{k}} & -v_{\mathbf{k}} \\ -v_{\mathbf{k}} & u_{\mathbf{k}} \end{pmatrix} \tag{A.3}$$

where $u_{\mathbf{k}} = \cosh(\theta_{\mathbf{k}})$, $v_{\mathbf{k}} = \sinh(\theta_{\mathbf{k}})$, and $\tanh(2\theta_{\mathbf{k}}) = n_0 U_{\mathrm{BB}}(\mathbf{k})/\big(\epsilon_{\mathbf{k}} + n_0 U_{\mathrm{BB}}(\mathbf{k})\big)$. Diagonalization by $S_{\mathbf{k}}$ leads to the Bogoliubov dispersion relation

$$\varepsilon_{\mathbf{k}} = \sqrt{\epsilon_{\mathbf{k}}\big(\epsilon_{\mathbf{k}} + 2n_0 U_{\mathrm{BB}}(\mathbf{k})\big)}\,. \tag{A.4}$$

The bound state of the Hamiltonian in Eq. A.1 is obtained from

$$\begin{pmatrix} \epsilon_{\mathbf{k}} + n_0 U_{\mathrm{BB}}(\mathbf{k}) & n_0 U_{\mathrm{BB}}(\mathbf{k}) \\ n_0 U_{\mathrm{BB}}(\mathbf{k}) & \epsilon_{\mathbf{k}} + n_0 U_{\mathrm{BB}}(\mathbf{k}) \end{pmatrix} \begin{pmatrix} u_{\mathrm{B},\mathbf{k}} \\ v_{\mathrm{B},\mathbf{k}} \end{pmatrix} + \int_{\mathbf{k}'} \tilde{V}_{\mathrm{IB}}(\mathbf{k}-\mathbf{k}') \begin{pmatrix} u_{\mathrm{B},\mathbf{k}'} \\ v_{\mathrm{B},\mathbf{k}'} \end{pmatrix} = -\varepsilon_{\mathrm{B}} \begin{pmatrix} u_{\mathrm{B},\mathbf{k}} \\ v_{\mathrm{B},\mathbf{k}} \end{pmatrix}. \tag{A.5}$$

Formally solving for $v_{\mathrm{B},\mathbf{k}}$ in Eq. A.5 results in

$$v_{\mathrm{B},\mathbf{k}} = \int_{\mathbf{k}'} G(-\varepsilon_{\mathrm{B}})_{\mathbf{k}\mathbf{k}'}\, n_0 U_{\mathrm{BB}}(\mathbf{k}')\, u_{\mathrm{B},\mathbf{k}'}\,, \tag{A.6}$$

where $G^{-1}(E)_{\mathbf{k}\mathbf{k}'} = \big(E - \epsilon_{\mathbf{k}} - n_0 U_{\mathrm{BB}}(\mathbf{k})\big)\,\delta^{(d)}(\mathbf{k}-\mathbf{k}') - \tilde{V}_{\mathrm{IB}}(\mathbf{k}-\mathbf{k}')$. Inserting $v_{\mathrm{B},\mathbf{k}}$ of Eq. A.6 back in the equation satisfied by $u_{\mathrm{B},\mathbf{k}}$ results in

$$\begin{aligned} &\big(\epsilon_{\mathbf{k}} + n_0 U_{\mathrm{BB}}(\mathbf{k})\big) u_{\mathrm{B},\mathbf{k}} + \int_{\mathbf{k}'} \tilde{V}_{\mathrm{IB}}(\mathbf{k}-\mathbf{k}')\, u_{\mathrm{B},\mathbf{k}'} \\ &+ n_0 U_{\mathrm{BB}}(\mathbf{k}) \int_{\mathbf{k}'} G(-\varepsilon_{\mathrm{B}})_{\mathbf{k}\mathbf{k}'}\, n_0 U_{\mathrm{BB}}(\mathbf{k}')\, u_{\mathrm{B},\mathbf{k}'} = -\varepsilon_{\mathrm{B}}\, u_{\mathrm{B},\mathbf{k}}\,. \end{aligned} \tag{A.7}$$

Applying standard perturbation theory to Eq. A.7 in the regime $n_0 U_{\mathrm{BB}}(0) \ll \varepsilon_B$, $u_{\mathrm{B},\mathbf{k}}$ is obtained as the bound state of $-\hbar^2\nabla^2/2m_{\mathrm{red}} + V_{\mathrm{IB}}(\mathbf{x})$ up to corrections of $\mathcal{O}(n_0 U_{\mathrm{BB}}(0)/\varepsilon_{\mathrm{B}})$. Thus, to leading order in $n_0 U_{\mathrm{BB}}(0)/\varepsilon_{\mathrm{B}}$, $u_{\mathrm{B},\mathbf{x}} = \eta_{\mathbf{x}}$ and $v_{\mathrm{B},\mathbf{x}} = 0$.

Appendix B

Explicit form of variational equations

In this appendix, for the sake of completeness, we first derive the general form of variational equations in 3.44 for the case $\Gamma = 0$. Then we specialize the variational equations solved to obtain the variational states and energies of the many-body bound states presented in this work. The coherent state $\alpha_{\mathbf{x}}$ satisfies the following nonlinear integro-differential equation

$$\begin{aligned}
&\left[h_0 + \int_{\mathbf{x}'} U_{\mathrm{BB}}(\mathbf{x}-\mathbf{x}')|\varphi_{\mathrm{rep},\mathbf{x}'}|^2\right]\alpha_{\mathbf{x}} + \int_{\mathbf{x}'} U_{\mathrm{BB}}(\mathbf{x}-\mathbf{x}')\,\varphi^*_{\mathrm{rep},\mathbf{x}}\varphi_{\mathrm{rep},\mathbf{x}'}\,\alpha_{\mathbf{x}'} \\
&+ \int_{\mathbf{x}'} U_{\mathrm{BB}}(\mathbf{x}-\mathbf{x}')\,\varphi_{\mathrm{rep},\mathbf{x}'}\varphi_{\mathrm{rep},\mathbf{x}}\,\alpha^*_{\mathbf{x}'} \\
&+ \int_{\mathbf{x}'} U_{\mathrm{BB}}(\mathbf{x}-\mathbf{x}')\left[\tilde{\varphi}^*_{\mathbf{x}'}\tilde{\varphi}_{\mathbf{x}} - \varphi^*_{\mathrm{rep},\mathbf{x}'}\varphi_{\mathrm{rep},\mathbf{x}} + \Delta\langle :\hat{\phi}^{(\mathrm{B})\dagger}_{\mathbf{x}'}\hat{\phi}^{(\mathrm{B})}_{\mathbf{x}}:\rangle\right]\alpha_{\mathbf{x}'} \\
&+ \int_{\mathbf{x}'} U_{\mathrm{BB}}(\mathbf{x}-\mathbf{x}')\left[|\tilde{\varphi}_{\mathbf{x}'}|^2 - |\varphi^*_{\mathrm{rep},\mathbf{x}'}|^2 + \Delta\langle :\hat{\phi}^{(\mathrm{B})\dagger}_{\mathbf{x}'}\hat{\phi}^{(\mathrm{B})}_{\mathbf{x}'}:\rangle\right]\alpha_{\mathbf{x}} \\
&+ \int_{\mathbf{x}'} U_{\mathrm{BB}}(\mathbf{x}-\mathbf{x}')\left[\tilde{\varphi}_{\mathbf{x}'}\tilde{\varphi}_{\mathbf{x}} - \varphi_{\mathrm{rep},\mathbf{x}'}\varphi_{\mathrm{rep},\mathbf{x}} + \Delta\langle :\hat{\phi}^{(\mathrm{B})}_{\mathbf{x}'}\hat{\phi}^{(\mathrm{B})}_{\mathbf{x}}:\rangle\right]\alpha^*_{\mathbf{x}'} \\
&+ \int_{\mathbf{x}'} U_{\mathrm{BB}}(\mathbf{x}-\mathbf{x}')\tilde{\varphi}_{\mathbf{x}}\,\alpha^*_{\mathbf{x}'}\alpha_{\mathbf{x}'} + \int_{\mathbf{x}'} U_{\mathrm{BB}}(\mathbf{x}-\mathbf{x}')\tilde{\varphi}_{\mathbf{x}'}\,\alpha^*_{\mathbf{x}'}\alpha_{\mathbf{x}} \\
&+ \int_{\mathbf{x}'} U_{\mathrm{BB}}(\mathbf{x}-\mathbf{x}')\tilde{\varphi}^*_{\mathbf{x}'}\,\alpha_{\mathbf{x}'}\alpha_{\mathbf{x}} + \int_{\mathbf{x}'} U_{\mathrm{BB}}(\mathbf{x}-\mathbf{x}')\,\alpha^*_{\mathbf{x}'}\alpha_{\mathbf{x}'}\alpha_{\mathbf{x}} \\
&+ \int_{\mathbf{x}'} U_{\mathrm{BB}}(\mathbf{x}-\mathbf{x}')\varphi_{\mathrm{rep},\mathbf{x}}\,\langle :\hat{\phi}^{(\mathrm{B})\dagger}_{\mathbf{x}'}\hat{\phi}^{(\mathrm{B})}_{\mathbf{x}'}:\rangle + \int_{\mathbf{x}'} U_{\mathrm{BB}}(\mathbf{x}-\mathbf{x}')\varphi_{\mathrm{rep},\mathbf{x}'}\,\langle :\hat{\phi}^{(\mathrm{B})\dagger}_{\mathbf{x}'}\hat{\phi}^{(\mathrm{B})}_{\mathbf{x}}:\rangle \\
&+ \int_{\mathbf{x}'} U_{\mathrm{BB}}(\mathbf{x}-\mathbf{x}')\varphi^*_{\mathrm{rep},\mathbf{x}'}\,\langle :\hat{\phi}^{(\mathrm{B})}_{\mathbf{x}}\hat{\phi}^{(\mathrm{B})}_{\mathbf{x}'}:\rangle + \int_{\mathbf{x}'} U_{\mathrm{BB}}(\mathbf{x}-\mathbf{x}')\,\langle :\hat{\phi}^{(\mathrm{B})\dagger}_{\mathbf{x}'}\hat{\phi}^{(\mathrm{B})}_{\mathbf{x}'}\hat{\phi}^{(\mathrm{B})}_{\mathbf{x}}:\rangle \\
&+ \left[h_0 + \int_{\mathbf{x}'} U_{\mathrm{BB}}(\mathbf{x}-\mathbf{x}')|\varphi_{\mathrm{rep},\mathbf{x}'}|^2\right]\langle\hat{\phi}^{(\mathrm{B})}_{\mathbf{x}'}\rangle + \int_{\mathbf{x}'} U_{\mathrm{BB}}(\mathbf{x}-\mathbf{x}')\,\varphi^*_{\mathrm{rep},\mathbf{x}}\varphi_{\mathrm{rep},\mathbf{x}'}\,\langle\hat{\phi}^{(\mathrm{B})}_{\mathbf{x}'}\rangle \\
&+ \int_{\mathbf{x}'} U_{\mathrm{BB}}(\mathbf{x}-\mathbf{x}')\,\varphi_{\mathrm{rep},\mathbf{x}'}\varphi_{\mathrm{rep},\mathbf{x}}\langle\hat{\phi}^{(\mathrm{B})\dagger}_{\mathbf{x}'}\rangle - \lambda u_{\mathrm{B},\mathbf{x}} + \lambda^* v_{\mathrm{B},\mathbf{x}} = 0\ ,
\end{aligned} \tag{B.1}$$

where $\tilde{\varphi}_{\mathbf{x}} = \varphi_{\mathrm{rep},\mathbf{x}} + \langle\hat{\phi}^{(\mathrm{B})}_{\mathbf{x}}\rangle$, $\Delta\langle :\hat{\phi}^{(\mathrm{B})(\dagger)}_{\mathbf{x}}\hat{\phi}^{(\mathrm{B})}_{\mathbf{y}}:\rangle = \langle :\hat{\phi}^{(\mathrm{B})(\dagger)}_{\mathbf{x}}\hat{\phi}^{(\mathrm{B})}_{\mathbf{y}}:\rangle - \langle\hat{\phi}^{(\mathrm{B})(\dagger)}_{\mathbf{x}}\rangle\langle\hat{\phi}^{(\mathrm{B})}_{\mathbf{y}}\rangle$, and the expectation value $\langle\cdots\rangle$ is taken over $\left|\psi_{(\mathrm{B})}\right\rangle$. The states $\left|\psi_{(\mathrm{B})}\right\rangle$, respectively, the energies of the metastbale states are the eigenstates, respectively, eigen energies of

$$\hat{H}_{\mathrm{eff,B}} = \sum_{n,m=0} \hat{H}_{n,m}[\alpha^*_{\mathbf{x}}, \alpha_{\mathbf{x}}]\, \hat{b}^{\dagger n} \hat{b}^{m} \,, \tag{B.2}$$

in the Fock space of $\hat{b}$, determined by exact diagonalization. The explicit eigenvalue problem is

$$\sum_{l} \sum_{n,m=0}^{2} \hat{H}_{n,m}[\alpha^*_{\mathbf{x}}, \alpha_{\mathbf{x}}]\, \langle k|\, \hat{b}^{\dagger n} \hat{b}^{m}\, |l\rangle\, \psi_l = E\, \psi_k \,, \tag{B.3}$$

where E is the energy of the many-body bound state $\left|\psi_{(\mathrm{B})}\right\rangle = \sum_n \psi_n \left|n\right\rangle_{\mathrm{B}}$.

By applying the assumptions and approximations we made in this work, the equation B.1 satisfied by $\alpha_{\mathbf{x}}$ reduces to the following simplified equation

$$\begin{aligned} &\left[h_0 + 3U_0 \tilde{\varphi}^2_{\mathbf{x}} + 2U_0 \eta^2_{\mathbf{x}} \Delta\langle \hat{b}^\dagger \hat{b}\rangle + \eta^2_{\mathbf{x}} \Delta\langle \hat{b}^2\rangle\right] \alpha_{\mathbf{x}} + 3U_0\, \tilde{\varphi}_{\mathbf{x}}\, \alpha^2_{\mathbf{x}} + U_0\, \alpha^3_{\mathbf{x}} + 2\, U_0 \varphi_{\mathrm{rep},\mathbf{x}}\, \eta^2_{\mathbf{x}} \langle \hat{b}^\dagger \hat{b}\rangle \\ &+ U_0 \varphi_{\mathrm{rep},\mathbf{x}}\, \eta^2_{\mathbf{x}} \langle \hat{b}^2\rangle + U_0\, \eta^3_{\mathbf{x}} \langle \hat{b}^\dagger \hat{b}^2\rangle + \left[h_0 + 2\, U_0 \varphi^2_{\mathrm{rep},\mathbf{x}} \langle \hat{b}\rangle + U_0\, \varphi^2_{\mathrm{rep},\mathbf{x}} \langle \hat{b}^\dagger\rangle\right] \eta_{\mathbf{x}} - \lambda \eta_{\mathbf{x}} = 0 \,. \end{aligned} \tag{B.4}$$

In Eq. B.4, we made use of the fact that $\alpha_{\mathbf{x}}$ can be taken to be real, $\alpha_{\mathbf{x}} = \alpha^*_{\mathbf{x}}$.

Appendix C

Charged particle in magnetic field

C.1 Free charged particle in a uniform magnetic field

We consider a free particle with charge q and mass m confined in a two dimensional surface and moving in the background of a uniform magnetic field $\mathbf{B} = B\,\mathbf{n}$, where B is the magnetic flux density and $\mathbf{n}$ is the normal to the surface. It is convenient to express relevant quantities in terms of the natural units of the system, which are listed in the table C.1. The Hamiltonian is

$$\hat{H}_0[\mathbf{A}_a] = -\frac{1}{2}\Big(\nabla - i\varsigma\mathbf{A}_a(\hat{\mathbf{x}})\Big)^2\,, \tag{C.1}$$

where $\mathbf{A}_a(\mathbf{x})$ is the vector potential in gauge a corresponding to the background magnetic field, $\nabla \times \mathbf{A}_a(\mathbf{x}) = \mathbf{B}$, and $\varsigma = \operatorname{sgn}(qB)$. Upon a gauge transformation from a to b, the vector potential transforms as $\mathbf{A}_b(\mathbf{x}) = \mathbf{A}_a(\mathbf{x}) + \nabla\Lambda_{a\to b}(\mathbf{x})$. The wavefunctions transform as $\psi_b(\mathbf{x}) = e^{i\Lambda_{a\to b}}\,\psi_a(\mathbf{x})$, and the Hamiltonian transforms as

$$\hat{H}_0[\mathbf{A}_a]\,\psi_a(\mathbf{x}) = \hat{H}_0[\mathbf{A}_a]\,e^{i\Lambda_{b\to a}}\,\psi_b(\mathbf{x}) = e^{i\Lambda_{b\to a}}\hat{H}_0[\mathbf{A}_a - \nabla\Lambda_{b\to a}]\psi_b(\mathbf{x}) = e^{i\Lambda_{b\to a}}\hat{H}_0[\mathbf{A}_b]\psi_b\,, \tag{C.2}$$

which results in the well-known transformation law for Hamiltonian,

$$\hat{H}_0[\mathbf{A}_a] = e^{i\Lambda_{b\to a}}\,\hat{H}_0[\mathbf{A}_b]\,e^{-i\Lambda_{b\to a}}\,. \tag{C.3}$$

A note on the orientation convention. Because of the dependence of cyclotron orbits to the sign of the charge, it is important to fix the convention for the orientation of the magnetic field, the particle charge and other quantities in the system. We fix the normal to the surface $\mathbf{n}$ and choose two orthonormal in-plane directions $\mathbf{x}$ and $\mathbf{y}$ such that $(\mathbf{x}, \mathbf{y}, \mathbf{n})$ form a right-handed frame. There are four different possibilities for the magnetic field direction and charge sign as listed below,

- $\varsigma = \operatorname{sgn}(qB) > 0$: $z = (x + iy)/\sqrt{2}$ is the natural complex variable.
- $\varsigma = \operatorname{sgn}(qB) < 0$: $z = (x - iy)/\sqrt{2}$ is the natural complex variable.

In the following, we obtain the Landau level spectrum in different gauges and geometries.

	length	momentum	frequency	energy	flux	vector potential
unit	l_B	p_B	ω_B	$\hbar\omega_\mathrm{B}$	Φ_0	$2\pi l_\mathrm{B}/\Phi_0$
name	magnetic length	–	cyclotron frequency	cyclotron energy	flux quantum	–
definition	$\sqrt{\hbar/m\omega_\mathrm{B}}$	$\hbar/l_\mathrm{B}$	$\lvert qB\rvert/mc$	$\hbar\omega_\mathrm{B}$	$hc/\lvert q\rvert$	$2\pi l_\mathrm{B}/\Phi_0$

Table C.1: Natural units of the free charged particle in a uniform magnetic field.

C.1.1 Gauge invariant formulation of Landau levels

In this section, general relations and properties for the single particle system of a charged particle in a magnetic field are given. To this end, it is convenient to introduce the *kinetic momentum* operator $\hat{\mathbf{\Pi}} = \hat{\mathbf{p}} - \varsigma\mathbf{A}(\hat{\mathbf{x}})$ and the *magnetic momentum operator* $\hat{\mathbf{\Gamma}} = \hat{\mathbf{p}} - \varsigma\mathbf{A}(\hat{\mathbf{x}}) + \varsigma\mathbf{n}\times\mathbf{x}$ where $\mathbf{n} = \mathbf{B}/|\mathbf{B}|$ and we define the symmetric gauge as $\mathbf{A}_\text{sym}(\mathbf{x}) = (1/2)\,\mathbf{n}\times\mathbf{x}$. The commutation relations between different components of kinetic and magnetic momenta are

$$[\hat{\Pi}_i, \hat{\Pi}_j] = \varsigma \cdot i\, \varepsilon_\text{ijk}\, \mathbf{n}_\text{k}\,, \tag{C.4}$$

$$[\hat{\Pi}_i, \hat{\Gamma}_j] = 0\,, \tag{C.5}$$

$$[\hat{\Gamma}_i, \hat{\Gamma}_j] = \varsigma \cdot (-i)\varepsilon_\text{ijk}\, \mathbf{n}_\text{k}\,, \tag{C.6}$$

$$[\hat{\Pi}_i, \hat{\text{A}}_{\text{sym}\,j}] = \varsigma \cdot \Big(-\frac{i}{2}\Big)\varepsilon_\text{ijk}\, \mathbf{n}_\text{k}\,. \tag{C.7}$$

Interpretation of magnetic momentum in terms of guiding center of mass coordinates The equations of motion of the classical system of a free charged particle in a magnetic field is derived from the following Lagrangian

$$L(\mathbf{x}, \dot{\mathbf{x}}) = \frac{m}{2}\,\dot{\mathbf{x}}^2 + \frac{q}{c}\,\mathbf{A}(\mathbf{x})\cdot\dot{\mathbf{x}}\,, \tag{C.8}$$

from which the conjugate momentum $\mathbf{p} = \partial L/\partial\dot{\mathbf{x}}$ reads as

$$\mathbf{p} = m\dot{\mathbf{x}} + \frac{q}{c}\mathbf{A}(\mathbf{x})\,. \tag{C.9}$$

From Eq. C.9 and the definition of kinetic momentum, it is clear that $\boldsymbol{\pi} = m\dot{\mathbf{x}}$. The classical equations of motion follows from Euler-Lagrange equations [1]

$$m\ddot{\mathbf{x}} = \frac{q}{c}\,\dot{\mathbf{x}}\times\mathbf{B}\,. \tag{C.10}$$

---

[1] Alternatively, the EOM can be obtained from Hamilton equations, although they look more involved.

Using Eq. C.10 and the definition of kinetic momentum,

$$\frac{d}{dt}\Big(\mathbf{p} - \frac{q}{c}\,\mathbf{A}(\mathbf{x}) - \frac{q}{c}\,\mathbf{x}\times\mathbf{B}\Big) = 0\,, \tag{C.11}$$

which leads to the definition of magnetic momentum $\boldsymbol{\gamma} = \mathbf{p} - \frac{q}{c}\,\mathbf{A}(\mathbf{x}) + \frac{q}{c}\,\mathbf{B}\times\mathbf{x}$ as a constant of motion, i.e.

$$\dot{\boldsymbol{\gamma}} = \frac{d}{dt}\Big(\mathbf{p} - q/c\,\mathbf{A}(\mathbf{x}) + q/c\,\mathbf{B}\times\mathbf{x}\Big) = 0\,. \tag{C.12}$$

We can gain further insight into the meaning of this definition by noting that the classical equation of motion imply the following time dependence for the particle position

$$\mathbf{x}(t) = \mathbf{x}_0 + \mathbf{r}(t)\,, \tag{C.13}$$

such that

$$m\,\boldsymbol{\omega}\times(\boldsymbol{\omega}\times\mathbf{r}) = \frac{q}{c}\,\dot{\mathbf{r}}\times\mathbf{B}\,, \tag{C.14}$$

with $\boldsymbol{\omega} = -\omega_{\mathrm{B}}\,\mathbf{n}$. Thus $s\mathbf{r}\times\mathbf{n} = \dot{\mathbf{r}}/\omega_{\mathrm{B}}$, or equivalently $\mathbf{r} = \varsigma\mathbf{n}\times\dot{\mathbf{r}}/\omega_{\mathrm{B}}$. From Eq. C.13 we obtain the relation between the magnetic momentum and the center of orbit as

$$\boldsymbol{\gamma} = \varsigma m\omega_{\mathrm{B}}\mathbf{n}\times\Big(\mathbf{x}(t) - \mathbf{r}(t)\Big) = \varsigma m\omega_{\mathrm{B}}\mathbf{n}\times\mathbf{x}_0\,. \tag{C.15}$$

Eq. C.15 establishes the relation between the magnetic momentum $\boldsymbol{\gamma}$ and the center of orbit - or the guiding center - as $\boldsymbol{\gamma}=\varsigma m\omega_{\mathrm{B}}\mathbf{n}\times\mathbf{x}_0$.

Going back to the discussion on gauge invariant single particle properties of the system, the commutation relations in Eqs. C.4, C.5 and C.6 can be expressed in a more clear form. We note that $i\varepsilon_{\mathrm{ijk}}\,\mathbf{n}_{\mathrm{k}} = -(\,\sigma_{\mathrm{y}}\,)_{\mathrm{ij}}$ where σ_{y} is the $y-$Pauli matrix. By diagonalizing σ_{y},

$$\begin{aligned}&\varsigma\sigma_{\mathrm{y}} = U_\varsigma\,\varsigma D_{\mathrm{y}}\,U_\varsigma^\dagger\\ &U_\varsigma = \frac{1}{\sqrt{2}}\begin{pmatrix}1 & 1\\ i\varsigma & -i\varsigma\end{pmatrix}\,,\quad D_{\mathrm{y}} = \begin{pmatrix}1 & 0\\ 0 & -1\end{pmatrix}\,,\quad U^\dagger = \frac{1}{\sqrt{2}}\begin{pmatrix}1 & -i\varsigma\\ 1 & i\varsigma\end{pmatrix}\,,\end{aligned} \tag{C.16}$$

we can arrange $\hat{\Pi}_i$ and $\hat{\Gamma}_i$ operators in a matrix and define

$$\begin{pmatrix}\hat{\Pi}_{-,\varsigma}\\ \hat{\Pi}_{+,\varsigma}\end{pmatrix} = U_\varsigma^\dagger\begin{pmatrix}\hat{\Pi}_1\\ \hat{\Pi}_2\end{pmatrix} = \begin{pmatrix}(\hat{\Pi}_1 - i\varsigma\hat{\Pi}_2)/\sqrt{2}\\ (\hat{\Pi}_1 + i\varsigma\hat{\Pi}_2)/\sqrt{2}\end{pmatrix}\,,\quad \begin{pmatrix}\hat{\Gamma}_{-,\varsigma}\\ \hat{\Gamma}_{+,\varsigma}\end{pmatrix} = U_\varsigma^\dagger\begin{pmatrix}\hat{\Gamma}_1\\ \hat{\Gamma}_2\end{pmatrix} = \begin{pmatrix}(\hat{\Gamma}_1 - i\varsigma\hat{\Gamma}_2)/\sqrt{2}\\ (\hat{\Gamma}_1 + i\varsigma\hat{\Gamma}_2)/\sqrt{2}\end{pmatrix}\,. \tag{C.17}$$

Thus,

$$(-\varsigma\sigma_{\mathrm{y}})\begin{pmatrix}\hat{\Pi}_1\\ \hat{\Pi}_2\end{pmatrix} = U_\varsigma\,(-D_{\mathrm{y}})\,U_\varsigma^\dagger\,U_\varsigma\begin{pmatrix}\hat{\Pi}_{-,\varsigma}\\ \hat{\Pi}_{+,\varsigma}\end{pmatrix} = U_\varsigma\begin{pmatrix}-\varsigma\hat{\Pi}_{-,\varsigma}\\ \varsigma\hat{\Pi}_{+,\varsigma}\end{pmatrix}\,, \tag{C.18}$$

and the same transformation rules hold for $\hat{\Gamma}_i$'s. The commutation relations C.4 to C.6 now reads

$$\begin{aligned}&[\,\hat{\Pi}_{+,\varsigma},\hat{\Pi}_{-,\varsigma}\,] = [\,\hat{\Gamma}_{-,\varsigma},\hat{\Gamma}_{+,\varsigma}\,] = 1\\ &[\,\hat{\Pi}_{\pm,\varsigma},\hat{\Gamma}_{\pm,\varsigma}\,] = 0\,.\end{aligned} \tag{C.19}$$

Furthermore, we have

$$\hat{\Pi}_{-,\varsigma} = \hat{\Pi}^{\dagger}_{+,\varsigma}\,, \quad \hat{\Gamma}_{+,\varsigma} = \hat{\Gamma}^{\dagger}_{-,\varsigma}\,. \tag{C.20}$$

We consider the case of positive and negative charge separately.

- $\underline{\varsigma > 0}$: We readily observe the correspondence $\hat{\Pi}_1 \longmapsto \hat{X}$, $\hat{\Pi}_2 \longmapsto \hat{P}$ thus $\hat{\Pi}_1$ and $\hat{\Pi}_2$ constitute a pair of canonically conjugate variables - this statement also holds for the classical mechanics of a charged particle in a magnetic field. Moreover, $\hat{\Pi}_+$ and $\hat{\Pi}_-$ serve as annihilation, respectively, creation operator associated to $\hat{\Pi}_1$ and $\hat{\Pi}_2$,

  $$\hat{a} \,\equiv\, i\hat{\Pi}_+ = i\frac{\hat{\Pi}_1 + i\hat{\Pi}_2}{\sqrt{2}}\,, \quad \hat{a}^{\dagger} \,\equiv\, -i\hat{\Pi}_- = -i\frac{\hat{\Pi}_1 - i\hat{\Pi}_2}{\sqrt{2}}\,. \tag{C.21}$$

  Interestingly, we can express the Hamiltonian $\hat{\mathrm{H}} = -1/2\,(\nabla - i\mathbf{A}(\mathbf{x})\,)^2$ in terms of $\hat{a}$ and $\hat{a}^{\dagger}$,

  $$\hat{\mathrm{H}} = \frac{1}{2}\Big(\hat{\Pi}_1^2 + \hat{\Pi}_2^2\Big) = \hat{\Pi}_-\hat{\Pi}_+ + \frac{1}{2} = \hat{a}^{\dagger}\hat{a} + \frac{1}{2}\,, \tag{C.22}$$

  which gives the Landau level structure. We can construct creation and annihilation operators corresponding to $\hat{\Gamma}_1$ and $\hat{\Gamma}_2$ accordingly

  $$\hat{b} \,\equiv\, i\hat{\Gamma}_- = i\frac{\hat{\Gamma}_1 - i\hat{\Gamma}_2}{\sqrt{2}}\,, \quad \hat{b}^{\dagger} \,\equiv\, -i\hat{\Gamma}_+ = -i\frac{\hat{\Gamma}_1 + i\hat{\Gamma}_2}{\sqrt{2}}\,, \tag{C.23}$$

  which gives the guiding-center degeneracy. Hereafter, we make extensive use of the results in Eqs. C.19, C.20, C.22, and C.27. We note that, the interpretation of $\hat{\Pi}_{\pm}$ and $\hat{\Gamma}_{\pm}$ in terms of creation and annihilation operators are quite general and works in any gauge. The Landau levels then are the harmonic oscillator states created by $\hat{a}^{\dagger}$ and $\hat{b}^{\dagger}$,

  $$|n, m\rangle = \frac{(\hat{a}^{\dagger})^n(\hat{b}^{\dagger})^m}{\sqrt{n!m!}}\;|0, 0\rangle\,. \tag{C.24}$$

- $\underline{\varsigma < 0}$: In this case, $\hat{\Pi}_1 \longmapsto \hat{P}$, $\hat{\Pi}_2 \longmapsto \hat{X}$. The role of $\hat{\Pi}_+$ and $\hat{\Pi}_-$ as creation and annihilation operators is now changed compared to the positively charged case, meaning that

  $$\hat{a}^{\dagger} \,\equiv\, -i\hat{\Pi}_+ = -i\frac{\hat{\Pi}_1 + i\hat{\Pi}_2}{\sqrt{2}}\,, \quad \hat{a} \equiv i\hat{\Pi}_- = i\frac{\hat{\Pi}_1 - i\hat{\Pi}_2}{\sqrt{2}}\,. \tag{C.25}$$

  the Hamiltonian is now

  $$\hat{\mathrm{H}} = \frac{1}{2}\Big(\hat{\Pi}_1^2 + \hat{\Pi}_2^2\Big) = \hat{\Pi}_+\hat{\Pi}_- + \frac{1}{2} = \hat{a}^{\dagger}\hat{a} + \frac{1}{2}\,, \tag{C.26}$$

  which gives the Landau level structure. We can construct creation and annihilation operators corresponding to $\hat{\Gamma}_1$ and $\hat{\Gamma}_2$ accordingly,

  $$\hat{b}^{\dagger} \,\equiv\, -i\hat{\Gamma}_- = -i\frac{\hat{\Gamma}_1 - i\hat{\Gamma}_2}{\sqrt{2}}\,, \quad \hat{b} \equiv i\hat{\Gamma}_+ = i\frac{\hat{\Gamma}_1 + i\hat{\Gamma}_2}{\sqrt{2}}\,, \tag{C.27}$$

In the following, we look into the Landau level structure in different gauges in more details.

C.2 Landau levels in the symmetric gauge

The symmetric gauge is suitable for studying geometries with rotational symmetry, e.g. spherical, disk, and corbino geometry. Below we will outline the description of the system in symmetric gauge.

C.2.1 General theory

The vector potential in symmetric gauge is $\mathbf{A}_{\text{sym}}(\mathbf{x}) = 1/2\,\mathbf{n}\times\mathbf{x}$. When rotational symmetry is present, it is convenient to use complex variables

$$z_\varsigma = \frac{x + i\varsigma y}{\sqrt{2}}\,, \quad \bar{z}_\varsigma = \frac{x - i\varsigma y}{\sqrt{2}}\,. \tag{C.28}$$

The inverse transformations reads as

$$x = \frac{z_\varsigma + \bar{z}_\varsigma}{\sqrt{2}}\,, \quad y = \frac{\varsigma(z_\varsigma - \bar{z}_\varsigma)}{i\sqrt{2}}\,. \tag{C.29}$$

In the complex coordinates, the position vector takes the form

$$\mathbf{x} = x\,\hat{\mathbf{x}} + y\,\hat{\mathbf{y}} = z_\varsigma \left(\frac{\hat{\mathbf{x}} - i\varsigma\hat{\mathbf{y}}}{\sqrt{2}}\right) + \bar{z}_\varsigma \left(\frac{\hat{\mathbf{x}} + i\varsigma\hat{\mathbf{y}}}{\sqrt{2}}\right) = z_\varsigma\,\hat{\boldsymbol{\epsilon}}_{+,\varsigma} + \bar{z}_\varsigma\,\hat{\boldsymbol{\epsilon}}_{-,\varsigma}\,, \tag{C.30}$$

so z_ς and $\bar{z}_\varsigma$ correspond to circular polarizations $+,\varsigma$ and $-,\varsigma$,

$$\hat{\boldsymbol{\epsilon}}_{+,\varsigma} = \frac{\hat{\mathbf{x}} - i\varsigma\hat{\mathbf{y}}}{\sqrt{2}}\,, \quad \hat{\boldsymbol{\epsilon}}_{-,\varsigma} = \frac{\hat{\mathbf{x}} + i\varsigma\hat{\mathbf{y}}}{\sqrt{2}}\,, \tag{C.31}$$

with the inverse relations

$$\hat{\mathbf{x}} = \frac{1}{\sqrt{2}}\Big(\hat{\boldsymbol{\epsilon}}_{+,\varsigma} + \hat{\boldsymbol{\epsilon}}_{-,\varsigma}\Big)\,, \quad \hat{\mathbf{y}} = \frac{i\varsigma}{\sqrt{2}}\Big(\hat{\boldsymbol{\epsilon}}_{+,\varsigma} - \hat{\boldsymbol{\epsilon}}_{-,\varsigma}\Big)\,. \tag{C.32}$$

We have the following orthogonality relations for $\hat{\boldsymbol{\epsilon}}_{+,\varsigma}$ and $\hat{\boldsymbol{\epsilon}}_{-,\varsigma}$,

$$\hat{\boldsymbol{\epsilon}}^*_{+,\varsigma} = \hat{\boldsymbol{\epsilon}}_{-,\varsigma}\,, \quad \hat{\boldsymbol{\epsilon}}^*_{+,\varsigma}\cdot\hat{\boldsymbol{\epsilon}}_{+,\varsigma} = \hat{\boldsymbol{\epsilon}}^*_{-,\varsigma}\cdot\hat{\boldsymbol{\epsilon}}_{-,\varsigma} = 1\,, \quad \hat{\boldsymbol{\epsilon}}^*_{+,\varsigma}\cdot\hat{\boldsymbol{\epsilon}}_{-,\varsigma} = \hat{\boldsymbol{\epsilon}}^*_{-,\varsigma}\cdot\hat{\boldsymbol{\epsilon}}_{+,\varsigma} = 0 \tag{C.33}$$

The derivatives with respect to z_ς and $\bar{z}_\varsigma$ and their inverses are as the following,

$$\begin{cases} \partial_{z_\varsigma} = \partial_{z_\varsigma}x\,\partial_x + \partial_{z_\varsigma}y\,\partial_y = \frac{1}{\sqrt{2}}\Big(\partial_x - i\varsigma\partial_y\Big), \\ \partial_{\bar{z}_\varsigma} = \partial_{\bar{z}_\varsigma}x\,\partial_x + \partial_{\bar{z}_\varsigma}y\,\partial_y = \frac{1}{\sqrt{2}}\Big(\partial_x + i\varsigma\partial_y\Big)\,, \end{cases} \tag{C.34}$$

with the inverse relations

$$\begin{cases} \partial_x = \partial_x z_\varsigma\,\partial_{z_\varsigma} + \partial_x\bar{z}_\varsigma\,\partial_{\bar{z}_\varsigma} = \frac{1}{\sqrt{2}}\Big(\partial_{z_\varsigma} + \partial_{\bar{z}_\varsigma}\Big)\,, \\ \partial_y = \partial_y z_\varsigma\,\partial_{z_\varsigma} + \partial_y\bar{z}_\varsigma\,\partial_{\bar{z}_\varsigma} = \frac{i\varsigma}{\sqrt{2}}\Big(\partial_{z_\varsigma} - \partial_{\bar{z}_\varsigma}\Big)\,. \end{cases} \tag{C.35}$$

One can easily check that the following relations hold

$$\begin{aligned} &{z_\varsigma}^\dagger = \bar{z}_\varsigma\,, \quad \partial^\dagger_{\bar{z}_\varsigma} = -\partial_{z_\varsigma}\,, \\ &[\,\partial_{z_\varsigma}, z_\varsigma\,] = [\,\partial_{\bar{z}_\varsigma}, \bar{z}_\varsigma\,] = 1\,, \quad [\,\partial_{z_\varsigma}, \bar{z}_\varsigma\,] = [\,\partial_{\bar{z}_\varsigma}, z_\varsigma\,] = 0\,. \end{aligned} \tag{C.36}$$

Here for completeness, we derive the form of kinetic and magnetic momenta,

$$i\hat{\boldsymbol{\Pi}} = \ \nabla - i\varsigma\mathbf{A}(\mathbf{x}) = \hat{\boldsymbol{\epsilon}}_{+,\varsigma}\, i\hat{\Pi}_{+,\varsigma} + \hat{\boldsymbol{\epsilon}}_{-,\varsigma}\, i\hat{\Pi}_{-,\varsigma}\,, \tag{C.37}$$

$$i\hat{\boldsymbol{\Gamma}} = \ \nabla + i\varsigma\mathbf{A}(\mathbf{x}) = \hat{\boldsymbol{\epsilon}}_{+,\varsigma}\, i\hat{\Gamma}_{+,\varsigma} + \hat{\boldsymbol{\epsilon}}_{-,\varsigma}\, i\hat{\Gamma}_{-,\varsigma}\,. \tag{C.38}$$

As before, we have the following hermitian conjugation relations for $\hat{\Pi}_{\pm,\varsigma}$ and $\hat{\Gamma}_{\pm,\varsigma}$ as well as the definition of harmonic oscillator modes $\hat{a}$ and $\hat{b}$,

$$\begin{aligned} \hat{\Pi}^\dagger_{+,\varsigma} &= \hat{\Pi}_{-,\varsigma}\,, \\ \hat{\Gamma}^\dagger_{+,\varsigma} &= \hat{\Gamma}_{-,\varsigma}\,, \end{aligned} \tag{C.39}$$

$$\begin{aligned} \hat{a}_\varsigma &\equiv i\hat{\Pi}_{+,\varsigma}\,, \quad \hat{a}^\dagger_\varsigma \equiv -i\hat{\Pi}_{-,\varsigma} \\ \hat{b}_\varsigma &\equiv i\hat{\Gamma}_{-,\varsigma} \quad\ \hat{b}^\dagger_\varsigma \equiv -i\hat{\Gamma}_{+,\varsigma}\,, \end{aligned} \tag{C.40}$$

with the following commutation relations

$$\begin{aligned} &[\,\hat{\Pi}_{+,\varsigma}, \hat{\Pi}_{-,\varsigma}\,] = 1\,, \\ &[\,\hat{\Pi}_{\pm,\varsigma}, \hat{\Gamma}_{\pm,\varsigma}\,] = 0\,, \\ &[\,\hat{\Gamma}_{-,\varsigma}, \hat{\Gamma}_{+,\varsigma}\,] = 1\,. \end{aligned} \tag{C.41}$$

In terms of $z_\varsigma, \bar{z}_\varsigma, \partial_{z_\varsigma}, \partial_{\bar{z}_\varsigma}$,

$$\begin{aligned} \hat{\Pi}_{+,\varsigma} &= -i\hat{a}_\varsigma = -i\Big(\partial_{\bar{z}_\varsigma} + z_\varsigma/2\Big)\,, \quad \hat{\Gamma}_{+,\varsigma} = i\hat{b}^\dagger_\varsigma = -i\Big(\partial_{\bar{z}_\varsigma} - z_\varsigma/2\Big)\,, \\ \hat{\Pi}_{-,\varsigma} &= i\hat{a}^\dagger_\varsigma = -i\Big(\partial_{z_\varsigma} - \bar{z}_\varsigma/2\Big)\,, \quad \hat{\Gamma}_{-,\varsigma} = -i\hat{b}_\varsigma = -i\Big(\partial_{z_\varsigma} + \bar{z}_\varsigma/2\Big)\,. \end{aligned} \tag{C.42}$$

The normal angular momentum component $\hat{L}_3$ takes the following form

$$\hat{L}_3 = \varsigma\left(z_\varsigma\partial_{z_\varsigma} - \bar{z}_\varsigma\partial_{\bar{z}_\varsigma}\right) = \varsigma\left(\hat{b}^\dagger\hat{b} - \hat{a}^\dagger\hat{a}\right)\,, \tag{C.43}$$

where we used the following relations

$$\begin{aligned} \nabla &= \hat{\boldsymbol{\epsilon}}_{+,\varsigma}\,\partial_{\bar{z}_\varsigma} + \hat{\boldsymbol{\epsilon}}_{-,\varsigma}\,\partial_{z_\varsigma} = \hat{\boldsymbol{\epsilon}}^*_{+,\varsigma}\,\partial_{z_\varsigma} + \hat{\boldsymbol{\epsilon}}^*_{-,\varsigma}\,\partial_{\bar{z}_\varsigma}\,, \\ \mathbf{A}_{\text{sym}}(\mathbf{x}) &= \frac{i}{2}\varsigma\, z_\varsigma\,\hat{\boldsymbol{\epsilon}}_{+,\varsigma} - \frac{i}{2}\varsigma\,\bar{z}_\varsigma\,\hat{\boldsymbol{\epsilon}}_{-,\varsigma} \end{aligned} \tag{C.44}$$

We expand the Hamiltonian in Eq. C.1 as

$$H = -\frac{1}{2}\left(\nabla^2 - i2\varsigma\mathbf{A}_{\text{sym}}(\mathbf{x})\cdot\nabla - \mathbf{A}_{\text{sym}}(\mathbf{x})^2\right)\,. \tag{C.45}$$

By making use of the following identities

$$\begin{cases} \nabla^2 = 2\,\partial_{\bar{z}_\varsigma z_\varsigma}\,, \\ \mathbf{A}_{\mathrm{sym}}(\mathbf{x})^2 = \bar{z}_\varsigma z_\varsigma/2\,, \\ -i2\,\mathbf{A}_{\mathrm{sym}}(\mathbf{x})\cdot\nabla = (-i)\,(\,x\partial_y - y\partial_x\,) = L_3\,, \\ L_3 = \varsigma\left(z\partial_z - \bar{z}\partial_{\bar{z}}\right), \end{cases} \tag{C.46}$$

thus, the Hamiltonian in Eq. C.45

$$H = -\frac{1}{2}\Big(2\partial_{\bar{z}_\varsigma z_\varsigma} - \bar{z}_\varsigma z_\varsigma/2 + \varsigma L_3\Big) = -\frac{1}{2}\Big(2\partial_{\bar{z}_\varsigma z_\varsigma} - \bar{z}_\varsigma z_\varsigma/2 + (z_\varsigma\partial_{z_\varsigma} - \bar{z}_\varsigma\partial_{\bar{z}_\varsigma})\Big)\,. \tag{C.47}$$

Interestingly, the form of the Hamiltonian is invariant under the change of variables $\varsigma \to -\varsigma$ and $z_\varsigma \to z_{-\varsigma}$. We further have

$$\begin{aligned} &\partial_{\bar{z}z}\, e^{-\alpha|z|^2} = e^{-\alpha|z|^2}\left[\partial_{\bar{z}z} + \alpha^2\bar{z}z - \alpha\,(\,z\partial_z + \bar{z}\partial_{\bar{z}}\,) - \alpha\right], \\ &(\,z\partial_z - \bar{z}\partial_{\bar{z}}\,)\, e^{-\alpha|z|^2} = e^{-\alpha|z|^2}\,(\,z\partial_z - \bar{z}\partial_{\bar{z}}\,)\,, \end{aligned} \tag{C.48}$$

Thus, for the action of the Hamiltonian on states in the lowest Landau level, we have

$$\begin{aligned} H\, e^{-\alpha|z|^2} &= -\frac{1}{2}\, e^{-\alpha|z|^2}\left\{2\left[\partial_{\bar{z}z} + \alpha^2\bar{z}z - \alpha\,(\,z\partial_z + \bar{z}\partial_{\bar{z}}\,) - \alpha\right] - \bar{z}z/2 + \varsigma\,(\,z\partial_z - \bar{z}\partial_{\bar{z}}\,)\right\} \\ &= e^{-\alpha|z|^2}\left\{H - \alpha^2\bar{z}z + \alpha(z\partial_z + \bar{z}\partial_{\bar{z}}) + \alpha\right\} \end{aligned} \tag{C.49}$$

for $\alpha = 1/2$, the above expression reduced to

$$H\left(e^{-|z|^2/2}\, f(z)\right) = e^{-|z|^2/2}\left(-\,\partial_{\bar{z}z} + \bar{z}\partial_{\bar{z}} + \frac{1}{2}\right) f(z) = \frac{1}{2} e^{-|z|^2/2}\, f(z)\,. \tag{C.50}$$

Eq. C.50 means that the ground state of the Hamiltonian is of the form of a Gaussian factor times a holomorphic function. The Landau levels in a symmetric gauge are

$$|n, m\rangle = \mathcal{N}^{(\mathrm{sym})}_{n,m}\;\cdot\; z_\varsigma^{m-n}\cdot e^{-r^2/4}\, L_n^{(m-n)}\!\left(\frac{r^2}{2}\right) = \mathcal{N}^{(\mathrm{sym})}_{n,m}\;\cdot\; z_\varsigma^{m-n}\cdot e^{-|z_\varsigma|^2/2}\, L_n^{(m-n)}\!\left(|z_\varsigma|^2\right), \tag{C.51}$$

where the normalization factor $\mathcal{N}^{(\mathrm{sym})}_{n,m}$ is

$$\mathcal{N}^{(\mathrm{sym})}_{n,m} = (-1)^n \frac{\sqrt{n!}}{\sqrt{2\pi m!}}\,. \tag{C.52}$$

C.3 Haldane Pseudopotentials

In order to quantify two-body interactions in the lowest Landau level, it is instructive to consider the two-body scattering problem in a magnetic field. To this end, consider the following Hamiltonian,

$$H = \frac{1}{2}\boldsymbol{\Pi}_1^2 + \frac{1}{2}\boldsymbol{\Pi}_2^2 + V\Big(|\mathbf{x}_1 - \mathbf{x}_2|\Big)\,, \tag{C.53}$$

As in the previous section, the complex coordinates for the particles are $z_{\varsigma_1,1}$ and $z_{\varsigma_2,2}$, where the helicities ς_1 and ς_2 can in principle be different, but since the final form of the Hamiltonian is independent of the helicity, we hereby drop the indices ς_1 and ς_2. We transform to the center-of-mass and relative coordinates

$$\begin{cases} Z = \Big(z_1 + z_2\Big)/2\,, \quad z = z_1 - z_2\,, \\ z_1 = Z + z/2\,, \quad z_2 = Z - z/2\,, \end{cases} \tag{C.54}$$

where the Jacobian of the transformation is unity. The corresponding transformation rules for the derivatives read as

$$\begin{cases} \partial_{z_1} = \partial_{z_1}Z\,\partial_Z + \partial_{z_1}z\,\partial_z = (1/2)\partial_Z + \partial_z\,, \\ \partial_{z_2} = \partial_{z_2}Z\partial_Z + \partial_{z_2}z\,\partial_z = (1/2)\partial_Z - \partial_z\,, \end{cases} \tag{C.55}$$

The kinetic term in the Hamiltonian for general degree of freedoms x and y, $(1/2)\boldsymbol{\Pi}^2$ can be written in terms of complex coordinates as

$$\frac{1}{2}\boldsymbol{\Pi}^2 = -\partial_{\bar{z}z} + \frac{\bar{z}z}{4} - \frac{1}{2}\Big(z\partial_z - \bar{z}\partial_{\bar{z}}\Big)\,, \tag{C.56}$$

thus, the kinetic part of the Hamiltonian can be factored into a center-of-mass and a relative coordinate contribution,

$$\begin{aligned} H_0^{(\mathrm{CM})} &= -\frac{1}{2}\partial_{\bar{Z}Z} + \frac{2\bar{Z}Z}{4} - \frac{1}{2}\Big(Z\partial_Z - \bar{Z}\partial_{\bar{Z}}\Big)\,, \\ H_0^{(\mathrm{rel})} &= -2\partial_{\bar{z}z} + \frac{1}{4}\Big(\frac{\bar{z}z}{2}\Big) - \frac{1}{2}\Big(z\partial_z - \bar{z}\partial_{\bar{z}}\Big)\,, \end{aligned} \tag{C.57}$$

the lowest Landau level wavefunction with $M = 0$, $m = 0$ reads as

$$|m_1 = 0, m_2 = 0\rangle = |M = 0, m = 0\rangle = \frac{1}{\sqrt{2\pi}^2}\, e^{-\Big(|z_1|^2 + |z_2|^2\Big)/2} = \frac{1}{\sqrt{2\pi}^2}\, e^{-\Big(2|Z|^2 + (1/2)|z|^2\Big)}\,, \tag{C.58}$$

and the creation operator for the center-of-mass and relative angular momenta reads as

$$B^\dagger = \frac{1}{\sqrt{2}}\Big(-\partial_{\bar{Z}} + Z\Big)\,, \quad b^\dagger = \frac{1}{\sqrt{2}}\Big(-2\partial_{\bar{z}} + \frac{z}{2}\Big)\,, \tag{C.59}$$

and the states with total angular momentum M and relative angular momentum m can be constructed by applying $B^\dagger$ and $b^\dagger$ operators consecutively on the state in Eq. C.58,

$$|M,m\rangle = \frac{B^{\dagger M} b^{\dagger m}}{\sqrt{M!}\sqrt{m!}}\,|0,0\rangle = \frac{1}{2^{M/2}\sqrt{2\pi M!}}\Big(2Z\Big)^M e^{-|Z|^2}\cdot\frac{1}{2^{m/2}\sqrt{2\pi m!}}(z)^m\,e^{-|z|^2/4}. \tag{C.60}$$

For defining Haldane pseudopotentials, we need the following overlaps

$$\langle m_1,m_2|M,m\rangle = (-1)^{m-m_1}\,2^{-(M+m)/2}\left(\frac{m_1!m_2!}{M!m!}\right)^{1/2}\left[\sum_{k=0}^{M}(-1)^k\binom{M}{k}\binom{m}{m_1-k}\right]\delta_{M+m,m_1+m_2}. \tag{C.61}$$

Matrix elements of a central potential $\langle m_3,m_4|\,V(r)\,|m_1,m_2\rangle$ only depends on the relative angular momentum index m. Furthermore, $V(r)$ conserves the total angular momentum and relative angular momentum, thus

$$\langle M',m'|\,V(r)\,|M,m\rangle = \delta_{M'M}\delta_{m'm}\,\langle m'|\,V(r)\,|m\rangle\ , \tag{C.62}$$

thus the potential operator is

$$\begin{aligned} V &= \sum_{M',M}\sum_{m',m}\langle M',m'|\,V\,|M,m\rangle\ |M',m'\rangle\!\langle M,m| \\ &= \sum_m \langle m|\,V\,|m\rangle\left(\sum_M |M,m\rangle\!\langle M,m|\right), \\ &= \sum_m \langle m|\,V\,|m\rangle\,P_m\,, \end{aligned} \tag{C.63}$$

where P_m is the projection operator on two-particle states with relative angular momenta m. In terms of states $|m_1,m_2\rangle$, its matrix elements read

$$\langle m_3,m_4|\,P_m\,|m_1,m_2\rangle = \sum_M \langle m_3,m_4|M,m\rangle\,\langle M,m|m_1,m_2\rangle\ , \tag{C.64}$$

thus,

$$\langle m_3,m_4|\,V\,|m_1,m_2\rangle = \sum_m V_m\left(\sum_M \langle m_3,m_4|M,m\rangle\,\langle M,m|m_1,m_2\rangle\right). \tag{C.65}$$

C.4 Quantum Hall effect on spherical geometry

We consider a spherical surface with radius r enclosing a magnetic monopole located at the origin. The magnetic flux density threading the sphere is

$$\mathbf{B} = \frac{\Phi}{2r^2}\boldsymbol{\Omega}\,, \tag{C.66}$$

where Φ is the monopole total flux, and $\boldsymbol{\Omega}$ is the radial unit vector. The vector potential satisfies the equation

$$\nabla\times\mathbf{A} = \frac{\Phi}{2r^2}\boldsymbol{\Omega}\,. \tag{C.67}$$

There are a number of gauge fixing choices, corresponding to different configuration of a semi-infinite solenoid carrying the magnetic flux, as the following,

- Solenoid on $z<0$ axis, axial vector potential $\mathbf{A}=A^N_\phi(\theta)\boldsymbol{\phi}$,

$$A^N_\phi(\theta)=\frac{\Phi}{2r}\tan(\theta/2)\,. \tag{C.68}$$

- Solenoid on $z>0$ axis, axial vector potential $\mathbf{A}=A^S_\phi(\theta)\boldsymbol{\phi}$,

$$A^S_\phi(\theta)=-\frac{\Phi}{2r}\cot(\theta/2)\,. \tag{C.69}$$

- A solenoid carrying half of the flux on $z>0$ axis and a solenoid carrying the other half on $z<0$ axis, axial vector potential $\mathbf{A}=A_\phi(\theta)\boldsymbol{\phi}$, $A_\phi(\theta)=1/2(A^N_\phi(\theta)+A^S_\phi(\theta))$,

$$A_\phi(\theta)=-\frac{\Phi}{2r}\cot(\theta)\,. \tag{C.70}$$

We proceed with the last gauge choice. The covariant derivative $\mathbf{D}=\nabla-i\mathbf{A}(\mathbf{x})$ in spherical coordinates reads as

$$\mathbf{D}=\nabla-i\mathbf{A}(\mathbf{x})=\boldsymbol{\Omega}\,\partial_r+\frac{\boldsymbol{\theta}}{r}\partial_\theta+\frac{\boldsymbol{\phi}}{r\sin(\theta)}\Big(\partial_\phi+i\frac{\Phi}{2}\cos(\theta)\Big)\,. \tag{C.71}$$

We define the orbital (kinetic) angular momentum $\boldsymbol{\Lambda}$ to be

$$\boldsymbol{\Lambda}=\mathbf{x}\times(m\dot{\mathbf{x}})=\mathbf{x}\times\boldsymbol{\Pi}, \tag{C.72}$$

for which the well-known expression for the magnitude of the angular momentum holds,

$$\boldsymbol{\Lambda}^2=(\mathbf{x}\cdot\mathbf{x})(\boldsymbol{\Pi}\cdot\boldsymbol{\Pi})-(\mathbf{x}\cdot\boldsymbol{\Pi})^2+i\hbar(\mathbf{x}\cdot\boldsymbol{\Pi})\,, \tag{C.73}$$

resulting in the analoguous relation between Laplacian operator and total angular momentum

$$\boldsymbol{\Pi}^2=\frac{\boldsymbol{\Lambda}^2}{r^2}+(-i\hbar)^2\,\frac{1}{r^2}\partial_r\Big(r^2\partial_r\Big)\,. \tag{C.74}$$

In the spherical coordinates,

$$\boldsymbol{\Lambda}=(-i)\boldsymbol{\phi}\,\partial_\theta-(-i)\boldsymbol{\theta}\,\frac{1}{\sin(\theta)}\Big(\partial_\phi+i\,\varsigma S\cos(\theta)\Big)\,. \tag{C.75}$$

It can be shown that for the quantum mechanical problem, $[r^2,H]=0$, such that the radius will remain constant and terms involving radial derivatives can be ignored (this is trivially true for a particle confined on a sphere). Thus, the Hamiltonian can be rewritten in terms of $\boldsymbol{\Lambda}$,

$$H=\frac{1}{2mr^2}\boldsymbol{\Lambda}^2\,. \tag{C.76}$$

In spherical coordinates, $\mathbf{\Pi}^2$ explicitly reads

$$\begin{aligned}\mathbf{\Pi}^2 &= (-i\hbar)^2\Big(\nabla^2 - i2\,\varsigma\mathbf{A}\cdot\nabla - \mathbf{A}^2\Big)\\ &= (-i\hbar)^2\left(\frac{1}{r^2}\partial_r(r^2\partial_r) + \frac{1}{r^2\sin(\theta)}\partial_\theta\Big(\sin(\theta)\partial_\theta\Big) + \frac{1}{r^2\sin^2(\theta)}\Big(\partial_\phi + i\,\varsigma\frac{\Phi}{2}\cos(\theta)\Big)^2\right).\end{aligned} \tag{C.77}$$

From Eq. C.77, we obtain the following expression for $\mathbf{\Lambda}^2$

$$\mathbf{\Lambda}^2 = (-i\hbar)^2\left(\frac{1}{\sin(\theta)}\partial_\theta\Big(\sin(\theta)\partial_\theta\Big) + \frac{1}{\sin^2(\theta)}\Big(\partial_\phi + i\,\varsigma\frac{\Phi}{2}\cos(\theta)\Big)^2\right). \tag{C.78}$$

From the theory of classical electrodynamics it is a known fact that the angular momentum of a charged particle with charge q in a magnetic monopole with charge Q such that $\mathbf{B} = (Q/r^2)\mathbf{\Omega}$ is $\mathbf{L}_{\text{em}} = -(qQ/c)\mathbf{\Omega}$. In the natural units, $\mathbf{B} = (\Phi/2)\mathbf{\Omega}/r^2$ and $\mathbf{L}_{\text{em}} = -\varsigma(\Phi/2)\,\mathbf{\Omega}$. The total angular momentum of the system thus is $\mathbf{L} = \mathbf{\Lambda} - \varsigma S\mathbf{\Omega}$, and is a constant of motion. Here $S = (\Phi/2)$ is the spin of the charged particle. The usual angular momentum commutation relations follows as

$$[L_i, L_j] = i\varepsilon_{ijk}L_k\,, \tag{C.79}$$

which is consistent with the following commutation relations for $\mathbf{\Lambda}$ components,

$$[\Lambda_i, \Lambda_j] = i\varepsilon_{ijk}(\Lambda_k + \varsigma S\,\Omega_k). \tag{C.80}$$

in spherical coordinates,

$$\mathbf{L} = -\varsigma S\,\mathbf{\Omega} + (-i)\boldsymbol{\phi}\,\partial_\theta - (-i)\boldsymbol{\theta}\,\frac{1}{\sin(\theta)}\Big(\partial_\phi + i\,\varsigma S\cos(\theta)\Big)\,, \tag{C.81}$$

with the components

$$\begin{cases} L_3 = -i\partial_\phi\,,\\ L_1 = -\varsigma S\,\frac{\cos(\phi)}{\sin(\theta)} + i\sin(\phi)\,\partial_\theta + i\cot(\theta)\cos(\phi)\,\partial_\phi\,,\\ L_2 = -\varsigma S\,\frac{\sin(\phi)}{\sin(\theta)} - i\cos(\phi)\,\partial_\theta + i\cot(\theta)\sin(\phi)\,\partial_\phi\,.\end{cases} \tag{C.82}$$

As usual, the raising and lowering operators $L_\pm = L_1 \pm iL_2$, as below

$$L_\pm = e^{\pm i\phi}\left(\pm\,\partial_\theta + i\cot(\theta)\partial_\phi - \varsigma\frac{S}{\sin(\theta)}\right). \tag{C.83}$$

C.4.1 Spectrum of kinetic angular momentum

Eq. C.76 in dimensionless form $H=(1/2r^2)\mathbf{\Lambda}^2$ indicates that the spectrum of $\mathbf{\Lambda}^2$ gives the Landau levels. Given that $\mathbf{L}=\mathbf{\Lambda}-\varsigma S\mathbf{\Omega}$ and $\mathbf{\Lambda}\cdot\mathbf{\Omega}=0$, we have

$$\mathbf{\Lambda}^2=\mathbf{L}^2-S^2\,. \tag{C.84}$$

Since L_i's satisfy the angular momentum algebra, their representation exactly follows that of the angular momentum algebra, i.e. there exists a set of basis functions $Y_{Slm}(\theta,\phi)$ for the functions on the unit sphere such that

$$\begin{cases} \mathbf{L}^2\,Y_{Slm}=l(l+1)Y_{Slm}\,, \\ L_3\,Y_{Slm}=m\,Y_{Slm}\,, \end{cases} \tag{C.85}$$

where $l=0,1/2,1,3/2,\cdots$ and $m=-l,-l+1,\cdots,l$, and half-integer values of l are also allowed, in contrast to the case of orbital angular momentum in the ordinary quantum mechanics. To obtain the spectrum, we use the explicit representation of $\mathbf{\Lambda}^2$ in spherical coordinates as in Eq. C.78, and assume a solution of the type $Y_{Slm}(\theta,\phi)=e^{im\phi}P_{Slm}\Big(\cos(\theta)\Big)$, where $P_{Slm}\Big(\cos(\theta)\Big)$ satisfies the following differential equation,

$$\begin{aligned} &-\frac{1}{\sin(\theta)}\partial_\theta\Big(\sin(\theta)\partial_\theta\,P_{Slm}\Big(\cos(\theta)\Big)\Big) \\ &+\frac{1}{\sin^2(\theta)}\Big(m^2+2m\,\varsigma S\cos(\theta)+S^2\cos^2(\theta)\Big)\,P_{Slm}\Big(\cos(\theta)\Big)=\Big[l(l+1)-S^2\Big]\,P_{Slm}\Big(\cos(\theta)\Big)\,. \end{aligned} \tag{C.86}$$

Changing variable to $x=\cos(\theta)$, Eq. C.86 takes the form

$$\left\{-(1-x^2)d_x^2+2xd_x+\frac{1}{(1-x^2)}\Big(m+\varsigma S\,x\Big)^2\right\}P_{Slm}(x)=\Big[l(l+1)-S^2\Big]\,P_{Slm}(x)\,. \tag{C.87}$$

To proceed, we use the following identities

$$\begin{cases} d_x\,Q_{ab}(x)=Q_{ab}(x)\left(\frac{a-bx}{(1-x^2)}+d_x\right)\,, \\ d_x^2\,Q_{ab}(x)=Q_{ab}(x)\left[\frac{(a^2-b)+[2a(1-b)]x+b(b-1)x^2}{(1-x^2)^2}+\frac{2(a-bx)}{(1-x^2)}d_x+d_x^2\right]\,, \end{cases} \tag{C.88}$$

where $Q_{ab}(x)=(1+x)^{\frac{a+b}{2}}(1-x)^{\frac{b-a}{2}}$. By defining $R_{Slm}(x)$ as $P_{Slm}(x)=Q_{ab}(x)R_{Slm}(x)$, Eq. C.87 reduces to

$$\left\{(1-x^2)d_x^2+2[a-(b+1)x]d_x-\frac{C(x)}{(1-x^2)}\right\}R_{Slm}(x)=\Big[l(l+1)-S^2\Big]\,R_{Slm}\,, \tag{C.89}$$

where $C(x) = (-a^2 + b + m^2) + 2\Big(ab + \varsigma m S\Big)x + \Big(S^2 - b(b+1)\Big)x^2$. by setting $b = m$ and $a = -\varsigma S$, Eq. C.89 reduces to

$$\Bigg\{(1-x^2)d_x^2 - 2\Big(\varsigma S + (m+1)x\Big)d_x - \Big(m(m+1) - S^2\Big)\Bigg\} R_{Slm}(x) = \Big[-l(l+1) + S^2\Big] R_{Slm}\,. \tag{C.90}$$

Eq. C.90 is a hypergeometric equation of the form

$$(1-x^2)y'' + \Big(\beta - \alpha - (\alpha + \beta + 2)x\Big)y' + n(n + \alpha + \beta + 1)y = 0\,, \tag{C.91}$$

with $\alpha = m + \varsigma S$, $\beta = m - \varsigma S$ and $n = l - m$. Eq. C.91 has *jacobi polynomials* $P_n^{\alpha,\beta}(x)$ as its solutions, which are in the form

$$\begin{aligned} P_n^{\alpha,\beta}(x) &= \frac{(-1)^n}{2^n n!}(1-x)^{-\alpha}(1+x)^{-\beta}\frac{\mathrm{d}^n}{\mathrm{d}x^n}\Big[(1-x)^{\alpha+n}(1+x)^{\beta+n}\Big] \\ &= \frac{1}{2^n}\sum_{s=0}^{n}(-1)^{n-s}\binom{n+\alpha}{s}\binom{n+\beta}{n-s}(1-x)^{n-s}(1+x)^s\,. \end{aligned} \tag{C.92}$$

Putting the pieces together, we obtain the following expression for the *monopole harmonics* $Y_{Slm}(\theta,\phi)$,

$$Y_{Slm} = \mathcal{N}_{Slm}\cdot 2^{-m}\cdot e^{im\phi}\cdot(1+x)^{\frac{m-\varsigma S}{2}}(1-x)^{\frac{m+\varsigma S}{2}}\cdot P_{l-m}^{m+\varsigma S, m-\varsigma S}(x)\,. \tag{C.93}$$

with the normalization factor

$$\mathcal{N}_{Slm} = \sqrt{\frac{2l+1}{4\pi}\frac{(l-m)!(l+m)!}{(l-S)!(l+S)!}}\,. \tag{C.94}$$

C.5 Disk Geometry

In this section we introduce another rotationally symmetric geometry in infinite two dimensional systems which is the disk geometry. The proper gauge for the disk geometry is the symmetric gauge, whose properties where studied in details in previous sections. It is relevant for experimental realizations of the FQHE systems to confine interacting particles in optical traps, thus studying the properties of mobile particles in uniform gauge fields in the presence of a harmonic trap is important. Due to cylindrical symmetry of these configurations, the disk geometry is suitable to study these systems. To investigate the single particle physics of a charged particle in a magnetic field confined in a harmonic potential, we begin by the corresponding Hamiltonian, keeping all the dimensions of the quantities

$$H = \frac{1}{2m}\Bigg(-i\hbar\nabla - \frac{qB}{c}\frac{1}{2}\hat{\mathbf{n}}\times\mathbf{x}\Bigg)^2 + \frac{1}{2}m\omega_0^2 r^2\,. \tag{C.95}$$

We note that, an alternative form of the single particle Hamiltonian in the symmetric gauge, Eq. C.47 is

$$H = -\frac{\hbar^2}{2m}\nabla^2 - \frac{\varsigma\hbar\omega_{\mathrm{B}}}{2}\frac{L_z}{\hbar} + \frac{1}{2}m\omega_{\mathrm{B}}^2\frac{r^2}{4} = -\frac{\hbar\omega_{\mathrm{B}}}{2}\Bigg(\nabla^2 + \frac{\varsigma L_z}{\hbar} - \frac{r^2}{4}\Bigg)\,, \tag{C.96}$$

Eq. C.97 can also be written in a suitable form to include the trapping term,

$$\begin{aligned} H &= -\frac{\hbar^2}{2m}\nabla^2 - \frac{\varsigma\omega_{\rm B}}{2}\, L_z \,+ \frac{1}{2}m\Big(\omega_{\rm B}^2 + 4\omega_0^2\Big)\frac{r^2}{4} \\ &= \bigg[-\frac{\hbar^2}{2m}\nabla^2 - \frac{\varsigma\Omega_{\rm C}}{2}L_z + \frac{1}{2}m\Omega_{\rm C}^2\frac{r^2}{4}\bigg] + \frac{\varsigma(\Omega_{\rm C} - \omega_{\rm B})}{2}L_z\,. \end{aligned} \tag{C.97}$$

The Hamiltonian in Eq. C.97 has exactly the same eigenstates as the magnetic Hamiltonian in the symmetric gauge, with the renormalized cyclotron frequency $\Omega_{\rm C} = \sqrt{\omega_{\rm B}^2 + 4\omega_0^2}$.

C.6 Torus geometry

Although we do not use torus geometry for the purpose of calculations in this thesis, we nevertheless explain it in details, since it is directly relevant for extensions of the work performed in the last chater, especially for lattice systems such as moire fractional Chern insulators in twisted MoTe$_2$, and fractional Chern insulators in ultracold atomic systems. Investigating the Landau level structure on a torus is also advantageous for several other reasons. First, as a result of short-sightedness of spatial correlations in a FQHE system, the physics in the thermodynamic limit is known to be well reproduced from small systems confined to compact two dimensional surfaces. One way to realize the thermodynamic limit of a finite system is to impose periodic boundary conditions, which effectively puts the system on a torus. Torus geometry is also suitable to study currents since it allows non-contractible loop, a property not present in disk or spherical geometry. Here we first obtain the Landau levels of a particle for rectangular geometries, and then narrow down to the periodic boundary conditions.

For rectangular geometries, it is convenient to work with Landau gauges $\mathbf{A}_{\rm X}(\mathbf{x}) = -y\mathbf{e}_x$ and $\mathbf{A}_{\rm Y}(\mathbf{x}) = x\mathbf{e}_y$. In this gauges, the kinetic and magnetic momenta take the following form,

$$\begin{cases} \boldsymbol{\Pi}_{\rm X} = \mathbf{p} - \varsigma\mathbf{A}_{\rm X} = \mathbf{p} + \varsigma y\mathbf{e}_x \\ \boldsymbol{\Gamma}_{\rm X} = \mathbf{p} + \varsigma\mathbf{A}_{\rm Y} = \mathbf{p} + \varsigma x\mathbf{e}_y \end{cases} , \quad \begin{cases} \boldsymbol{\Pi}_{\rm Y} = \mathbf{p} - \varsigma\mathbf{A}_{\rm Y} = \mathbf{p} - \varsigma x\mathbf{e}_y \\ \boldsymbol{\Gamma}_{\rm Y} = \mathbf{p} + \varsigma\mathbf{A}_{\rm X} = \mathbf{p} - \varsigma y\mathbf{e}_x \end{cases} \tag{C.98}$$

Here, we choose to work with $\mathbf{A}_{\rm X}$. The Hamiltonian in this gauge takes the following form

$$H = \frac{1}{2}(-i\partial_x)^2 + \frac{1}{2}(-i\partial_y)^2 + (-i)\varsigma y\partial_x + \frac{1}{2}y^2\,. \tag{C.99}$$

The x-components of eigenfunctions are planewaves, such that eigenfunctions can be written as

$$\psi(\mathbf{x}) = \frac{e^{ik_x x}}{\sqrt{L_1}}\phi(y)\,. \tag{C.100}$$

The y-component of eigenfunctions $\phi(y)$ satisfy the time-independent Schrödinger equation with the following Hamiltonian

$$\tilde{H} = e^{-ik_x x}He^{ik_x x} = \frac{1}{2}(-i\partial_y)^2 + \frac{1}{2}(y + \varsigma k_x)^2\,, \tag{C.101}$$

which is just the Hamiltonian of simple harmonic oscillator with the normalized eigenfunctions

$$\phi_n(y) = \left(2^{n/2}\pi^{1/4}(n!)^{1/2}\right)^{-1} e^{-\frac{1}{2}(y+\varsigma k_x)^2} H_n(y+\varsigma k_x)\,. \tag{C.102}$$

We now consider a charged particle moving on a parallelogram surface with sides L_1 and L_2 forming an angle θ, thus the sides are parallel to $\mathbf{e}_1 = \mathbf{e}_x$ and $\mathbf{e}_2 = \cos\theta\,\mathbf{e}_x + \sin\theta\,\mathbf{e}_y$, respectively. The periodic boundary conditions are imposed by identifying opposite sides of the parallelogram. Given the twist angles ϕ_1 and ϕ_2, The periodic boundary conditions explicitly read

$$\begin{cases} \mathcal{T}(L_1\mathbf{e}_1)\,\psi(\mathbf{x}) = e^{i\phi_1}\psi(\mathbf{x})\,, \\ \mathcal{T}(L_2\mathbf{e}_2)\,\psi(\mathbf{x}) = e^{i\phi_2}\psi(\mathbf{x})\,, \end{cases} \tag{C.103}$$

where $\mathcal{T}(\mathbf{a}) = \exp(i\mathbf{a}\cdot\mathbf{\Gamma})$ is the magnetic translation along $\mathbf{a}$. Its explicit forms is

$$\begin{aligned} \mathcal{T}(\mathbf{a}) = e^{i\mathbf{a}\cdot\mathbf{\Gamma}_{\mathrm{X}}} &= \exp(-i\varsigma a_x a_y/2)\cdot\exp(a_y\partial_y)\cdot\exp(a_x\partial_x)\exp(i\varsigma a_y x) \\ &= \exp(i\varsigma a_x a_y/2)\cdot\exp(a_y\partial_y)\cdot\exp(i\varsigma a_y x)\exp(a_x\partial_x) \\ &= \exp(i\varsigma a_x a_y/2)\cdot\exp(i\varsigma a_y x)\cdot T(a_y\mathbf{e}_y)\,T(a_x\mathbf{e}_x)\,, \\ &= \exp(i\varsigma a_x a_y/2)\cdot\exp(i\varsigma a_y x)\cdot T(\mathbf{a})\,, \end{aligned} \tag{C.104}$$

Where $T(\mathbf{a})$ is the ordinary translation by $\mathbf{a}$, $T(\mathbf{a}) = \exp(i\mathbf{a}\cdot\hat{\mathbf{p}})$ On the lowest Landau level states of the form

$$\begin{aligned} \psi^{(0)}_{\mathrm{LLL}}(\mathbf{x};k_x) &= \frac{e^{-k_x^2/2}}{\pi^{1/4}\sqrt{L_1}}\,e^{-y^2/2}\,e^{ik_x(x+i\varsigma y)} \\ &= \frac{e^{ik_x x}}{\pi^{1/4}\sqrt{L_1}}\,e^{-(y+\varsigma k_x)^2/2}\,, \end{aligned} \tag{C.105}$$

the action of $\mathcal{T}(\mathbf{a})$ would be

$$\begin{aligned} \mathcal{T}(\mathbf{a})\,\psi^{(0)}_{\mathrm{LLL}}(\mathbf{x};k_x) = \frac{1}{\pi^{1/4}\sqrt{L_1}}&\exp(-i\varsigma a_x a_y/2)\exp\Big(i(k_x+\varsigma a_y)(x+a_x)\Big) \\ &\cdot\exp\Big(-\big(y+a_y+\varsigma k_x\big)^2/2\Big) \end{aligned} \tag{C.106}$$

From the first condition in Eq. C.103, the values of k_x are constrained to

$$k_x L_x = \phi_1 + 2\pi j_x\,. \tag{C.107}$$

Before proceeding further, we note that $\psi_{\mathrm{LLL}}(\mathbf{x})$ in the chosen gauge is localized around $y = \varsigma k_x$. Since the y-coordinate is restricted to $[-L_2/2\sin\theta, L_2/2\sin\theta)$, we have the following condition on k_x in addition to Eq. C.107,

$$-L_2\sin\theta \le \varsigma k_x \le L_2\sin\theta\,. \tag{C.108}$$

To fulfill the second condition in Eq. C.103, we have to superpose magnetic translations of a nominal LLL state $\psi^{(0)}_{\mathrm{LLL}}(\mathbf{x})$ (such as the one in Eq. C.105) by integer multiples of $L_2\mathbf{e}_2$

and with suitable weights. The normalized state fulfilling periodic boundary conditions reads as

$$\psi_{\mathrm{LLL}}(\mathbf{x}) = \left\{ \sum_{m=-\infty}^{+\infty} e^{-im\phi_2}\, \mathcal{T}^m(L_2\mathbf{e}_2) \right\} \psi^{(0)}_{\mathrm{LLL}}(\mathbf{x};k_x)\,. \tag{C.109}$$

Eq. C.109 explicitly reads

$$\begin{aligned}\psi_{\mathrm{LLL}}(\mathbf{x}) &= \frac{1}{\pi^{1/4}\sqrt{L_1}} \sum_{m=-\infty}^{+\infty} \exp\Big\{ -im\phi_2 - y^2/2 - k_x^2/2 + ie^{i\varsigma\theta} mL_2\Big[k_x + (1/2)\varsigma m L_2 \sin\theta\Big] \\ &\quad + i\Big[k_x + \varsigma m L_2 \sin\theta\Big] z_\varsigma \Big\} = \frac{1}{\pi^{1/4}\sqrt{L_1}} \sum_{m=-\infty}^{+\infty} i(-1)^m \exp(\alpha_0 + \alpha_1/2 + \alpha_2/4) \\ &\quad \cdot \exp\Big((\alpha_1 + \alpha_2 + i\pi)(m - 1/2)\Big) \exp\Big(\alpha_2 (m-1/2)^2\Big)\,,\end{aligned} \tag{C.110}$$

where

$$\begin{cases} \alpha_0 = -y^2/2 - k_x^2/2 + ik_x z_\varsigma\,, \\ \alpha_1 = -i\phi_2 + ik_x L_1 (L_2/L_1) e^{i\varsigma\theta} + i\,\varsigma(2\pi N_\phi)\, z_\varsigma/L_1\,, \\ \alpha_2 = (i/2)\varsigma(2\pi N_\phi)(L_2/L_1)e^{i\varsigma\theta}\,, \end{cases} \tag{C.111}$$

and $z_\varsigma = x + i\varsigma y$ (note the different convention used here as compared to earlier sections), such that Eq. C.110 can be written as

$$\begin{aligned}\psi_{\mathrm{LLL}}(\mathbf{x}) &= \frac{1}{\pi^{1/4}\sqrt{L_1}} \exp\Big\{ -y^2/2 - k_x^2/2 + (i/2)\Big(\tau_\varsigma k_x L_1 - \phi_2\Big) \\ &\quad + (i/4)\,\varsigma\,\pi N_\phi \tau_\varsigma + i\Big(k_x L_1 + \varsigma \pi N_\phi\Big) z_\varsigma / L_1 \Big\} \\ &\quad \cdot \sum_{m=-\infty}^{+\infty} i(-1)^m \exp\Big\{ i\pi\Big(\varsigma N_\phi \tau_\varsigma\Big)\Big(m - 1/2\Big)^2 \Big\} \exp\Big\{ i\varsigma(2\pi N_\phi)\Big(m - 1/2\Big)(z - z_0)/L_1 \Big\}\,,\end{aligned} \tag{C.112}$$

where $\tau_\varsigma = (L_2/L_1)e^{i\varsigma\theta}$ and

$$\begin{aligned} z_0 &= -\tau_\varsigma L_1 \left(\frac{\varsigma k_x L_1}{2\pi N_\phi} + \frac{1}{2} \right) - \frac{\varsigma L_1}{2N_\phi}\left(1 - \frac{\phi_2}{\pi}\right) \\ &= -\left(\frac{\varsigma k_x}{\sin\theta} + \frac{L_2}{2} \right) e^{i\varsigma\theta} - \frac{\varsigma L_1}{N_\phi}\left(\frac{\pi - \phi_2}{2\pi} \right). \end{aligned} \tag{C.113}$$

with these definitions, Eq. C.112 takes the more compact form

$$\begin{aligned}\psi_{\mathrm{LLL}}(\mathbf{x}) &= e^{-y^2/2} \cdot \frac{(-i)}{\pi^{1/4}\sqrt{L_1}} \exp\Big\{ -k_x^2/2 - (i/4)(\varsigma\pi N_\phi)\tau_\varsigma + ik_x z_0 \Big\} \\ &\quad \cdot \exp\Big\{ i(k_x L_1 + \varsigma \pi N_\phi)(z - z_0)/L_1 \Big\}\, \vartheta_1\left(\varsigma N_\phi \left(\frac{z - z_0}{L_1} \right) \middle| \varsigma N_\phi \tau_\varsigma \right)\end{aligned} \tag{C.114}$$

or equivalently

$$\begin{aligned}\psi_{\mathrm{LLL}}(\mathbf{x}) &= e^{-y^2/2}\cdot\frac{(-i)}{\pi^{1/4}\sqrt{L_1}}\exp\Big\{(1/2-i\varsigma\cot\theta)k_x^2-(i/4)(\varsigma\pi N_\phi)\tau_\varsigma\\ &\quad+(-1/2)ik_xL_1\Big(\tau_\varsigma+(\varsigma/N_\phi)(1-\phi_2/\pi)\Big)\Big\}\\ &\quad\cdot\exp\Big\{i(k_xL_1+\varsigma\pi N_\phi)(z-z_0)/L_1\Big\}\,\vartheta_1\left(\varsigma N_\phi\left(\frac{z-z_0}{L_1}\right)\middle|\varsigma N_\phi\tau_\varsigma\right).\end{aligned}\tag{C.115}$$

Yet another alternative form of $\psi_{\mathrm{LLL}}(\mathbf{x})$ can be written as

$$\begin{aligned}\psi_{\mathrm{LLL}}(\mathbf{x}) &= \exp\Big(\pi^2N_\phi^2/(2L_1^2)+k_x(\varsigma\pi N_\phi/L_1)\Big)\exp\Big((i/2)\Big(-\phi_2+[k_x+(1/2)\varsigma\pi N_\phi/L_1]L_1\tau_\varsigma\Big)\Big)\\ &\quad\cdot\psi^{(0)}_{\mathrm{LLL}}(x,y;k_x+\varsigma\pi N_\phi/L_1)\,\vartheta_1\left(\varsigma N_\phi\left(\frac{z-z_0}{L_1}\right)\middle|\varsigma N_\phi\tau_\varsigma\right)\\ &= \exp\Big((i/2)\Big[-\phi_2+\mathrm{Re}(\tau_\varsigma)\Big(k_xL_1+\varsigma\pi N_\phi/2\Big)\Big]\Big)\\ &\quad\cdot\psi^{(0)}_{\mathrm{LLL}}(x,y;k_x+\varsigma\pi N_\phi/L_1)\,\cdot\vartheta_1\left(\varsigma N_\phi\left(\frac{z-z_0}{L_1}\right)\middle|\varsigma N_\phi\tau_\varsigma\right)\\ &= \exp\Big((i/2)\Big(\phi_1\,\mathrm{Re}(\tau_\varsigma)-\phi_2\Big)+i\pi\Big(j+(\varsigma N_\phi/4)\Big)\,\mathrm{Re}(\tau_\varsigma)\Big)\\ &\quad\cdot\psi^{(0)}_{\mathrm{LLL}}(x,y;k_x+\varsigma\pi N_\phi/L_1)\,\vartheta_1\left(\varsigma N_\phi\left(\frac{z-z_0}{L_1}\right)\middle|\varsigma N_\phi\tau_\varsigma\right)\end{aligned}\tag{C.116}$$

Here, $\vartheta(z|\tau)$ is the odd elliptic theta function with the definition

$$\vartheta(z|\tau)=\sum_{m=-\infty}^{+\infty}i(-1)^m\,e^{i\pi\tau(m-1/2)^2}e^{i2\pi(m-1/2)z}\,.\tag{C.117}$$

if we denote the state $\psi_{\mathrm{LLL}}(\mathbf{x})$ in Eq. C.114 by

$$\psi_{\mathrm{LLL}}(x,y;j_x,\phi_1,\phi_2)\,,\tag{C.118}$$

then $\mathcal{T}(\mathbf{a})$ corresponds to the following mapping

$$\begin{aligned}\psi_{\mathrm{LLL}}(x,y;j_x,\phi_1,\phi_2)\;\rightarrow\;&\exp(i\varsigma a_xa_y/2)\exp(ik_xa_x)\\ &\cdot\psi_{\mathrm{LLL}}\Big(x,y;j_x+\varsigma\,L_1a_y/(2\pi),\phi_1,\phi_2-\varsigma\,\mathbf{z}\cdot(\mathbf{a}\times\mathbf{L}_2)\Big)\,.\end{aligned}\tag{C.119}$$

The states $\psi_{\mathrm{LLL}}(x,y;j_x,\phi_1,\phi_2)$ has the following property,

$$\begin{aligned}\psi_{\mathrm{LLL}}(x,y;j_x+\varsigma\,rN_\phi,\phi_1,\phi_2) &= \exp(-ir\phi_2)\exp\Big(-i(\varsigma/2)r^2L_2^2\sin\theta\cos\theta\Big)\\ &\quad\cdot\exp\Big(-i(\phi_1+2\pi j_x)r(L_2/L_1)\cos\theta\Big)\,\cdot\psi_{\mathrm{LLL}}(x,y;j_x,\phi_1,\phi_2)\,,\end{aligned}\tag{C.120}$$

C.6.1 Symmetries of the wavefunction in the torus geometry

For the purposes related to analytical and numerical investigations of FQHE states on toroiad geomteries, it is instructive to classify the symmetries of the system and map out the structure of the Hilbert space. In this section, we follow Haldane (1985) to find the many-body invariants of the fractional quantum Hall system on a torus. To this end, we first consider a system of N_p particles on a torus with principal vectors $\mathbf{L}_1 = L_1\mathbf{e}_1$ and $\mathbf{L}_2 = L_2\mathbf{e}_2$, residing on a torus with N_ϕ flux quantum piercing its surface, where $\mathbf{e}_z \cdot (\mathbf{L}_1 \times \mathbf{L}_2) = 2\pi N_\phi$. The filling factor $\nu = N_p/N_\phi$ is assumed to be rational, $\nu = p/q$ with p and q co-prime, $N_p = pN$ and $N_\phi = qN$ where N is the greatest common divisor of N_p and N_ϕ. First, we outline useful identities of the single-particle magnetic translation algebra,

I. $t(\mathbf{a})t(\mathbf{b}) = e^{i\mathbf{e}_z\cdot(\mathbf{a}\times\mathbf{b})/2}\, t(\mathbf{a}+\mathbf{b})$

II. $t(\mathbf{a})t(\mathbf{b}) = e^{i\mathbf{e}_z\cdot(\mathbf{a}\times\mathbf{b})}\, t(\mathbf{b})t(\mathbf{a})$

The property II is the consequence of the property I. The algebra above holds also for single particle translations in the many-body system, where the magnetic translation of the particle i by $\mathbf{a}$ is denoted by $t_i(\mathbf{a})$. By the requirement of periodic boundary conditions, the many-body wavefunctions should be simultaneous eigenfunctions of magnetic translations of each particle by integer multiples of the torus principal vectors $\mathbf{L}_1$ and $\mathbf{L}_2$, i.e. by vectors of the form $\mathbf{L}_{mn} = m\mathbf{L}_1 + n\mathbf{L}_2$, $(m,n) \in \mathbb{Z}^2$. By the property I, the eigenvalues of $t_i(\mathbf{L}_{mn})$ are given as $e^{i\theta^i_{mn}}$ with $\theta^i_{mn} = \pi mnN_\phi + m\phi_1 + n\phi_2$, and the (anti-)symmetry of the many-body wavefunctions imply that $\theta^i_{mn} = \theta^j_{mn}$ for each pair i,j of particles. The physical states in the Hilbert space thus are subject to a selection rule that for every pair of states $|\alpha\rangle$ and $|\beta\rangle$, the observable composed by from dyads $|\alpha\rangle\langle\beta|$ has to remain invariant under magnetic translations $t_i(\mathbf{L}_{mn})$ for all i and $\mathbf{L}_{mn}$, i.e. $[t_i(\mathbf{L}_{mn}), |\alpha\rangle\langle\beta|] = 0$. This implies that both $|\alpha\rangle$ and $|\beta\rangle$ should have the same eigenvalues $e^{i\theta_{mn}}$. Thus we focus on the Hilbert space $H(\phi_1,\phi_2)$ parameterized by the two twist angles ϕ_1 and ϕ_2 and the operators which leave it invariant.

The many-body system further has another symmetry, namely the invariance under center-of-mass (CM) translations, defined by the collective translations of all the particles,

$$T(\mathbf{a}) = \prod_{i=1}^{N_p} t_i(\mathbf{a}). \tag{C.121}$$

A "relative translation" operator $\tilde{t}_i(\mathbf{a})$ can thus be defined using Eq. C.121 by the decomposition of $t_i(\mathbf{a})$ in terms of the CM translation and the relative translation,

$$t_i(\mathbf{a}) = T\bigg(\frac{\mathbf{a}}{N_p}\bigg)\tilde{t}_i(\mathbf{a})\,, \quad \Rightarrow \quad \tilde{t}_i(\mathbf{a}) = T\bigg(-\frac{\mathbf{a}}{N_p}\bigg)t_i(\mathbf{a})\,. \tag{C.122}$$

The relative translation operator can further be written as

$$\tilde{t}_i(\mathbf{a}) = \prod_{j=1}^{N_p} t_i\bigg(\frac{\mathbf{a}}{N_p}\bigg)t_j\bigg(-\frac{\mathbf{a}}{N_p}\bigg)\,. \tag{C.123}$$

By definition, $\tilde{t}_i$'s satisfy the property $\prod_{i=1}^{N_p} \tilde{t}_i(\mathbf{a}) = 1$. It is straightforward to obtain the following relations for the composition of operators t_i, T and $\tilde{t}_i$,

$$T(\mathbf{a})T(\mathbf{b}) = e^{iN_p\,\mathbf{e}_z\cdot(\mathbf{a}\times\mathbf{b})}\,T(\mathbf{b})T(\mathbf{a})\,, \tag{C.124}$$

$$\tilde{t}_i(\mathbf{a})\tilde{t}_i(\mathbf{b}) = e^{i(1-1/N_p)\,\mathbf{e}_z\cdot(\mathbf{a}\times\mathbf{b})}\,\tilde{t}_i(\mathbf{b})\tilde{t}_i(\mathbf{a})\,, \tag{C.125}$$

$$t_i(\mathbf{a})T(\mathbf{b}) = e^{i\mathbf{e}_z\cdot(\mathbf{a}\times\mathbf{b})}\,T(\mathbf{b})t_i(\mathbf{a})\,, \tag{C.126}$$

$$t_i(\mathbf{a})\tilde{t}_i(\mathbf{b}) = e^{i(1-1/N_p)\,\mathbf{e}_z\cdot(\mathbf{a}\times\mathbf{b})}\,\tilde{t}_i(\mathbf{b})t_i(\mathbf{a})\,, \tag{C.127}$$

$$\tilde{t}_i(\mathbf{a})T(\mathbf{b}) = T(\mathbf{b})\tilde{t}_i(\mathbf{a})\,, \tag{C.128}$$

and the translation property for $\tilde{t}_i$ and T results to the following algebra similar to the property I above,

$$\begin{aligned} T(\mathbf{a})T(\mathbf{b}) &= e^{iN_p\,\mathbf{e}_z\cdot(\mathbf{a}\times\mathbf{b})/2}\,T(\mathbf{a}+\mathbf{b})\,,\\ \tilde{t}_i(\mathbf{a})\tilde{t}_i(\mathbf{b}) &= e^{i(1-1/N_p)\,\mathbf{e}_z\cdot(\mathbf{a}\times\mathbf{b})/2}\,\tilde{t}_i(\mathbf{a}+\mathbf{b})\,. \end{aligned} \tag{C.129}$$

Eqs. C.124 to C.129 have important implications. First, let us examine them in more details. Eq. C.128 has the intuitive interpretation that the relative translations remain independent of the CM translations, thus all $\tilde{t}_i$'s are invariant under the application of T's and can be simultaneously diagonalized. Eq. C.126 implies that on CM translations of the form $T(\mathbf{L}_{mn}/N_\phi)$ keep the Hilbert space $H(\phi_1,\phi_2)$ invariant. Furthermore, by Eq. C.124 it is evident that only T's of the form $T(q\mathbf{L}_{mn}/N_\phi)$ commute with $T(\mathbf{L}_{kl}/N_\phi)$. More explicitly,

$$\begin{aligned} T\left(\frac{\mathbf{L}_{mn}}{N_\phi}\right)T\left(\frac{\mathbf{L}_{kl}}{N_\phi}\right) &= e^{i(N_p/N_\phi^2)\,\mathbf{e}_z\cdot(\mathbf{L}_{mn}\times\mathbf{L}_{kl})}\,T\left(\frac{\mathbf{L}_{kl}}{N_\phi}\right)T\left(\frac{\mathbf{L}_{mn}}{N_\phi}\right)\\ &= e^{i(N_p/N_\phi^2)\,\mathbf{L}_{mn}\cdot(\mathbf{L}_{kl}\times\mathbf{e}_z)}\,T\left(\frac{\mathbf{L}_{kl}}{N_\phi}\right)T\left(\frac{\mathbf{L}_{mn}}{N_\phi}\right), \end{aligned} \tag{C.130}$$

Thus, $T(\mathbf{L}_{kl}/N_\phi)$ changes the eigenvalues of $T(\mathbf{L}_{mn}/N_\phi)$ of the form $\exp\Big(i\mathbf{K}\cdot\mathbf{L}_{mn}/N_\phi\Big)$ to $\exp\Big(i\Big(\mathbf{K}+(N_p/N_\phi)\mathbf{L}_{kl}\times\mathbf{e}_z\Big)\cdot\mathbf{L}_{mn}/N_\phi\Big)$, meaning that $\mathbf{K}\to\mathbf{K}+(N_p/N_\phi)\mathbf{L}_{kl}\times\mathbf{e}_z$. This means that $T(\mathbf{L}_{mn}/N_\phi)$ can at most have q distinct eigenvalues with eigenstates produced by application of an arbitrary $T(\mathbf{L}_{kl})$, since $(N_p/N_\phi^2)\mathbf{L}_{mn}\cdot(\mathbf{L}_{kl}\times\mathbf{e}_z) = 2\pi(p/q)(ml-nk)\in 2\pi(p/q)\mathbb{Z}$, and $ml-nk$ runs over all integers if m and n are co-prime. We thus can choose a representative primitive vector $\mathbf{L}_0$ and consider the eigenvalues of $T(\mathbf{L}_0/N_\phi)$. Since $T(\mathbf{L}_0/N_\phi)$ remains invariant under $T(q\mathbf{L}_{mn}/N_\phi)$, the operators $T(q\mathbf{L}_{mn}/N_\phi)$ act invariantly in each eigensubspace of $T(\mathbf{L}_0/N_\phi)$.

Eigenvalues of $\tilde{t}_i(p\mathbf{L}_{mn})$ and $T(q\mathbf{L}_{mn}/N_\phi)$: First we remark on the eigenvalues of $\tilde{t}_i(p\mathbf{L}_{mn})$. For a hexagonal Bravais lattice - which is the highest symmetry PBC - we have the $\pi/3$-rotational symmetry. Over the state with trivial translational symmetry, we also have $\tilde{t}_i(p\mathbf{L}_1) = \tilde{t}_i(-p\mathbf{L}_1) = \tilde{t}_i(p\mathbf{L}_2)$. This two conditions result in the following constraint on $\tilde{t}_i(p\mathbf{L}_{mn})$'s applied on this state,

$$\tilde{t}_i(p\mathbf{L}_1) = \tilde{t}_i(-p\mathbf{L}_1) = \tilde{t}_i(p\mathbf{L}_2) = \tilde{t}_i(p\mathbf{L}_1 - p\mathbf{L}_2)\,, \tag{C.131}$$

which together with Eq. C.125 and Eq. C.129 results in

$$\tilde{t}_i(p\mathbf{L}_1) = \tilde{t}_i(p\mathbf{L}_2) = (-1)^{pq(N_p-1)}\,, \tag{C.132}$$

Over the state with the trivial translational symmetry. We also note that the CDW operator $\sum_{i=1}^{N_p} \exp(i\mathbf{Q}\cdot\mathbf{x}_i)$ shifts the states from one eigensubspace of $\tilde{t}_i(p\mathbf{L}_{mn})$ to another, given that $\exp(\mathbf{Q}\cdot\mathbf{L}_{mn}) = 1$, i.e. $\mathbf{Q}$ is compatible with PBC. This conventions mean that the eigenvalues of $\tilde{t}_i(p\mathbf{L}_{mn})$ are

$$\tilde{t}_i(p\mathbf{L}_{mn}) \to (-1)^{pq(N_p-1)} \exp\Big(-iq(\mathbf{k}\cdot\mathbf{L}_{mn})/N_\phi\Big)\,, \tag{C.133}$$

By the convention in Eq. C.133, first the definition of $\mathbf{k}=0$ is totally fixed as the state fulfilling the conditions in Eq. C.131 and invariance under $\pi-3$ rotations, and second, the CDW operator acts on the eigenstates of $\tilde{t}_i(\mathbf{L}_{mn})$ by merely shifting $\mathbf{k}$ to $\mathbf{k}+\mathbf{Q}$. These results totally determine the eigenvalues of $\tilde{t}_i(\mathbf{L}_{mn})$. The eigenvalues of $T(q\mathbf{L}_{mn}/N_\phi)$ result from the eigenvalues of $\tilde{t}_i(p\mathbf{L}_{mn})$ and $t_i(p\mathbf{L}_{mn})$, and are equal to

$$T\left(\frac{q\mathbf{L}_{mn}}{N_\phi}\right) \to (-1)^{pq(N_p-1)}\, e^{ip\theta_{mn}+iq(\mathbf{k}\cdot\mathbf{L}_{mn})/N_\phi}\,. \tag{C.134}$$

It is also straightforward to see that the set $\{T(q\mathbf{L}_{mn}/N_\phi + r\mathbf{L}_0/N_\phi)\}$ constitute a maximally commuting set and the CM wavefunction cannot be the eigenstate of any other $T(\mathbf{L}_{mn}/N_\phi)$. In view of the above symmetries, the kinetic part of the many-body Hamiltonian $H_{\text{kin}} = 1/(2m)\sum_{i=1}^{N_p} |\mathbf{e}_z\times\mathbf{\Pi}_i|^2$ can be separated as a sum of the CM kinetic term $H_{\text{kin}}^{\text{CM}} = 1/(2mN_p)|\sum_{i=1}^{N_p}\mathbf{e}_z\times\mathbf{\Pi}_i|^2$ and a relative kinetic term

$$H_{\text{kin}}^{\text{rel}} = \sum_{i<j}\frac{1}{2mN_p}|\mathbf{e}_z\times(\mathbf{\Pi}_i-\mathbf{\Pi}_j)|^2\,, \tag{C.135}$$

and in accordance, the wavefunction can be split as a product of a CM component and a relative component $\Psi = \Psi^{\text{c.m.}}\otimes\Psi^{\text{rel}}$ where $\mathbf{k}$ is a good quantum number for Ψ^{rel}.

C.7 Hilbert space invariant subspaces of the system on a torus

To employ the symmetry properties derived in the last section on the states of the Hilbert space and use these symmetries to partition the Hilbert space, we first form the slater determinant of the states $\psi_{\text{LLL}}(x,y;j_x,\phi_1,\phi_2)$ to obtain the many-body state

$$\begin{aligned}&\Psi_{\text{LLL}}^{(\text{MB})}\Big(\{x_1,y_1,\cdots,x_{N_p},y_{N_p}\};\{j_{x1},j_{x2},\cdots,j_{xN_p}\},\phi_1,\phi_2\Big)\\&=\frac{1}{\sqrt{N_p!}}\sum_{\pi\in S_{N_p}}(-1)^\pi\,\psi_{\text{LLL}}(x_1,y_1;j_{x\pi(1)},\phi_1,\phi_2)\cdots\psi_{\text{LLL}}(x_{N_p},y_{N_p};j_{x\pi(N_p)},\phi_1,\phi_2)\,.\end{aligned} \tag{C.136}$$

Next, we evaluate the action of $\tilde{t}_i(p\mathbf{L}_{mn})$ on $\Psi^{(\mathrm{MB})}_{\mathrm{LLL}}$,

$$\begin{aligned}
\tilde{t}_i(p\mathbf{L}_{mn})\,&\Psi^{(\mathrm{MB})}_{\mathrm{LLL}}\Big(\{x_1, y_1, \cdots, x_{N_p}, y_{N_p}\}; \{j_{x1}, j_{x2}, \cdots, j_{xN_p}\}, \phi_1, \phi_2\Big) \\
&= \exp(-inp\phi_2)\exp\Big(-i(\varsigma/2)n^2p^2L_2^2\,\mathrm{sin}\theta\mathrm{cos}\theta\Big) \\
&\times \exp\Big(-i\phi_1 np(L_2/L_1)\mathrm{cos}\theta\Big)\exp\Big(i\varsigma\pi pqn(N_p-1)\Big(m+n(L_2/L_1)\mathrm{cos}\theta\Big)\Big) \\
&\times \exp\Big[-i(2\pi p/N_p)\Big(m+n(L_2/L_1)\mathrm{cos}\theta\Big)\Big(\sum j_{x,k}\Big)\Big] \\
&\times \frac{1}{\sqrt{N_p!}}\sum_{\pi\in S_{N_p}}(-1)^\pi\,\psi_{\mathrm{LLL}}(x_1, y_1; j_{x\pi(1)}-\varsigma nq, \phi_1, \phi_2)\cdots \\
&\psi_{\mathrm{LLL}}(x_{N_p}, y_{N_p}; j_{x\pi(N_p)}-\varsigma nq, \phi_1, \phi_2) \\
&= e^{i\tilde{\theta}_{mn}}\,\Psi^{(\mathrm{MB})}_{\mathrm{LLL}}(x, y; \{j_{x1}-\varsigma nq, j_{x2}-\varsigma nq, \cdots j_{xN_p}-\varsigma nq\}, \phi_1, \phi_2)\,,
\end{aligned} \tag{C.137}$$

where the phase $\tilde{\theta}_{mn}$ is

$$\begin{aligned}
\tilde{\theta}_{mn} = &-np\phi_2 - (\varsigma/2)n^2p^2L_2^2\,\mathrm{sin}\theta\mathrm{cos}\theta - \phi_1 np(L_2/L_1)\mathrm{cos}\theta \\
&+\Big[\varsigma\pi pqn(N_p-1) - (2\pi p/N_p)\Big(\sum j_{x,k}\Big)\Big]\Big(m+n(L_2/L_1)\mathrm{cos}\theta\Big)\,.
\end{aligned} \tag{C.138}$$

Now we calculate the action of $T(\mathbf{a})$ on $\Psi^{(\mathrm{MB})}_{\mathrm{LLL}}$,

$$\begin{aligned}
&T(\mathbf{a})\Psi^{(\mathrm{MB})}_{\mathrm{LLL}}\Big(\{x_1, y_1, \cdots, x_{N_p}, y_{N_p}\}; \{j_{x1}, j_{x2}, \cdots, j_{xN_p}\}, \phi_1, \phi_2\Big) = \\
&\quad\exp\Big(i\varsigma a_x a_y N_p/2\Big)\exp(iN_p k_x a_x) \\
&\quad\Psi^{(\mathrm{MB})}_{\mathrm{LLL}}\Big(\{x_1, y_1, \cdots, x_{N_p}, y_{N_p}\}; \\
&\quad\{j_{x1}+\varsigma L_1 a_y/(2\pi), j_{x2}+\varsigma L_1 a_y/(2\pi), \cdots, j_{xN_p}+\varsigma L_1 a_y/(2\pi)\}, \phi_1, \phi_2-\varsigma\,\mathbf{e}_z\cdot(\mathbf{a}\times\mathbf{L}_2)\Big)\,.
\end{aligned} \tag{C.139}$$

In particular, the action of $T(\mathbf{L}_{mn}/N_\phi)$ will result in

$$\begin{aligned}
T(\mathbf{L}_{mn}/N_\phi)&\Psi^{(\mathrm{MB})}_{\mathrm{LLL}}\Big(\{x_1, y_1, \cdots, x_{N_p}, y_{N_p}\}; \{j_{x1}, j_{x2}, \cdots, j_{xN_p}\}, \phi_1, \phi_2\Big) = \\
&\exp\Big(i\varsigma\pi n(p/q)\Big(m+n(L_2/L_1)\mathrm{cos}\theta\Big)\Big) \\
&\times\exp\Big(i(p/q)\phi_1\Big(m+n(L_2/L_1)\mathrm{cos}\theta\Big)\Big) \\
&\times\exp\Big(i(2\pi/N_\phi)\Big(\sum j_k\Big)\Big(m+n(L_2/L_1)\mathrm{cos}\theta\Big)\Big) \\
&\times\Psi^{(\mathrm{MB})}_{\mathrm{LLL}}\Big(\{x_1, y_1, \cdots, x_{N_p}, y_{N_p}\}; \{j_{x1}+\varsigma n, j_{x2}+\varsigma n, \cdots, j_{xN_p}+\varsigma n\}, \phi_1, \phi_2\Big)\,,
\end{aligned} \tag{C.140}$$

and similarly, the action of $T(q\mathbf{L}_{mn}/N_\phi)$ would be

$$\begin{aligned}
&T(q\mathbf{L}_{mn}/N_\phi)\Psi^{(\mathrm{MB})}_{\mathrm{LLL}}\Big(\{x_1, y_1, \cdots, x_{N_p}, y_{N_p}\}; \{j_{x1}, j_{x2}, \cdots, j_{xN_p}\}, \phi_1, \phi_2\Big) = \\
&\exp\Big(i\varsigma\pi npq\Big(m + n(L_2/L_1)\mathrm{cos}\theta\Big)\Big) \cdot \exp\Big(ip\phi_1\Big(m + n(L_2/L_1)\mathrm{cos}\theta\Big)\Big) \\
&\cdot \exp\Big(i(2\pi q/N_\phi)\Big(\sum j_k\Big)\Big(m + n(L_2/L_1)\mathrm{cos}\theta\Big)\Big) \\
&\cdot \Psi^{(\mathrm{MB})}_{\mathrm{LLL}}\Big(\{x_1, y_1, \cdots, x_{N_p}, y_{N_p}\}; \{j_{x1} + \varsigma nq, j_{x2} + \varsigma nq, \cdots, j_{xN_p} + \varsigma nq\}, \phi_1, \phi_2\Big)\,, \\
&= \exp(i\Theta_{mn})\, \Psi^{(\mathrm{MB})}_{\mathrm{LLL}}\Big(\{x_1, y_1, \cdots, x_{N_p}, y_{N_p}\}; \{j_{x1} + \varsigma nq, j_{x2} + \varsigma nq, \cdots, j_{xN_p} + \varsigma nq\}, \phi_1, \phi_2\Big)\,,
\end{aligned} \tag{C.141}$$

where the phase Θ_{mn} reads

$$\Theta_{mn} = \Big[\varsigma\pi npq + p\phi_1 + (2\pi q/N_\phi)\Big(\sum j_k\Big)\Big]\Big(m + n(L_2/L_1)\mathrm{cos}\theta\Big) \tag{C.142}$$

Above equations show that the following states simultaneously diagonalize $\tilde{t}_i(p\mathbf{L}_{mn})$ and $T(q\mathbf{L}_{mn}/N_\phi)$,

$$|(s, j), \mathcal{L}\rangle = \frac{1}{\sqrt{N}} \sum_{r=0}^{|\mathcal{L}|-1} e^{i(2\pi/N)rs} \Psi^{(\mathrm{MB})}_{\mathrm{LLL}}\Big(\underline{x}, \underline{y}; \{j_{x1} - \varsigma rq, j_{x2} - \varsigma rq, \cdots, j_{xN_p} - \varsigma rq\}; \phi_1, \phi_2\Big)\,, \tag{C.143}$$

where $\mathcal{L}$ indexes the equivalence class of states $\Psi^{(\mathrm{MB})}_{\mathrm{LLL}}(\underline{x}, \underline{y}; \{j_{x1}, j_{x2}, \cdots, j_{xN_p}\}, \phi_1, \phi_2)$ which map to itself by a finite number $\mathcal{L}$ times application of $T(q\mathbf{L}_{mn}/N_\phi)$.

Especial case of a rectangular geometry with vanishing twist angle: In this case, there are following simplified forms for the important quantities

$$\psi_{\mathrm{LLL}}(\mathbf{x}) = \psi^{(0)}_{\mathrm{LLL}}(x, y; k_x + \varsigma\pi N_\phi/L_1)\, \vartheta_1\left(\varsigma N_\phi\left(\frac{z - z_0}{L_1}\right)\middle|\varsigma N_\phi\tau_\varsigma\right)\,, \tag{C.144}$$

where

$$z_0 = -\frac{\varsigma L_1}{2N_\phi} - i\Big(k_x + \varsigma\frac{L_2}{2}\Big)\,. \tag{C.145}$$

It is evident that the location of zeros of the wavefuction $\psi_{\mathrm{LLL}}(\mathbf{x})$ in Eq. C.144 are on the real axis and are distributed as the following,

$$z_l = z_0 + \varsigma\Big(\frac{L_1}{N_\phi}\Big)l, \quad l = 0\,, \cdots, N_\phi - 1\,. \tag{C.146}$$

Over the Slater determinant constructed from this state, the action of $T(q\mathbf{L}_{mn}/N_\phi)$ and $\tilde{t}_i(p\mathbf{L}_{mn})$ equal to

$$\begin{aligned}
&T(q\mathbf{L}_{mn}/N_\phi)\Psi^{(\mathrm{MB})}_{\mathrm{LLL}} = \exp(i\Theta_{mn})\, \Psi^{(\mathrm{MB})}_{\mathrm{LLL}}\Big(\underline{x}, \underline{y}; \{j_{x1} + \varsigma nq, j_{x2} + \varsigma nq, \cdots, j_{xN_p} + \varsigma nq\}, \phi_1, \phi_2\Big)\,, \\
&\tilde{t}_i(p\mathbf{L}_{mn})\Psi^{(\mathrm{MB})}_{\mathrm{LLL}} = \exp(i\tilde{\theta}_{mn})\, \Psi^{(\mathrm{MB})}_{\mathrm{LLL}}(x, y; \{j_{x1} - \varsigma nq, j_{x2} - \varsigma nq, \cdots j_{xN_p} - \varsigma nq\}, \phi_1, \phi_2)\,,
\end{aligned} \tag{C.147}$$

and the phases $\tilde{\theta}_{mn}$ and Θ_{mn} read

$$\begin{aligned} \Theta_{mn} &= \varsigma\pi mnpq + \frac{2\pi m}{N}\Big(\sum j_i\Big)\,, \\ \tilde{\theta}_{mn} &= \varsigma\pi mnpq(N_p-1) - \frac{2\pi m}{N}\Big(\sum j_i\Big)\,, \end{aligned} \tag{C.148}$$

C.7.1 Numerical excat diagonalization of FQH systems on different geometries

Having laid out the structure of Landau levels in different geometries, we now explain how to perform numerical exact diagonalization for finite system sizes. To this end, one needs to evaluate the matirx elements of $\hat{H}_{\text{FQH}}$ in Eq. 4.12 over the basis of N-particle states in the lowest Landau level. Regardless of the geometry, the N-particle states in Landau levels are of the form

$$|n_1, m_1; \cdots; n_N, m_N\rangle = \hat{a}^{\dagger}_{n_1,m_1}\cdots\hat{a}^{\dagger}_{n_N,m_N}|\emptyset\rangle\,, \tag{C.149}$$

where $\hat{a}^{\dagger}_{n,m}$ creates a particle in the $|n,m\rangle$ state. The second quantized form of $\hat{H}_{\text{FQH}}$ then reads

$$\hat{H}_{\text{FQH}} = \frac{1}{2}\sum_{m_1,\cdots,m_4}\sum_{n_1,\cdots,n_4} V^{n_1,n_2,n_3,n_4}_{m_1,m_2,m_3,m_4}\,\hat{a}^{\dagger}_{n_3,m_3}\hat{a}^{\dagger}_{n_4,m_4}\hat{a}_{n_2,m_2}\hat{a}_{n_1,m_1}\,, \tag{C.150}$$

where $V^{n_1,n_2,n_3,n_4}_{m_1,m_2,m_3,m_4} = \langle n_3, m_3; n_4, m_4|\,V(\mathbf{x}_1-\mathbf{x}_2)\,|n_1,m_1;n_2,m_2\rangle$. The standard way to evaluate $V^{n_1,n_2,n_3,n_4}_{m_1,m_2,m_3,m_4}$ is by Fourier transforming the potential $V(\mathbf{x})$ and re-writing the matrix element as

$$V^{n_1,n_2,n_3,n_4}_{m_1,m_2,m_3,m_4} = \int\frac{d^2q}{(2\pi)^2}\,\mathcal{F}_{n_3,n_1}(\eta_{\mathbf{q}})\mathcal{F}^{*}_{m_3,m_1}(\eta_{\mathbf{q}})\mathcal{F}^{*}_{n_2,n_4}(\eta_{\mathbf{q}})\mathcal{F}_{m_2,m_4}(\eta_{\mathbf{q}})\,. \tag{C.151}$$

To obtain Eq. C.151, we note that $\langle n', m'|\,e^{i\mathbf{q}\cdot\mathbf{x}}\,|n,m\rangle = \mathcal{F}_{n',n}(\eta_{\mathbf{q}})\mathcal{F}^{*}_{m',m}(\eta_{\mathbf{q}})$, where

$$\mathcal{F}_{m',m}(\eta_{\mathbf{q}}) = \langle m'|\,e^{\eta_{\mathbf{q}}\hat{a}^{\dagger}-\eta^{*}_{\mathbf{q}}\hat{a}}\,|m\rangle = \begin{cases} \sqrt{\frac{m!}{m'!}}e^{-|\eta_{\mathbf{q}}|^2/2}\,\eta_{\mathbf{q}}^{m'-m}L_m^{(m'-m)}\Big(|\eta_{\mathbf{q}}|^2\Big)\,, & m' \geq m \\ \mathcal{F}^{*}_{m,m'}(-\eta_{\mathbf{q}})\,, & m < m' \end{cases} \tag{C.152}$$

is a form factor, $L_n^{(\alpha)}(x)$ is an associated Laguerre polynomial, $|m\rangle$'s are harmonic oscillator eigenstates with destruction operator $\hat{a}$, and $\eta_{\mathbf{q}} = 1/\sqrt{2}(q_x + i\varsigma q_y)$. In the spherical geometry, which we used in the current thesis, a more feasible way to obtain the matrix elements is outlined below. To this end, we note that on a sphere with radius R, the Hamiltonian in the lowest Landau level can be written as

$$\hat{H}_{\text{FQH}} = \frac{1}{2}\sum_{l=0}^{\infty} V_l\sum_{m=-l}^{l}(-1)^m : \hat{\bar{\rho}}_{l(-m)}\,\hat{\bar{\rho}}_{lm} : \,. \tag{C.153}$$

where $\hat{\bar{\rho}}(\mathbf{\Omega}) = \hat{\mathcal{P}}_{\text{LLL}}\hat{\rho}(\mathbf{\Omega})\hat{\mathcal{P}}_{\text{LLL}}$ is the LLL-projected density operator, $\hat{\bar{\rho}}_{lm} = \int d\Omega\,\hat{\bar{\rho}}(\mathbf{\Omega})$, and the Haldane pseudo-potentials are given by

$$V_l = 2\pi\int_0^{\pi} d\theta\sin(\theta)\,P_l(\cos\theta)\,V\Big(2R\sin(\theta/2)\Big)\,. \tag{C.154}$$

The density operators $\hat{\hat{\rho}}_{lm}$ explicitly read

$$\begin{aligned}\hat{\hat{\rho}}_{lm} &= \sum_{m',m''} \left(\int d\Omega \, Y^*_{QQm''}(\mathbf{\Omega}) Y^*_{0lm}(\mathbf{\Omega}) Y_{QQm'}(\mathbf{\Omega}) \right) \hat{a}^\dagger_{0,m''} \hat{a}_{0,m'} \\ &= \sum_{m',m''} (-1)^{Q-m'} \, S^*(\{-Q,0,Q\},\{Q,l,Q\},\{-m',m,m''\}) \, \hat{a}^\dagger_{0,m''} \hat{a}_{0,m'} \,,\end{aligned} \tag{C.155}$$

where $S(\{Q_1,Q_2,Q_3\},\{l_1,l_2,l_3\},\{m_1,m_2,m_3\})$ is the overlap integral of monopole spherical harmonics, and has a known expression in terms of Wigner $3j$ symbols (see chapter 2 of Ref. [105] for more details and explicit expressions). Having the above information, it is straightforward to numerically construct the whole Hamiltonian by having the matrix form of $\hat{a}^{(\dagger)}_{n,m}$ operators and the Haldane pseudo-potentials.

Acknowledgment

I would first and foremost like to thank my supervisor, Prof. Fabian Grusdt, for granting me the opportunity to pursue my PhD in his group and for his steadfast support throughout this journey. His guidance has been invaluable in every aspect of my PhD, both scientifically and financially, including his support for the numerous conferences, schools, and business travels I attended. I am immensely grateful for his exceptional generosity, patience, and boundless encouragement and motivation over the years. I am especially thankful to him for his care about my academic career, allowing me to participate in impactful projects like the Bose polaron review, which will be crucial for my future career development. Beyond being an outstanding supervisor, he is a brilliant theoretical physicist, and I have truly enjoyed doing physics with him. His enthusiasm, positivity, and unique approach to physics have been inspiring, and I am incredibly proud to be part of his group.

I would like to also sincerely thank my other supervisor, Prof. Nathan Goldman, for supervising me during the first one and a half year of my PhD. I would like to especially thank him for being extremely supportive, considerate, approachable and patient, especially during the first year when the pandemic has made the life of everyone harder. I am grateful for the countless hours we had for discussing physics, and always impressing me by the breadth of knowledge and understanding he has on topological physics and nearly everything related to synthetic systems. My current and future academic standing is hugely indebted for the works I had done with him during the first few years of my PhD. I especially want to thank him for making that legendary travel for the Solvay Conference to Brussels possible.

In addition, it has been a great honor and privilage for me be a student of Prof. Ataç İmamoğlu during my master's studies at ETH Zürich, and later to work with him on the optical investigations of fractional quantum Hall systems during my PhD. His increadibly deep knownledge and understanding of a wast collection of fields in quantum science and technology has always inspired me to learn more and broaden my horizons, and his unique thinking style has had an ever-lasting impact on how I view physical phenomena. I always learn new physics whenever I have a discussion with him, which makes every discussion an invaluable opportunity. Without his inputs and ideas, the main work on the exciton-quantum Hall system in this thesis would have not been possible.

I want to take a pause here and emphasize again that without the support and countless inputs of all of my professors, the work in this thesis was not been possible.

I also would like to thank Prof. Monika Aidelsburger for being part of my thesis advisory

board. Although we had a couple of rather short meetings during my PhD, her care and approachability was absolutely crucial for me when things were though during the first year.

Next, I would like to thank my office mates, Hannah, Simon and Lukas. All of them are really talented young physicists, and it was a great pleasure for me to share office with them. I would like to thank Lukas for all the intersting and engaging discussions we had about every thing from physics to politics, and for being open-minded and receptive. I would like to thank Hannah for being so kind and considerate. I used to distract her a lot by my silly questions and mobile alarms exactly at 14:00, and I hope she was not so disturbed by them. I always appreciate the deep focus she has on her work. I would like to thank Simon for being an outstandingly competent computational physicist, and for helping me with my computer-related issue, which have always improved my quality of life incredibly.

I would like to also take the chance and thank all the current and former members of the Grusdt group, for being always kind, friendly and helpful and making a really comfortable atmosphere in the group. My special thanks also goes to all the members of the Schollwöck chair, for being fantastic people.

Especial thanks goes to Nihal, Marcel, Héloïse, Nico and Aurela, and members of the von Delft chair for all the time we spent playing at the game nights, going to concerts, eating together, inviting me to their own place, and many lovely and unforgettable memories. In addition, I would like to sincerely thank all my friends from the university and high school, whose company has always been extremely valuable for me. I can’t possibly name everyone, so I’ll refrain from listing names to be fair to all.

I also want to express my gratitude to my wonderful landlord, Mr. Nicola Rossiello Bianco, as well as my current and former housemates Federico, Luca, Silvestre, Daniel, Mekan, and Mina. Nicola is truly one of the most remarkable people I have ever met, and I feel incredibly fortunate to have spent my time in Munich in his beautiful palace. I wish him a long life filled with endless joy and happiness, and all the best for his family.

I cannot thank my incredible family enough. Words cannot fully capture the deep love and respect I have for each of them, especially my mother and father. My parents and grandparents, and my aunts and uncles, are immensely precious gifts that God has blessed me with, and I am endlessly grateful for them. From the bottom of my heart, let me say, Thank you.

Bibliography

[1] V. Ahufinger, A. Sanpera, P. Pedri, L. Santos und M. Lewenstein, *Physical Review A—Atomic, Molecular, and Optical Physics* **69** (2004), 053604.

[2] A. Alexandrov und N. Mott, *Reports on Progress in Physics* **57** (1994), 1197.

[3] A. Alexandrov und J. Ranninger, *Physical Review B* **24** (1981), 1164.

[4] A. Alexandrov, J. Ranninger und S. Robaszkiewicz, *Physical Review B* **33** (1986), 4526.

[5] A.S. Alexandrov: *Polarons in advanced materials*, Band 103. Springer Science & Business Media, 2008.

[6] Z.I. Alferov, *Semiconductors* **32** (1998), 1.

[7] G. Alfimov, P. Kevrekidis, V. Konotop und M. Salerno, *Physical Review E* **66** (2002), 046608.

[8] P.M. Anderson, J.P. Hirth und J. Lothe: *Theory of dislocations.* Cambridge University Press, 2017.

[9] E.Y. Andrei, D.K. Efetov, P. Jarillo-Herrero, A.H. MacDonald, K.F. Mak, T. Senthil, E. Tutuc, A. Yazdani und A.F. Young, *Nature Reviews Materials* **6** (2021), 201.

[10] L.P. Ardila, G. Astrakharchik und S. Giorgini, *Physical Review Research* **2** (2020), 023405.

[11] L.P. Ardila und S. Giorgini, *Physical Review A* **92** (2015), 033612.

[12] J.K. Asbóth, L. Oroszlány und A. Pályi, *Lecture notes in physics* **919** (2016).

[13] L. Asteria, D.T. Tran, T. Ozawa, M. Tarnowski, B.S. Rem, N. Fläschner, K. Sengstock, N. Goldman und C. Weitenberg, *Nature physics* **15** (2019), 449.

[14] G.E. Astrakharchik, L.A.P. Ardila, K. Jachymski und A. Negretti, *Nature Communications* **14** (2023), 1647.

[15] N. Baldelli, B. Juliá-Díaz, U. Bhattacharya, M. Lewenstein und T. Graß, *Physical Review B* **104** (2021), 035133.

[16] J. Bardeen, L.N. Cooper und J.R. Schrieffer, *Physical review* **108** (1957), 1175.

[17] H. Bartolomei, M. Kumar, R. Bisognin, A. Marguerite, J.M. Berroir, E. Bocquillon, B. Placais, A. Cavanna, Q. Dong, U. Gennser et al. , *Science* **368** (2020), 173.

[18] A. Bisianov, M. Wimmer, U. Peschel und O. Egorov, *Physical Review A* **100** (2019), 063830.

[19] M. Blake, R.A. Davison und S. Sachdev, *Physical Review D* **96** (2017), 106008.

[20] I. Bloch, J. Dalibard und S. Nascimbene, *Nature Physics* **8** (2012), 267.

[21] I. Bloch, J. Dalibard und W. Zwerger, *Reviews of modern physics* **80** (2008), 885.

[22] A. Bohrdt, E. Demler und F. Grusdt, *Physical Review Letters* **127** (2021), 197004.

[23] A. Bohrdt, L. Homeier, I. Bloch, E. Demler und F. Grusdt, *Nature Physics* **18** (2022), 651.

[24] K.I. Bolotin, F. Ghahari, M.D. Shulman, H.L. Stormer und P. Kim, *Nature* **462** (2009), 196.

[25] M. Born und R. Oppenheimer, *Annalen der Physik* **84** (1927), 457.

[26] R.W. Boyd, A.L. Gaeta und E. Giese. In *Springer Handbook of Atomic, Molecular, and Optical Physics*. Springer (2008), Seiten 1097–1110.

[27] C.C. Bradley, C. Sackett und R. Hulet, *Physical Review Letters* **78** (1997), 985.

[28] O.M. Braun und Y.S. Kivshar: *The Frenkel-Kontorova model: concepts, methods, and applications*. Springer, 2004.

[29] M.E. Cage, K. Klitzing, A. Chang, F. Duncan, M. Haldane, R.B. Laughlin, A. Pruisken und D. Thouless: *The quantum Hall effect*. Springer Science & Business Media, 2012.

[30] A. Camacho-Guardian, N. Goldman, P. Massignan und G.M. Bruun, *Physical Review B* **99** (2019), 081105.

[31] Y. Cao, V. Fatemi, A. Demir, S. Fang, S.L. Tomarken, J.Y. Luo, J.D. Sanchez-Yamagishi, K. Watanabe, T. Taniguchi, E. Kaxiras et al. , *Nature* **556** (2018), 80.

[32] Y. Cao, V. Fatemi, S. Fang, K. Watanabe, T. Taniguchi, E. Kaxiras und P. Jarillo-Herrero, *Nature* **556** (2018), 43.

[33] R. Carles und C. Sparber, *arXiv preprint arXiv:1101.3136* (2011).

[34] A.H. Castro Neto, F. Guinea, N.M. Peres, K.S. Novoselov und A.K. Geim, *Reviews of modern physics* **81** (2009), 109.

[35] J. Catani, G. Lamporesi, D. Naik, M. Gring, M. Inguscio, F. Minardi, A. Kantian und T. Giamarchi, *Physical Review A* **85** (2012), 023623.

[36] A. Cerjan, M. Wang, S. Huang, K.P. Chen und M.C. Rechtsman, *Light: Science & Applications* **9** (2020), 178.

[37] T. Chakraborty und P. Pietiläinen: *The quantum Hall effects: integral and fractional*, Band 85. Springer Science & Business Media, 2013.

[38] K. Chen, N.V. Prokof'ev und B.V. Svistunov, *Physical Review A* **98** (2018), 041602.

[39] F. Chevy, *Physical Review A—Atomic, Molecular, and Optical Physics* **74** (2006), 063628.

[40] C. Chin, R. Grimm, P. Julienne und E. Tiesinga, *Reviews of Modern Physics* **82** (2010), 1225.

[41] R.S. Christensen, J. Levinsen und G.M. Bruun, *Physical review letters* **115** (2015), 160401.

[42] A. Christianen, J.I. Cirac und R. Schmidt, *Physical Review A* **105** (2022), 053302.

[43] A. Christianen, J.I. Cirac und R. Schmidt, *Physical Review Letters* **128** (2022), 183401.

[44] L.W. Clark, N. Schine, C. Baum, N. Jia und J. Simon, *Nature* **582** (2020), 41.

[45] M. Combescot und S.Y. Shiau: *Excitons and Cooper pairs: two composite bosons in many-body physics*. Oxford University Press, 2015.

[46] R. Combescot und S. Giraud, *Physical review letters* **101** (2008), 050404.

[47] R. Combescot, A. Recati, C. Lobo und F. Chevy, *Physical review letters* **98** (2007), 180402.

[48] E.M. Conwell, *Proceedings of the National Academy of Sciences* **102** (2005), 8795.

[49] N. Cooper, J. Dalibard und I. Spielman, *Reviews of modern physics* **91** (2019), 015005.

[50] O. Cotleţ: *Bose-Fermi mixtures with electrons and polaritons*. ETH Zurich, Dissertation, 2019.

[51] P. Čubela, A. Bohrdt, M. Greiner und F. Grusdt, *Physical Review B* **107** (2023), 035105.

[52] A. Damjanović, I. Kosztin, U. Kleinekathöfer und K. Schulten, *Physical Review E* **65** (2002), 031919.

[53] S. Das Sarma, S. Adam, E. Hwang und E. Rossi, *Reviews of modern physics* **83** (2011), 407.

[54] R.A. Davison, W. Fu, A. Georges, Y. Gu, K. Jensen und S. Sachdev, *Physical Review B* **95** (2017), 155131.

[55] J. Devreese, *arXiv preprint arXiv:1611.06122* (2016).

[56] J.T. Devreese und F. Peeters: *Polarons and excitons in polar semiconductors and ionic crystals*, Band 127. Springer Science & Business Media, 2013.

[57] M. Di Liberto und N. Goldman, *Preprint at https://arxiv. org/pdf/2111.13572. pdf* (2021).

[58] O.K. Diessel, J. von Milczewski, A. Christianen und R. Schmidt, *Physical Review Research* **6** (2024), 023239.

[59] M. Drescher, M. Salmhofer und T. Enss, *Physical Review Research* **2** (2020), 032011.

[60] M. Drescher, M. Salmhofer und T. Enss, *Physical Review A* **103** (2021), 033317.

[61] M. Duda, X.Y. Chen, A. Schindewolf, R. Bause, J. von Milczewski, R. Schmidt, I. Bloch und X.Y. Luo, *Nature Physics* **19** (2023), 720.

[62] D. Dzsotjan, R. Schmidt und M. Fleischhauer, *Physical Review Letters* **124** (2020), 223401.

[63] D. Emin, *Physical review letters* **62** (1989), 1544.

[64] J. Etrych, G. Martirosyan, A. Cao, C.J. Ho, Z. Hadzibabic und C. Eigen, *arXiv preprint arXiv:2402.14816* (2024).

[65] Z.F. Ezawa: *Quantum Hall effects: Field theoretical approach and related topics.* World scientific, 2008.

[66] G. Fano, F. Ortolani und E. Colombo, *Physical Review B* **34** (1986), 2670.

[67] F. Fassioli, R. Dinshaw, P.C. Arpin und G.D. Scholes, *Journal of The Royal Society Interface* **11** (2014), 20130901.

[68] M. Ferretti, R. Hendrikx, E. Romero, J. Southall, R.J. Cogdell, V.I. Novoderezhkin, G.D. Scholes und R. Van Grondelle, *Scientific reports* **6** (2016), 1.

[69] A.L. Fetter und J.D. Walecka: *Quantum theory of many-particle systems.* Courier Corporation, 2012.

[70] B. Field, J. Levinsen und M.M. Parish, *Physical Review A* **101** (2020), 013623.

[71] E. Fradkin: *Field theories of condensed matter physics.* Cambridge University Press, 2013.

[72] T. Fukuhara, A. Kantian, M. Endres, M. Cheneau, P. Schauß, S. Hild, D. Bellem, U. Schollwöck, T. Giamarchi, C. Gross et al. , *Nature Physics* **9** (2013), 235.

[73] Z. Gang und P. Grech, *Communications in Partial Differential Equations* **42** (2017), 731.

[74] A.K. Geim und I.V. Grigorieva, *Nature* **499** (2013), 419.

[75] S. Girvin, A. MacDonald und P. Platzman, *Physical review letters* **54** (1985), 581.

[76] S. Girvin, A. MacDonald und P. Platzman, *Physical Review B* **33** (1986), 2481.

[77] P. Glidic, O. Maillet, A. Aassime, C. Piquard, A. Cavanna, U. Gennser, Y. Jin, A. Anthore und F. Pierre, *Physical Review X* **13** (2023), 011030.

[78] M. Goerbig, *Reviews of Modern Physics* **83** (2011), 1193.

[79] D. González-Cuadra, A. Dauphin, P.R. Grzybowski, M. Lewenstein und A. Bermudez, *Physical Review Letters* **125** (2020), 265301.

[80] M. Goryca, J. Li, A.V. Stier, T. Taniguchi, K. Watanabe, E. Courtade, S. Shree, C. Robert, B. Urbaszek, X. Marie et al. , *Nature communications* **10** (2019), 4172.

[81] L. Gor'Kov und I. Dzyaloshinskii, *Sov. Phys. JETP* **26** (1968), 449.

[82] T. Graß, O. Cotlet, A. İmamoğlu und M. Hafezi, *Physical Review B* **101** (2020), 155127.

[83] T. Graß, B. Juliá-Díaz, N. Baldelli, U. Bhattacharya und M. Lewenstein, *Physical Review Letters* **125** (2020), 136801.

[84] I.H. Grinberg, M. Lin, C. Harris, W.A. Benalcazar, C.W. Peterson, T.L. Hughes und G. Bahl, *Nature communications* **11** (2020), 974.

[85] E. Gross, *Annals of Physics* **19** (1962), 234.

[86] F. Grusdt und E. Demler, *Quantum Matter at Ultralow Temperatures* **191** (2015), 325.

[87] F. Grusdt und E. Demler. In *Quantum Matter at Ultralow Temperatures.* IOS Press (2016), Seiten 325–411.

[88] F. Grusdt, R. Schmidt, Y.E. Shchadilova und E. Demler, *Physical Review A* **96** (2017), 013607.

[89] F. Grusdt, N.Y. Yao, D. Abanin, M. Fleischhauer und E. Demler, *Nature communications* **7** (2016), 11994.

[90] F. Grusdt, N.Y. Yao und E. Demler, *Physical Review B* **100** (2019), 075126.

[91] N.E. Guenther, P. Massignan, M. Lewenstein und G.M. Bruun, *Physical review letters* **120** (2018), 050405.

[92] N.E. Guenther, R. Schmidt, G.M. Bruun, V. Gurarie und P. Massignan, *Physical Review A* **103** (2021), 013317.

[93] F.D.M. Haldane, *Physical Review Letters* **51** (1983), 605.

[94] F.D.M. Haldane und E.H. Rezayi, *Physical review letters* **54** (1985), 237.

[95] E.H. Hall et al. , *American Journal of Mathematics* **2** (1879), 287.

[96] M.Z. Hasan und C.L. Kane, *Reviews of modern physics* **82** (2010), 3045.

[97] J. Hoeller und A. Alexandradinata, *Physical Review B* **98** (2018), 024310.

[98] O. Hryhorchak, G. Panochko und V. Pastukhov, *Journal of Physics B: Atomic, Molecular and Optical Physics* **53** (2020), 205302.

[99] M.G. Hu, M.J. Van de Graaff, D. Kedar, J.P. Corson, E.A. Cornell und D.S. Jin, *Physical review letters* **117** (2016), 055301.

[100] I.N. Hulea, S. Fratini, H. Xie, C.L. Mulder, N.N. Iossad, G. Rastelli, S. Ciuchi und A.F. Morpurgo, *Nature materials* **5** (2006), 982.

[101] R.G. Hulet, J.H. Nguyen und R. Senaratne, *Review of Scientific Instruments* **91** (2020).

[102] A. Imamoglu, O. Cotlet und R. Schmidt, *Comptes Rendus. Physique* **22** (2021), 1.

[103] M. Iqbal, N. Tantivasadakarn, R. Verresen, S.L. Campbell, J.M. Dreiling, C. Figgatt, J.P. Gaebler, J. Johansen, M. Mills, S.A. Moses et al. , *Nature* **626** (2024), 505.

[104] S.K. Ivanov, Y.V. Kartashov, A. Szameit, L. Torner und V.V. Konotop, *ACS Photonics* **7** (2020), 735.

[105] J.K. Jain: *Composite fermions.* Cambridge University Press, 2007.

[106] D. Jaksch und P. Zoller, *Annals of physics* **315** (2005), 52.

[107] T. Jonckheere, J. Rech, B. Grémaud und T. Martin, *Physical Review Letters* **130** (2023), 186203.

[108] N.B. Jørgensen, L. Wacker, K.T. Skalmstang, M.M. Parish, J. Levinsen, R.S. Christensen, G.M. Bruun und J.J. Arlt, *Physical review letters* **117** (2016), 055302.

[109] G. Jotzu, M. Messer, F. Görg, D. Greif, R. Desbuquois und T. Esslinger, *Physical review letters* **115** (2015), 073002.

[110] M. Jürgensen, S. Mukherjee und M.C. Rechtsman, *Nature* **596** (2021), 63.

[111] M. Jürgensen und M.C. Rechtsman, *Physical review letters* **128** (2022), 113901.

[112] C. Kane, P. Lee und N. Read, *Physical Review B* **39** (1989), 6880.

[113] Y. Ke, X. Qin, F. Mei, H. Zhong, Y.S. Kivshar und C. Lee, *Laser & Photonics Reviews* **10** (2016), 995.

[114] P.G. Kevrekidis: *The discrete nonlinear Schrödinger equation: mathematical analysis, numerical computations and physical perspectives*, Band 232. Springer Science & Business Media, 2009.

[115] P.G. Kevrekidis, Y.S. Kivshar und A.S. Kovalev, *Physical Review E* **67** (2003), 046604.

[116] M.S. Kirsch, Y. Zhang, M. Kremer, L.J. Maczewsky, S.K. Ivanov, Y.V. Kartashov, L. Torner, D. Bauer, A. Szameit und M. Heinrich, *Nature Physics* **17** (2021), 995.

[117] Y.S. Kivshar und D.K. Campbell, *Physical Review E* **48** (1993), 3077.

[118] K.v. Klitzing, G. Dorda und M. Pepper, *Physical review letters* **45** (1980), 494.

[119] C. Kohstall, M. Zaccanti, M. Jag, A. Trenkwalder, P. Massignan, G.M. Bruun, F. Schreck und R. Grimm, *Nature* **485** (2012), 615.

[120] M. Koschorreck, D. Pertot, E. Vogt, B. Fröhlich, M. Feld und M. Köhl, *Nature* **485** (2012), 619.

[121] Y.E. Kraus, Y. Lahini, Z. Ringel, M. Verbin und O. Zilberberg, *Physical review letters* **109** (2012), 106402.

[122] A. Kumar, S. Sachdev und V. Tripathi, *Physical Review B* **106** (2022), L081120.

[123] I. Kylänpää und H.P. Komsa, *Physical Review B* **92** (2015), 205418.

[124] L. Landau und S. Pekar, *Zh. Eksp. Teor. Fiz* **18** (1948), 419.

[125] S. Larentis, H.C. Movva, B. Fallahazad, K. Kim, A. Behroozi, T. Taniguchi, K. Watanabe, S.K. Banerjee und E. Tutuc, *Physical Review B* **97** (2018), 201407.

[126] J.Y.M. Lee, C. Hong, T. Alkalay, N. Schiller, V. Umansky, M. Heiblum, Y. Oreg und H.S. Sim, *Nature* **617** (2023), 277.

[127] J. Léonard, S. Kim, J. Kwan, P. Segura, F. Grusdt, C. Repellin, N. Goldman und M. Greiner, *Nature* **619** (2023), 495.

[128] J. Levinsen, L.A.P. Ardila, S.M. Yoshida und M.M. Parish, *Physical Review Letters* **127** (2021), 033401.

[129] J. Levinsen, F.M. Marchetti, J. Keeling und M.M. Parish, *Physical Review Letters* **123** (2019), 266401.

[130] J. Levinsen, M.M. Parish und G.M. Bruun, *Physical Review Letters* **115** (2015), 125302.

[131] D. Leykam und Y.D. Chong, *Physical review letters* **117** (2016), 143901.

[132] T. Li, L. Duca, M. Reitter, F. Grusdt, E. Demler, M. Endres, M. Schleier-Smith, I. Bloch und U. Schneider, *Science* **352** (2016), 1094.

[133] W. Li und S.D. Sarma, *Physical Review A* **90** (2014), 013618.

[134] G.B. Liu, W.Y. Shan, Y. Yao, W. Yao und D. Xiao, *Physical Review B—Condensed Matter and Materials Physics* **88** (2013), 085433.

[135] M. Lohse, C. Schweizer, O. Zilberberg, M. Aidelsburger und I. Bloch, *Nature Physics* **12** (2016), 350.

[136] Y.E. Lozovik, I. Ovchinnikov, S.Y. Volkov, L. Butov und D. Chemla, *Physical Review B* **65** (2002), 235304.

[137] D. Lundholm und N. Rougerie, *Physical Review Letters* **116** (2016), 170401.

[138] L. Ma, P.X. Nguyen, Z. Wang, Y. Zeng, K. Watanabe, T. Taniguchi, A.H. MacDonald, K.F. Mak und J. Shan, *Nature* **598** (2021), 585.

[139] E. Macaluso et al. , (2020).

[140] A. MacDonald und S. Girvin, *Physical Review B* **34** (1986), 5639.

[141] P. Massignan, C.J. Pethick und H. Smith, *Physical Review A* **71** (2005), 023606.

[142] P. Massignan, N. Yegovtsev und V. Gurarie, *Physical review letters* **126** (2021), 123403.

[143] P. Massignan, M. Zaccanti und G.M. Bruun, *Reports on Progress in Physics* **77** (2014), 034401.

[144] F. Mei, J.B. You, D.W. Zhang, X. Yang, R. Fazio, S.L. Zhu und L.C. Kwek, *Physical Review A* **90** (2014), 063638.

[145] S. Mistakidis, G. Katsimiga, G. Koutentakis, T. Busch und P. Schmelcher, *Physical review letters* **122** (2019), 183001.

[146] S. Mittal, G. Moille, K. Srinivasan, Y.K. Chembo und M. Hafezi, *Nature Physics* **17** (2021), 1169.

[147] R. Morf und B. Halperin, *Physical Review B* **33** (1986), 2221.

[148] S. Mukherjee und M.C. Rechtsman, *Science* **368** (2020), 856.

[149] S. Mukherjee und M.C. Rechtsman, *Physical Review X* **11** (2021), 041057.

[150] A. Munoz De Las Heras, E. Macaluso und I. Carusotto, *Physical Review X* **10** (2020), 041058.

[151] S. Nakajima, T. Tomita, S. Taie, T. Ichinose, H. Ozawa, L. Wang, M. Troyer und Y. Takahashi, *Nature Physics* **12** (2016), 296.

[152] J. Nakamura, S. Liang, G.C. Gardner und M.J. Manfra, *Nature Physics* **16** (2020), 931.

[153] C. Nayak, S.H. Simon, A. Stern, M. Freedman und S. Das Sarma, *Reviews of Modern Physics* **80** (2008), 1083.

[154] S. Novikov, S.V. Manakov, L.P. Pitaevskii und V.E. Zakharov: *Theory of solitons: the inverse scattering method.* Springer Science & Business Media, 1984.

[155] K.S. Novoselov, A.K. Geim, S.V. Morozov, D. Jiang, M.I. Katsnelson, I.V. Grigorieva, S.V. Dubonos und A.A. Firsov, *nature* **438** (2005), 197.

[156] T. Ozawa, H.M. Price, A. Amo, N. Goldman, M. Hafezi, L. Lu, M.C. Rechtsman, D. Schuster, J. Simon, O. Zilberberg et al. , *Reviews of Modern Physics* **91** (2019), 015006.

[157] B. Paredes, P. Fedichev, J.I. Cirac und P. Zoller, *Physical Review Letters* **87** (2001), 010402.

[158] M.M. Parish, *Physical Review A* **83** (2011), 051603.

[159] N. Pernet, P. St-Jean, D.D. Solnyshkov, G. Malpuech, N. Carlon Zambon, Q. Fontaine, B. Real, O. Jamadi, A. Lemaître, M. Morassi et al. , *Nature Physics* **18** (2022), 678.

[160] N. Picqué und T.W. Hänsch, *Nature Photonics* **13** (2019), 146.

[161] D. Pimenov, A. Camacho-Guardian, N. Goldman, P. Massignan, G.M. Bruun und M. Goldstein, *Physical Review B* **103** (2021), 245106.

[162] D. Pines: *Theory of Quantum Liquids: Normal Fermi Liquids.* CRC Press, 2018.

[163] L. Pitaevskii und S. Stringari: *Bose-Einstein condensation and superfluidity*, Band 164. Oxford University Press, 2016.

[164] N. Prokof'ev und B. Svistunov, *Physical Review B* **77** (2008), 020408.

[165] N. Prokof'ev und B. Svistunov, *Physical Review B—Condensed Matter and Materials Physics* **77** (2008), 020408.

[166] M. Punk, P. Dumitrescu und W. Zwerger, *Physical Review A* **80** (2009), 053605.

[167] X.L. Qi und S.C. Zhang, *Reviews of modern physics* **83** (2011), 1057.

[168] Y.F. Qu, P.E. Dolgirev, E. Demler und T. Shi, *arXiv preprint arXiv:2209.10998* (2022).

[169] S.P. Rath und R. Schmidt, *Physical Review A* **88** (2013), 053632.

[170] P. Rivera, J.R. Schaibley, A.M. Jones, J.S. Ross, S. Wu, G. Aivazian, P. Klement, K. Seyler, G. Clark, N.J. Ghimire et al. , *Nature communications* **6** (2015), 6242.

[171] Y. Ronen, T. Werkmeister, D. Haie Najafabadi, A.T. Pierce, L.E. Anderson, Y.J. Shin, S.Y. Lee, Y.H. Lee, B. Johnson, K. Watanabe et al. , *Nature nanotechnology* **16** (2021), 563.

[172] M. Ruelle, E. Frigerio, J.M. Berroir, B. Plaçais, J. Rech, A. Cavanna, U. Gennser, Y. Jin und G. Fève, *Physical Review X* **13** (2023), 011031.

[173] K. Satzinger, Y.J. Liu, A. Smith, C. Knapp, M. Newman, C. Jones, Z. Chen, C. Quintana, X. Mi, A. Dunsworth et al. , *Science* **374** (2021), 1237.

[174] F. Scazza, G. Valtolina, P. Massignan, A. Recati, A. Amico, A. Burchianti, C. Fort, M. Inguscio, M. Zaccanti und G. Roati, *Physical review letters* **118** (2017), 083602.

[175] W. Schäfer und M. Wegener: *Semiconductor optics and transport phenomena.* Springer Science & Business Media, 2013.

[176] A. Schirotzek, C.H. Wu, A. Sommer und M.W. Zwierlein, *Physical review letters* **102** (2009), 230402.

[177] R. Schmidt und T. Enss, *SciPost Physics* **13** (2022), 054.

[178] R. Schmidt, T. Enss, V. Pietilä und E. Demler, *Physical Review A* **85** (2012), 021602.

[179] R. Schmidt, T. Enss, V. Pietilä und E. Demler, *Physical Review A—Atomic, Molecular, and Optical Physics* **85** (2012), 021602.

[180] R. Schmidt und M. Lemeshko, *Physical review letters* **114** (2015), 203001.

[181] R. Schmidt und M. Lemeshko, *Physical Review X* **6** (2016), 011012.

[182] R. Schmidt, H. Sadeghpour und E. Demler, *Physical review letters* **116** (2016), 105302.

[183] M.O. Scully und M. Zubairy: *Quantum Optics, Cambridge University Press, 1997.*, 2003.

[184] A. Shashi, F. Grusdt, D.A. Abanin und E. Demler, *Physical Review A* **89** (2014), 053617.

[185] Y.E. Shchadilova, R. Schmidt, F. Grusdt und E. Demler, *Physical review letters* **117** (2016), 113002.

[186] T. Shi, J. Pan und S. Yi, *arXiv preprint arXiv:1909.02432* (2019).

[187] Z.Y. Shi, S.M. Yoshida, M.M. Parish und J. Levinsen, *Physical Review Letters* **121** (2018), 243401.

[188] M. Sidler, P. Back, O. Cotlet, A. Srivastava, T. Fink, M. Kroner, E. Demler und A. Imamoglu, *Nature Physics* **13** (2017), 255.

[189] M. Sidler, P. Back, O. Cotlet, A. Srivastava, T. Fink, M. Kroner, E. Demler und A. Imamoglu, *Nature Physics* **13** (2017), 255.

[190] M.G. Skou, T.G. Skov, N.B. Jørgensen, K.K. Nielsen, A. Camacho-Guardian, T. Pohl, G.M. Bruun und J.J. Arlt, *Nature Physics* **17** (2021), 731.

[191] D. Smirnova, D. Leykam, Y. Chong und Y. Kivshar, *Applied Physics Reviews* **7** (2020).

[192] T. Smoleński, O. Cotlet, A. Popert, P. Back, Y. Shimazaki, P. Knüppel, N. Dietler, T. Taniguchi, K. Watanabe, M. Kroner et al. , *Physical review letters* **123** (2019), 097403.

[193] D. Solnyshkov, O. Bleu, B. Teklu und G. Malpuech, *Physical review letters* **118** (2017), 023901.

[194] T. Sowiński und M.Á. García-March, *Reports on Progress in Physics* **82** (2019), 104401.

[195] N. Spethmann, F. Kindermann, S. John, C. Weber, D. Meschede und A. Widera, *Physical review letters* **109** (2012), 235301.

[196] P. St-Jean, V. Goblot, E. Galopin, A. Lemaître, T. Ozawa, L. Le Gratiet, I. Sagnes, J. Bloch und A. Amo, *Nature Photonics* **11** (2017), 651.

[197] H. Stoof und M. Bijlsma, *Physical Review E* **47** (1993), 939.

[198] K.E. Strecker, G.B. Partridge, A.G. Truscott und R.G. Hulet, *Nature* **417** (2002), 150.

[199] C. Sulem und P.L. Sulem: *The nonlinear Schrödinger equation: self-focusing and wave collapse*, Band 139. Springer Science & Business Media, 2007.

[200] M. Sun, H. Zhai und X. Cui, *Physical Review Letters* **119** (2017), 013401.

[201] A. Szameit und S. Nolte, *Journal of Physics B: Atomic, Molecular and Optical Physics* **43** (2010), 163001.

[202] D. Thouless, *Physical Review B* **27** (1983), 6083.

[203] M. Tikhanovskaya, H. Guo, S. Sachdev und G. Tarnopolsky, *Physical Review B* **103** (2021), 075141.

[204] M. Tikhanovskaya, H. Guo, S. Sachdev und G. Tarnopolsky, *Physical Review B* **103** (2021), 075142.

[205] D.C. Tsui, H.L. Stormer und A.C. Gossard, *Physical Review Letters* **48** (1982), 1559.

[206] M. Verbin, O. Zilberberg, Y. Lahini, Y.E. Kraus und Y. Silberberg, *Physical Review B* **91** (2015), 064201.

[207] J. Vlietinck, J. Ryckebusch und K. Van Houcke, *Physical Review B—Condensed Matter and Materials Physics* **87** (2013), 115133.

[208] M. Wagner, R. Ołdziejewski, F. Rose, V. Köder, C. Kuhlenkamp, A. İmamoğlu und R. Schmidt, *arXiv preprint arXiv:2310.08729* (2023).

[209] G. Wang, A. Chernikov, M.M. Glazov, T.F. Heinz, X. Marie, T. Amand und B. Urbaszek, *Reviews of Modern Physics* **90** (2018), 021001.

[210] S. Watanabe, K. Ando, K. Kang, S. Mooser, Y. Vaynzof, H. Kurebayashi, E. Saitoh und H. Sirringhaus, *Nature Physics* **10** (2014), 308.

[211] X.G. Wen, *International Journal of Modern Physics B* **4** (1990), 239.

[212] X.G. Wen: *Quantum field theory of many-body systems: from the origin of sound to an origin of light and electrons.* OUP Oxford, 2004.

[213] X.G. Wen: *Quantum field theory of many-body systems: From the origin of sound to an origin of light and electrons.* Oxford university press, 2004.

[214] P. Wrzosek und K. Wohlfeld, *Physical Review B* **103** (2021), 035113.

[215] L. Wu, M. Salehi, N. Koirala, J. Moon, S. Oh und N. Armitage, *Science* **354** (2016), 1124.

[216] S. Wu, L. Cheng und Q. Wang, *Physical Review B* **100** (2019), 115430.

[217] S. Wu, V. Fatemi, Q.D. Gibson, K. Watanabe, T. Taniguchi, R.J. Cava und P. Jarillo-Herrero, *Science* **359** (2018), 76.

[218] S. Xia, D. Jukić, N. Wang, D. Smirnova, L. Smirnov, L. Tang, D. Song, A. Szameit, D. Leykam, J. Xu et al. , *Light: Science & Applications* **9** (2020), 147.

[219] D. Xiao, M.C. Chang und Q. Niu, *Reviews of modern physics* **82** (2010), 1959.

[220] Z.Z. Yan, Y. Ni, C. Robens und M.W. Zwierlein, *Science* **368** (2020), 190.

[221] N. Yegovtsev, P. Massignan und V. Gurarie, *Physical Review A* **106** (2022), 033305.

[222] S.M. Yoshida, S. Endo, J. Levinsen und M.M. Parish, *Physical Review X* **8** (2018), 011024.

[223] S.M. Yoshida, Z.Y. Shi, J. Levinsen und M.M. Parish, *Physical Review A* **98** (2018), 062705.

[224] D. Yoshioka: *The quantum Hall effect*, Band 133. Springer Science & Business Media, 2013.

[225] R. Yu, X.L. Qi, A. Bernevig, Z. Fang und X. Dai, *Physical Review B—Condensed Matter and Materials Physics* **84** (2011), 075119.

[226] Y. Zeng, Z. Xia, K. Kang, J. Zhu, P. Knüppel, C. Vaswani, K. Watanabe, T. Taniguchi, K.F. Mak und J. Shan, *Nature* **622** (2023), 69.

[227] C. Zhang, J. Sous, D. Reichman, M. Berciu, A. Millis, N. Prokof'ev und B. Svistunov, *Physical Review X* **13** (2023), 011010.

[228] S.C. Zhang, *International Journal of Modern Physics B* **6** (1992), 25.

[229] Y. Zhang, G. Sreejith und J. Jain, *Physical Review B* **92** (2015), 075116.

[230] O. Zilberberg, S. Huang, J. Guglielmon, M. Wang, K.P. Chen, Y.E. Kraus und M.C. Rechtsman, *Nature* **553** (2018), 59.